Exploring Novel Quantum Physics Using Ytterbium-171 in An Optical Cavity

by

Zeyang Li

B.S., Peking University (2017)
M.S., Massachusetts Institute of Technology (2019)

Submitted to the Department of Physics
in partial fulfillment of the requirements for the degree of

Doctor of Philosophy in Physics

at the

MASSACHUSETTS INSTITUTE OF TECHNOLOGY

May 2023

© 2023 Zeyang Li. All rights reserved.

The author hereby grants to MIT a nonexclusive, worldwide, irrevocable, royalty-free license to exercise any and all rights under copyright, including to reproduce, preserve, distribute and publicly display copies of the thesis, or release the thesis under an open-access license.

Author .....
Department of Physics
April 29, 2023

Certified by .....
Vladan Vuletic
Lester Wolfe Professor of Physics
Thesis Supervisor

Accepted by .....
Lindley Winslow
Associate Department Head of Physics

Exploring Novel Quantum Physics Using Ytterbium-171 in An Optical Cavity

by

Zeyang Li

Submitted to the Department of Physics
on April 29, 2023, in partial fulfillment of the
requirements for the degree of
Doctor of Philosophy in Physics

Abstract

In this thesis, I present the development of a cavity quantum electrodynamics (CQED) system using single or multiple ensembles of ytterbium-171 atoms and its use for quantum metrology and quantum information science investigations.

We develop and study a unified theoretical framework that describes CQED spin systems. We unify the two major roles of cavity light: the measurement of the atomic state and the *catalyst* for generating entanglement. The obtained model agrees well with the experimental results. We utilize this framework to implement and optimize a variety of quantum metrological applications.

With optimized parameters guided by the theoretical model, we achieve a near-unitary spin squeezing in the ground state manifold of ytterbium atoms. We observe a metrological gain of 6.5(4)dB, while the inferred metrological gain without measurement limitation can reach 13dB. In a second experiment, we coherently transfer the entanglement from the ground state manifold to the optical clock transition for its 10^5 times faster phase accumulation and higher relative accuracy compared with an rf-clock. We infer a 4.4dB of improvement in performance, which is the first demonstration of the quantum entanglement-assisted optical clock operation.

We also implement a time-reversal-based quantum metrology protocol. We demonstrate that this method benefits practical quantum metrology since it improves the signal-to-noise ratio by amplifying the signal rather than reducing the noise. Notably, it is insensitive to the measurement noise, the dominant limitation in previous experiments. With the time-reversal protocol, we observed a 12.8(9)dB metrological gain and a record high 11.8(5)dB gain of phase sensitivity.

We further bring it to quantum information science. We explore the out-of-time-ordered correlators (OTOCs), a benchmark of how fast the quantum information "scrambles" into the whole quantum many-body system. We demonstrate that the time-reversal method can efficiently use the quantum scrambler's exponentially fast dynamics as a way to improve the signal.

Altogether, we have built and upgraded the machine of this lab to be able to perform complicated quantum experiments. We can coherently and uniformly prepare

and initialize the atomic states, and use the cavity to generate quantum entanglement or undo it among the atomic ensemble. We not only improve the attainable performance of precision measurement but also extend the investigation of quantum metrology to the field of quantum information science.

Thesis Supervisor: Vladan Vuletic
Title: Lester Wolfe Professor of Physics

Acknowledgments

From the workforce point of view, the Yb clock lab has experienced three stages. The first stage, or the first generation, is mainly contributed by the first two PhD students from our lab: Akio Kawasaki and Boris Braverman. They built the lab from scratch, literally.

I joined the Yb clock lab in 2017, roughly seven years after the first generation of students started with an empty room. They had made fantastic contributions to this beautiful apparatus. Both of them devoted all their efforts to the primary goal of this lab: to demonstrate that the entanglement-assisted optical atomic clock can outperform the traditional optical atomic clock. I and other second generations: senior postdocs Edwin Pedrozo (joined 2016) and Simone Colombo (joined Sept 2017), another postdoc Albert Adiyatullin (with us 2019-2021), and two other PhD students, Chi Shu (joined Jan 2017 and graduated 2022) and Enrique (joined 2016), carried on what they left and had successfully built the very first prototype spin squeezing enhanced optical clock in the middle 2020.

We, the second generation, started a transition to a combination of pushing the technical limit and pursuing interesting physics with a good-enough apparatus, and produced some meaningful results. As we are near the end of our time in the Yb-clock lab, I am confident that the experiment's future is bright, and the majority of possibilities are now left for the fabulous third generation to explore. Gustavo Velez and Matthew Radzihovsky, two enthusiastic junior PhD students with solid technical and scientific backgrounds, are going to lead the experiments for the next few years.

Here seems like a good chance for me to thank many people. First, I want to thank my research advisor Professor Vladan Vuletić, who not only offered me a chance to conduct such an interesting research project in atomic physics, but also showed me what a good physicist should be like: work hard, never stop learning, and be curious about everything. Vladan offered me great freedom of what to do, and he could always find the exciting features hidden in their superficial, trivial forms.

I also want to express my thanks to all current and previous members of the

Ybclock team. I marginally overlapped with the first generations, even though, they have taught me a lot about science and how to do science both in-person and virtually. Most of the time in the lab, I spent with other second generations. The other PhD student Chi Shu joined the lab half year earlier than I did. He taught me a lot about electronics – something I had never learned before I joined the lab – and optical techniques. Without his help, I believe that half of the projects we have done so far would either be unable to finish or be extensively delayed. The three postdocs in the ^{171}Yb team are outstanding physicists and highly instructed me. Edwin is very hard working: he showed me that physicists sometimes indeed work 24x7. Simone joined around the same time as I did and made me realize that postdocs usually, indeed, know much more physics and work much more efficiently than beginning PhDs. Albert came from a semiconductor background, which is quite different but very important for us to advance one significant application of semiconductor techniques: diode laser.

I got a lot of help from the whole Vuletić group as well. Zak taught me a lot about electronics and introduced the modern control system: labscript, to our group. Beili taught me the funny difference between AOD and AOM, which saved me a lot of time. Also, in my last year, I had an opportunity to overlap a bit with the Rydberg lab. I gained a completely new feeling studying something quite different while having enough knowledge to understand things. You guys are very nice and we had some fun, Wenchao Xu, Tamara Sumarac, and Emily Qiu.

And in general, the Harvard-MIT Center of Ultracold Atom (CUA) is a great platform. All the PIs are very knowledgeable and nice. I am really honored to discuss physics with them during CUA events. Among all the PIs, I want to thank most to professor Wolfgang Ketterle, my academic advisor and the instructor of the online 8.421/422 courses. These two courses set me a solid background for atomic physics and I always learn something new while revisiting these lectures. The students and postdocs here are also fabulous. Especially, I have strong relations with a bunch of peers that I know even before being here: Muqing Xu from Markus' group, Yicheng Bao from John's group, Pai Peng and Changhao Li from Paola's group, and Jinggang Xiang from Wolfgang's group. We regularly meet and chat about interesting stuff in

and outside of physics. Specifically, I want to thank Pai and Jinggang, my previous roommates. We lived together for two years until COVID tore us apart. I also learned a lot from other more senior or younger PhD students in CUA, like Hengyun (Harry) Zhou from Misha's group, Li Du and Yu-Kun Lu from Wolfgang's group, Akira Sone, Mo Chen, Yi-Xiang Liu, Ken Xuan Wei and Guoqing Wang from Paola's group, Yu Wang from Kang-Kuen's group, Ognjen Markovic and Lin Su from Markus' group. Also, I want to thank our MIT-side CUA assistant Joanna Welch for her hard work.

Beyond the CUA, the MIT physics department is also a very helpful and welcoming organization. I want to thank Cathy and Sydney, the two very kind and warm assistants. Also, I learned a lot of physics from other faculties here. Specifically, I want to thank Professor Soonwon Choi, who happened to be a previous CUA member but is now somehow affiliated with the CTP side. I really enjoy collaborating with such a theorist that have a very strong power to handle all scientific problems of his expertise but also knows quite a lot about other fields, even in experiments.

I am grateful for another important part of my life here at MIT: the Fuyun Chinese Comedy Club. As a big fan of Xiangsheng (a traditional and popular Chinese comedy), I am very glad that I got to know and joined Fuyun in my early PhD life. It helped me get through some challenging periods and brought me tons of happiness. Just before writing this piece, I watched my four public performances again and realized how Xiangsheng's power helped me become a better person.

Most of all, I want to thank my family members who support me without condition: my respectful father and first mentor of science, Zhiqiang Li; my lovely mother and first mentor of life, Yi Qin; my grandparents, Hongjun Qin and Huiying Li, and my uncle Qiang Qin. With all your support, I have finally become the person I wanted to be. I hope I have made all of you proud. And, at the very end, I thank my soul mate Yuxin Kan. Thanks for your support emotionally and physically from the beginning of my PhD till now and to the future.



Contents

1 Introduction **35**

1.1 Quantum Entanglement: Maybe the Most Familiar Stranger 36

1.2 What to Investigate: Collective Spin States 37

1.3 Cavity Quantum Electrodynamics 38

1.4 Thesis Outline 39

2 The Yb-Clock Lab **41**

2.1 Overview of the System 41

2.1.1 The Hardware 42

2.1.2 Software Control and Analyss 43

2.1.3 Towards Remote Control 45

2.2 Laser System Upgrades 46

2.2.1 399nm Laser System 46

2.2.2 556nm Green Light System 51

2.2.3 578nm Clock Laser System 53

2.2.4 759nm Magic Wavelength Trap Laser System 57

3 How to Model A CQED Spin System **61**

3.1 Introduction and Explanation 61

3.2 Interaction between an atomic ensemble and a cavity mode 66

3.2.1 Atomic states and operators 67

3.2.2 Classical light field inside a cavity containing an atomic ensemble 68

3.3 Effective light-induced Hamiltonian for collective atomic state 72

3.3.1 Light-induced coherent effects on the collective atomic spin . . 73
3.4 Light-atom entanglement and non-unitary evolution of the collective atomic state . . . 75
3.4.1 Quantum Fisher Information Available in A Coherent State of Light: A Measurement Effect . . . 76
3.4.2 Measurement Backaction . . . 79
3.4.3 Example: (Strong) Cavity Measurement of the Atomic State . 81
3.4.4 Example: (Weak) Quantum Nondemolition Measurement Squeezing Experiments . . . 85
3.4.5 Gaussian State Representation . . . 86
3.4.6 Photon scattering: Individual Dephasing . . . 89
3.5 First-principle approach . . . 90

4 Quantum Metrology 101 **95**
4.1 The Building Block: Rabi and Ramsey Sequence . . . 96
4.2 Quantifying The Amount of Information a Measurement Carries . . . 99
4.3 Chain of QFI . . . 100
4.4 Readout . . . 101

5 Near-Unitarity and Hamiltonian Dynamics **105**
5.1 Review of Non-Unitary Behaviors . . . 105
5.2 Inhomogeneous and Homogeneous Coupling . . . 107
5.2.1 Experimental Protocol . . . 108
5.2.2 Conclusion and Outlook . . . 116
5.3 Wineland parameter . . . 116
5.4 Experimental Results . . . 121

6 Coherent Operation on the Optical Clock Transition **129**
6.1 Introduction . . . 130
6.2 Characterizing the OLC performance . . . 130
6.3 Squeezing on the Clock Transition . . . 135

6.4 Stability and Allan Deviation . . . 137
6.5 Outlook . . . 138

7 Time-Reversal of the Hamiltonian and Its Applications on Quantum Metrology 141
7.1 Introduction . . . 142
7.2 Characterizing the Reversibility . . . 144

8 Exponential Dynamics on An Unstable Trajectory; Out-of-Time-Ordered Correlators 153
8.1 Introduction to The Big Idea: Quantum Scrambling . . . 155

9 One Small Step For the Machine, One Big Step For the System 165
9.1 Overview of the Ongoing Upgrading . . . 165
9.1.1 Fast Rabi Oscillation . . . 165
9.1.2 Belt Lattice . . . 168
9.1.3 Incoherent Pump to the Clock State . . . 170
9.2 Potential Fun Physics With the Upgraded System . . . 170
9.2.1 Quantum Erasure With a Faster Rabi Drive . . . 170
9.2.2 Exploring the Quantum Few-body Chaotic System . . . 171
9.2.3 Clock State CQED . . . 172
9.2.4 Degenerate Fermi Gas with CQED . . . 173
9.3 Conclusions and Directions for the Future . . . 175

A Numerical Methods 177
A.1 Full Quantum Numerics . . . 177
A.1.1 Unitary Evolution . . . 178
A.1.2 Lindbladian and Master Equation . . . 178
A.2 Truncated Wigner Approximation . . . 179

B C4PO-board 183

Glossary 184

List of Figures

1-1 Early citation numbers for [108, Kitagawa, Ueda 1993]. 37

1-2 "Moore's Law" of atomic clocks' fractional frequency uncertainty. Blue data and line represent RF clock results, while red data and line represent optical clock results. RF data are extracted from NIST's review [132]. Optical data are from reviews [45, 134, 46] or recent results [21]. 39

2-1 **Personal understanding of the Labscript suite logic.** The hardware communicates with the software, and the data are analyzed, all within the same suite. 44

2-2 399nm Laser's power splitting. 46

2-3 **Two similar 399nm locking schemes.** (a) has better mode matching, and (b) saves power from the low efficiency in the fiber coupling. 47

2-4 Doppler-free Yb isotope spectroscopy for ${}^1S_0 \rightarrow {}^1P_1$ transition. $\mathbf{F} = \mathbf{J} + \mathbf{I}$. Bosonic isotopes (even atomic number) are isospin free ($\mathbf{I} = 0$), and fermionic isotopes are with isospins: $I_{171} = 1/2, I_{173} = 5/2$. The ground state ${}^1S_0$ has $\mathbf{J} = 0$, so only nuclear Zeeman splitting could exist, and spans much less than MHz. Thus we only label isotopes with their ${}^1P_1$ total angular momentum, and there are two slopes for Yb-171 and three slopes for Yb-173 (the $F = 7/2$ one is overlapping with $F = 3/2$). Yellow slopes marked by nonlinear crossover signal (CO) are from nonlinear crossover signals. Yb-168's abundance is only 0.13%; therefore, the slope is almost invisible, and Yb-175 and Yb-169 are not stable with half lifetime 4.2 days and 32 days such that they cannot exist in the HCL and our ytterbium oven. 49

2-5 The 399nm imaging system. 50

2-6 Imaging of atoms using on-resonance 399nm transition. 50

2-7 **Optics about the 556nm laser.** (a) Green light splitting station optical path scheme. (b) Frequency shifting in both 1112nm and 556nm. 51

2-8 Optical scheme of the infrared (1157nm) part of the clock laser before power amplification. 54

2-9 The mount of the PDH EOM and the fielding of its modulation signal. 55

2-10 The gain profile of the SOA at different input power. 56

2-11 The optics scheme of the Ti:Sapphire laser. The laser beam is expanded to be better coupled to optical fibers. 58

2-12 Control panels of the M2 Laser. Left is the SolsTiS panel, which controls the etalon of the Ti:Sapphire. Right is the Equinox panel, which controls the pump diode and the output power. 58

3-1 (a) Schematic diagram of an ensemble of atoms interacting with a single-mode cavity of length L. The incident field $\mathcal{E}_{\text{in}}$ builds up in the cavity to the value $\mathcal{E}_c$. The cavity field is coherently scattered by the atoms into the cavity with amplitude $\mathcal{E}_M$, and coherently radiated through the cavity mirrors to give the transmitted and reflected fields $\mathcal{E}_t$ and $\mathcal{E}_r$. The cavity field scatters from the atoms into free space with amplitude $\mathcal{E}_{4\pi}$, and from the cavity mirrors with amplitude $\mathcal{E}_{sc}$, which is assumed to be zero in a lossless cavity. (b) Level diagram of the atomic three-level system. $|\uparrow\rangle = |g\rangle$ and $|e\rangle$ are the two states interacting with the cavity light. ω_a, ω_c and ω_l are the atomic, cavity resonance frequencies and the probing light frequency, respectively. $\Delta = \omega_l - \omega_a$ and $\delta = \omega_l - \omega_c$ are the detunings of probing light from atomic and cavity resonance, respectively. The curve on the right represents the cavity transmission spectrum in the presence of atoms, and $2g$ is the vacuum Rabi splitting due to the light-atom interaction when $\omega_a = \omega_c$. The sphere in the bottom right represents a Bloch sphere formed by the N atoms of spin $\frac{1}{2}$, and the shaded distribution represents a CSS pointing along polar and azimuthal angles (θ, ϕ) in spherical coordinates where each atom is in a superposition state $\cos(\theta/2)\,|\uparrow\rangle + \sin(\theta/2)\mathrm{e}^{i\phi}\,|\downarrow\rangle$. . . 63

3-2 Precision of estimation of an unknown parameter x by measurement of a coherent state of light $|\alpha\rangle$. A change dx in some parameter x modifies the amplitude (blue) and phase (green) of $|\alpha(x)\rangle$. The optimum amount of information about dx can be extracted by measuring the state quadrature along the direction of change $\partial\alpha/\partial x$ of the coherent state, which in general, is a combination of phase and amplitude measurements. The shot noise of the coherent state of light (color-shaded area) limits the precision of the measurement. 77

3-3 (a) QFI per scattered photon per atom for different types of measurements. The solid blue line and the yellow dashed line correspond to the amplitude and phase components of the total QFI F_{A} and F_{ϕ}, respectively. The green dotted line represents the QFI $F_{\mathrm{A}}^{\mathrm{chirp}}$ for a chirped two-color measurement of the transmission amplitude through the cavity, which equals the total QFI $F_{\mathrm{A}} + F_{\phi}$; (b) The normalized total QFI for a chirped two-color measurement as a function of the cavity-atom detuning. The QFI is quite sensitive to the symmetry of the transmission lineshape, see text. 82

3-4 Measurement quality of the system σ_d^2 (variance of measurement spin noise normalized to SQL) for the chirped two-color measurement, with total atom number $N = 1000$, single atom cooperativity $\eta = 1.8$ and the total quantum efficiency for detecting photons is $q = 0.15$. The solid black curve corresponds to the theoretical model including both the total QFI and Raman scattering noise, and the dashed black curve only includes the QFI contained in the transmission amplitude. The red points are experimental data from [25]. The detection limit σ_d^2 first improves with photon number n_d as the fractional photon shot noise is reduced, and then increases with n_d due to spontaneous Raman scattering. 84

3-5 Illustration of the effects of the atom-light interaction on a CSS. (a) Original CSS on the equator of the Bloch sphere, $\langle S_z \rangle = 0$. (b) The effect of a single-shot optical measurement (see text) with usable QFI F_{use} and total QFI F_{tot}, which displaces the state along S_z based on the measurement and yields a resolution beyond the SQL (measurement-based spin squeezing), while broadening it along S_y due to the measurement backaction. (c) The envelope arising from averaging over many repeated measurements shows broadening along S_y. (d) Phase shift $\Delta\phi$ due to the atom-light interaction in zeroth order, Eq. 3.18. (e) The effect of single-axis twisting with shearing strength Q. (f) The complete final state for cavity spin squeezing with all phase shift, shearing, and state broadening due to unused information F contained in the light field. The equations below each plot give parametric expressions $(\tilde{S}_y, \tilde{S}_z) = (\cos\theta, \sin\theta)$ with $\theta \in [0, 2\pi)$ for the uncertainty ellipses of the atomic states which are indicated by dotted lines in the same colors as the states. In (c-f) the dashed red circle represents the uncertainty circle for the original CSS for comparison. 86

3-6 Linear increasing of the variance of $\hat{S}_y$ for an initial CSS along S_x direction under the effective collective dephasing Lindbladian operator. 93

4-1 Spectroscopy fringes for (blue) Rabi sequence and (orange) Ramsey sequence. In the Ramsey sequence, we use (left) $\Omega\tau_{\text{Ramsey}} = 10$ and (right) $\Omega\tau_{\text{Ramsey}} = 3$. 98

4-2 CSS and SSS Ramsey sequence. 102

5-1 Raman sideband cooling scheme. (a) An optical cavity along the Z-direction (gravity-direction) simultaneously resonates to both $|^1S_0, m_F = 1/2\rangle - |^3P_1, m_F = 3/2\rangle$ transition at 556 nm and the optical lattice beam at 759 nm. σ^+-polarized optical pumping beam and σ^+-polarized Raman beam are sent through the optical cavity. a frequency scanning σ^+ probe beam is sent through the optical cavity near resonance to measure atom number. An additional π-polarized Raman beam is applied with 15° against the X-direction lattice in the X-Y plane. The optical clock beam is aligned to the X-direction optical lattice to probe atomic temperature in that direction. Time-of-flight imaging with $^1S_0 - ^1P_1$ at 399 nm is performed at 35° against the X-direction in the X-Y plane. (b) With $B_z = 13.5$ G, Zeeman splittings at $^3P_1$ and $^1S_0$ are 20 MHz and 10kHz respectively. σ^+- and π-polarized Raman beams are red-detuned by 10 MHz to the $|^1S_0, m_F = 1/2, n\rangle - |^3P_1, m_F = 1/2\rangle$ or $|^1S_0, m_F = -1/2, n-1\rangle - |^3P_1, m_F = 1/2\rangle$ transitions with the resonant two-photon condition between the two ground states. 109

5-2 Clock state excitation spectroscopy of an atomic cloud loaded into a 2D optical lattice (a) without and (b) with 200ms cooling. Clock pulse lengths of 5 ms and 20 ms in (a) and (b) are applied, respectively. At high temperatures, the large cloud spanned over the harmonic trap, producing a broadening of the clock spectroscopy lineshapes on both the resonance and the trap frequency. At low temperatures, the quantized motion takes over and suppresses the red sideband. Assuming a thermal distribution of the atom, sidebands and carrier are fitted the apparent temperature of the cloud is calculated to be $T = 20 \pm 2\,\mu$K and $T = 1.8 \pm 0.5\,\mu$K with mean occupation number $\overline{n} = 6$ and $\overline{n} = 0.2$ respectively. Broad Doppler Gaussian profile is manually fitted to take into account floating atoms. 141 kHz and 90 kHz standard derivation imply temperatures of 22 μK and 10 μK, respectively. 111

5-3 Theory from [16], considering a factor of 2 difference between apparent temperature and actual. The difference from the theory for purple points (pi pulse) is due to the fraction of atoms that are not in the 2D trap. It increases when the temperature is higher. *Cooling performances of Raman sideband cooling of ^{171}Yb. X-direction atomic temperatures with different cooling times are measured using the fitting method outlined in Fig. 5-2. The direct measurement quantity is the collective cooperativity NC normalized to the initial condition.* 113

5-4 Cavity readouts during the cooling process. (a) Signatures of atomic reorganization due to cooling. Collective cooperativity $N_{\mathrm{eff}}C_{\mathrm{eff}}$ evolution with cooling time, normalized to the initial one. The gray band is calculated from the expected collective cooperativity, assuming that the cooling process drops the atoms weakly coupled to the cooling cavity mode. The lower limit of the band is collective cooperativity when we drop all atoms except those within 1 % of the maximal coupling; similarly, the upper limit is the expectation for the case where we drop all atoms except those within 10% of the maximal coupling. The inset shows the inferred survival rate $N_{\mathrm{tot}}(t)/N_{\mathrm{tot}}(0)$ as a function of the cooling time t. (b) Effective cooperativity as a function of the cooling time. The dashed line is a double-exponential fit. The illustrations on the side are schematics of atomic distribution among the incommensurate trapping and coupling lattices. Initially, atoms are evenly distributed in the trapping lattice, and after long-time cooling, the atoms are concentrated in lattice sites with high overlap with the coupling lattice. 114

5-5 Results of cavity feedback squeezing for a cavity that is resonant with the atomic transition, $\omega_c = \omega_a$. (a) Squeezing strength Q, quantum Fisher information F and inverse Wineland parameter ξ^{-2} at fixed scattered photon number $n_\gamma^{\mathrm{sc}} = 400$ and collective cooperativity $N_\uparrow \eta = 900$. (These parameters correspond to the conditions of the experiment described in Ref. [25]). For the Q plot, red branches stand for positive Q and blue branches for negative Q. In this calculation, the curvature of the Bloch sphere has been ignored, and the results do not depend on the single-atom cooperativity η. (b) Inverse Wineland parameter including the effect of the Bloch sphere curvature for different scattered photon number n_γ^{sc} calculated for the parameters $N = 1000$, $\langle S_z \rangle = 0$, and $\eta = 1.8$. Both (a) and (b) assume $\kappa/\Gamma = 2.8$ as in the experiment of Refs. [25, 168]. 117

5-6 (a, b) the optimal Wineland parameter with respect to the optimized photon number at given N and detuning, without (a) and with (b) Bloch sphere curvature effect, where from bottom to top the atom numbers are $N = \{1, 2, 4, 8, 16\} \times 500$. The single-atom cooperativity is $\eta = 1.8$. The green dots indicate the maximum Wineland parameter for a given atom number. (c, d) show the optimum detuning and maximum Wineland parameter as a function of atom number, corresponding to the parameters of the green dots in subfigures (a, b); the data points correspond to numerical simulations and the solid lines represent fits that hold for large atom number $N \gg 1$. 120

5-7 (a) Experimental setup. A one-dimensional optical lattice at λ_t=759 nm (red) traps the atoms. Light at λ=556 nm light (green), whose transmission is detected using a dichroic mirror (D) and a single-photon counter (SPC), is used for squeezing and probing. (b) Relevant energy levels of ^{171}Yb with ground state $\left|^1S_0, I=\frac{1}{2}\right\rangle$ and excited state $\left|^3P_1, F=\frac{3}{2}\right\rangle$. The Zeeman splitting in $\left|^3P_1, F=\frac{3}{2}\right\rangle$ is $\Delta_z/(2\pi)$=18.5 MHz for a magnetic field B_z=13.6 G along the cavity axis. (c) Cavity transmission spectrum showing vacuum Rabi splitting for $N\eta$=1800, as well as the two squeezing light pulses ω_{l1} and ω_{l2}. (d) Simplified representation of the squeezing and measurement sequence. (e) Quasiprobability distributions for a CSS (red) and SSS (blue). 122

5-8 Measured normalized spin noise $\sigma^2(\alpha)$, as a function of the state rotation angle α, for shearing strengths $Q = 0.3$ (blue circles), $Q = 2.2$ (green squares), $Q = 4.5$ (yellow triangles), and $Q = 6.3$ (red diamonds). For visualization, the data measured at α=0 are displayed at α=0.02 rad. The solid lines are theoretical fits. States in the violet region below the dashed line at $\sigma^2 = \sigma_d^2 = 0.11$ (detection limit) cannot be directly observed. Inset: σ_{st}^2 of SSS after subtracting measurement noise σ_d^2 for the same parameters. 124

5-9 Shearing strength Q (filled blue squares) and excess broadening factor F (red circles) plotted vs. the number p_t of transmitted photons. The open red circles correspond to the directly measured data with the theoretical model without free parameters (dotted red line), the solid circles are after subtraction of measurement noise σ_d^2 with a parameter-free model without (solid red line) and with (dashed red line) Bloch-sphere-curvature-induced broadening. 125

5-10 (a) Wineland metrological gain ξ_W^2 (blue), measured spin noise reduction ξ_-^2 (green), and inferred SSS noise ξ_{st}^2 (red) as a function of shearing strength Q. ξ_-^2 is limited by the measurement resolution and ξ_{st}^2 by the curvature of the Bloch sphere. (b) Ramsey contrast as a function of Q with initial contrast as only fitting parameter (solid line). (c) Allan deviation of a phase measurement for a CSS (black squares) with SQL (dashed line) and for a SSS with $Q = 3.8$ (p_t=130), $F = 0.8$ (red data). The red solid line is fit to the first three data points. The reduction in measurement time over the SQL is a factor of 3.7(2), represented by the orange star in (a). 126

6-1 **Setup and squeezed-clock sequence. a**, ^{171}Yb atoms are trapped inside an optical cavity in a two-dimensional magic-wavelength optical lattice along the x and z directions (red beams). Light for optical pumping and spin squeezing (green) is applied along the cavity axis z, while the clock laser (yellow) propagates along x. **b**, Energy levels and transitions. Purple, green, and yellow pulses indicate the ground-state radiofrequency (RF) transition $|\downarrow\rangle \rightarrow |\uparrow\rangle$, squeezing transition $\left|^1S_0, m_I = \frac{1}{2}\right\rangle \rightarrow \left|^3P_1, m_F = \frac{3}{2}\right\rangle$ at ω_{at}, and optical-clock transition $|\uparrow\rangle \rightarrow |e\rangle$, respectively. The system evolves either in the ground-state manifold $\{|\downarrow\rangle, |\uparrow\rangle\}$ (purple Bloch sphere), or in the clock-state manifold $\{|g\rangle, |e\rangle\}$ (yellow Bloch sphere). The cavity frequency ω_c is tuned in resonance with the squeezing transition, $\omega_c = \omega_{at}$. **c**, Spin squeezing. Strong coupling of the atoms to the cavity results in vacuum Rabi splitting of the cavity resonance (red peaks). A laser is applied detuned from the Rabi peak at frequency ω_{sq} (green peak) to produce a SSS via cavity feedback [25]. **d**, Squeezed-clock sequence. A SSS is prepared in the ground-state manifold $\{|\downarrow\rangle, |\uparrow\rangle\}$, transferred to the clock manifold $\{|g\rangle, |e\rangle\}$, evolved in a Ramsey sequence for time τ_R, and mapped back onto $\{|\downarrow\rangle, |\uparrow\rangle\}$, where a state measurement is performed. The evolution of the quantum state is depicted on the Bloch spheres for the RF (purple) and optical (yellow) transitions. 132

6-2 **Squeezed state tomography. a**, Rabi spectroscopy of the $|\uparrow\rangle \rightarrow |e\rangle$ transition to the clock state. The pulse duration is 0.22 ms. **b**, Rabi oscillations on the clock transition. **c**, Tomographic measurements of the SSS before (purple diamond) and after (orange circle) mapping onto the clock transition and back show very similar degrees of squeezing. The theoretical expectation for a state with $\xi_-^2 = -5.9$ dB is shown as a gray solid line. Two measured data points for a CSS are also shown (blue squares). The shaded area indicates the region below the SQL. Error bars represent 1σ statistical confidence interval. 134

6-3 **Spin noise and Wineland parameter on the clock transition as a function of time.** The measured normalized S_z spin noise ξ^2 (solid circles) and model (dashed lines) for the CSS (purple) and the SSS with squeezed axis aligned along S_z (dark-red) increases slowly with time. The increase is caused by the finite 800-ms lifetime of the state $|e\rangle$ due to scattering of the trapping light. The Wineland parameter ξ_W^2 (open squares) depends in addition on the contrast loss due to shortening of the atomic collective spin $|\langle\vec{S}\rangle|$ (inset, blue data points for CSS, red for SSS, with exponential fits). The solid lines represent the predicted Wineland parameter using the fit to the measured contrast. τ_{LO} indicates the coherence time of the LO. Error bars represent 1σ statistical confidence interval. 136

6-4 **Stability improvement with the squeezed clock.** In all three subfigures, the blue shaded area represents the region below the SQL, while the gray shaded area in a, b, represents the additional contribution from LO phase noise. **a**, Inferred single-clock cycle stability (self-comparison Allan deviation divided by $\sqrt{2}$ [2]) for a CSS (sequence *C1*, blue) and a SSS (*S1*, red) with Ramsey time $\tau_{S1} = 0.17$ ms. The squeezed clock operates within the gray region set by SQL and LO phase noise because the quantum projection noise is reduced below the SQL. **b**, Allan deviation for a SSS (sequence *S2*, green) with longer Ramsey time $\tau_{S2} = 1.16$ ms, where the total noise is dominated by the LO noise. Inset: Ramsey fringes vs. LO phase φ_{opt} of the second Ramsey π-pulse for *S2*. **c**, Data for *C1* and *S1* after subtraction of the LO phase noise, where the latter has been calculated from the data for *S2*. The dashed lines indicate the expected performance estimated from the separately measured Wineland parameter ξ_W^2, see Fig. 6-3. The other parameters for these measurement are: atom number $N = 300 \pm 30$, single-cycle time T_C=4s, Ramsey contrast $C_{C1} = 0.91(1)$ for CSS, $C_{S1} = 0.85(1)$ and $C_{S2} = 0.70(1)$ for SSS. Error bars represent 1σ statistical confidence interval. 137

7-1 **Setup and sequence. a.** ^{171}Yb atoms are trapped inside an optical cavity in an optical lattice. Light for state preparation, entanglement generation, and state measurement (green) is sent through the cavity along the z axis. The static magnetic field defines the quantization axis parallel to z. **b.** SATIN protocol sequence with the quantum-state evolution (top) and relevant energy-levels and cavity mode (bottom). Wigner quasiprobability distribution functions describing the collective quantum state are calculated for an ensemble of $N = 220$ atoms, and are represented on the generalized Bloch sphere for the ground-state manifold $\{|\downarrow\rangle, |\uparrow\rangle\}$. An entangling light pulse is passed through the cavity detuned by $+\Delta$ from the $|\uparrow\rangle \rightarrow |e\rangle$ transition and the cavity mode. This light generates the nonlinear OAT Hamiltonian $\hat{H} \propto \hat{S}_z^2$ which shears the initial CSS state (green arrows on the generalized Bloch sphere), the state depicted here corresponds to a shearing angle of $Q = 0.7\sqrt{N} = 10.4$. A rotation φ about the S_y axis displaces the state such that $\langle \hat{S}_z \rangle = \varphi S_0$; this rotation can be induced both by a direct resonant rf-pulse or effectively via a compound sequence $\mathcal{R}_y(\pi/2)\mathcal{R}_z(\varphi)\mathcal{R}_y(-\pi/2)$ as in Ramsey spectroscopy with squeezed states ($\mathcal{R}_j(\alpha)$ denotes a rotation of angle α about the j axis). We first characterize the protocol by applying a direct rotation along the y axis while later we implement it in a phase sensitive Ramsey sequence, where the $\mathcal{R}_z(\varphi)$ results from the accumulated phase in a spin echo sequence. Subsequently, a (dis)entangling light pulse is sent through the cavity detuned by $-\Delta$ from the $|\uparrow\rangle \rightarrow |e\rangle$ transition and the cavity mode. This pulse generate the negative OAT Hamiltonian $-\hat{H}$ which causes the quantum state to evolve effectively "backwards in time". With $\varphi = 0$ the quantum state evolves back to the original CSS, while for a small angle ($\varphi \neq 0$) the final state is displaced by an angle $m\varphi$ from the original CSS, where m is the SATIN signal amplification. 143

7-2 **State evolution during SATIN sequence. a.** Histograms showing the distributions of along the S_y axis measured at different times during the SATIN sequence. The system transitions from Gaussian states (blue histogram) to strongly non-Gaussian states (red, orange). After reversing the sign of the Hamiltonian, the original CSS is almost recovered (orange, lower plot). The solid lines are the predicted distributions from a theoretical model including finite contrast $\mathcal{C}$, measurement resolution $\sigma^2_{meas} = 0.15$ (i.e., a resolution of 6 atoms for $N = 220$), and excess broadening from light-atom entanglement $\mathcal{I}$. The Bloch spheres show the expected Wigner quasi-probability distributions at the corresponding times. **b.** The normalized S_y variance ($\sigma^2_y \equiv 2(\Delta S_y)^2/S_0$) as a function of the unshearing strength $\tilde{Q}_-$ for $\tilde{Q}_+ = 0.5$. The dashed line shows the model prediction. **c.** Measured variances of S_y resulting from shearing with $\tilde{Q}_+$ (solid circles), and after the corresponding unshearing $\tilde{Q}_-$ (open circles), with $\tilde{Q}_- = -\tilde{Q}_+$. Solid lines are theoretical predictions, including $\mathcal{C}$, σ^2_{meas} and $\mathcal{I}$. All error bars represent 1σ statistical uncertainty resulting from 100 to 150 experimental realizations. Error bars of σ^2_y are inferred by bootstrapping the data. 145

7-3 **Signal amplification and metrological gain.** All data are taken with $N = 220 \pm 12$ atoms. **a.** The mean value $\langle \hat{S}_y \rangle / S_0$ as a function of the angle φ. The solid black line is the maximal signal that can be reached with a CSS. Dashed lines represent calculations, solid lines are the linear fit to the data for small φ. **b.** The signal amplification as a function of the shearing parameter $\tilde{Q}_+$. The solid line is the model prediction. **c.** The resulting metrological gain $\mathcal{G}$ as a function of the squeezing strength $\tilde{Q}_+$, solid line shows the model prediction. The gray area represents the metrological gain accessible with a simple OAT squeezing in the same system with a measurement resolution $\sigma^2_{meas} = 0.15$ in variance (-8.2 dB). Error bars represent 1σ confidence intervals. 147

7-4 **Scaling of sensitivity with atom number and comparison with previous results. a.** Block diagram showing a SATIN scheme applied to a Ramsey interferometry experiment. Here the compound sequence of pulses that maps the phase accumulated during the Ramsey time into a phase displacement about the S_y axis. **b.** Phase Allan deviation plot of Ramsey spin echo interferometry performed with a CSS (purple circles) and an optimally over-squeezed state in a SATIN protocol (red circles). In both cases we used 340±20 atoms in the interferometer. The shaded purple area indicates the region below the SQL. The data for the SATIN sequence is fitted to a white noise model (red dashed line) showing 11.8±0.5 dB of metrological gain over the SQL. **c.** Comparison with previous results. Blue data: BEC experiments [77, 11, 152, 111, 201, 133]. Red data: Thermal atoms [4, 207, 38, 88, 25, 92]. Dark gray data: Ions [150, 18, 174]. Light gray data: Rydberg atoms in a tweezer array [161]. Green data: squeezing generated in an optical-lattice clock [168]. Squares are expected metrological gains, obtained by quantum state characterization. Stars refer to directly measured phase-sensitivity gain. Solid symbols are obtained in this work. Error bars represent 1σ confidence interval. Horizontal error bars are smaller than the markers. 149

8-1 **Equivalence of time-reversal based quantum metrology beyond the standard quantum limit (SATIN) and the fidelity out-of-time-order correlator (FOTOC).** The Bloch spheres and the shaded regions represent the Hilbert spaces and the states' Wigner distribution, respectively. The blue lines describe the procedures from the quantum information science point of view, while the red lines are in the quantum metrology language. 155

8-2 **Time-reversal based exponential growth of sensitivity in a system with an unstable fixed point. A**, Classically, for a trajectory with a positive Lyapunov exponent $\lambda_1 > 0$ an initial signal (displacement) $\delta(0)$ increases exponentially over time. For quantum dynamics, however, an initial overlap between two states is preserved under unitary evolution. To amplify the signal similarly to the classical case, one needs to evolve the state under the nonlinear $\hat{H}$, resulting in decreased quantum fluctuations along a direction with negative Lyapunov coefficient $\lambda_2 < 0$. A displacement along this direction followed by application of the negative Hamiltonian $-\hat{H}$ (such that $\lambda_{1,2} \to -\lambda_{1,2}$) is then used to amplify the signal. These plots also correspond to the Bloch sphere, where the S_y and S_z axes are labeled as in the left subplot of the middle row. **B**, Experimental setup. The LMG Hamiltonian is generated by the interaction of the collective atomic spin with light inside a cavity on the transition $|\uparrow\rangle \to |e\rangle$, while a radiofrequency magnetic field is applied to rotate the atomic spin. 156

8-3 **Collective-spin evolution in the CQED system. A,** Numerical calculation of the normalized variance ξ_+^2 of the antisqueezed direction as a function of $S\chi t$ and $\Omega/S\chi$ with linecuts representing the measurements in **B**, **C**. **B,** The antisqueezing for a given $S\chi t = 1.8$ as a function of the rotation strength Ω. The shaded region indicates exponential growth, while in the other regions the time evolution is either quasi-periodic or growing polynomially. **C,** Comparison of antisqueezing ξ_+^2 between the fastest exponential growth for a critical rotation strength $\Omega = S\chi$, and the polynomial growth of pure OAT ($\Omega = 0$). The two Bloch spheres represent the lines of classical evolution in both situations. The dashed and dash-dotted red lines represent exponential growth based on the theoretically predicted Lyapunov exponent and the full numerical result, respectively. The gray dashed line is calculated for $\Omega = 0$. Inset: logarithmic plot for $\Omega = S\chi$ showing the exponential growth of ξ_+^2. **D,** The Binder cumulant, characterizing the shape of the distribution, for the antisqueezed direction for the critical LMG condition $\Omega = S\chi$ vs. time t. Insets: spin distribution with $S\chi t = 0$ (blue) and $S\chi t = 2$ (purple), with the latter being strongly non-Gaussian. 158

8-4 **Metrological gain with exponential LMG time-reversal protocol.** The squared signal amplification G^2 (pink open circles) and system noise N^2 (blue solid squares) vs. time t. The orange dashed line represents the exponential growth of the anti-squeezing shown in Fig. 8-3, representing an upper bound to the QFI. The blue dash-dotted line is the calculated noise due to residual light-atom entanglement. The maximum metrological gain is 6.8(4) dB. 160

8-5 **FOTOC and OTOC extracted from quantum state tomography. A**, Experimental Wigner functions obtained from quantum state tomography after the LMG SATIN protocol with different signal displacements $\delta\phi$ (for $\Omega = S\chi$ and $t = 0.57(S\chi)^{-1}$). The dashed circle indicates the orginal CSS state. **B**, The solid blue line is a quadratic fit used to extract the OTOC $\mathcal{I}$ (see text and eq. 8.3). 161

8-6 **Comparison between quantum information and quantum metrology parameters for the LMG model.** The red open circles, solid green squares, and solid blue diamonds represent the antisqueezing, metrological gain, and OTOC, respectively. All quantities increase initially exponentially with time with a fitted Lyapunov exponent $\lambda_Q = 1.01(3)S\chi$ that agrees well with the theoretical prediction $\lambda_Q = S\chi$. The OTOC errorbars are obtained by using the bootstrapping method [80]. For longer times $t \gtrsim (S\chi)^{-1}$, the metrological gain and OTOC decrease due to decoherence caused by light-atom entanglement, as is well captured by the theoretical model (solid blue line). 163

9-1 Related Yb-171 energy levels and the driving fields. Replicated from [98]. 166

9-2 Top row: $\theta = 10°, 30°, 40°$, and bottom row: $\theta = 50°, 60°, 60°$, where the last one zoomed in time axis. $\theta = 60°$ is the closest to the paper setup [98]. 167

9-3 Optical Rabi oscillations with 1.2 mW power (supposedly) and 400kHz Optical Rabi Frequency using circularly polarized light. 167

9-4 Locating the position of the MOT and overlapping it with the transverse lattice. Figure adopted from [209]. 168

9-5 Atoms are moving with the belt lattice's transportation. 169

9-6 Hamiltonian from left to right: $\hat{H}_0 = \chi(\hat{S}_{z,(1)}+\hat{S}_{z,(1)})^2, \hat{H}_1 = \chi\hat{S}^2_{z,(1)}, \hat{H}_2 = \chi\hat{S}^2_{z,(2)}$ 172

9-7 The cavity field's amplitude and phase for the symmetric clock situation. 173

9-8 Left: Extended energy level of ytterbium-171 atom. Right: Generation of degenerate Fermi gas by pumping to the dark metastable $^3P_0$ clock state. 175

A-1 Variance along x-direction for a CSS under the OAT Hamiltonian. The blue line is from the analytical formula (A.14), and the red dashed line is interpolated numerical results from the truncated Wigner approximation method. 182

B-1 Solidworks rendering of the C4PO. Left: double-pass AOM. Right: Green power splitting station. 183

Citations to Previously Published Work

Some of the chapters in this thesis have appeared in print elsewhere. By chapter number, they are

- Chap. 3: *Collective Spin-Light and Light-Mediated Spin-Spin Interactions in an Optical Cavity*, Zeyang Li, Boris Braverman, Simone Colombo, Chi Shu, $\cdots$, Vladan Vuletić, PRX Quantum 3, 020308, 2022 ([125]).

- Chap. 5: (1) *Near-Unitary Spin Squeezing in* ^{171}Yb, Boris Braverman, Akio Kawasaki, Edwin Pedrozo, Simone Colombo, Chi Shu, Zeyang Li, $\cdots$, Vladan Vuletić, Phys. Rev. Lett 122, 223203, 2019, and (2) *Two-photon Resolved-Sideband Raman Cooling of* ^{171}Yb *in an optical cavity*, Chi Shu, Simone Colombo, Zeyang Li, $\cdots$, Vladan Vuletić, Phys. Rev. Lett , 2023 ([25, 35]).

- Chap. 6: *Entanglement on an optical atomic-clock transition*, Edwin Pedrozo, Simone Colombo, Chi Shu, Albert Adiyatullin, Zeyang Li, $\cdots$, and Vladan Vuletić, Nature 588, 414-418, 2020 ([168]).

- Chap. 7: *Time-reversal-based quantum metrology with many-body entangled states*, Simone Colombo, Albert Adiyatullin, Edwin Pedrozo, Zeyang Li, $\cdots$, and Vladan Vuletić, Nature Physics 18, 925-930, 2022 ([35]).

- Chap. 8: *Improving Metrology with Quantum Scrambling*, Zeyang Li, Simone Colombo, Chi Shu, $\cdots$, Vladan Vuletić, Science, 2023 ([126]).

And the results in Chap. 9 are actively being transformed into a more scientifically organized form of writing. I hope we can soon see familiar graphs in some manuscripts.

In addition to the aforementioned publications, I have published a few papers in various journals. These can be summarized in a few different categories:

- Experimental progress led by the first generation: (1) *Geometrically asymmetric optical cavity for strong atom-photon coupling*, Akio Kawasaki, Boris Braverman, Edwin Pedrozo, Chi Shu, Simone Colombo, Zeyang Li, $\cdots$, Vladan Vuletić, Phys. Rev. A 99, 013437, 2019, and (2) *Trapping* ^{171}Yb *Atoms into a One-Dimensional Optical Lattice with Small Waist*, Akio Kawasaki, Boris Braverman, Edwin Pedrozo, Chi Shu, Simone Colombo, Zeyang Li, Vladan Vuletić, Phys. Rev. A 102, 013114, 2020 ([101, 102]).

- Theoretical works using the Ybclock underlying system: "Generating Extreme Spin Squeezing", Sebastian C. Carrasco, Michael H. Goerz, Zeyang Li, Simone Colombo, Vladan Vuletić, Vladimir S. Malinovsky, Phys. Rev. Applied 17, 064050, 2022 ([27]).

- Works outside the Ybclock and Vuletić group: (1) *Comparing many-body localization length via non-perturbative construction of local integrals of motion*, Pai Peng, Zeyang Li, Haoxiong Yan, Ken Xuan Wei, Paola Cappellaro, Phys. Rev. B 100, 214203, 2019, and (2) *Scalable quantum tomography with fidelity estimation*, Jun Wang, Zhao-Yu Han, Song-Bo Wang, Zeyang Li, Liang-Zhu Mu, Heng Fan, and Lei Wang, Phys. Rev. A 101, 032321, 2020, ([170, 232])

Chapter 1

Introduction

In the thesis title, I used "Exploring Novel Quantum Physics Using ytterbium-171 in An Optical Cavity". This is way too abstract, even for experts in this field. Here I would like to break it up into three interesting components, raise three questions respectively, and answer them in this chapter. The answers, however, will lead to more questions, that will eventually be discussed throughout this thesis.

First of all, Novel Quantum Physics. When talking about it, what I really mean are fascinating phenomena of quantum physics based on quantum entanglement. But quantum entanglement can be perceived very differently in different fields of study. What view will we use in this thesis?

Besides that, the title suggests that we are investigating ytterbium-171. This specific atom has an ideal spin-1/2 ground state structure and is commonly used for clock operation: a type of research that focuses on the collective response of atoms. Thus, what we will deal with is collective spin physics; but what does it mean, and why do we care about it?

Finally, we investigate the atoms in an Optical Cavity, which forms a Cavity Quantum Electrodynamics (CQED) system. What's specific about adding this extra component, and is there anything new in our system?

With all these questions, I would like to discuss the three components with a little bit more, before giving the essential details.

1.1 Quantum Entanglement: Maybe the Most Familiar Stranger

Most physics major students should know something about quantum entanglement. However, physicists from different specific divisions focus more on their own direction of study; thus, their understanding and perspective of quantum entanglement can differ significantly. For instance, astrophysicists might view quantum entanglement as a specific modification to stellar objects, such as a strongly interacting Fermionic system of neutron stars. Condensed matter physicists may classify quantum entanglement as a way to categorize topological orders. Additionally, quantum information physicists may consider quantum entanglement as a resource for performing certain quantum tasks, such as computing or communicating.

In this thesis, I will mostly focus on the quantum metrology point of view of quantum entanglement. Since essentially these are all about quantum entanglement, these perspectives overlap largely; however, the quantum metrological way of thinking is, to me, the most straightforward way and directly relates to the field of metrology and sensing.

The field of quantum-enhanced metrology studies how quantum entanglement helps phase estimation, an essential concept in the field of metrology that I will review in Chap. 4. Since the scenario is restricted to phase estimation, only some specific forms of quantum entanglement are useful. Such entanglement and its impact on phase estimation are quantified by the Quantum Fisher Information (QFI). This quantity is not common to the other communities studying quantum entanglement; however, I will try to convince the audience that in certain contexts, the QFI can also provide properties similar to other characterizations of quantum entanglement, like entanglement entropy and out-of-time-ordered correlators.

1.2 What to Investigate: Collective Spin States

Problems with collective spin states are not new. Since the framework of the quantum angular momentum was established, early quantum physicists have tried to understand the properties of the collective state of many spins. As early as 1940, Theodore Holstein developed the simplifications to such systems [86] which we are still using nowadays. However, to make the external control interact solely with the collective spin state is not easy: one has to create a very symmetric and coherent environment to control the collective state, and it was even impossible to observe nonlinear interacting phenomena from a collective spin system. Thus when Kitagawa and Ueda proposed the one-axis twisting and two-axis twisting method to generate spin squeezing in 1993 [108], not many physicists were eager to investigate such phenomena experimentally since these types of Hamiltonian evolution were not yet ready. In fact, the Kitagawa-Ueda paper, which we now view as seminal work, was turned down by Physical Review Letters. See Fig. 1-1, prior to 2001, this paper was rarely cited.

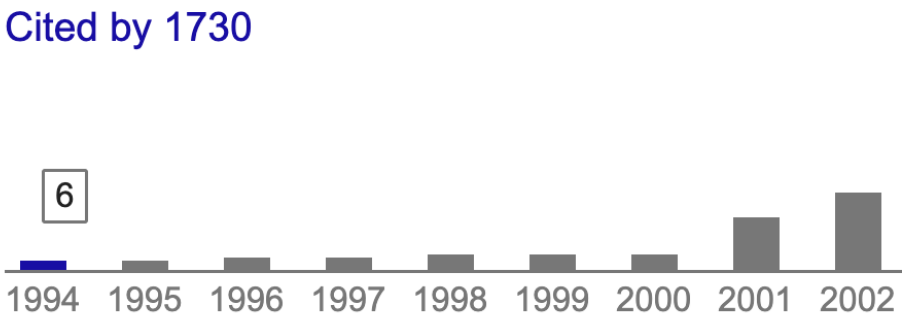


Figure 1-1: Early citation numbers for [108, Kitagawa, Ueda 1993].

What happened around 2000? At that time, scientists realized that a light-matter quantum interface is a perfect tool for collective spin physics. Under certain conditions, the light mode indeed coherently couples to the collective states [113, 115, 114]. To further ensure that only one optical mode coherently couples to all the spins, the usage of an optical cavity seems very straightforward, where the density of optical

modes is discretized such that the original spectrally flat energy density distribution is reallocated into a few specific modes. This, in turn, makes the interaction between atoms and light greatly enhanced [178, 106, 151].

Of course, different techniques aiming for similar physics were developed in other systems. One example relies on the spinor Bose-Einstein Condensation (BEC) system: the great coherence of BEC and the collisional spin-spin interaction makes this system also promising to investigate features of collective spin states [69, 184]; also, some long-range interactions such as dipolar interaction in NV centers and Rydberg-Rydberg interaction can be approximately considered as collective spin states which thus can be used to generate spin squeezing [19, 53, 84]. For the rest of the thesis, I will restrict the discussion to the collective spin physics inside an optical cavity.

1.3 Cavity Quantum Electrodynamics

As mentioned above, the optical cavity is very beneficial for investigating collective spin systems since the cavity mode not only intrinsically couples to all atoms but also couples very strongly [106, 222, 125].

As also mentioned earlier, I want to focus on some metrological aspects of this system. Using the cavity in this direction began as early as 2010 [121, 199, 200]. However, these proof-of-principle results were not very well accepted by the community of quantum metrology, as the technical improvements led the rapid progress at that time. As one can see in Fig. 1-2, the optical clock's fractional frequency uncertainty increases dramatically at the speed of 4dB/yr. However, the speed was slowed down to 1db/yr afterward, and the significance of cavity squeezing became clearer.

Naturally, questions pop up in our minds. Would the entanglement really work and help state-of-the-art clocks and precision measurements? Is squeezing the only way to help? Are there any other slightly more complicated add-ons to make the metrology even better? Are there more things to be done in collective spin physics?

With these questions in mind, I shall present my thesis, and try to answer some of them in detail.

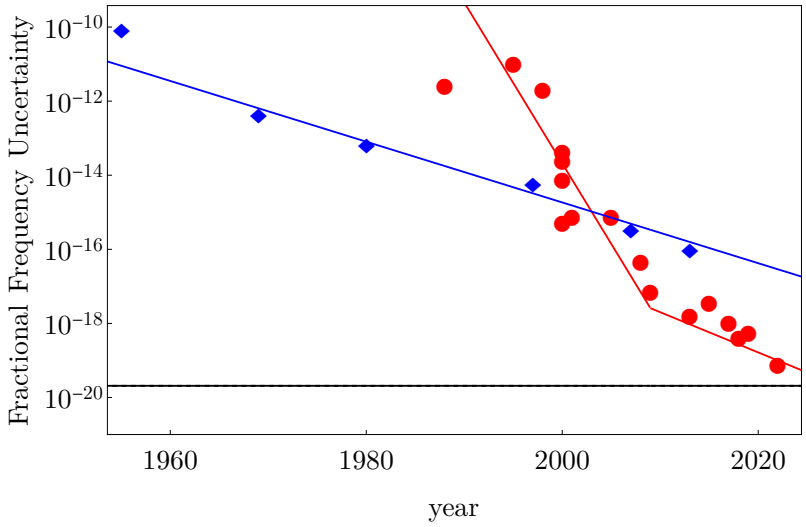


Figure 1-2: "Moore's Law" of atomic clocks' fractional frequency uncertainty. Blue data and line represent RF clock results, while red data and line represent optical clock results. RF data are extracted from NIST's review [132]. Optical data are from reviews [45, 134, 46] or recent results [21].

1.4 Thesis Outline

The remainder of this thesis is structured as follows. In Chap. 2, I first introduce the experimental apparatus used for this thesis. The design is mostly similar to the one described in the previous generation's thesis [100, 24], with some essential upgrades. In Chap. 3, I will describe how to treat and model the system such that we can reduce it to a simple collective spin physics. I will then discuss one of the major applications of the system I described: quantum metrology, in Chap. 4.

Starting from Chap. 5 I will introduce the results developed during my Ph.D. In Chap. 5 I will focus on previous near-unitary results since these are essential for all other results and benchmark the major difference between our system and other similar systems. Then in Chap. 6 I will further demonstrate our control of the clock transition and how we obtained improvements in optical clocks. Then comes a completely innovative breakthrough in this field: a time-reversal control of the Hamiltonian. I will start with the record-high metrological gain we obtained for a Ramsey sequence in Chap. 7. Then by generalizing this to more complicated dynamics, we found a link between quantum information science and quantum metrology under the

time-reversal control in Chap. 8.

Finally, in Chap. 9 I will discuss a few ongoing exciting projects we are about to accomplish: upgrading the system to accommodate more than one ensemble. With these simple upgrades, one can now do much more interesting physics with the collective spin system, including investigating quantum few-body chaos and operating a continuous version of the clock.

Chapter 2

The Yb-Clock Lab

In this chapter, I will briefly explain our experimental apparatus, especially what I have upgraded since the first generation [100, 24], together with Shu [209] and the postdocs (AKA the second generation).

2.1 Overview of the System

Before I dive into the details, it may be helpful to describe the experimental sequence briefly. Here I will summarize the procedure in a not-too-detailed manner, i.e., I will not specify exactly how each physical procedure is accomplished; instead, I will mention abstractly what happened to the system. These procedures might seem simple based on our knowledge at this moment, but several of them were very innovative and provided substantial advances in the field when they were invented.

The typical experiment proceeds as follows: a ytterbium oven at 300°C constantly produces hot ytterbium atoms with a flux of 10^{10} atoms/s. The atoms are trapped and cooled by the magneto-optical trap (MOT) generated by the blue (399nm) laser, which is on resonance with the 28MHz wide transition ${}^1S_0 \leftrightarrow {}^1P_1$, and the MOT magnetic coil. Then suddenly, we turn off the blue laser and ramp the magnetic coil values such that the atoms first move with the magnetic field to a designated location, where they are further cooled by the green (556nm, on resonance with the 180kHz narrow transition ${}^1S_0 \leftrightarrow {}^3P_1$) MOT for a lower temperature [103]. Then we

turn off the green laser as well, and turn on the red (759nm) laser through the cavity to load the atoms into the optical lattices formed by the red laser, then turn the MOT coils off. Applying an additional bias magnetic field of 13G which defines the quantization axis, we then optically pump the atoms by sending σ^+-polarized green light through the cavity. After that, we apply a certain portfolio of RF magnetic fields close to the resonance of the ground state magnetic splitting, and send a near-resonance green light through the cavity, and/or yellow (578nm) light through the same transverse direction as the red transverse lattice. Finally, we send near resonant green light again, through the cavity while ramping the frequency, as a measurement of the atomic state.

We need our apparatus to handle all the procedures. For that purpose, at a high level, the lab needs hardware and software parts. The hardware controls all the devices, while the software translates our abstract way of describing the sequences into specific instructions to those hardware devices with certain time sequences. I will discuss both separately. Since we are working on a software transition without changing the hardware too much, the hardware part would only be a supplement to the previous Ph.D. theses describing this experiment of the lab [100, 24, 209].

2.1.1 The Hardware

Let's start with the hardware, the backbone of the experiment. We can further split the hardware here into roughly three important ingredients: the container of the major experiment (the vacuum system), the tools to generate conditions for the experiments (lasers, magnetic field controls, frequency generators, etc.), and the final measurement (photon counter). The vacuum system is exactly the one the first generation built: the obtained ultra-high vacuum (UHV) ensures us a second-long atom lifetime with reasonably strong trapping. The measurement tool is also the same: we count individual photons transmitted through the cavity and record their arrival times using a fast counting board P7888.

The middle part, tools to provide an appropriate electromagnetic environment for experiments, are very complicated. These are also very similar to the first generation's

machine, but we also made our own upgrades. Let's start with the low-frequency magnetic field controls. We drive the field by sending currents through different magnetic field coils. The currents are provided by the metal-oxide-semiconductor field-effect transistor (MOSFET) and feedback based on a small sensing resistor. Such setups control the MOT magnetic field gradient, the bias coil for nuclear Zeeman splitting, and even our 10kHz RF drive on the ground state spin. Recently, we also tested a few more tools, such as using the audio amplifier to drive the RF coil and using green lasers to generate fast rotations, which I will explain in detail later.

The electric fields interacting with the atoms are mostly at optical frequencies, i.e., via laser fields. We have many different lasers, but most frequently, we use blue 399nm laser, green 556nm laser, yellow 578nm laser, and red 759nm laser. These lasers need to be frequency stabilized. The 399nm laser is stabilized by the vapor lamp since the related transition has a very wide lineshape; the rest of the lasers are all locked to Ultra low expansion (ULE) glass cavity. No matter how we lock the frequency, one needs to generate frequency shifts via Electro-Optic Modulators (EOMs) or Acoustic-Optic Modulators (AOMs). Both modulators should be supplied with high-power RF electric fields[1]. To drive such high-power RF signals, we use a two-stage amplification after the source, and the source is either from AD9959 Direct Digital Synthesis (DDS) or from a voltage-controlled oscillator (VCO).

The above summarizes our hardware system. The details of upgrades will be introduced in Sec. 2.2, while the ongoing upgrades and the related interesting physics will be later discussed in Chap. 9.

2.1.2 Software Control and Analyss

After more than 10 years of using Labview as the software tool to control the system, we finally abandoned this obsolete "visual programming language", and adopted a modern controlling and analyzing system: the labscript suite. One can find a more

[1]Note that for EOMs, an alternative application would be using them as a phase shifter with low-frequency voltage. This will be essential for the optical feedback of the laser, which will be discussed later.

complete introduction to this suite at https://labscriptsuite.org/ and at [12, 215]. Here I briefly introduce each component of this suite and leave the details to another thesis from our lab [144].

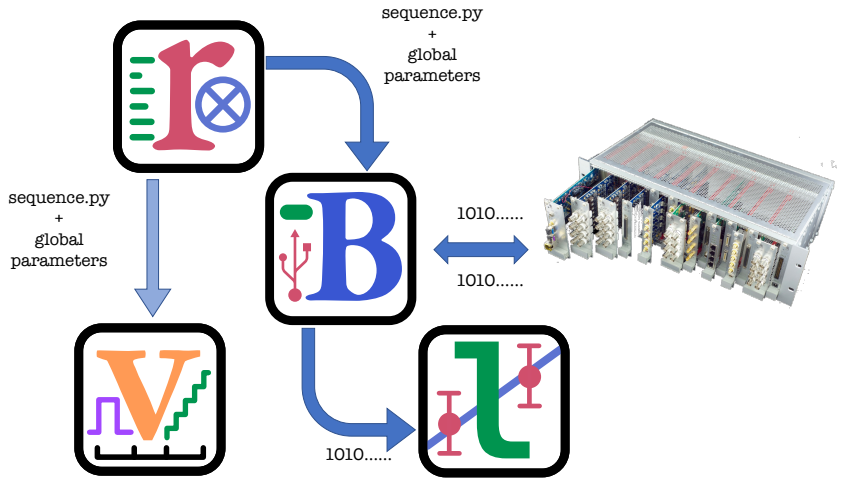


Figure 2-1: **Personal understanding of the Labscript suite logic.** The hardware communicates with the software, and the data are analyzed, all within the same suite.

The Labscript suite has four major components whose structure is illustrated in Fig. 2-1: runmanager (r), blacs (B), lyse (l) and runviewer (V). Their roles are as follows: essentially, the computer communicates with the hardware via `blacs`. The `blacs` initially compiles a "connection table" which indicates what the hardware apparatuses are and how to control them (the driver and the API that `blacs` understands). After that, each experiment needs one copy of the abstract form of sequence description (usually we write in `.py` scripts) and the set of global variables as parameters. The global variables are controlled and maintained on `runmanager`, which also specifies what sequence to run next. The hardware also measures things via voltage I/O, photon counting, camera imaging, or other forms, which is also controlled by and communicated with `blacs`. Based on these measurements, `lyse` will analyze the results in both shot-by-shot and multi-shot hyper-analysis forms. The `runviewer` is an independent tool. It can visualize the sequence that the `blacs` will send to the apparatus. This can map the abstract sequence to exactly which device is doing what, thus very handy to debug.

The labscript suite automatically supports many devices, ranging from the National Instrument card to cameras from a wide range of brands. However, each experiment would have its own devices that are either unique or uncommon. The Labscript allows one to write its own interpretation of those devices such that they can be used by the `.py` file similar to other devices; for us, we have a few different FPGA modules and a photon counter.

Besides, we have a bunch of other software tools, such as a few laser control interfaces; these will be discussed when I introduce them later.

2.1.3 Towards Remote Control

The need for remote control first arises during the lockdown due to COVID. Motivated by the success of another CUA cold atom lab which was upgraded to operate 7×24 taking data, we are eager to make our machine remotely controllable. Here, I will provide ideas on how this could be achieved. However, I will leave the majority of the tasks for the third generation.

On a good day, the minimal daily routine requires turning lasers and other powers on and off, rotating a few knobs, and engaging the switches for a few lock boxes, and that's it. However, even remotely controlling these is not an easy task.

The first step would be turning things on and off. A voltage-controlled relay will do this job easily.

Then it comes to when lasers get out of the lock. We need the scheme to detect the unlock. For lasers locked to ULE cavities (and the experimental cavity locked to the laser), this can be detected via the drop of the transmission. This relies on the feature of a real-time detector which can interrupt the running of the labscript. This is not yet developed.

For the lasers locked to the atomic feature (like the 399nm laser that I will discuss in Sec. 2.2.1), we have to implement a between-sequence feedback by unlocking the laser, characterize the feature (i.e., by measuring the SD and mean of the error signals of the range) and use electric-controlled rotational mount to bring the error signal to the desired value and adjust the error lockpoint. These have been implemented

individually but not yet integrated into the full system.

In short, a fully remotely controllable system is very promising, and I hope the Ybclock lab would achieve this in near future.

2.2 Laser System Upgrades

2.2.1 399nm Laser System

Toptica DL-PRO Solution

For first-generation students, the 399nm laser was a pain to play with. First of all, the single diode is not powerful enough for all our applications mentioned above. Thus they used a master-slave laser system, where the master laser is firstly stabilized using an external cavity diode laser (ECDL). Then, by sending two counter-propagating lasers into a ytterbium hollow-cathode lamp (HCL), they successfully locked the laser by the dichroic atomic vapor laser lock (DAVLL) technique [36] to the transition related to the ^{171}Yb isotope we are interested in. After the slave laser, there were around 120mW of 399nm power spread in many modes, and only a tiny portion of it could be collected by the single-mode fiber, which barely satisfied the purpose.

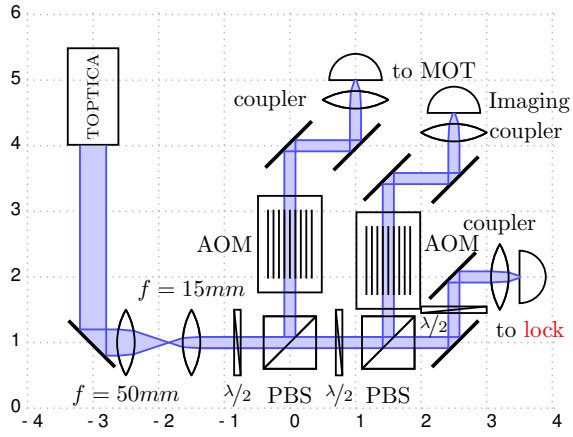


Figure 2-2: 399nm Laser's power splitting.

That's not yet finished. To maintain the high level of output, we need to operate the slave laser always at a high current, which makes it age very rapidly. Consequently,

we could not inject it with no other transverse modes excited in late 2020. Since we were also bothered by the pandemic, we decided to move to a more stable laser system commercially available at TOPTICA (DLC-DL-PRO-HP-399), with a single mode output at 150mW and mode-hop free frequency tuning range of 20GHz. We also adopted the modulation transfer spectroscopy, as in [233], to lock the 399nm laser such that we now can faithfully get rid of the broad Doppler background, which sometimes has even stronger noise than our locking signal for the DAVLL locking. The full scheme is shown in Fig. 2-2. The output from the TOPTICA laser is firstly beam shaped then split into two paths: the major path with more than 85mW (50mW after fiber) goes to the MOT, and 10mW (5mW after fiber) is sent to a separate lock path as in Fig. 2-3. Check the values!!! Especially Imaging powers!!!

Locking scheme and error signal

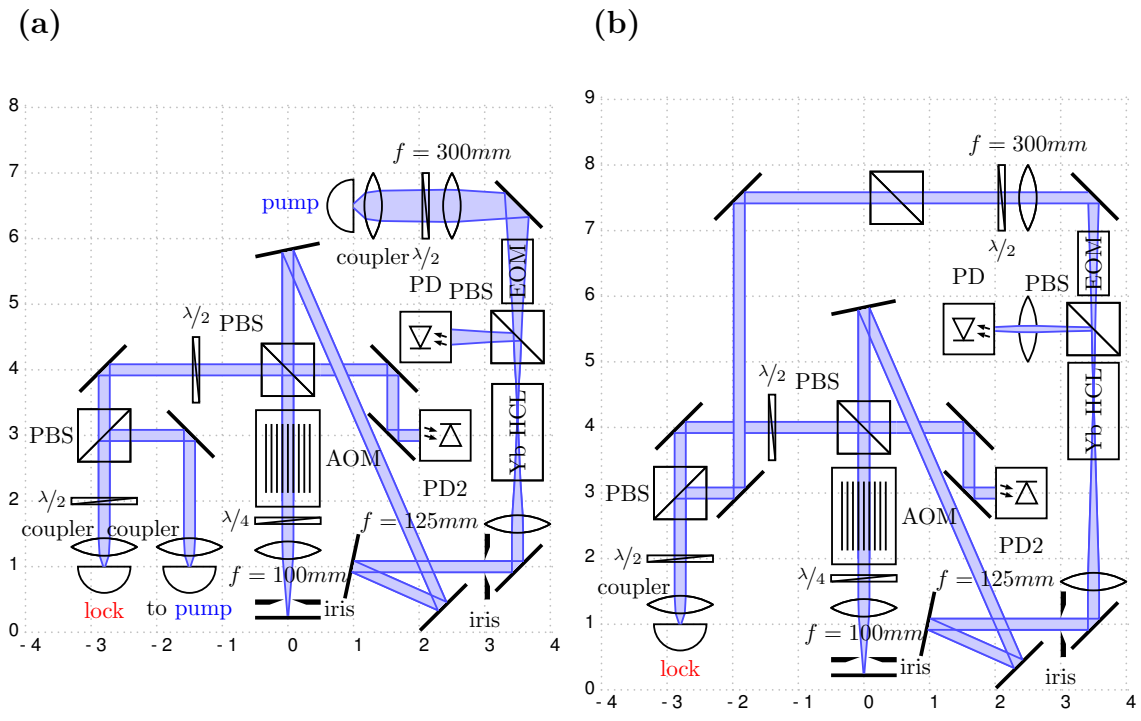


Figure 2-3: **Two similar 399nm locking schemes.** (a) has better mode matching, and (b) saves power from the low efficiency in the fiber coupling.

As you can note, in Fig. 2-3(a) and (b), we have two different methods for sending the beam to the HCL. In both cases, the power is allocated by the $\lambda/2$ plate and

the PBS. In Fig. 2-3(a), The laser path splits to the probe path (passing the PBS) and the pump path (sending into the "to pump" fiber coupler), where the pump path is connected through fiber for historical reasons such that minimal (re-)alignment is required. The pump is then focused by a $f = 300mm$ lens and sent through a modulated EOM, and generates a saturation absorption on ytterbium atoms in the HCL. The probe light then goes into a standard double-pass AOM setup with a $\lambda/4$ waveplate to let it through the PBS and is then shifted by 80MHz (40MHz in each pass). Then the light is focused by a $f = 125mm$ lens and sent into the ytterbium HCL to interfere with the saturation absorption generated by the pump, and collected by the PD. The signal in PD is amplified and mixed with the same frequency modulating the EOM and then low-passed. We obtain a clean error signal of ytterbium 399nm lines by tuning the mixing phase. The typical error signal that we lock to is as in Fig. 2-4, and with the TOPTICA DLC, we can turn on/off and lock/unlock/relock the laser remotely.

We note that this method sacrifices the power during the fiber of the "pump" path. In Fig. 2-3(b), this is directly free-space sent for probe the HCL, and thus the optics are fine-tuned to make the beam mode match. We thus obtain a larger error signal.

On the other hand, both methods have the probe path that goes into another PBS, and the majority is reflected back to the AOM, while a small portion passes through and is collected by a photodetector PD2. Due to the drift of the polarization after the fiber connection from Fig. 2-2 to Fig. 2-3, the power to the probe path and the pump path is drifting all the time. We stabilize it by measuring the PD2 and feedback to the first $\lambda/2$ plate, which is electronically controlled by a Thorlabs Motorized Precision Rotation Mount. This makes sure the power on the probe path is fixed, and since the pump is strong enough to generate saturation, the power does not affect our signal much.

Imaging And Andor Zyla 5.5 sCMOS Camera

As early as 2020, we were looking for ways to fluorescence or absorption image the atoms. An early test was done to obtain the atomic ensemble's size before and after

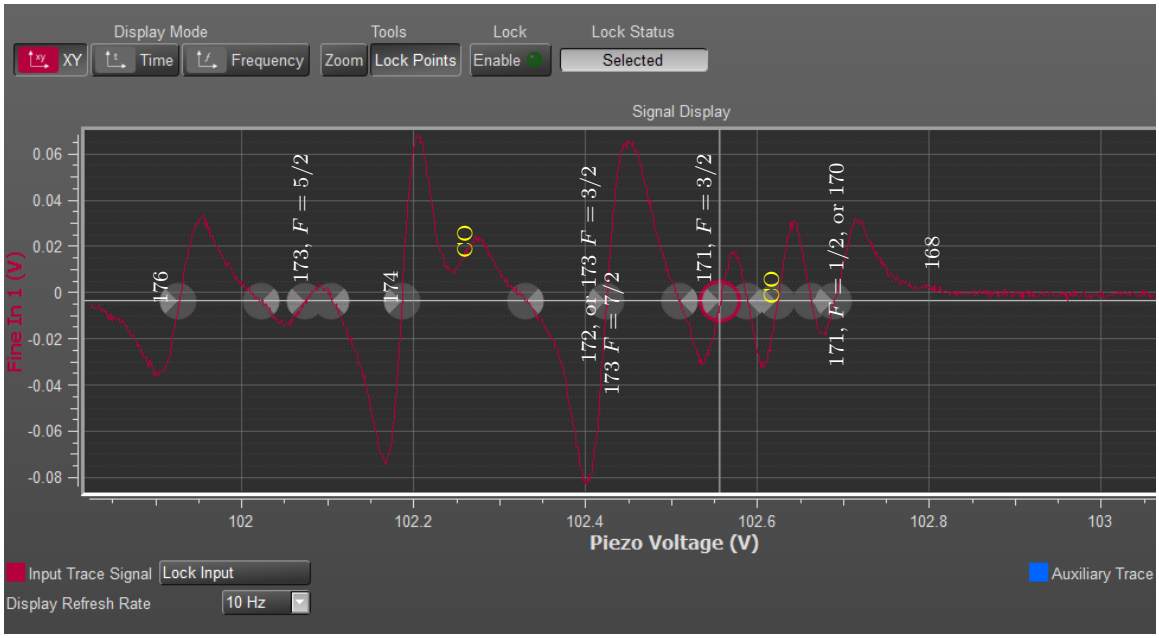


Figure 2-4: Doppler-free Yb isotope spectroscopy for ${}^1S_0 \rightarrow {}^1P_1$ transition. $\mathbf{F} = \mathbf{J} + \mathbf{I}$. Bosonic isotopes (even atomic number) are isospin free ($\mathbf{I} = 0$), and fermionic isotopes are with isospins: $I_{171} = 1/2, I_{173} = 5/2$. The ground state ${}^1S_0$ has $\mathbf{J} = 0$, so only nuclear Zeeman splitting could exist, and spans much less than MHz. Thus we only label isotopes with their ${}^1P_1$ total angular momentum, and there are two slopes for Yb-171 and three slopes for Yb-173 (the $F = 7/2$ one is overlapping with $F = 3/2$). Yellow slopes marked by nonlinear crossover signal (CO) are from nonlinear crossover signals. Yb-168's abundance is only 0.13%; therefore, the slope is almost invisible, and Yb-175 and Yb-169 are not stable with half lifetime 4.2 days and 32 days such that they cannot exist in the HCL and our ytterbium oven.

the cooling, as we will discuss later in Chap. 5. Since then, we have not used the imaging system for many years, and thus the alignment is off.

For the next generation of experiments, we need to bring this imaging back to work. The optical path is fairly simple: we collect the imaging beam from the AOM as in Fig. 2-2, and send it to another fiber coupling near the chamber to make it a collimated beam. We align the beam to roughly overlap with the original camera since it should not be too off and then use the cavity measurement (see Section. 3.4.3 for details) to make sure that this beam can blow atoms away.

In the end, we realized that the imaging path is very abnormal since the coating is Thorlabs A coating, which is for 350 - 700 nm and is optimized and characterized for 532nm. For 399nm, many numbers may differ a bit. Once these errors add up, the

situation will get much more complicated. Thus, we use the geometry that a doublet $f_1 = 12.5$cm focal length lens (AC254-125-A) is placed roughly at the focal length away from the position of atoms, and another lens with the same specification is about $2f_1$ separated[2]. Then another lens (AC254-030-A) with a focal length $f_2 = 3$cm is placed $f_1 + f_2 = 15.5$cm away from the second lens, and a lens with the focal length $f_3 = f_1 = 12.5$cm is placed $f_2 + f_3$ away from the third lens. Finally, the camera is placed f_3 away from the last lens.

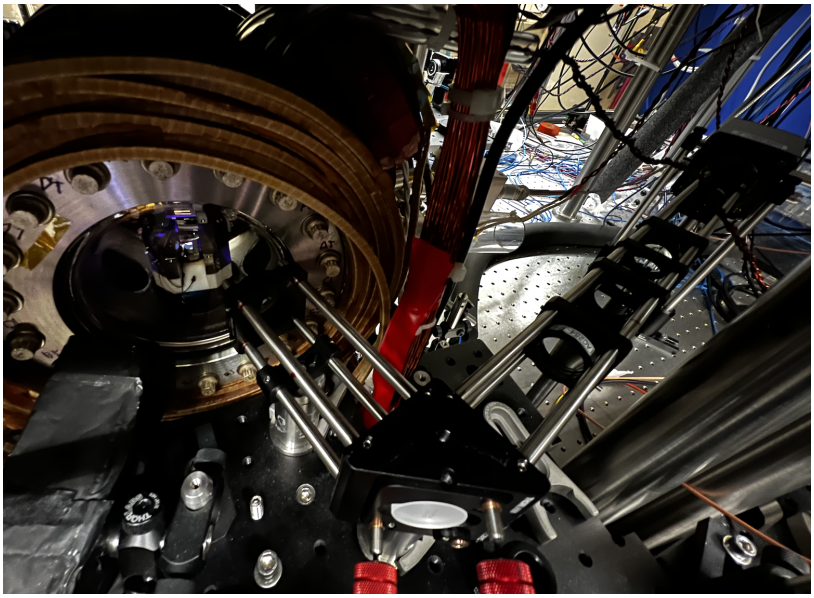


Figure 2-5: The 399nm imaging system.

In Fig. 2-6, I show the single shot imaging of atoms in MOT, loaded into the cavity lattice and loaded into the transverse lattice, respectively.

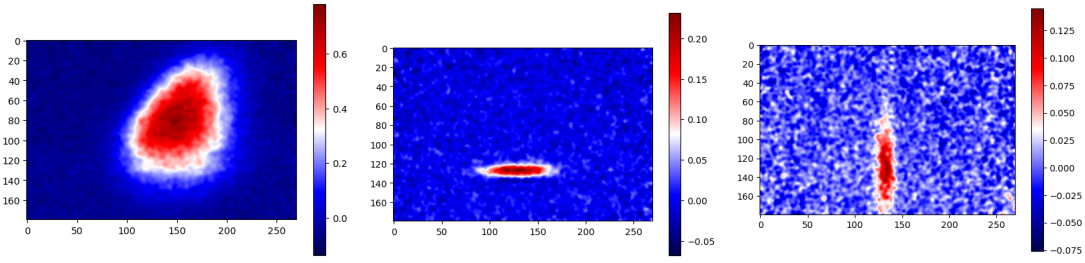


Figure 2-6: Imaging of atoms using on-resonance 399nm transition.

[2]Due to the inaccurate position of the first lens, the position of the second lens is optimized to separated 20cm$< 2f_1$ from the first lens

2.2.2 556nm Green Light System

The source and locking of the green light have not been changed. To be more compact, we remade the optics into almost a single plate. The 1112nm light comes from the Menlo Systems' P/N Orange one-SHG laser. Most of the power goes into the frequency doubler and then to the splitting station. The light is split into four major paths: (1) the probe light, which will send through the cavity to either measure the atomic state or mediate atom-atom interaction, (2) the strong portion goes to the MOT for a second stage cooling and trapping, (3) for the optical pumping also through the cavity to initialize the atomic state, and (4) the transverse Raman cooling path. Around 18mW goes into the MOT path while other paths all together take around 1mW.

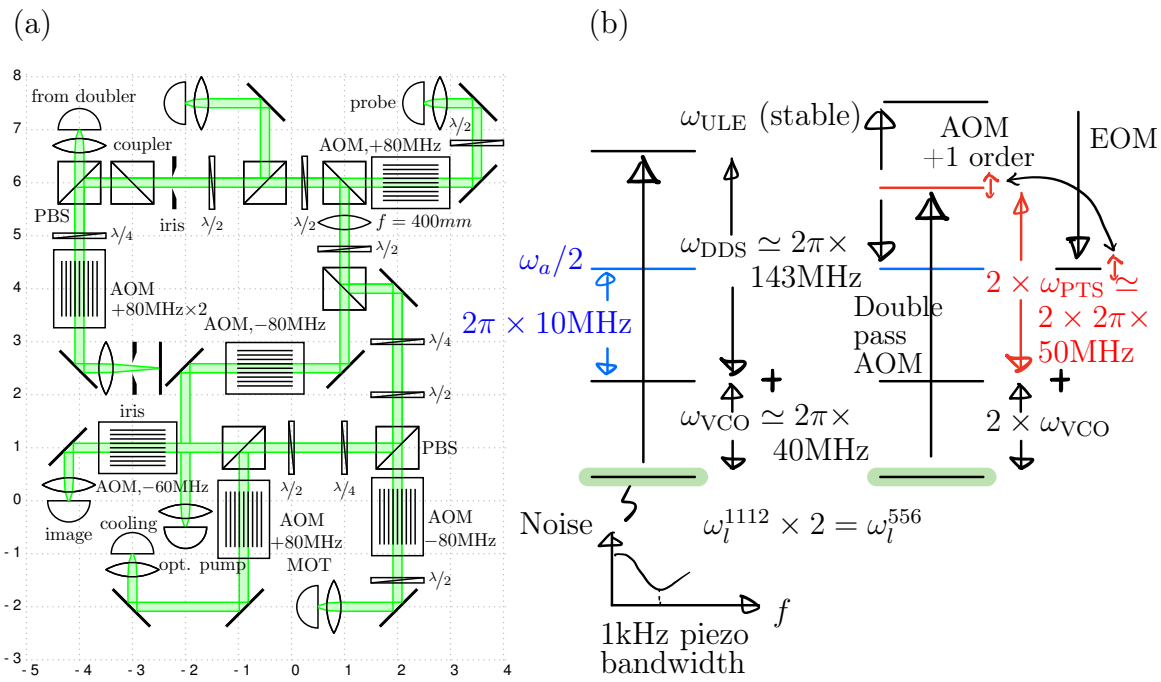


Figure 2-7: **Optics about the 556nm laser.** (a) Green light splitting station optical path scheme. (b) Frequency shifting in both 1112nm and 556nm.

Frequency stabilization

One can notice that all of these paths go through the first double-pass AOM, and the reason is related to how we lock the frequency of the 1112nm laser. The laser

is locked by feeding back the error signal to the piezo, which significantly limits the bandwidth to 1kHz due to the phase lag in the driver. We adopted another method: instead of stabilizing the frequency of the laser ω_l^{1112} with such a low bandwidth, we actually stabilize the frequency shifted by an VCO feed EOM whose frequency can be rapidly tuned: $\omega_l^{1112} + \omega_{\mathrm{VCO}}$. Thus, to use the light, we must also shift exactly the same VCO frequency to stabilize the frequency we use. Note that what we really use is the frequency-doubled light at 556nm, i.e., $\omega_l^{556} = 2 \times \omega_l^{1112}$. Consequently, we must shift by twice the VCO frequency to reach a stabilized frequency $2 \times (\omega_l^{1112} + \omega_{\mathrm{VCO}}) = \omega_l^{556} + 2 \times \omega_{\mathrm{AOM}}$, and therefore a double-pass AOM is required; and in order to have a tiny frequency difference control, we add the VCO frequency by an FPGA-based DDS (Programmed Test Sources Inc., P/N PTS 3200) source as shown in Fig. 2-7(b). One may suggest that a single-pass AOM with frequency doubling the VCO to feed an AOM is an alternative; from the frequency perspective, this is correct. However, from the alignment perspective, this would be like the outgoing light's direction highly dependent on the VCO frequency, affecting the fiber coupling alignment afterward. Thus we adopt the double-pass approach, and it works very well.

This frequency after the double-pass AOM is stabilized to twice the ULE cavity resonance, which is roughly $2\pi \times 80$MHz above the atomic resonance. Thus we tune the MOT and the pumping path directly down to around the atomic resonance, and for the detailed changing of the frequency of these two paths, since they will not be on at the same time, can be controlled by the ω_{PTS} which goes into the double-pass AOM. The probe and transverse cooling paths are all shifted to $2\pi \times 160$MHz above the atomic resonance, and then use a final probe fiber-coupled EOM (ADVR, P/N WPM-P48P48-AL0) driven by an amplified RF signal driven by another VCO (Minicircuit ZOS-200+) around $2\pi \times 160$MHz, and directly controlled by an analog channel[3].

[3]four channels, actually: we combine two tones of RF signals, and we control the frequencies and amplitudes respectively so in total four channels; for most applications, we only use one of the tones.

Cooling Path

Among all the ports, the cooling path is new and is essential for the Raman sideband cooling used for clock operations. We will discuss the details of the cooling process in Chap. 5.

2.2.3 578nm Clock Laser System

The previous generation of students left us a working clock laser system, but to really probe ^{171}Yb 's 7mHz $^1S_0 \leftrightarrow {}^3P_0$ transition, we need to make it better. We found two practical ways: (1) to improve the current setup by understanding everything better and controlling all the possible noises, and (2) buy a much better though expensive commercial system and improve on top of that. (1) is essential later if we are going to build the best clock in the world, but (2) is good enough to save us time and produce proof-of-principle results. In this subsection, I will discuss our progress in both directions, and for more details, one can find in Chi Shu's thesis [209]. Also, I will explain a few new components compared to the clock laser in its unfinished form described in the previous generation's thesis [100, 24].

As in Fig. 2-8, the laser emitted from the Nanoplus DFB110130 is then mode-shaped by the anamorphic prism pair (Thorlabs PS875-C). Then the light passes a customized isolator based on the Isowave optical isolator with its output polarizer replaced by a standard HWP-PBS pair. We then use a 10% sampler (Thorlabs BSF10-C) to collect a tiny portion of light into the fiber EOM (iXblue NIR-MPX-LN-0.1) which is then sent back to the PBS that replaces the polarizer of the isolator, which reflects the light to the isolator and passed through. In total, this gives around 60dB lower power for the optical feedback of the laser.

Besides the feedback path, the majority of the laser beam passing the sampler is then isolated by another isolator. Then, using three HWP-PBS pairs, some of the light is collected for the PDH locking, for a Thorlabs SA200-8B confocal Fabry-Perot interferometer to determine the power distribution between multi transversal modes, for power amplification, and one additional auxiliary port.

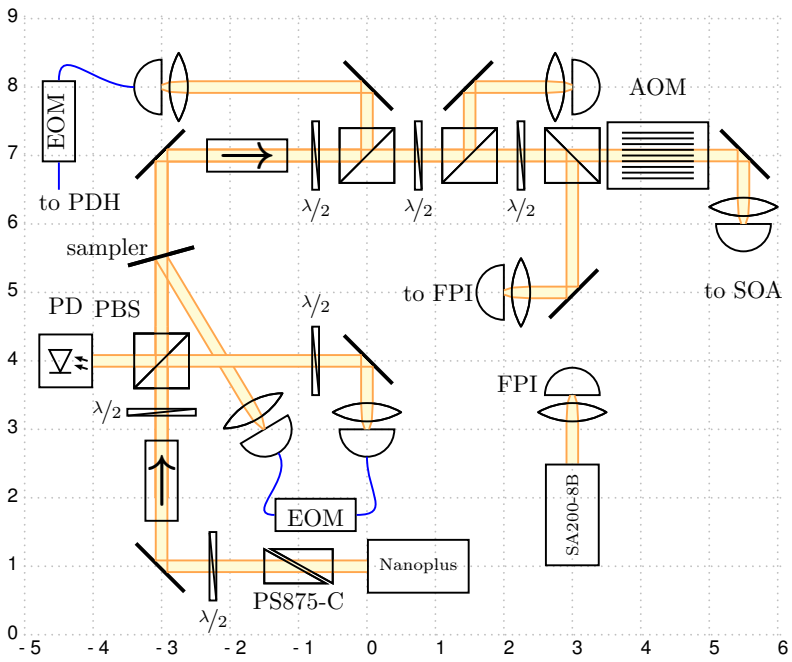


Figure 2-8: Optical scheme of the infrared (1157nm) part of the clock laser before power amplification.

As discussed later in Chap. 6, the performance of the clock laser in its original form does not provide long enough coherence time. As a consequence, we need to figure out the causes of the extra noises and fix them.

Fast ECDL Using the EOM Feedback. The EOM-based optical feedback forms the first step to improving over the first-generation clock laser. First of all, this is equivalent as the optical feedback via an external cavity, as the light sent back has a much reduced while controllable power via the HWP-PBS pair, and a variable phase which can be controlled to the modulation port of the EOM. In order to make it happen, we requested the specific high-impedance ($V_{\text{load}} > 10^4\Omega$) EOM from iXblue such that we can drive a few $V_\pi \sim 2V$ with very low power consumption. The EOM significantly increases the feedback bandwidth of the ECDL compared with the piezo-driving external cavity (which has mechanical bandwidth at kHz level), as demonstrated in a similar laser system by our group [246].

A technically challenging point is the feedback loop is physically very long: the fiber is in total more than 1m (by taking the refraction of index account, effectively

this gives 1.5m of optical length), and the free space optics, though very compact, is also 1m. Thus the total FSR is 120MHz, making it very easy to mode hopping. Thus we need the Fabry-Perot interferometer to see the different modes and adjust the feedback strength to maintain as single-mode as possible while still having the linewidth narrowed down.

Shielding of the PDH EOM. The most important technique for frequency stabilization is the PDH technique, where the EOM is its essential component. However, the EOM itself is not very good in terms of total-length stability, and thus the pyroelectric will cause extra polarization drift. Our EOM is PM-0K5-10-PFA-PFA from EOSPACE, and the observed polarization drift is very large. We thus made an enclosure of the EOM to reduce thermal fluctuation as in Fig. 2-9. We also shield the RF signal cable to minimize the crosstalk between adjacent RF frequencies for different applications.

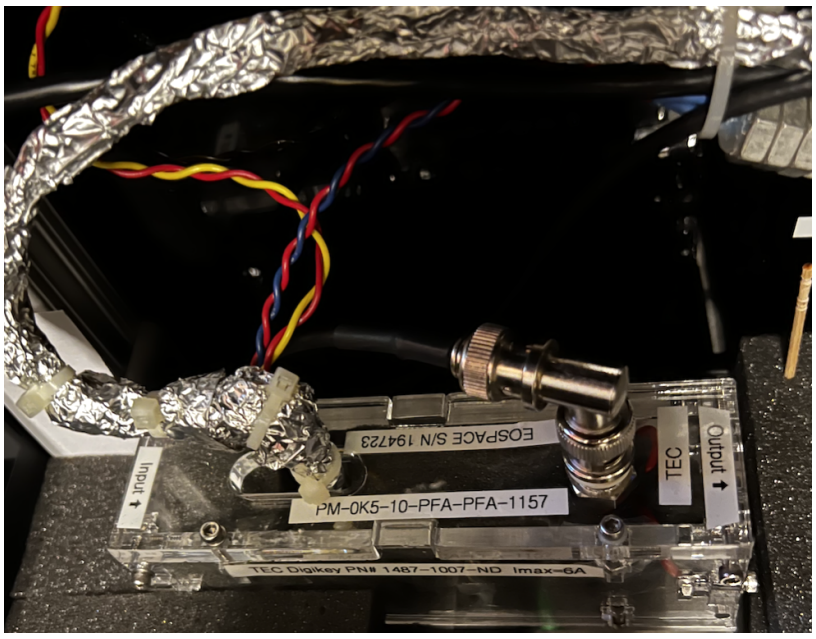


Figure 2-9: The mount of the PDH EOM and the fielding of its modulation signal.

Cancelling the Residual Amplitude Modulation (RAM). Despite the polarization drift that is largely stabilized using the enclosure structure, the RAM is one

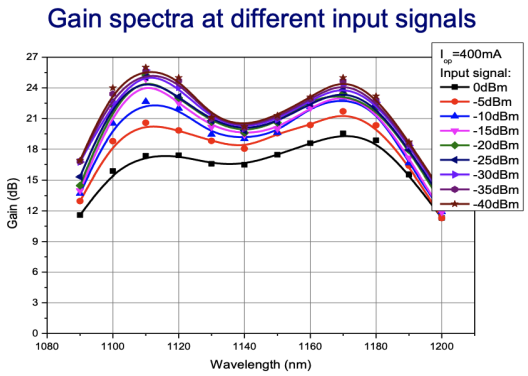


Figure 2-10: The gain profile of the SOA at different input power.

important undesired noise of laser locking error signal from the non-zero amplitude modulation, which occurs when phase modulation is based on the electro-optic effect. The idea was first proposed by John Hall [244], and more modern architecture can be found in [251].

Cancelling the Fiber noise. The fiber length could easily fluctuate thermally, and the tiny fluctuation would cause a huge phase error while delivering the laser through fibers. This is more severe when we're talking about the precise laser, such as the clock laser. Empirically, a 10-meter fiber would cause around 100Hz of frequency fluctuation, which is intolerable for clocks. Our clock laser's power amplification, frequency doubling, and final delivery are all through fibers; thus, this must be resolved. Fortunately, the power amplification stage's fiber length is very minimal. For the other two stages, we adopt the scheme [136] for our setup.

Power Amplification. We use the Innolume Semiconductor Optical Amplifiers (SOA) SOA-1140-90-PM-24dB to amplify the signal at 1157nm. The gain, at the current $I_{\text{op}} = 400\text{mA}$ is given by Fig. 2-10. With 1mW input, the SOA produces more than 60mW, and eventually saturates at 80mW with 10mW input, 35dB larger than the amplified spontaneous emission. The frequency doubling, which serves as the cavity, further suppresses the other modes, making the output laser beam clean in the spectrum.

2.2.4 759nm Magic Wavelength Trap Laser System

Story of the Upgrade

The story for the 759nm system is similar to the 399nm system, though the story is even more dramatic.

We were using the design from the first generation. That one worked pretty well, and there is even a paper about the whole system [246]. However, the master laser rapidly aged. Sometimes we even needed to relock the master laser every five minutes. In late 2019 we finally ordered the Ti:Sapphire laser from MSquared, which provides enough power for the transverse trap, which is necessary for the squeezed clock result that I will show in Chap. 6. Before its arrival, we used a tapered amplifier (TA), which worked fine for a while. However, the TA also burned on December 1st, 2020, which is right about the time we moved to work on the squeezing-unsqueezing project (discussed in detail in Chap. 7). Fortunately, the MSquared Ti:Sapphire arrived earlier, and we also set it up, so we can easily move to it. Everything was fine with the Ti:Sapphire until late 2021, when the power of the 532nm pump laser (aka Equinox) of the Ti:Sapphire dropped. In the beginning, this was a rare event, and the tech support could remotely fix the problem by realigning something inside the pump. This got much more frequency in 2022, even if we followed the suggestion to let the pump laser run at full current all the time to "stabilize" it. On the other hand, the MSquared system claimed to significantly revolutionize the Equinox system, which should be much more stable. Since we indeed needed more power, we got another one from MSquared in early 2022 and installed it in June. We even removed all the 399nm locking optics to install it, though resetting it up was not very difficult. And at least till now, both Ti:Sapphire systems have worked smoothly.

Optics for the Ti:Sapphire

The optics for both the 1st and the 2nd Ti:Sapphire are very similar as shown in Fig. 2-11. The logic is to split it into three paths: one for locking the frequency by PDH locking to the homebuilt ULE cavity [100, 24], one for sending through the

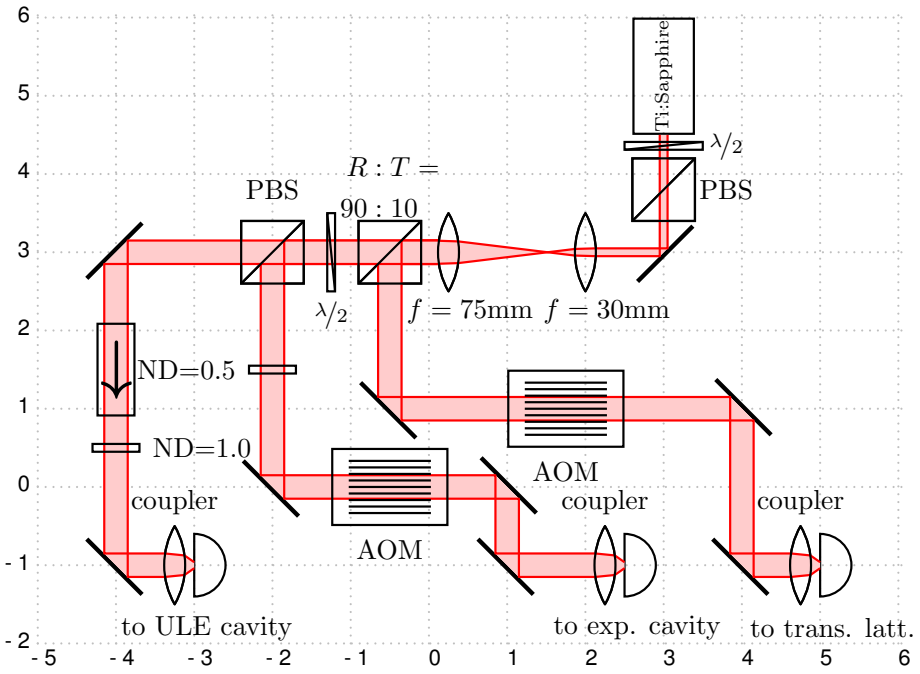


Figure 2-11: The optics scheme of the Ti:Sapphire laser. The laser beam is expanded to be better coupled to optical fibers.

experimental cavity, and the last one for transverse lattice.

Locking of the 759nm Ti:Sapphire

The 759nm Ti:Sapphire laser from M2 is intrinsically quiet; as long as we stabilize it to its internal etalon, it can be locked almost forever (the record is continuously locked for a week).

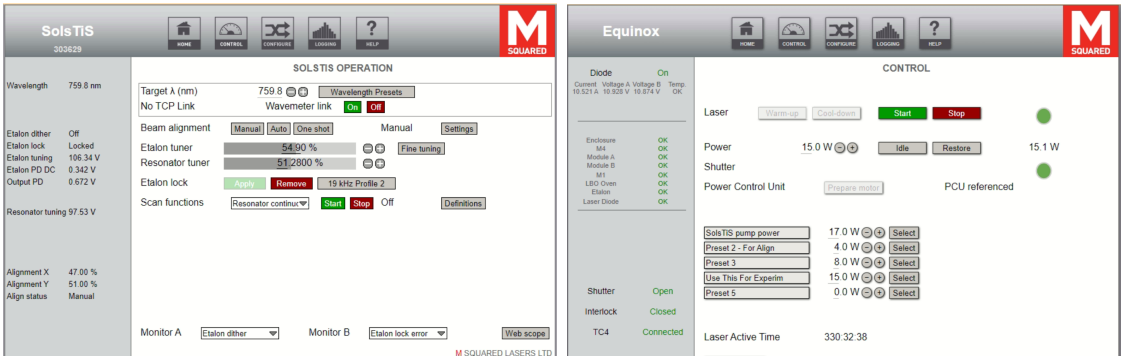


Figure 2-12: Control panels of the M2 Laser. Left is the SolsTiS panel, which controls the etalon of the Ti:Sapphire. Right is the Equinox panel, which controls the pump diode and the output power.

In order to make sure the etalon's position is not far off, we first measure the wavelength of the 759nm laser via the wavelength meter (Advantest TQ8325), and change the etalon tuner in the SolsTiS control panel to match with the record (394.80280THz now), ±40MHz. Then we engage the etalon locking and use the PDH signal and the Vescent D2-125 Laser Servo to generate PI signal feeding back to the piezo of the Ti:Sapphire.

Chapter 3

How to Model A CQED Spin System

With the apparatus described in Chap. 2, we might want to describe the spin system in more detail using concepts from atomic physics. And as I have promised, this should be about the (collective) spin degrees of freedom. The concepts included here are mostly developed in [125]. Besides what has already been covered there, I will also provide calculations of the system in a far atom-cavity detuned region as a comparison with a variety of other experiments that existed.

3.1 Introduction and Explanation

Though having emphasized the importance many times, I would still like to rephrase why our atoms and atom-like systems placed in an optical resonator are of particular interest. These systems are able to provide versatile experimental platforms to study many-body quantum physics, entanglement, quantum simulation and computation, quantum measurement, dissipative quantum systems, quantum networks, and a variety of other topics [180, 186, 65, 182, 238, 64, 165, 154, 41]. In these CQED systems, the optical cavity allows a photon to interact multiple times with all atoms on successive round trips, which substantially enhances the atom-light interaction as compared to free space. Often, the atom-light interaction is dominated by the coupling of the atoms to a single mode of the cavity. For a single atom, such a system is a nearly ideal experimental realization of the Jaynes-Cummings Hamiltonian [97], while for an

atomic ensemble, the system approximates the Tavis-Cummings Hamiltonian [223]. The interaction of atoms with multimode optical cavities has also been investigated [110, 64], and this type of system can produce even more complex dynamics both in the atomic and photonic subspaces [231, 49, 72, 71, 32, 110].

Typically, two or more atomic energy levels are relevant to the problem, so that the atomic state can be described by a spin degree of freedom, while each cavity mode constitutes a harmonic oscillator. And due to the feature that the cavity modes couple to the atomic transitions in a collective way, the reduced picture of using collective spin to describe the system starts to attract investigations.

To the lowest order, the atom-cavity interaction generates quantum correlations (entanglement) between the collective atomic spin and the light mode. What this means can be understood as the existence of atoms can be treated as a classical dielectric medium and, therefore, on the cavity side, causes a cavity resonance shift due to the increased phase accumulated during a round trip; on the atomic side, the cavity creates an AC Stark shift. These two behaviors of the atom-light interaction establish the correlations between the cavity photonic state and the atomic spin state.

Higher-order terms can lead to nonclassical states of the light (effective photon-photon interactions) [195, 229, 75], as well as nonclassical collective spin states (effective atom-atom interactions) [121, 199, 17, 38, 88, 87, 25, 253], or even hybrid spin-light states [239, 74]. Such entangled states are useful as building blocks for quantum metrology [135, 171, 10], quantum networks [105], quantum information processing [235], and as testbeds for the foundations of quantum mechanics [83].

Usually, the theoretical analyses of the generation of entangled atomic states in CQED systems have adopted one of two viewpoints: the first focuses on the measurement aspect, whereby the atom-light interaction transfers information about the atomic spin state onto the light field, and therefore a measurement of the light field can conditionally project the state of the atoms onto a collective entangled state [76, 113, 226, 212, 189, 94, 31, 143, 9]. Alternatively, one can view the system from a quantum feedback perspective [243, 131, 4, 250, 167], where the light-atom interaction maps the spin quantum noise onto the light field [4, 78, 79], and then the light

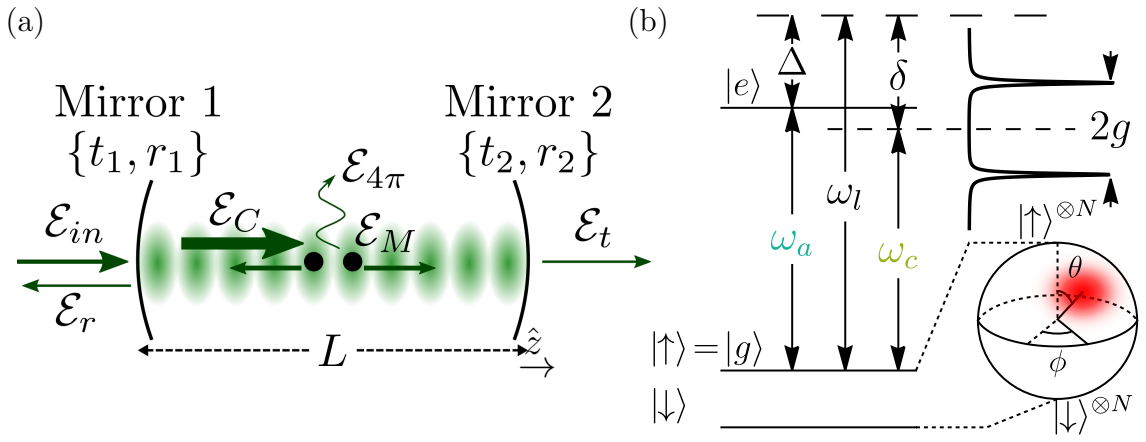


Figure 3-1: (a) Schematic diagram of an ensemble of atoms interacting with a single-mode cavity of length L. The incident field $\mathcal{E}_{\text{in}}$ builds up in the cavity to the value $\mathcal{E}_c$. The cavity field is coherently scattered by the atoms into the cavity with amplitude $\mathcal{E}_M$, and coherently radiated through the cavity mirrors to give the transmitted and reflected fields $\mathcal{E}_t$ and $\mathcal{E}_r$. The cavity field scatters from the atoms into free space with amplitude $\mathcal{E}_{4\pi}$, and from the cavity mirrors with amplitude $\mathcal{E}_{sc}$, which is assumed to be zero in a lossless cavity. (b) Level diagram of the atomic three-level system. $|\uparrow\rangle = |g\rangle$ and $|e\rangle$ are the two states interacting with the cavity light. ω_a, ω_c and ω_l are the atomic, cavity resonance frequencies and the probing light frequency, respectively. $\Delta = \omega_l - \omega_a$ and $\delta = \omega_l - \omega_c$ are the detunings of probing light from atomic and cavity resonance, respectively. The curve on the right represents the cavity transmission spectrum in the presence of atoms, and $2g$ is the vacuum Rabi splitting due to the light-atom interaction when $\omega_a = \omega_c$. The sphere in the bottom right represents a Bloch sphere formed by the N atoms of spin $\frac{1}{2}$, and the shaded distribution represents a CSS pointing along polar and azimuthal angles (θ, ϕ) in spherical coordinates where each atom is in a superposition state $\cos(\theta/2)\,|\uparrow\rangle + \sin(\theta/2)\mathrm{e}^{i\phi}\,|\downarrow\rangle$.

field acts back onto the spin [94], creating atomic entanglement without the necessity to perform any measurements (cavity feedback squeezing) [200, 130, 120, 40]. While the first approach to generating atomic entanglement builds upon the use of information contained in the light field, the second approach neglects that information altogether [221]. Hence, these two effects have so far been treated separately. Nonetheless, the two effects originate from the same Hamiltonian so that they are related, and both need to be considered in practical CQED experiments.

This chapter aims to obtain a unified description of both the measurement-induced and quantum-feedback-induced generation of entangled many-body spin states in CQED, considering both of these aspects on an equal footing. Our analysis remains valid in the regime where both atom-light and effective atom-atom interactions play a significant role in the system dynamics, and thus neither can be neglected.

We assume that the atomic transition is not saturated by the cavity field. This means the intracavity photon number per atom is much less than one, and the 2-level atomic structure is similar to a harmonic oscillator structure. Thus the assumption allows us to treat the optical field semi-classically, and derive analytical expressions for the intracavity, transmitted, reflected, and scattered fields, as well as the collective spin state.

The analysis presented here reveals universal features of the CQED system that remain valid for arbitrary detuning of the probe light frequency from the cavity and atomic resonances. We show that the atom-light entanglement strength (i.e., the measurement strength [78, 79, 99, 189] when the light field is used as a 'meter' for the atomic quantum state) at any light detuning or coupling strength is given by the product of three terms: the single-atom cooperativity, the normalized cavity transmission, and the total number of photons scattered by the atoms into free space. Thus, when the probe laser frequency is close to the cavity resonance (whether bare or dressed by atom-cavity interactions) and transmission is high, the atom-photon entanglement is the dominant effect. Consequently, the generation of interatomic entanglement in a 'heralded' fashion by performing a measurement on the light field [143, 28, 61, 52] is most efficiently accomplished by tuning the light field close to the (dressed) cavity

resonance.

On the other hand, when the detuning of the probe laser frequency from the cavity resonance far exceeds the cavity linewidth, and transmission through the atom-cavity system is low, the atom-light entanglement remains relatively weak, and higher-order terms take on the leading role [252], generating spin-spin correlations [199, 121, 25]. In this regime, first discovered in Ref. [252] using numerical simulations, the light acts as a *quantum catalyst*: the light field mediates the interaction between distant atomic spins, resulting in entangled many-body atomic states while becoming only weakly entangled with the atoms. Thus at the end of the interaction process, the state of the atom-light systems approximately factorizes into a fixed, coherent state of the light field and a collective atomic spin state displaying interatomic entanglement. Under appropriate conditions, this entanglement can take the form of a squeezing process where the quantum projection noise of the collective atomic spin is redistributed along specific directions, resulting in a squeezed spin state (SSS) [108, 241, 95]. Zhang *et al.* [252] have previously pointed out that it is possible to reduce the impact of atom-light entanglement on cavity-induced spin squeezing by optimizing the detuning of the probe beam from cavity resonance. However, their analysis is only valid in the limit of a large detuning between the atomic and the cavity resonances, while a number of experiments use smaller detunings to maximize the light-atom interaction strength, and reduce the sensitivity to technical noise [38, 25].

The treatment presented here provides a complete analytical description that applies for arbitrary detunings between the incident light field, the cavity mode, and the atomic resonance, and for both weak and strong atom-light coupling, both in terms of the single-atom cooperativity and the collective cooperativity. Our analysis provides a unified framework that describes both effects of measurement and quantum feedback and can thus be used for analyzing and comparing, over the full range of parameters, CQED experiments that aim to generate entangled atomic states.

The rest of this chapter is organized as follows: we will first develop a general unified theory. In Sec. 3.2, we describe the general setup of the CQED system and the assumptions underlying our approach. We also define the collective spin state

and obtain an effective spin Hamiltonian with the semi-classical coherent light field in the cavity. Then we focus on the residual effects of the light on the atomic state. In Sec. 3.3, we introduce the unitary effect, i.e., the Hamiltonian, that the light has on the atomic state. Due to the symmetry, this Hamiltonian only occurs on the collective spin states. In Sec. 3.4, we will discuss the generated light-atom entanglement, especially the concept of quantum Fisher information (QFI) of the light in the context of the CQED system. Then we will use the first principle method to derive the exact same two effects under a master equation description in Sec. 3.5. In addition, in Sec. 3.4.6, we discuss an effect of the light that breaks the symmetry: individual dephasing due to incoherent scattering into free space. The strong cavity-atom interaction already efficiently suppresses this effect, leaving the residual decoherence as a small contrast loss of the collective spin state.

3.2 Interaction between an atomic ensemble and a cavity mode

An ensemble of two-level atoms inside a cavity with non-degenerate modes is well-described by the Tavis-Cummings Hamiltonian [97, 223]. This Hamiltonian is valid if the interaction with one electromagnetic mode dominates. The excitation of the cavity mode by an incident light field and dissipation by decay from the cavity or by atomic scattering of the cavity photons into free space are not part of the Tavis-Cummings Hamiltonian, but can be included phenomenologically [62, 196], or from first principles [3, 192]. This approximation of a single cavity mode with external driving and dissipation is in excellent agreement with the majority of CQED experiments where the interaction with other transverse or longitudinal cavity modes can be ignored [17, 213, 148, 197, 74]. For many applications, it is desirable to have an analytical and more intuitive description of the atom-light interaction that can be directly applied to existing experiments and used to guide future applications. Such experiments often deal with nearly classical light beams containing many photons,

where a quantization of the electromagnetic field (beyond the effects of photon shot noise) is not needed. In this case, it is possible to derive simpler and analytical expressions for the light-atom and the light-mediated spin-spin interaction, as we discuss below.

When the optical cavity containing an ensemble of atoms is illuminated by a continuously applied laser beam or a long laser pulse (coherent state of light), one can often approximate the intracavity, transmitted and reflected light fields as remaining coherent states, even when the interaction with the atoms is included (for a discussion of the limits of this approximation, see Sec. 3.2.2). In this limit, the photon annihilation and creation operators can be substituted by the photonic coherent state's complex index (or its conjugate) plus a small correction, reducing the problem to the interaction of atoms with a classical electromagnetic field plus photon shot noise. This approach is possible as long as tuning the cavity by the atomic spin variation results in small changes of the intracavity field, i.e. when the atom-cavity interaction can be linearized. Based on the corresponding effective Hamiltonian describing the interaction of an ensemble of atomic spins with a classical electromagnetic field, we can then find analytical solutions for the evolution of the coupled atom-cavity system, and use these expressions to gain physical insight into the entanglement process.

3.2.1 Atomic states and operators

We consider an atomic level structure where each individual atom in the ensemble has ground-state levels $|\downarrow\rangle$ and $|\uparrow\rangle$, constituting a spin-$\frac{1}{2}$ system, as well as an electronically excited state $|e\rangle$ that couples only to the state $|\uparrow\rangle$. The collective spin operators are defined as the sum of the spin operators of the N atoms,

$$\hat{S}_{x,y,z} = \frac{1}{2}\sum_{j=1}^{N} \hat{\sigma}^{j}_{x,y,z} \tag{3.1}$$

where the $\hat{\sigma}^j_{x,y,z}$ are the atoms' Pauli matrices. Among all possible spin states in the 2^N-dimensional Hilbert space, there is a subspace of symmetric states which satisfy

$$\langle \hat{\boldsymbol{S}}^2 \rangle = \left\langle \hat{S}_x^2 + \hat{S}_y^2 + \hat{S}_z^2 \right\rangle = S(S+1), \tag{3.2}$$

where $S = N/2$ is the largest possible value for the total spin. As long as the system's Hamiltonian is symmetric in all spins $\boldsymbol{\sigma}^j$ and the initial state is in this subspace, the system will remain within this $(N+1)$-dimensional subspace that is much smaller than the full Hilbert space of dimension 2^N.

We can represent those collective atomic states on a Bloch sphere with radius $\sqrt{S(S+1)}$, e.g., in terms of their Wigner quasiprobability distribution [202]. In quantum metrology and other applications, the atomic ensemble is initially prepared in a coherent spin state (CSS) [5], defined as the product state with all individual spins pointing along the same direction. The CSS along polar and azimuthal angles (θ, ϕ), as illustrated in Fig. 3-1 (b), has the following expansion in terms of Dicke states $|S, S_z\rangle$, the joint eigenstates of $\hat{\boldsymbol{S}}^2$ and $\hat{S}_z$ in the symmetric subspace [48, 5, 50]:

$$\begin{aligned} |\theta, \phi\rangle = \sum_{S_z=-S}^{S} \binom{2S}{S+S_z}^{1/2} \left(\sin\frac{\theta}{2}\right)^{S+S_z} \left(\cos\frac{\theta}{2}\right)^{S-S_z} \\ \times e^{-i(S+S_z)\phi} |S, S_z\rangle \end{aligned} \tag{3.3}$$

For a CSS pointing along the x-axis, as in Fig. 3-1(b), the uncertainties satisfy and saturate the Heisenberg uncertainty principle $\Delta S_y \Delta S_z = |\langle [\hat{S}_y, \hat{S}_z] \rangle|/2 = S/2$. Due to rotational symmetry, we have $\Delta S_y = \Delta S_z = \sqrt{S/2}$. In general, a CSS has a standard deviation $\sqrt{S/2}$ along any direction perpendicular to its mean spin $\langle \boldsymbol{S} \rangle$.

3.2.2 Classical light field inside a cavity containing an atomic ensemble

We consider the interaction of the atoms with a single standing-wave cavity mode, schematically shown in Fig. 3-1. We assume that all N atoms are fixed at the cavity

antinodes, which provides the maximum atom-light coupling, which can be achieved by double wavelength trapping [119], site-dependent selection [245]. The more general case of distributed atom positions can be mapped onto the case of uniform coupling by means of correction factors (of order unity) to the atom number and interaction strength [222, 89], where the attainable entanglement is suppressed if the temperature is too high. Nonetheless, we will discuss experimental methods to overcome such problems in Sec. 5.2. Apart from photon shot noise, we assume the light field to be classical, i.e., we use coherent states of light in the description. Then the two-level atom can be approximated as a harmonic oscillator. In the opposite limit, the ensuing saturation of the atomic state would prevent the atoms from absorbing further photons. This would effectively induce photon-photon interactions, and in this limit, the intracavity field can no longer be described by a coherent state, as has been shown both in the optical domain CQED [204] and in circuit QED systems [15]. In this work, we always consider a linear atomic response far below saturation. Note that a linear response also applies to the intermediate probing regime where the average photon number can exceed one but is still much smaller than the number of atoms.

The power transmission and reflection coefficients of the mirrors $i = 1, 2$ are denoted by $T_i = |t_i|^2$ and $R_i = |r_i|^2$, respectively. In general, the mirrors have losses and therefore $R_i + T_i < 1$. In the following discussion, we consider lossless mirrors ($R_i + T_i = 1$), while in [125], we establish a mapping of a cavity composed of realistic mirrors with loss onto one with lossless mirrors by means of additional optical components.

In the following part, we introduce several quantities and relations that characterize the coupling between the atomic ensemble and the cavity. These relations are derived in Ref. [222].

The cavity-enhanced single-atom cooperativity at an antinode is defined as [222, Eq. (30)]

$$\eta = \frac{24\mathcal{F}}{\pi k^2 w^2}, \tag{3.4}$$

where $k = 2\pi/\lambda$ is the wave number of the light, w is the mode waist ($1/e^2$ intensity radius) of the TEM_{00} cavity mode, and $\mathcal{F} \approx 2\pi/(2 - R_1 - R_2)$ is the cavity finesse for a lossless cavity with mirror power reflectivities $R_1, R_2 \approx 1$.

To simplify the following expressions, we define a position-independent mode amplitude $\mathcal{E}$ via the relation [210]

$$\mathcal{E} = E(0,0,z)\sqrt{\frac{\epsilon_0 c \pi w^2(z)}{2}}. \tag{3.5}$$

This definition applies to a Gaussian beam propagating in the $\hat{z}$ direction with an $1/e^2$ intensity radius $w(z)$ at a distance z from the mode waist which is located at $z = 0$. $E(0,0,z)$ is the electric field on the mode axis at an antinode at z. The thus defined mode amplitudes of the incident, cavity, transmitted, and reflected fields are denoted by $\mathcal{E}_{\mathrm{in}}$, $\mathcal{E}_c$, $\mathcal{E}_t$, and $\mathcal{E}_r$, respectively.

The atomic parameter that determines the coupling of the atoms to the cavity is the atomic polarizability $\tilde{\alpha}$. For a single two-level atom with transition frequency ω_a and natural linewidth Γ, the polarizability is given by [222, Eq. (1)]

$$\tilde{\alpha} = 6\pi\epsilon_0 c^3 \frac{\Gamma/{\omega_a}^2}{{\omega_a}^2 - {\omega_l}^2 - i(\omega_l^3/{\omega_a}^2)\Gamma}. \tag{3.6}$$

In extreme cases where the total solid angle subtended by the cavity modes is significant such as in [81], the atomic linewidth Γ in the denominator should be replaced by an effective linewidth [81]; however, for most optical cavities the differences are negligible ($< \%1$). In the limit of moderate detuning from atomic resonance $\Delta = \omega_l - \omega_a \ll \omega_a$ and strong but not ultrastrong coupling between atoms and light, corresponding to the condition of the rotating-wave approximation, the atomic polarization can be approximated by a Lorentzian lineshape:

$$\tilde{\alpha} \approx 6\pi\epsilon_0 \frac{c^3}{\omega_a^3} \frac{i}{1 - \frac{i\Delta}{\Gamma/2}} = 6\pi\epsilon_0 \frac{c^3}{\omega_a^3} \left(\mathcal{L}_d(x_a) + i\mathcal{L}_a(x_a)\right). \tag{3.7}$$

Here $x_a \equiv \frac{\Delta}{\Gamma/2}$ is the normalized detuning of the probe laser (ω_l) from the atomic resonance (ω_a), while $\mathcal{L}_d(x_a) = -\frac{x_a}{1+x_a^2}$ and $\mathcal{L}_a(x_a) = \frac{1}{1+x_a^2}$ are the Lorentzian dispersive

and absorptive lineshapes, respectively [222].

The amplitude of the intracavity field can then be expressed as

$$\mathcal{E}_c = \frac{\mathcal{F}}{\pi} \frac{it_1}{1 + N\eta\mathcal{L}_a(x_a) - i(x_c + N\eta\mathcal{L}_d(x_a))} \mathcal{E}_{\text{in}}, \tag{3.8}$$

where $x_c \equiv \frac{\delta}{\kappa/2}$ with $\delta = \omega_l - \omega_c$ is the normalized light-cavity detuning, κ is the full-width half-maximum cavity linewidth, and t_1 is the amplitude transmission coefficient of the input mirror. The real part of the denominator of Eq. (3.8) corresponds to the absorptive part of the atomic susceptibility, while the imaginary part combines the dispersive part of the atomic response with the phase shift that occurs when probing an empty cavity away from resonance.

The transmitted and reflected field amplitudes $\mathcal{E}_t, \mathcal{E}_r$ are similarly given by

$$\mathcal{E}_t = -\frac{\mathcal{F}}{\pi} \frac{t_1 t_2 e^{ikL}}{1 + N\eta\mathcal{L}_a(x_a) - i(x_c + N\eta\mathcal{L}_d(x_a))} \mathcal{E}_{\text{in}} \tag{3.9}$$

and

$$\mathcal{E}_r = \left[r_1 - \frac{\mathcal{F}}{\pi} \frac{t_1^2 r_2 e^{2ikL}}{1 + N\eta\mathcal{L}_a(x_a) - i(x_c + N\eta\mathcal{L}_d(x_a))} \right] \mathcal{E}_{\text{in}}. \tag{3.10}$$

Here L is the length of the standing-wave cavity, and t_2 is the amplitude transmission coefficient of the output mirror. The transmitted field is simply proportional to the intracavity field, while the reflected field is a superposition of the light directly reflected off the input mirror (the term with r_1) and the field leaking out of the cavity (second term).

From Eq. (3.9), it follows that the power transmission of a symmetric and lossless cavity is given by

$$\mathcal{T}_0 = \frac{|\mathcal{E}_t|^2}{|\mathcal{E}_{\text{in}}|^2} = \frac{1}{(1 + N\eta\mathcal{L}_a(x_a))^2 + (x_c + N\eta\mathcal{L}_d(x_a))^2}. \tag{3.11}$$

The atomic absorption (first term in the denominator) is determined by the atom number N, the single-atom cooperativity η, and the absorptive Lorentzian lineshape $\mathcal{L}_a$, while the dispersion of the atom-cavity system (second term in the denominator)

is given by N, η, and the dispersive Lorentzian $\mathcal{L}_d$. The transmission of an asymmetric cavity with mirror power transmissions $T_{1,2} = |t_{1,2}|^2$ is given by

$$\mathcal{T} = \frac{4T_1T_2}{(T_1+T_2)^2}\mathcal{T}_0. \tag{3.12}$$

The ratio of the photon scattering rate into free space $\mathcal{S}$ to the photon transmission rate $\mathcal{T}$ can be simply expressed as [222]:

$$\frac{\mathcal{S}}{\mathcal{T}} = \frac{2\pi}{T_2\mathcal{F}}N\eta\mathcal{L}_a(x_a) \tag{3.13}$$

The scattering rate into free space is proportional to the rate of photon transmission, the collective cooperativity $N\eta$, and the absorptive atomic lineshape $\mathcal{L}_a$.

3.3 Effective light-induced Hamiltonian for collective atomic state

The light shift experienced by a polarizable object, in this case, an atomic ensemble, subject to an electric field $\hat{E} = 2\hat{E}_c$ at an antinode of the cavity is given by the Hamiltonian [68]

$$\hat{H}_{\text{dip}} = -\frac{1}{2}\left|\hat{E}\right|^2\text{Re}(\alpha) = -2\left|\hat{E}_c\right|^2\text{Re}(\alpha), \tag{3.14}$$

where α is the atomic polarizability. For $\hat{N}_\uparrow = \hat{S}_z + S$ atoms interacting with the intracavity field, this Hamiltonian using Eqs. 3.7 and 3.8 can be expressed as

$$\begin{aligned}\hat{H}_{\text{dip}} &= -\left(\hat{S}_z + S\right)\eta\frac{|\hat{\mathcal{E}}_c|^2}{\omega}\frac{\pi}{\mathcal{F}}\mathcal{L}_d(x_a) \\ &= -\hbar\Omega\hat{n}_c\left(\hat{S}_z + S\right).\end{aligned} \tag{3.15}$$

Here $\Omega = \pi\eta\mathcal{L}_d(x_a)\kappa/\mathcal{F}$ is the light shift per intracavity photon and $\hat{n}_c = |\hat{\mathcal{E}}_c|^2/(2\hbar\omega\kappa)$ is the intracavity photon number. The operator $\hat{\mathcal{E}}_c$, as in (3.8), is a function of the number of atoms coupling to the cavity, which equals $\hat{N}_\uparrow$ because only atoms in $|\uparrow\rangle$

state are coupled to the cavity. Since $\hat{N}_\uparrow = \hat{S}_z + S$, the intracavity photon number $\hat{n}_c$ becomes a function of $\hat{S}_z$. The above Hamiltonian corresponds to an interaction term of the form $\hbar\Omega\hat{c}^\dagger\hat{c}S_z$ in the second quantization formalism of Ref. [122, Eq. (2)], with c being the photon annihilation operator for the cavity mode, plus an S_z-independent average shift of the cavity mode frequency $\omega_c \to \tilde{\omega}_c = \omega_c - \Omega S$. This additional, S_z-independent term can take a different form when both spin levels are coupled to excited states as in Ref. [122], instead of just one of the levels, as in the present analysis. Subtracting the average frequency shift, i.e., measuring the cavity detuning relative to $\tilde{\omega}_c$, we arrive at the effective atomic Hamiltonian

$$\hat{H} = -\hbar\Omega\hat{n}_c\hat{S}_z \tag{3.16}$$

This Hamiltonian depends on atomic parameters only through the collective (symmetric) spin operator $\hat{S}_z$, and therefore the atomic state remains in the symmetric subspace of maximal spin S defined in (3.2) under the action of this Hamiltonian. The Hamiltonian depends on the light field only through the intracavity photon number $\hat{n}_c$ or intensity $|\hat{\mathcal{E}}_c|^2$. The Hamiltonian $\hat{H}$, as given by Eq. (3.16), can also be obtained by generalizing the Tavis-Cummings Hamiltonian [223], or through the procedure described in the Supplemental Information of Ref. [40].

3.3.1 Light-induced coherent effects on the collective atomic spin

For a CSS at the equator with $\langle\hat{S}_z\rangle = 0$, it is natural to expand the $\hat{S}_z$-dependent intracavity photon number $\hat{n}_c(\hat{S}_z)$ in the Hamiltonian (3.16) into a Taylor series in terms of $\hat{S}_z$:

$$\hat{H} = -\hbar\Omega\hat{S}_z\sum_{j=0}^{\infty}\frac{S_z^j}{j!}\left(\frac{\partial^j\hat{n}_c}{\partial S_z^j}\right)_{S_z=0}. \tag{3.17}$$

The leading term of this expansion is the phase-shift $\hat{H}_0 = -\hbar\Omega\langle\hat{n}_c\rangle\hat{S}_z$ with $\langle\hat{n}_c\rangle = \hat{n}_c(S_z = 0)$, which generates a rotation of the collective atomic spin about the z-axis of the Bloch sphere. This simply represents the light shift on the atoms associated

with the average intracavity photon number $\langle \hat{n}_c \rangle = n_c(S_z = 0)$. Using Eqs. (3.8) and (3.13), the atomic phase shift after a time τ is

$$\Delta\phi = \Omega \langle n_c \rangle \tau = \eta n_\gamma^{\mathrm{t}} \frac{T_1 + T_2}{2T_2} \mathcal{L}_d(x_a) = -\frac{n_\gamma^{\mathrm{sc}}}{2\langle N_\uparrow \rangle} x_a, \tag{3.18}$$

which has been expressed in terms of the average transmitted photon number n_γ^{t} or the average scattered photon number n_γ^{sc}. Here $\hat{N}_\uparrow = \hat{S}_z + S$ is the atom number operator in the state $|\uparrow\rangle$, and we can use $\langle \hat{N}_\uparrow \rangle = N/2$ in the vicinity of the equator. The ratio of atomic phase shift $\Delta\phi$ to the transmitted photon number is independent of the atom number, but is proportional to the single-atom cooperativity η, which makes the phase shift measurement a convenient way to measure η without requiring an accurate calibration of the atom number.

The first-order term in Eq. (3.17) is the non-linear light-mediated spin-spin interaction term

$$\hat{H}_1 = -\hbar\chi \hat{S}_z^2. \tag{3.19}$$

This term represents an $\hat{S}_z$-dependent rotation of the atomic spin about the z-axis. H_1 is also known as the one-axis twisting Hamiltonian [108, 212]. Here we see how the cavity light can act as a quantum catalyst that causes an effective spin-spin interaction S_z^2 between distant atoms. This type of interaction can, e.g., produce SSSs, as first proposed by Kitagawa and Ueda [108]. The shearing parameter χ in $\hat{H}_1$ is given by

$$\chi = -\eta \mathcal{L}_d(x_a) \left(1 - x_c x_a + \langle \hat{N}_\uparrow \rangle \eta\right) \mathcal{T}_0 \frac{\mathcal{S}}{\langle \hat{N}_\uparrow \rangle}. \tag{3.20}$$

We see that the light-mediated one-axis twisting $\hat{S}_z^2$ is proportional to the scattered photon number: without photon scattering, there is no shearing of the atomic spin. On the other hand, the shearing strength is proportional to the cooperativity, and therefore a better cavity (or a larger number of atoms) allows one to reduce the decoherence associated with the scattering of photons into free space for a given desired shearing [138].

The shearing acting over a time τ produces a shearing strength Q, which is defined

as the differential phase displacement along S_y per unit S_z [199, 121]. Its relation to the OAT Hamiltonian (3.19) can be understood as follows: this is the differential of the geometric phase accumulation, which equals to the differential of the real phase obtained by the state, and thus Q equals to the second order derivatives of the phase $S_z^2\chi\tau$, with a prefactor of S to amplify the effect by the Bloch sphere radius

$$Q = S\frac{\mathrm{d}^2 \arg\left(e^{iS_z^2\chi\tau}\right)}{\mathrm{d}S_z^2} = 2S\chi\tau = N\chi\tau. \tag{3.21}$$

For our specific CQED system, in the vicinity of the equator of the Bloch sphere where $S_z = 0$, the shearing strength Q caused by the atom-light interaction is given by

$$Q = -2\eta\mathcal{L}_d(x_a)(1 - x_c x_a + S\eta)\mathcal{T}_0 n_\gamma^{\mathrm{sc}}, \tag{3.22}$$

where $\langle\hat{N}_\uparrow\rangle = N/2 = S$, such that $\langle\hat{S}_z\rangle = 0$, has been used. Q is proportional to the number of photons scattered by the ensemble and can be used as a parameter that characterizes the spin squeezing [199, 121, 25], as explained later in Sec. 5.3.

3.4 Light-atom entanglement and non-unitary evolution of the collective atomic state

When deriving the above results for the evolution of the collective atomic spin state and spin squeezing, we have treated the light field as classical, and described the atomic evolution as a unitary evolution governed by the effective Hamiltonian $\hat{H}$ given in Eq. (3.16). In doing so, we have so far ignored the effect of photon shot noise fluctuations on the atomic spin, or equivalently, the light-atom entanglement that builds up during this process [122]. If the information contained in the light field about the atomic ensemble remains unused, or equivalently, if the quantum state of the reflected, scattered, and transmitted light fields is traced over, this results in a decohering process in the atomic subspace, and a mixed, rather than pure, quantum state of the atoms. In the following, we first characterize the information about

the atomic state contained in a light field after the interaction, as quantified by the Fisher information of the light (Section 3.4.1). We then discuss the back action on the atomic state if this information remains unused (Section 3.4.2). This can be used to either directly measure the quantum state (Section 3.4.3) or generate the squeezed state from the measurement (Section 3.4.4). We summarize the effects for Gaussian states (Section 3.4.5), which have an intuitive geometric meaning. And finally, we quantify the contrast loss due to the scattering of photons into free space (Section 3.4.6), which on the other hand, is an individual dephasing process that kicks our quantum state out of the original Hilbert space.

3.4.1 Quantum Fisher Information Available in A Coherent State of Light: A Measurement Effect

In Sec. 3.2.2 we derived the amplitude and phase of the coherent state of light inside the cavity in the presence of the atoms, Eq. (3.8). This coherent state $|\alpha\rangle$ will depend on the number of atoms and their spin state. The light field leaking out of the cavity, as given by Eqs. (3.9) and (3.10), can then be used to deduce information about the atomic ensemble. In general, assume we have a coherent state of light $|\alpha\rangle$ depends on some physical parameter x, i.e. $|\alpha\rangle = |\alpha(x)\rangle$. We can use the quantity QFI to develop the measurement uncertainty, where the detailed and more general definition will be given in Sec. 4.2. Specifically, the QFI is [23, 43, 171]:

$$\tilde{F}(x)\left[|\alpha(x)\rangle\right] = 4\left(\langle\partial_x\alpha(x)|\partial_x\alpha(x)|\partial_x\alpha(x)|\partial_x\alpha(x)\rangle - |\langle\partial_x\alpha(x)|\alpha(x)|\partial_x\alpha(x)|\alpha(x)\rangle|^2\right), \tag{3.23}$$

where the state derivative is defined as

$$|\partial_x\alpha(x)\rangle \equiv \frac{\partial\,|\alpha(x)\rangle}{\partial x} = \lim_{\epsilon\to 0}\frac{|\alpha(x+\epsilon)\rangle - |\alpha(x)\rangle}{\epsilon}. \tag{3.24}$$

With tedious calculations as in Appendix D of [125], one has

$$\tilde{F}(x) = 4\left|\frac{\partial\alpha}{\partial x}\right|^2, \tag{3.25}$$

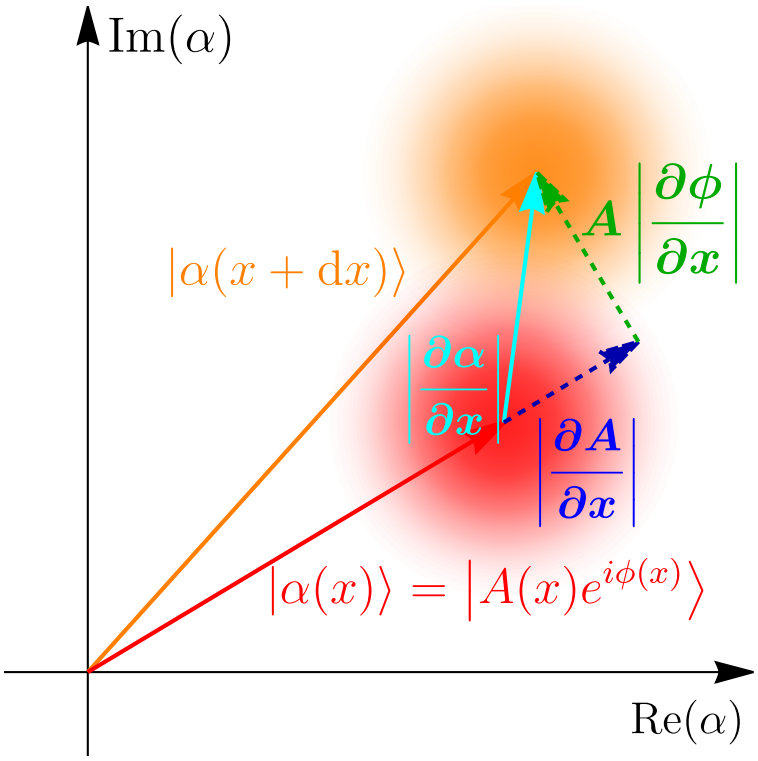


Figure 3-2: Precision of estimation of an unknown parameter x by measurement of a coherent state of light $|\alpha\rangle$. A change dx in some parameter x modifies the amplitude (blue) and phase (green) of $|\alpha(x)\rangle$. The optimum amount of information about dx can be extracted by measuring the state quadrature along the direction of change $\partial\alpha/\partial x$ of the coherent state, which in general, is a combination of phase and amplitude measurements. The shot noise of the coherent state of light (color-shaded area) limits the precision of the measurement.

and the quantum Cramér-Rao bound [82, 23, 135, 171] for the variance associated with estimating the parameter x is given by

$$(\Delta x)^2 = \left(2\left|\frac{\partial\alpha}{\partial x}\right|\right)^{-2} \tag{3.26}$$

Often measurements are performed on either the power or the phase of the light field emanating from the cavity. In this case, it is useful to consider the amplitude A and phase ϕ of the coherent state, $\alpha = Ae^{i\phi}$, in order to separate the QFI into its amplitude component $\tilde{F}_A$ and phase component $\tilde{F}_\phi$,

$$\tilde{F}(x) = \tilde{F}_A + \tilde{F}_\phi = 4\left|\frac{\partial A}{\partial x}\right|^2 + 4A^2\left|\frac{\partial\phi}{\partial x}\right|^2. \tag{3.27}$$

In general, neither amplitude nor phase alone contains the full information about the atomic system available in the light field. Nevertheless, the full QFI can always be extracted by performing a homodyne measurement of the coherent state $|\alpha\rangle$ with optimized phase offset and amplitude (see Fig. 3-2). If we only measure the transmitted and reflected power instead of performing the optimum state detection, the variance in the estimation of parameter x will equal $\tilde{F}_A^{-1}$ with the best analysis.

In the context of the CQED system displayed in Fig. 3-1, the expression for the QFI, Eq. (3.25), leads to two consequences. If the parameter x is chosen to be the collective atomic spin S_z (see Section 3.2.1), then Eq. (3.25) quantifies the amount of entanglement between the collective atomic state and light, or equivalently, the information imprinted onto the state of the light by the atoms. So the QFI of the light with respect to the atomic state, normalized to the atomic state shot noise, tell us how much measurement-based spin squeezing can be attained by an optimal probing scheme. Second, even if the light is not used for measurement, as in cavity feedback squeezing [121, 199], the QFI still describes the amount of excess quantum backaction on the atomic state by the input light: discarding the information contained in the light field, or equivalently, tracing over the state of the light field, results in the excess variance of the atomic spin state above the minimum imposed by the Heisenberg

uncertainty relations for angular momentum.

3.4.2 Measurement Backaction

In quantum mechanics, any process that yields information about some variables is associated with backaction onto any non-commuting variables to maintain the uncertainty relation [33, 55, 247, 146]. If that information is not used, the uncertainty relation becomes a true inequality, and the initially pure quantum state turns into a mixed state, exhibiting excess broadening. In the case of spin squeezing, the effective Hamiltonian, Eq. (3.16), entangles the S_z component of the atomic spin with the intracavity photon number, such that the light field leaving the cavity serves as a meter of S_z. Hence in this case, one can think of the unused information contained in the light field as causing additional broadening in the S_z direction compared to the information about S_z that would be available to a perfect observer. From an alternative viewpoint, the original S_z distribution remains unchanged. Still, the photon shot noise of the light causes an additional broadening of S_y compared to a (noiseless) classical light field due to the uncertainty in the light shift on the atoms [199, 122]. These processes result in a mixed state of the atomic spin with $\Delta S_z \Delta S_y > S/2$.

To quantify those effects, consider a CSS pointing along the x-axis as in Fig. 3-5(a). From Eq. (3.16), we know that photons only couple to the S_z quadrature, and therefore the backaction-induced antisqueezing must manifest itself in the S_y quadrature. The coherent light probes the physical quantity S_z and therefore generates a back action quantified by the QFI in the light field $\tilde{F}$. We define the normalized QFI of the light,

$$F = \frac{2}{S}\tilde{F}. \tag{3.28}$$

The quantity $1 + F$ represents the factor by which a perfect measurement of the light field can reduce the spin variance below the SQL variance of the CSS,

$$(\Delta S_z)^2_{\text{cond}} = \frac{S}{2\,(1+F)}, \tag{3.29}$$

and the back action by the probing light thus causes broadening in the S_y direction, resulting in a total variance

$$(\Delta S_y)^2 = \frac{S}{2}(1+F)\,, \tag{3.30}$$

Here the first term $S/2$ accounts for the variance of the original CSS, while the second term $FS/2$ is due to the back action.

The complete information about the spin state of the ensemble is contained in the field amplitudes and phases of the transmitted light, reflected light, and free-space scattering. We note that the electric field amplitude $\mathcal{E}$ is related to the coherent-state index α in Sec. 3.4.1 via $\mathcal{E} = \alpha\sqrt{2\hbar\omega/\tau}$, where τ is the probing time. Therefore, we can use Eqs. (3.9), (3.10) and (3.25) to evaluate the total QFI about the atomic state that is available in the light field:

$$F = \frac{\langle \hat{N}_\uparrow\rangle \tau}{\hbar\omega}\left(T_2 + T_1 R_2 + \frac{\pi}{\mathcal{F}}\langle \hat{N}_\uparrow\rangle \eta \mathcal{L}_a(x_a)\right)\left|\frac{\partial \mathcal{E}_c}{\partial N_\uparrow}\right|^2. \tag{3.31}$$

Using the expression for the intracavity field, Eq. (3.8), we can simplify (3.31) to obtain

$$\begin{aligned} F &= 2\, n_\gamma^{\mathrm{sc}}\, \eta\, \mathcal{L}_a(x_a)\left(1 + x_a^2 + \frac{S\eta}{2}\right)\mathcal{T}_0 \\ &= 2\, n_\gamma^{\mathrm{sc}} \eta \mathcal{L}_a(x_a)\left(1 + x_a^2 + \frac{\nu}{4}\right)\mathcal{T}_0, \end{aligned} \tag{3.32}$$

where $\nu = N\eta$ and $\langle N_\uparrow\rangle = N/2 = S$ has been substituted. For fixed $\langle N_\uparrow\rangle\eta$, the spectrum of the coupled atom-cavity system (3.8)-(3.10) remains the same, while according to (3.32) the QFI carried by photons scales linearly with the cooperativity η. This equation also demonstrates an important principle of optical measurements: The information available about the system is inevitably proportional to the average number of photons that have been scattered into free space n_γ^{sc}. The higher the cavity cooperativity η, the more information about the atomic system can be extracted per scattered photon. Note that in the limit of small photon numbers, it is possible to gain more information per scattered photon by the use of postselected measurements, see,

e.g., Refs. [143, 73]. However, averaged over many realizations of the measurement, the available information gain is proportional to the scattered photon number, as expressed by Eq. (3.32). When this information F is extracted from the light field, it can serve to conditionally squeeze the atomic spin noise in the S_z direction by a factor $(1+F)^{-1}$, i.e., $(\Delta S_z)^2_{cond} = \frac{S/2}{1+F}$. At the same time, ΔS_y is increased by the back action to $(\Delta S_y)^2 = \frac{S}{2}(1+F)$, thus maintaining the Heisenberg uncertainty for angular momentum, $\Delta S_y \Delta S_z \geq \frac{S}{2}$. If the information in the light field remains unused, then the increased ΔS_y describes the broadening of the state along S_y that at the microscopic level is due to the photon shot noise in the incident light.

The complete QFI expressed by Eq. (3.32) can further be separated into two parts. The first two terms inside the parenthesis correspond to the information contained in the transmitted and reflected light fields that do not provide access to the state of any individual atom, but only to the collective spin, i.e., the symmetric state of the atoms. On the other hand, the last term, which is proportional to the collective cooperativity $S\eta$, originates from free-space scattering, and reveals local spin fluctuations that take the system out of the symmetric spin space.

With the help of Eq. (3.22), we can write a relation between the Fisher information F and the squeezing parameter Q:

$$\frac{Q}{F} = x_a \frac{1 - x_c x_a + S\eta}{1 + x_a^2 + \frac{S\eta}{2}}. \tag{3.33}$$

3.4.3 Example: (Strong) Cavity Measurement of the Atomic State

In this section, we derive the spin resolution that can be obtained with an optical measurement probing the cavity. A more specific discussion is provided in Ref. [230]. Related approaches to the non-destructive detection of the atom number using a high-finesse cavity have been investigated in Ref. [31, 85].

Our goal here is to derive the measurable amount of Fisher information $F_{\text{meas}}(S_z)$ about the collective atomic spin operator $S_z = N_\uparrow - N_\downarrow$ that is available in the light

field. This information is contained in the reflected and transmitted fields $\mathcal{E}_r$ and $\mathcal{E}_t$, but not in the scattered light, so it is not the same as total Fisher information, Eq. (3.31). The measurement resolution of S_z is thus characterized by the Fisher information contained in the reflected and transmitted fields,

$$F_{\text{meas}}(S_z) = 4\tau T_{\text{tot}} \left| \frac{\partial \mathcal{E}_c}{\partial S_z} \right|^2, \tag{3.34}$$

where $T_{\text{tot}} = T_2$ in the case where only the transmitted photons are measured, and $T_{\text{tot}} = T_1 + R_2 T_1 \approx T_1 + T_2$ when both the transmitted and reflected photons are detected. Evaluating Eq. (3.34) using Eq. (3.8), we find

$$F_{\text{meas}}(S_z) = 4\tau T \frac{\mathcal{F}^2}{\pi^2} T_1 |\mathcal{E}_{\text{in}}|^2 \eta^2 \mathcal{L}_a(x_a) \mathcal{T}_0^2, \tag{3.35}$$

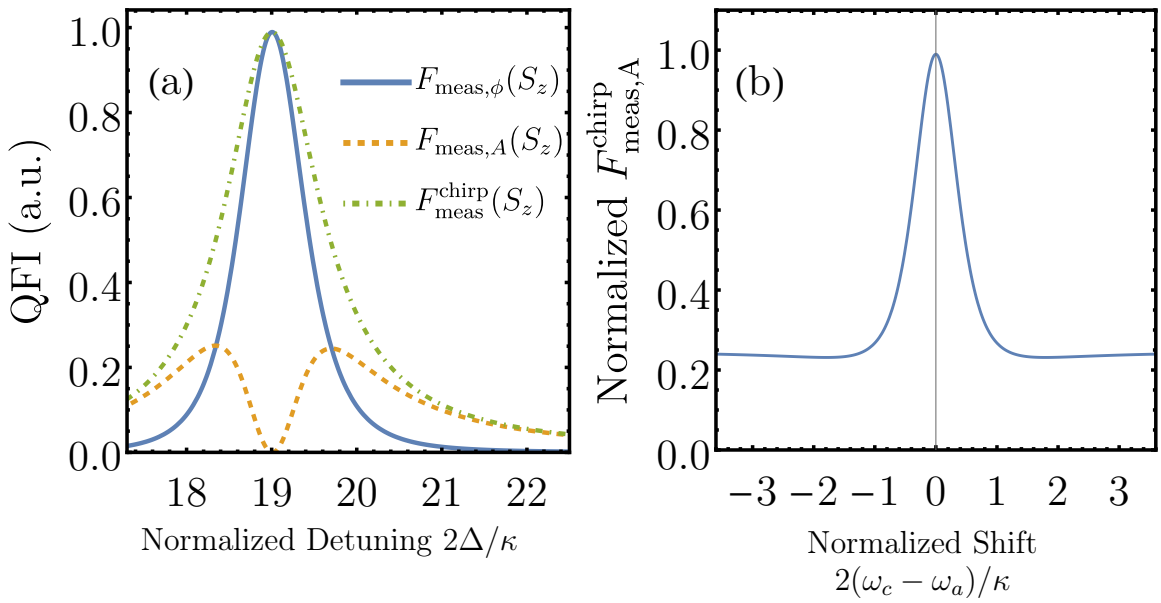


Figure 3-3: (a) QFI per scattered photon per atom for different types of measurements. The solid blue line and the yellow dashed line correspond to the amplitude and phase components of the total QFI F_{A} and F_ϕ, respectively. The green dotted line represents the QFI $F_{\text{A}}^{\text{chirp}}$ for a chirped two-color measurement of the transmission amplitude through the cavity, which equals the total QFI $F_{\text{A}} + F_\phi$; (b) The normalized total QFI for a chirped two-color measurement as a function of the cavity-atom detuning. The QFI is quite sensitive to the symmetry of the transmission lineshape, see text.

Experimentally, the intensity of the light field can be measured directly by a

photodetector, while a measurement of the phase requires interference with a signal that oscillates at a similar optical frequency. As shown in Fig. 3-3(a), the measurable Fisher information is contained primarily in the phase component of the light field. Usually, a homodyne or heterodyne measurement is used to retrieve the information contained in the phase. For a situation where the cavity is on resonance with the atomic transition, and the coupled system exhibits a spectrum with Rabi splitting, it is possible to use the transmitted or reflected light in a two-color chirp measurement with two balanced sidebands [24, 25]. In this measurement scheme, one generates two balanced sidebands with frequencies $\omega_\pm = \omega_c \pm \omega_m$, where ω_m is the modulation frequency that can be controlled. The transmitted field represents an interference of the two components with a beat note at $2\omega_m$, which contains the desired phase information. The QFI of the transmitted light in such a measurement is

$$F_{\mathrm{t}}^{\mathrm{chirp}} = 4\tau T \left| \frac{\partial \mathcal{E}_c^{\mathrm{chirp}}}{\partial S_z} \right|^2 , \tag{3.36}$$

which equals the sum of the QFI contained in the two sidebands. In addition to recovering all of the QFI from the transmitted field, this two-color measurement scheme suppresses the effects of laser and cavity noise by probing both cavity resonances at the same time. However, this approach requires a symmetric transmission lineshape, as in Fig. 3-3(b). The simulation is performed with a cavity linewidth $\kappa = 2\pi \times 520\,\mathrm{kHz}$ and an atomic linewidth $\Gamma = 2\pi \times 184\,\mathrm{kHz}$, corresponding to the parameters of the experiment in Refs. [25, 168]. The simulation shows that for $N_\uparrow \eta = N_\downarrow \eta = 900$, when the cavity is detuned by only $\kappa/10$ from atomic resonance, the total Fisher information in the two-color chirp measurement drops by a factor of 2. Therefore when using this scheme, it is very important to keep the cavity in resonance with the atomic transition, or, equivalently, to make the cavity transmission lineshape symmetric around the bare-cavity resonance.

For the systems where Raman scattering occurs, like for our ^{171}Yb or Rb CQED systems, an atom in the state $|\downarrow\rangle$ can be excited by a cavity photon to the state $|e,\downarrow\rangle$ and subsequently, spontaneously decay into $|\uparrow\rangle$. This causes an undesired random

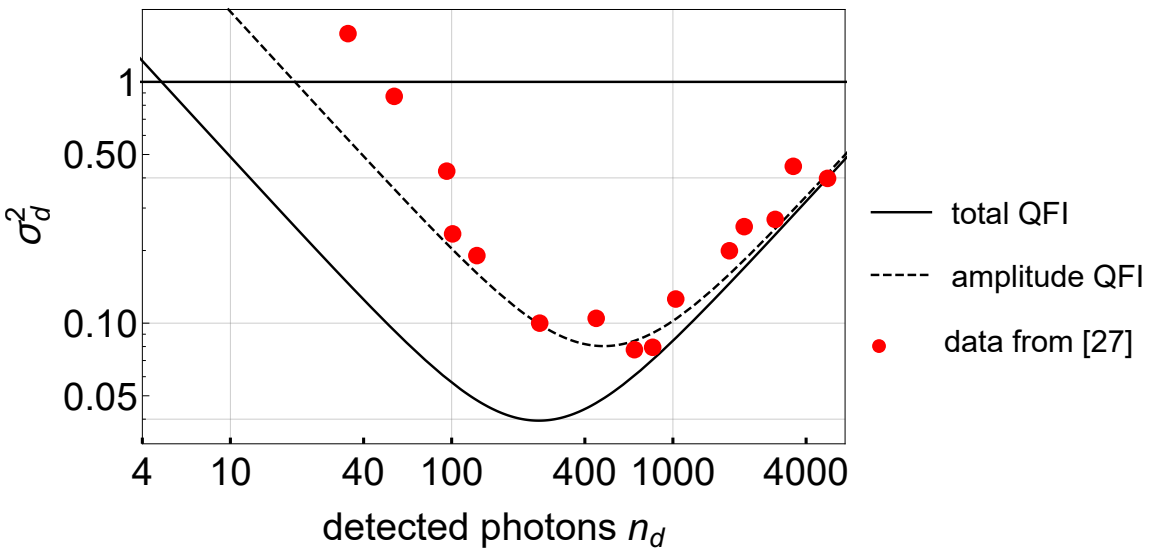


Figure 3-4: Measurement quality of the system σ_d^2 (variance of measurement spin noise normalized to SQL) for the chirped two-color measurement, with total atom number $N = 1000$, single atom cooperativity $\eta = 1.8$ and the total quantum efficiency for detecting photons is $q = 0.15$. The solid black curve corresponds to the theoretical model including both the total QFI and Raman scattering noise, and the dashed black curve only includes the QFI contained in the transmission amplitude. The red points are experimental data from [25]. The detection limit σ_d^2 first improves with photon number n_d as the fractional photon shot noise is reduced, and then increases with n_d due to spontaneous Raman scattering.

spin-flip and results in an additional variance

$$(\Delta S_z)_{\mathrm{R}}^2 = R_{\downarrow\uparrow}\tau \tag{3.37}$$

where $R_{\downarrow\uparrow}$ is the Raman scattering rate on the particular spin flipping transition $|\downarrow\rangle \to |e\downarrow\rangle \to |\uparrow\rangle$, and τ is the probing time.

The Raman scattering effect sets the limit of the performance of the optical S_z measurement. The variance of the S_z measurement is composed of two terms, one being the inverse attainable QFI contained in the light field, and the other the Raman scattering induced spin flip noise as in Eq. (3.37):

$$(\Delta S_z)_{\mathrm{meas}}^2 = \frac{1}{1+F_{\mathrm{meas}}} + (\Delta S_z)_{\mathrm{R}}^2 \tag{3.38}$$

The result from both contributions is summarized in Fig. 3-4. At small photon

number n_γ^{meas}, the detected variance is dominated by the low QFI contained in the light field, and therefore scales as $1/n_\gamma^{\text{meas}}$. In the limit of large photon number, the variance is dominated by the Raman scattering and scales linearly with n_γ^{meas}. For the parameters of Fig. 3-4, corresponding to the experiment in Ref. [25], the best measurement quality is obtained with ~ 500 detected photons, and corresponds to a resolution of 11 dB below the SQL. The measured resolution was 3 dB above the theoretical optimal resolution with the same parameters.

3.4.4 Example: (Weak) Quantum Nondemolition Measurement Squeezing Experiments

The measurement of the collective atomic state can, on the other hand, be used as a weak measurement where the whole process scatters a negligible amount of incoherent photons. Thus the state remains in the same Hilbert space but is projected into a reduced range of the $\hat{S}_z$ distribution. This coincides with people's dream of generating metrological useful quantum states, which I will describe in more detail in Chap. 4.

This idea, also known as quantum non-demolition measurement (QND), is first discussed [113, 218] and implemented [114] in dilute free-space quantum gas systems, and the first proof of metrological spin squeezing is achieved later in 2009 [4]. People also realized that the cavity, which offers strong atom-light interaction and reduced incoherence in the process, should, in principle, gives better performance. Such a method is first demonstrated in a far-detuned (dispersive) atom-cavity system [199], and similarly in [88].

However, we know that in the dispersive regime, the cavity's nonlinearity only acts as a perturbative second-order effect, which is significantly reduced. The measurement should also work in the Rabi-splitting regime, which we discussed a lot previously. This has been theoretically analyzed in [31]. Meanwhile, many groups have also done such experiments [30, 17, 38].

In [31], and related works in James Thompson's group, the measurement is inferred by analyzing one of the Rabi splitting peaks. As seen in Fig. 3-3, at the peak, the

QFI is indeed completely in the phase direction. That, however, doesn't mean that in general, the measurement is most efficient by measuring the phase.

Here we introduce a method to use the feature of the symmetric property of the vacuum Rabi splitting to down-convert the optical frequency information using the self-heterodyne to the RF frequency and, therefore, fully capture using the fast photon counter card.

3.4.5 Gaussian State Representation

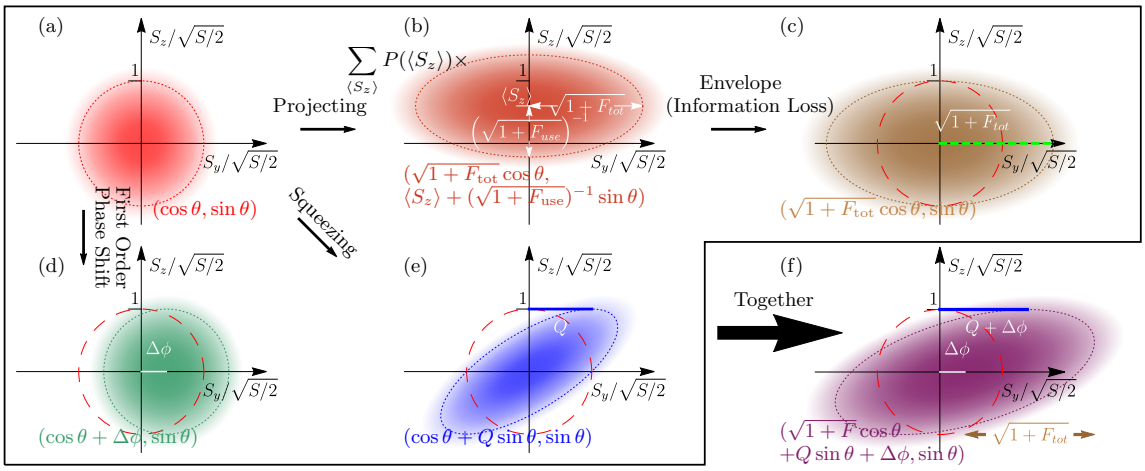


Figure 3-5: Illustration of the effects of the atom-light interaction on a CSS. (a) Original CSS on the equator of the Bloch sphere, $\langle S_z \rangle = 0$. (b) The effect of a single-shot optical measurement (see text) with usable QFI F_{use} and total QFI F_{tot}, which displaces the state along S_z based on the measurement and yields a resolution beyond the SQL (measurement-based spin squeezing), while broadening it along S_y due to the measurement backaction. (c) The envelope arising from averaging over many repeated measurements shows broadening along S_y. (d) Phase shift $\Delta\phi$ due to the atom-light interaction in zeroth order, Eq. 3.18. (e) The effect of single-axis twisting with shearing strength Q. (f) The complete final state for cavity spin squeezing with all phase shift, shearing, and state broadening due to unused information F contained in the light field. The equations below each plot give parametric expressions $(\tilde{S}_y, \tilde{S}_z) = (\cos\theta, \sin\theta)$ with $\theta \in [0, 2\pi)$ for the uncertainty ellipses of the atomic states which are indicated by dotted lines in the same colors as the states. In (c-f) the dashed red circle represents the uncertainty circle for the original CSS for comparison.

In this part, I will develop a simple formalism to describe the transformation of Gaussian states in the limit where the state occupies a small region on the Bloch

sphere. Collective spin states near the CSS are good examples of Gaussian states that have significant roles in quantum information science [235]. The CSS state can be described by a symmetric Gaussian distribution when projected along any spin quadrature perpendicular to the spin's mean direction. When the shearing parameter Q and the QFI F are small, the local Bloch sphere can be approximated by a 2D Cartesian frame, and the state can be represented by a Gaussian distribution. This also corresponds to the Holstein-Primakoff approximation [86].

The CSS along the x-axis has a Wigner quasi-probability distribution $P(S_y, S_z) \propto \mathrm{e}^{-2(S_y^2+S_z^2)/N}$, or,

$$P(S_y, S_z) \propto \exp\left[-\frac{1}{2}\begin{pmatrix} S_y & S_z \end{pmatrix} \Sigma^{-1} \begin{pmatrix} S_y \\ S_z \end{pmatrix}\right], \tag{3.39}$$

where the inverse covariance matrix Σ^{-1} is an identity matrix with a prefactor of the standard quantum limit (SQL) unit of variance: $\Sigma^{-1} = (2/S)\,\mathbb{I}_2$. Other Gaussian states that are centered along the x-axis can all be described similarly but with a different inverse covariance matrix.

Let's look at an example: starting from a CSS along the x axis, entangled atomic states can be generated via a Hamiltonian unitary evolution as discussed in Sec. 3.2, or by a measurement as described in Sec. 3.4.

First, consider the one-axis twisting, $\hat{H}_2 = -\hbar\chi\hat{S}_z^2$. In an infinitesimal time step $\mathrm{d}t$, the one-axis twisting transforms a point on the collective Bloch sphere according to

$$\begin{pmatrix} S_y(t+\mathrm{d}t) \\ S_z(t+\mathrm{d}t) \end{pmatrix} = \begin{pmatrix} 1 & N\chi\mathrm{d}t \\ 0 & 1 \end{pmatrix} \begin{pmatrix} S_y(t) \\ S_z(t) \end{pmatrix},$$

which generates a unitary evolution of the covariance matrix as

$$\Sigma(t+\mathrm{d}t) = U\Sigma(t)U^\dagger, \tag{3.40}$$

where

$$U = \begin{pmatrix} 1 & N\chi \mathrm{d}t \\ 0 & 1 \end{pmatrix}.$$

When including the non-unitary effect of the QFI, the covariance matrix transforms such that the product of eigenvalues is no longer normalized to the SQL. With constant strength of measurement, i.e. a QFI that increases linearly in time, the broadening along the S_y axis is also linear in time, i.e., the $(1,1)$ element of the covariance matrix evolves as

$$\Sigma(1,1)(t+\mathrm{d}t) = \Sigma(1,1)(t) + \dot{F}\mathrm{d}t \tag{3.41}$$

where $\dot{F}$ is the normalized QFI rate, and with a constant probing rate, $\dot{F} = F/t$ and $\dot{Q} = Q/t = N\chi$. It turns out that the effects described by Eqs. (3.40) and (3.41) commute with each other, giving

$$\Sigma = \frac{N}{4}\begin{pmatrix} 1+F+Q^2 & Q \\ Q & 1 \end{pmatrix}. \tag{3.42}$$

One can apply the above discussion of the covariance matrix to the parametric description of the $1/e$ boundary of the quasi-probability distribution on the Bloch sphere. For example, the squeezing transforms the curve $(\cos\theta, \sin\theta)^{\mathrm{T}}$ to $U\cdot(\cos\theta, \sin\theta)^{\mathrm{T}} = (\cos\theta + N\chi\mathrm{d}t\sin\theta, \sin\theta)^{\mathrm{T}}$, as shown in Fig. 3-5 (e). For the effect of QFI induced broadening, using (3.39) we have that the new boundary is given by

$$\tilde{S}_y^2/(1+\dot{F}\mathrm{d}t) + \tilde{S}_z^2 = 1,$$

which corresponds to a parametric description of $(\tilde{S}_y, \tilde{S}_z) = (\sqrt{1+\dot{F}\mathrm{d}t}\cos\theta, \sin\theta)$ where $\theta \in [0, 2\pi)$. Note that for individual measurements, the state is actually projected to a random state centered at $(\langle S_z\rangle, 0)$ with a probability $P(\langle S_z\rangle) \propto \exp(-2S_z^2/N)$ and a variance along the z-direction that is reduced by a factor of $1+F_{\mathrm{use}}$. Here F_{use} is the usable fraction of the total QFI but broadened along the

y-direction as quantified by the same F_{tot} we discussed above. This individual projection looks like the one in Fig. 3-5 (b); however, if we only care about the deterministic effect where the light state is traced over, the effect is depicted as in Fig. 3-5 (c).

In addition, in this description, the atomic state can deviate from the x-axis by the first order phase shift effect $\hat{H}_0 = -\hbar\Omega\langle\hat{n}_c\rangle\hat{S}_z$, which translates $(\cos\theta, \sin\theta)$ to $(\cos\theta + \Delta\tilde{\phi}, \sin\theta)$, as in Fig. 3-5 (d). Here $\Delta\tilde{\phi}$ is the normalized phase shift and relates to the phase shift $\Delta\phi$ in (3.18) by $\Delta\tilde{\phi} = \sqrt{N}\Delta\phi$.

3.4.6 Photon scattering: Individual Dephasing

When one photon is scattered by the atomic ensemble into free space, the particular atom that scatters this photon gains a random phase (or equivalently, is projected into a particular internal state) and therefore no longer retains coherence with the other atoms. Given n_γ^{sc} scattered photons and an average number of scattered photons per atom $p = n_\gamma^{\text{sc}}/N$, the Poissonian probability for any particular atom to not have scattered any photons is given by

$$C_{\text{sc}} = \frac{p^0 e^{-p}}{0!} = e^{-n_\gamma^{\text{sc}}/N}. \tag{3.43}$$

This is also the contrast limit of a phase-sensitive atomic signal, as measured, e.g., in a Ramsey sequence, due to photon scattering. As we have seen above (Eq. (3.22)), light-induced spin squeezing is impossible without scattering photons, and thus some contrast loss is inevitable. Therefore, in practical applications, one must carefully balance the potential metrological gain provided by spin squeezing against the detrimental effects of decoherence.

Besides the scattering-induced contrast loss, there exists another type of contrast loss that is due to the antisqueezing of the state around the Bloch sphere, perpendicular to the squeezed direction, which shortens the average collective spin vector $|\langle\mathbf{S}\rangle| = C_{\text{Bloch}}S$. (This process occurs even in the absence of photon scattering simply due to the deformation of the state.) This contrast loss is well approximated by $C_{\text{Bloch}} = \exp\left(-\frac{Q^2}{2N}\right)$. Combining those two contrast loss mechanisms, we obtain the

total contrast as

$$C = C_{\mathrm{sc}} C_{\mathrm{Bloch}} = \exp\left(-\frac{n_\gamma^{\mathrm{sc}} + Q^2/2}{N}\right). \tag{3.44}$$

This fundamental contrast reduction for phase-sensitive measurements affects the performance of spin-squeezed atomic clocks [88, 38, 168, 92] and other interference-based atomic sensors [4, 207, 25, 7].

3.5 First-principle approach

The approach developed in Sec. 3.3 and Sec. 3.4 is based on semiclassical cavity field, and our imposed photon shot noise on coherent photonic state, but the obtained effective Hamiltonian (3.15) is equivalent to a microscopic model, as also similarly presented in Ref. [40]. Here we derive our Hamiltonian from a microscopic model of the atom-light interaction in the mean-field limit. We consider a three-level atom as in Sec. 3.2, and an optical cavity mode (represented by its annihilation operator $\hat{b}$) interacting with the $|\uparrow\rangle$ state with coupling strength $g = \sqrt{\eta\kappa\Gamma}/2$ [222]. Also, we define the raising and lowering operators $\hat{a}_{e,\uparrow}^{(\dagger)}$ for the atomic states. The full Hamiltonian is

$$\begin{aligned}\hat{H} = &\underbrace{\omega_c \hat{b}^\dagger \hat{b}}_{H_{\mathrm{c}}} + \underbrace{\omega_a \hat{a}_e^\dagger \hat{a}_e}_{H_{\mathrm{a}}} + \underbrace{g\left(\hat{b}\hat{a}_e^\dagger \hat{a}_\uparrow + h.c.\right)}_{H_{\mathrm{int}}} \\ &+ \underbrace{\sqrt{\frac{\kappa}{2}\frac{2T_1}{T_1+T_2}}\left[\beta^* \hat{b}^{-i\omega_l t} + \beta \hat{b}^\dagger e^{i\omega_l t}\right]}_{\hat{H}_{\mathrm{drive}}},\end{aligned} \tag{3.45}$$

and the atomic and cavity field decay is described by the Lindblad master equation:

$$\dot{\rho} = i[\hat{H}, \rho] + \frac{1}{2}\sum_j \left(\left[\hat{L}_j \rho, \hat{L}_j^\dagger\right] + \left[\hat{L}_j, \rho \hat{L}_j^\dagger\right]\right), \tag{3.46}$$

and the corresponding Lindblad operators are

$$\hat{L}_c = \sqrt{\kappa}\hat{b}, \hat{L}_a = \sqrt{\Gamma}\hat{a}_e\hat{a}_\uparrow^\dagger.$$

In the unsaturated regime, we can use a mean-field approximation so that the operator $a_\uparrow^{(\dagger)}$ can be replaced by $\sqrt{N_\uparrow}$, and the first line can be considered as a coupled harmonic oscillator problem. We can diagonalize the system into new modes described by annihilation operator $\hat{c}_+, \hat{c}_-$:

$$\hat{H}_\mathrm{c} + \hat{H}_\mathrm{a} + \hat{H}_\mathrm{int} = \omega_+\hat{c}_+^\dagger\hat{c}_+ + \omega_-\hat{c}_-^\dagger\hat{c}_-, \tag{3.47}$$

where

$$\omega_\pm = \frac{\omega_a + \omega_c \pm \sqrt{4g^2N_\uparrow + (\omega_a - \omega_c)^2}}{2}$$

and

$$\hat{c}_\pm = \frac{\omega_\pm - \omega_c}{\sqrt{(\omega_\pm - \omega_c)^2 + g^2N_\uparrow}}\hat{a}_e + \frac{g\sqrt{N_\uparrow}}{\sqrt{(\omega_\pm - \omega_c)^2 + g^2N_\uparrow}}\hat{b},$$

and the driving Hamiltonian H_drive can be written as

$$\begin{aligned}
\hat{H}_\mathrm{drive} = &\sqrt{\frac{\kappa}{2}\frac{2T_1}{T_1+T_2}}\frac{1}{\omega_+ - \omega_-}\times \\
&\Bigg[\beta^* e^{-i\omega_l t}\Big(\sqrt{(\omega_+ - \omega_a)^2 + g^2N_\uparrow}\hat{c}_+ - \sqrt{(\omega_- - \omega_a)^2 + g^2N_\uparrow}\hat{c}_-\Big) \\
&+ \beta e^{i\omega_l t}\Big(\sqrt{(\omega_+ - \omega_a)^2 + g^2N_\uparrow}\hat{c}_+^\dagger - \sqrt{(\omega_- - \omega_a)^2 + g^2N_\uparrow}\hat{c}_-^\dagger\Big)\Bigg].
\end{aligned}$$

Lastly, the Lindblad operators can also be expressed in these new modes:

$$\begin{aligned}
\hat{L}_c &= \sqrt{\kappa}\hat{b} = \sqrt{\kappa}\frac{1}{\omega_+ - \omega_-} \\
&\times \left(\sqrt{(\omega_+ - \omega_a)^2 + g^2N_\uparrow}\hat{c}_+ - \sqrt{(\omega_- - \omega_a)^2 + g^2N_\uparrow}\hat{c}_-\right), \\
\hat{L}_a &= \sqrt{N_\uparrow\Gamma}\hat{a}_e = \sqrt{N_\uparrow\Gamma}\frac{1}{\omega_+ - \omega_-}
\end{aligned}$$

$$\times \left(\sqrt{(\omega_+ - \omega_c)^2 + g^2 N_\uparrow} \hat{c}_+ - \sqrt{(\omega_- - \omega_c)^2 + g^2 N_\uparrow} \hat{c}_- \right).$$

Using the Reiter and Sørensen method [183], we can adiabatically eliminate the cavity field as well as the excited state by eliminating the $\pm$ modes, and therefore obtain the effective Hamiltonian in the $\hat{a}_\uparrow$ manifold. Further, we can assume that

- $\kappa|\beta|^2 \frac{2T_1}{T_1+T_2} \langle \hat{b}^\dagger \hat{b} \rangle \ll (\omega_l - \omega_{a,c})^2$
- $g^2 \frac{2T_1}{T_1+T_2} \langle \hat{b}^\dagger \hat{b} \rangle \ll (\omega_l - \omega_{a,c})^2$

which simplifies the obtained Hamiltonian to

$$\hat{H}_{\text{eff}} = \Delta_{\text{eff}} \hat{a}_\uparrow^\dagger \hat{a}_\uparrow, \tag{3.48}$$

where

$$\begin{aligned} \Delta_{\text{eff}} = &- |\beta|^2 \frac{2T_1}{T_1+T_2} \frac{g^2}{\kappa\Gamma} (1 + 2(\omega_l - \omega_a)^2/\Gamma^2)^2 \times \\ &\big[((1 + 2(\omega_l - \omega_a)^2/\Gamma^2)^2 + g^2 N_\uparrow/\kappa\Gamma)^2 \\ &+ (2(\omega_l - \omega_c)/\kappa \cdot (1 + 2(\omega_l - \omega_a)^2/\Gamma^2)^2) \\ &- 2(\omega_l - \omega_a)/\Gamma \cdot g^2 N_\uparrow/\kappa\Gamma)^2 \big]^{-1}, \end{aligned}$$

which is equivalent to Eq. (3.15).

On the other hand, this system also has its new effective Lindblad operator $\hat{\mathcal{L}} = \hat{a}_\uparrow^\dagger \hat{a}_\uparrow$. This can be simplified by removing the constant term in the Lindblad operator, such that $\hat{\mathcal{L}} \to \hat{S}_z$, and serves as the collective dephasing:

$$\mathcal{L}_{\text{eff}}[\rho] = \hat{S}_z \rho \hat{S}_z - 1/2(\hat{S}_z^2 \rho + \rho \hat{S}_z^2), \tag{3.49}$$

$$\dot{\rho} = -i[\hat{H}_{\text{eff}}, \rho] + \gamma_C \mathcal{L}_{\text{eff}}[\rho]. \tag{3.50}$$

And, using the numerics discussed in Appendix A or analytical formula derived in [203], this gives the linear increase in the variance of $\hat{S}_y$ when the initial state is prepared around the equator, as shown in Fig. 3-6. This agrees with the measure-

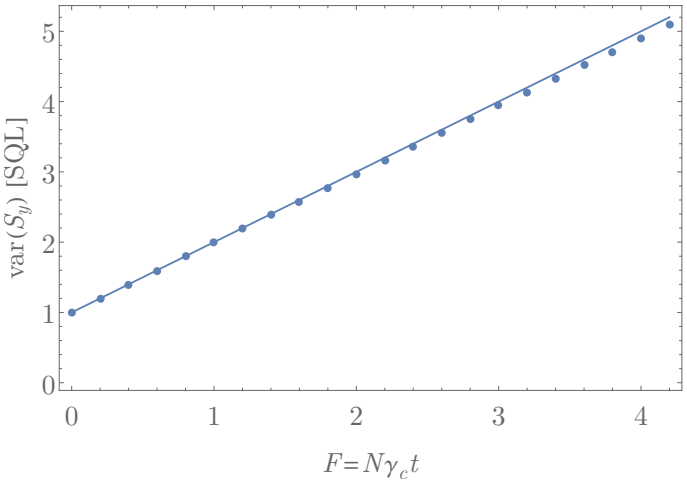


Figure 3-6: Linear increasing of the variance of $\hat{S}_y$ for an initial CSS along S_x direction under the effective collective dephasing Lindbladian operator.

ment broadening formalism (3.30), as well as the Gaussian understanding derived in Sec. 3.4.5. This also shows that $F = N\gamma_C t$ which agrees with our analytic derivation.

Chapter 4

Quantum Metrology 101

Quantum technologies harness quantum entanglement and therefore revolutionize many subjects like computing, communications, and measurements. Quantum computing and quantum communications draw broad attention from general audiences, but using quantum technologies in measurement, or more formally, quantum metrology, is less known yet much more practical and better developed.

Currently, the most precise measurements are all done by spectroscopy, as the 1981 Nobel laureate Arthur Schawlow said:

> Never measure anything but frequency!

Using the spectroscopy method, humans have achieved many successes by far, including the measurement of the fine constant using atom-interferometry [249], Laser Interferometer Gravitational-Wave [1], dark matter/fifth force [37, 93, 58, 164, 162], electron dipole moment [187], gravitational red-shift [21, 46], and test of fundamental laws of physics like the Lorentz symmetry [193]. The idea is simple: one just divides the line of a certain frequency response (aka spectrum) to resolve the exact frequency of interest.

Specifically, the response may not only be reflected as the "amount", or amplitude, of certain quantities. Quantum mechanics, or even earlier, wave dynamics, had shown that the phase is also an essential part of physical reality, and thus can also respond to the external environment. In addition, the phase is usually even more sensitive,

and the majority of metrology based on interferometer like [1] relies on the field of phase estimation.

The spin squeezing that I discussed in Chap. 3 is the most commonly used example of entanglement-assisted phase estimation. There are, however, much more ways to use entanglement, and some of them are quite counterintuitive.

I will briefly review the quantum-enhanced phase estimation subject in this chapter. I will start with the basic phase estimation processes, including the Ramsey and Rabi sequences, which are likely taught in every AMO course. Then I will generalize the idea to the clock-related non-quantum metrology concepts. Later I will introduce how quantum entanglement changes and improves/degrades things, especially for the collective spin system and clock-related operations. With this knowledge, we will be prepared to understand most results from Chap. 5-8.

4.1 The Building Block: Rabi and Ramsey Sequence

Isidor Isaac Rabi developed the famous Rabi sequence in 1938 [179] in nuclear magnetic resonance systems. Later Rabi suggested using this method to build the atomic clock in 1945, though due to the fluctuating power and other technical limitations at that time, the central peak actually averaged over many unwanted signals and thus broadened, making the result not desired. In short, this ambitious goal was not achieved.

In 1949, Norman Ramsey developed the seminal Ramsey sequence based on Rabi's sequence, which nowadays becomes an essential part of modern quantum metrology and phase estimation. Many fields use it today, like the atom interferometer, RF atomic clocks, and gravitational wave detection.

The ultimate performance for the ideal version of both sequences is the same (up to a constant factor). They, however, have a different dependence on the noise spectrum [14] of the local oscillator, which decides what sequence to use. For example, the state-of-the-art optical clock experiments in JILA [20] have a larger high-frequency noise which makes them choose the Rabi sequence, which decays faster for high fre-

quencies.

Ultimately, the clock operation relies on the clock container (the atoms) and the local oscillator (the laser). The procedure is to interrogate the atoms with the laser, and we want to use a sequence to convert the resulting clock state population into a discriminator for the detuning of the clock laser from resonance. The sequence should let the system evolve under a certain form of the Hamiltonian, which is sensitive to a very tiny frequency difference. The most common ones are the Ramsey or Rabi spectroscopy sequence. To understand these sequences, we restrict ourselves to a two-level system defined by the two clock-related states (ground state $|g\rangle$ and excited clock state $|c\rangle$). Both sequences begin with the atoms prepared fully in the ground state.

For the Rabi sequence, the Hamiltonian is simple: the Rabi drive along x-direction always exists. The length of the continuously applied laser is set to be $T_{\text{Rabi}} = \pi/\Omega$, where Ω is the Rabi frequency of the clock light and is assumed constant. For a detuning of the clock light Δ, after the π-length pulse, the probability of being in the excited state is given by

$$P_e(\Delta) = \frac{\Omega^2}{\Delta^2 + \Omega^2} \sin\left(\frac{\pi\sqrt{\Delta^2 + \Omega^2}}{2\Omega}\right)^2 \tag{4.1}$$

For the Ramsey sequence, the Hamiltonian is piece-wise. Initially, the Hamiltonian is $\hat{H}_{\pi/2,y} = \Omega\hat{S}_y + \Delta\hat{S}_z$ with $\Omega \gg |\Delta|$ and it lasts for $\tau_{\pi/2} = \pi/(2\Omega)$. Then the drive is off; thus, the Hamiltonian, in the rotating frame, is $\hat{H}_{\text{ramsey}} = \Delta\hat{S}_z$, which lasts for τ_{ramsey}. Lastly, another drive with a different phase is applied $\hat{H}_{\pi/2,x} = \Omega\hat{S}_x + \Delta\hat{S}_z$ with the same length $\tau_{\pi/2} = \pi/(2\Omega)$. The final population of the excited state is given by

$$\begin{aligned} P_e(\Delta) =& \frac{4\Omega^2 \sin^2\left(\frac{\pi\sqrt{\Delta^2+\Omega^2}}{4\Omega}\right)}{\left(\Delta^2+\Omega^2\right)^2} \times \\ & \left[\sqrt{\Delta^2+\Omega^2}\cos\left(\frac{\pi\sqrt{\Delta^2+\Omega^2}}{4\Omega}\right)\cos\left(\frac{\Delta\tau_{\text{Ramsey}}}{2}\right)\right. \end{aligned} \tag{4.2}$$

$$- \Delta \sin\left(\frac{\pi\sqrt{\Delta^2+\Omega^2}}{4\Omega}\right)\sin\left(\frac{\Delta\tau_{\text{Ramsey}}}{2}\right)\Bigg]^2,$$

and by assuming $\Omega \gg |\Delta|$, this reduces to

$$P_e(\Delta) \sim \frac{1}{2} + \sin(\Delta\tau_{\text{Ramsey}}). \tag{4.3}$$

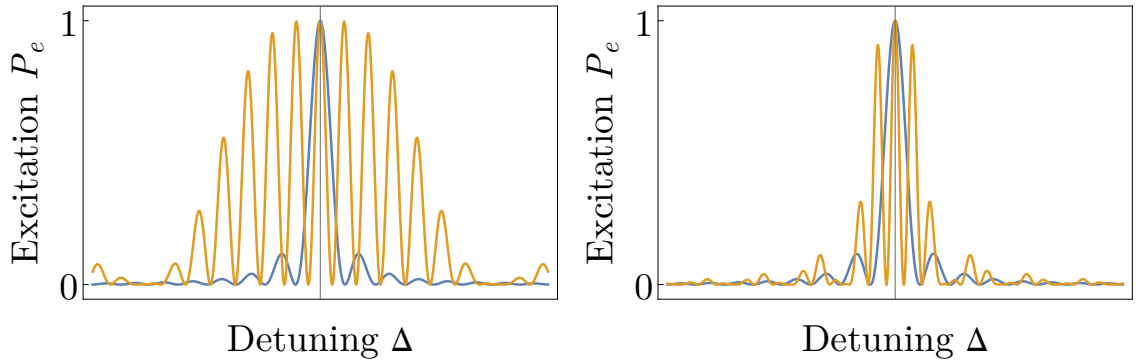


Figure 4-1: Spectroscopy fringes for (blue) Rabi sequence and (orange) Ramsey sequence. In the Ramsey sequence, we use (left) $\Omega\tau_{\text{Ramsey}} = 10$ and (right) $\Omega\tau_{\text{Ramsey}} = 3$.

We can notice that if we let $T_{\text{Rabi}} = \tau_{\text{Ramsey}}$ which corresponds to the same interrogation time, the FWHM for a Rabi sequence is 1.6 times larger than that for a Ramsey sequence. This means that the performances of these two sequences are off by just this factor, given the same signal-to-noise ratio and interrogation times.

Of course, these are the ideal cases, and from the final population, we can infer the constant Δ. When the Δ is no longer a constant (DC), our sequences would have their own frequency response to the $\Delta(t)$. For the clock operations, a frequency much higher than one over the interrogation time is not useful, and ideally, the sequence should not be sensitive to those. As investigated in [14], the Rabi sequence is better against those noises. However, once the AC signal is of interest, one would need to develop new sequences for those applications, and at the same time, the bandwidth of the metrology is also important [34].

4.2 Quantifying The Amount of Information a Measurement Carries

The above discussion is very close to the actual clock operation if not exactly the same. The missing link is how we measure the quantity P_e, which can be used to infer the Δ and feedback to the laser frequency.

In this section, we review, to my understanding, the most important concept in modern data analysis: Bayesian statistics. Within Bayesian statistics, I will talk about one important concept that we already mentioned: Fisher information and its quantum version.

The idea of Fisher information is simple: consider if a measurement X is randomly sampled from a given distribution parameterized by some quantity $P(X;\theta)$, then by this measurement, what amount of information we learn about this parameter?

This is quantified by the Fisher information as [59]

$$\mathcal{I}(\theta) = \mathrm{E}\left[\left(\frac{\partial}{\partial\theta}\log P(X;\theta)\right)^2 \middle| \theta\right] = \int_{\mathbb{R}}\left(\frac{\partial}{\partial\theta}\log P(x;\theta)\right)^2 f(x;\theta)\,dx. \tag{4.4}$$

However, a quantity of "information" is meaningless unless it can be mapped to how accurately one can estimate the parameter θ. This is established by the Cramér-Rao bound [39, 181]:

$$\mathrm{var}(\hat{\theta}) \geq \frac{1}{\mathcal{I}(\theta)}. \tag{4.5}$$

In (4.4) one can see that the "sharper" the features in $P(x;\theta)$, the larger information it gains. Using (4.5), this also means the more accurate the estimation can be. This agrees well with our intuitive understanding of squeezed states, as the squeezing makes the distribution narrow, which then has larger Fisher information and a less ultimate limit on estimation error.

This concept generalizes to the quantum regime very smoothly. In quantum mechanics, the quantum state intrinsically has the distribution feature. By projecting

to different bases μ, the corresponding distribution $P_\mu(X;\theta)$ gives the Fisher information of θ by this distribution $\mathcal{I}_\mu(\theta)$, and the quantum Fisher information (QFI) is defined as [171]

$$\mathcal{I}_Q(\theta) \equiv \max_{\{\mu\}} \mathcal{I}_\mu(\theta). \tag{4.6}$$

The form developed in Sec. 3.4.1 is a specific kind of QFI where the quantum state is a coherent state of light.

The quantum Cramér-Rao bound also exists and preserves its classical form [82, 23, 135, 171]:

$$\mathrm{var}(\hat{\theta}) \geq \frac{1}{\mathcal{I}_Q(\theta)}. \tag{4.7}$$

4.3 Chain of QFI

The overall question can then be considered as a chain of inferences from the raw measurement data to the final random variable (physical quantity), i.e., the phase of interest.

For the case of the phase estimation using the collective spin state inside an optical cavity, as the one developed in Chap. 3, the chain is as follows:

$$\boxed{\text{Photon Statistics } n = |\alpha|^2} \xrightarrow{P(n|\hat{N}_\uparrow)} \boxed{\hat{S}_z = (\hat{N}_\uparrow - \hat{N}_\downarrow)/2} \xrightarrow{P(\hat{S}_z|\rho(\theta))} \boxed{\rho(\theta)} \xrightarrow{\text{sequence}} \boxed{\theta}. \tag{4.8}$$

The reverse of the equation (4.8) is similar to the "generative model" in machine learning and is easier to understand. Basically, we have a signal θ and use a sequence like the Ramsey sequence to encode it into the system and form $\rho(\theta)$. From that state, one quantumly samples it using the basis of Dicke states $|S, S_z\rangle$, and then uses the photon statistics to infer which specific Dicke state it is projected into.

In Sec. 3.4.1, I have already shown, without very detailed arguing, the photon to

Dicke state's QFI. I showed that, with certain photon statistics, to what extent one can infer the $\hat{N}_\uparrow$. The derivation includes the setup using the transmitted light's pure amplitude information, pure phase information, and the optimized way of utilizing the information: the Chirp method.

The sequence's sensitivity, or similarly, the QFI, is also clear, as explained earlier in Sec. 4.1.

The only missing step is where the squeezed state or quantum entanglement kicks in. The entanglement makes the distribution along certain axis dramatically sharper or has more of sharper features.

We explicitly express how θ is encoded into $\rho(\theta)$. Without loss of generality, we can first consider the pure state condition $\rho(\theta) = |\psi_\theta\rangle \langle\psi_\theta|$ and use the Ramsey sequence. To lowest order as in (4.3), we have

$$|\psi_\theta\rangle = \hat{U}_{\pi/2,x} e^{-i\hat{S}_z\theta} |\psi_0\rangle , \tag{4.9}$$

where $\hat{U}_{\pi/2,x}$ is the $\pi/2$ rotation in the middle.

For the specific operator of interest $\hat{S}_z$ and the pure state condition $\rho(\theta) = \hat{U}_{\pi/2,x} |\psi_\theta\rangle \langle\psi_\theta| \hat{U}^\dagger_{\pi/2,x}$, such Fisher information is given by [171]

$$\mathcal{I}_Q(S_z; |\psi_\theta\rangle) = 4\mathrm{var}(S_z)_{|\psi_\theta\rangle}. \tag{4.10}$$

At first glimpse, the whole protocol seems trivial: just by generating a pure state with large $\mathrm{var}(S_z)$, then the small rotation angle θ against $\hat{S}_z$ can be estimated precisely. However, there is a logical step missing. The Cramér-Rao bound does not guide how to read the θ out properly.

4.4 Readout

The proper reading-out method that saturates the Cramér-Rao bound is highly non-trivial. We start with the simplest case of using an uncorrelated CSS.

Quantum states intrinsically have quantum fluctuations. The CSS state as in the

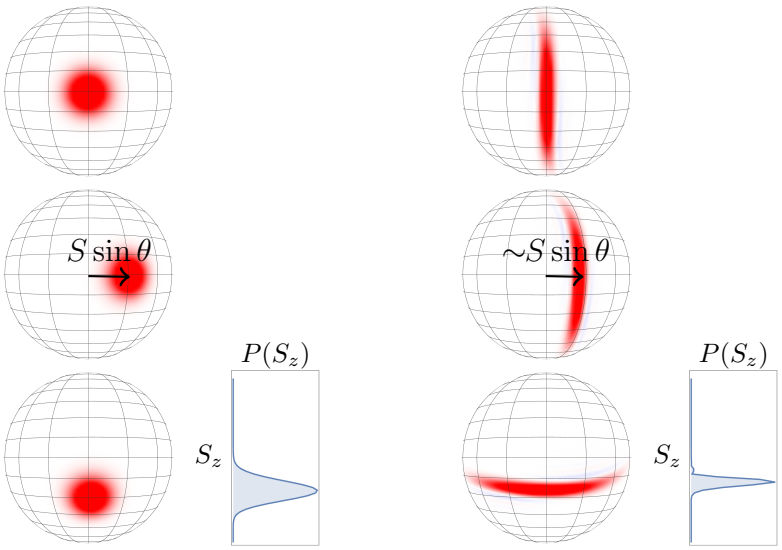


Figure 4-2: CSS and SSS Ramsey sequence.

final step in Fig. 4-2 has $\langle S_z\rangle = -S\sin\theta$, and the quantum fluctuation $\mathrm{var}(S_z) = \frac{S}{2}\cos^2\theta$. From this method, the Fisher information, as the lower bound of the QFI, is

$$\mathcal{I}_{CSS} = N,$$

which also saturates the QFI as in (4.10) of a CSS.

Naïvely, the SSS can be seen as a slightly modified version of CSS with a reduction of the quantum noise along the direction of interest. As in Fig. 4-2, the Ramsey sequence for SSS is very similar. The usage of the same method by inferring θ from $\langle S_z\rangle$ and $\Delta\theta$ from ΔS_z should also be valid to the first order. This is also called the method of moments [171].

Does this saturate the QFI of a SSS? For a slightly squeezed state, it seems so, but in general, it doesn't. Since we are looking for the signal-to-noise ratio, we need to characterize them separately. The amount of the noise is characterized by the Kitagawa-Ueda parameter [108]

$$\xi^2_{\mathrm{KU}} = \Delta S_z^2/\Delta S^2_{z,\mathrm{SQL}}, \tag{4.11}$$

where ΔS_z^2 is the variance of the S_z measurement and, $\Delta S^2_{z,\mathrm{SQL}} = S/2$ is the same

quantity for uncorrelated particles in the absence of contrast loss. Meanwhile, the signal in Fig. 4-2 is not exactly $S\sin\theta$; the difference is characterized by

$$C := \max_{\alpha} \frac{\langle \hat{S}_\alpha \rangle}{S}. \tag{4.12}$$

Together, we obtain the Wineland parameter [241, 240], which finally gives the signal-to-noise readout protocol of the Ramsey sequence using CSS and SSS

$$\mathcal{I}_{SSS,m} = \mathcal{I}_{CSS}\xi^{-2} = N\frac{C^2}{\xi^2_{\mathrm{KU}}}, \tag{4.13}$$

where the subscript m stands for the method of moments.

For arbitrary states, the Bayesian estimation can saturate the QFI but requires a lot of prior knowledge about the distribution under different θ. That means once the system is fully characterized, this method is of great use, as demonstrated in [216] and explained in [171].

Without such prior knowledge, if the state is obtained using the Hamiltonian evolution, we propose a method of reading out via time reversal. I will preserve the discussion until Chap. 7 and Chap. 8.

Chapter 5

Near-Unitarity and Hamiltonian Dynamics

As explained in Chap. 3, the remaining entanglement between the photon leaving the cavity-atom system and the collective spin state causes a non-demolishing measurement. This can be used to generate a squeezed state with a random $\langle \hat{S}_z \rangle$. Such randomness is contrary to deterministic dynamics governed by the Hamiltonian.

In quantum metrology, either the measurement-based method or the OAT will work to improve the precision of measuring physical quantities. However, in most cases, unitary dynamics is essential for investigating much more general quantum physics, like quantum simulation and quantum information.

5.1 Review of Non-Unitary Behaviors

Unitary time evolution, the textbook idea of how quantum mechanics works, is actually really hard to achieve in real quantum systems. For example, to prepare the cold atomic cloud, one must let atoms scatter many photons, in an incoherent manner, which is thus non-unitary. Though in the last step of preparation, the incoherent optical pumping helps to reinitialize the collective spin state to a perfect pure state, in general, the optical process is always accompanied by non-unitarity.

The optical cavity, as described in Chap. 2, can, of course, improve the coherence

by strongly enhancing the atom's interaction with one specific light mode. Still, decoherence happens in such systems, mostly in the following three forms of decoherence.

The first one is inhomogeneous coupling. This is an effect that we neglect when we treat the cavity's response to atoms in Sec. 3.2.2 for simplicity. But naïvely one can find the atoms couple differently to the cavity, and the difference will cause them to decohere.

The second source is collective dephasing, and in our system, such dephasing is induced by the cavity field's measurement effect. The semiclassical description is developed in Sec. 3.4.2, and in Sec. 3.5, we also develop the formalism of describing such a measurement in terms of collective dephasing $\mathcal{L}_{\text{eff}}[\rho] = \hat{S}_z\rho\hat{S}_z - 1/2(\hat{S}_z^2\rho + \rho\hat{S}_z^2)$.

The last form of non-unitary comes from individual dephasing due to spontaneous emission. This can also be seen as the effect of an imperfect cavity or finite cooperativity, as discussed in Sec. 3.4.6.

One may ask why we care about unitarity so much, given the fact that in many leading results of similar systems like in [88], the state, in the end, is very non-unitary. The answer is that the optimal clock performance for such non-unitary states only improves very little, if not even worse, than that of the CSS [26].

This statement is indeed too harsh, and in fact, we do realize that with certain specific methods (like the time-reversal-based method discussed in Chap. 7-8), one can still use the features for entanglement-assisted quantum metrology. However, at least for building the best clock, such non-unitarity is fatal.

In the rest of this chapter, I'm going to present how to overcome the first kind of non-unitarity in Sec. 5.2, and how to minimize the effect of the second and third kinds of non-unitarity in Sec. 5.3, with the experimental demonstration in Sec. 5.4. Fundamentally, by improving the atom-cavity cooperativity, one can obtain a system where the last two types of non-unitarity can be suppressed to negligible.

5.2 Inhomogeneous and Homogeneous Coupling

The coupling between the atoms at position $\mathbf{x}$ and the cavity mode depends on the local cavity field mode pattern $\mathbf{E}(\mathbf{x})$. The standing-wave Fabry-Perot cavity, however, has a very rapidly varying cavity mode within one optical wavelength of the cavity mode. Moreover, due to the incommensurate between the trapping cavity mode and the probing cavity mode, each atom's weight in the collective process, for example, the collective spin state I introduced in Sec. 3.2.1, would be very different.

In [222, Tanji-Suzuki et al. (2011)], the effect of the inhomogeneous coupling is discussed in the context of the cavity field. Since the internal atomic state is not the problem of interest, one can use a collective coupling parameter to describe the effect:

$$H = \frac{1}{N}\sum_{j=1}^{N} \cos^2 kz_j = \left\langle \cos^2 kz \right\rangle, \tag{5.1}$$

where k is the cavity mode's wavevector. By doing so, the effective collective cooperativity between atom and cavity mode is the $(N\eta)_{\text{eff}} = NH\eta$. By assuming either a homogeneous distribution over z or incommensurate periodical distribution, $H = \langle \cos^2 kz \rangle = \frac{1}{2}$.

This assumption would be wrong if we further investigate the quantum fluctuation related to collective spin physics. This is resolved in the lowest orders in [89, Hu et al. (2015)], by introducing both the effective cooperativity and the effective atom number:

$$\eta_{\text{eff}} = \frac{\sum_{j=1}^{N} \eta_j^2}{\sum_{j=1}^{N} \eta_j} = \frac{\langle \eta^2 \rangle}{\langle \eta \rangle}, \tag{5.2}$$

$$N_{\text{eff}} = \frac{(N\eta)_{\text{eff}}}{\eta_{\text{eff}}}. \tag{5.3}$$

The higher-order correlations, however, would be inaccurate under this description. Thus, for general many-body physics, it would be better to resolve such inhomogeneity.

One way is to use the commensurate trap-probe dual-wavelength cavity. For

example, in [119], the probe light is Rb's 780nm transition while the trapping is at 1560nm. This clever design bypasses inhomogeneous coupling.

Similarly, one can use a traveling wave mode cavity such as the four-mirror Fabry-Perot cavity. Recently, a specific design has been proposed to further reduce the back-scattering [96], which is also beneficial to homogeneity.

However, both methods are not very generalizable. For example, in a clock-related problem, one needs the trap to be at exactly the magic wavelength, which is really hard to be somehow commensurate with the probe light. The traveling-light cavity is also challenging in problems like atom interferometers as one may want to introduce as less momentum kick as possible.

In another approach [245, Wu et al. (2021)], the authors proposed and implemented a scheme to remove atoms with small coupling strength. This sacrifices the maximum collective coupling one can get.

Here I will describe our method to overcome this problem, similarly to [245], but instead of removing weakly coupled atoms, we reorganize the distribution to make atoms relocated in strong probe-light positions. Moreover, the method also cools the atoms to the vibrational ground state. Together, this serves as the tool for more unitary evolution and eventually enables the optical clock operation, which I will talk about in Chap. 6.

5.2.1 Experimental Protocol

Atoms are first loaded into a bi-color mirror magneto-optical trap (MOT) [103] located inside the optical cavity. By adjusting bias magnetic fields, we adjust the MOT to overlap well with both the cavity mode and a one-dimensional standing-wave optical lattice formed by a magic wavelength $\lambda = 759$nm retro-reflected beam with a waist of 27 μm in the x-direction. The trap depth is $U_x/h = 460$ kHz. We then turn off the MOT beams and send the magic wavelength light into the cavity to generate an optical lattice along the gravity direction (z-direction) with a waist of 13.7 μm and trap depth $U_z/h = 2$ MHz at the atoms' position. The corresponding vibration frequencies are $\{\omega_x/(2\pi), \omega_y/(2\pi), \omega_z/(2\pi)\}$=$\{62, 3, 130\}$ kHz. To ensure that atoms

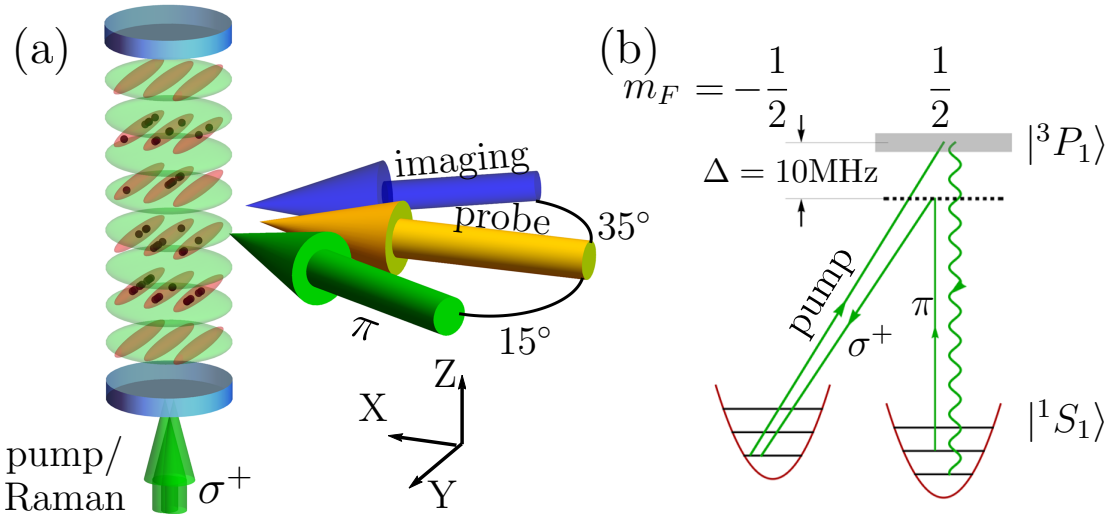


Figure 5-1: Raman sideband cooling scheme. (a) An optical cavity along the Z-direction (gravity-direction) simultaneously resonates to both $|^1S_0, m_F = 1/2\rangle - |^3P_1, m_F = 3/2\rangle$ transition at 556 nm and the optical lattice beam at 759 nm. σ^+-polarized optical pumping beam and σ^+-polarized Raman beam are sent through the optical cavity. a frequency scanning σ^+ probe beam is sent through the optical cavity near resonance to measure atom number. An additional π-polarized Raman beam is applied with 15° against the X-direction lattice in the X-Y plane. The optical clock beam is aligned to the X-direction optical lattice to probe atomic temperature in that direction. Time-of-flight imaging with $^1S_0 - {}^1P_1$ at 399 nm is performed at 35° against the X-direction in the X-Y plane. (b) With $B_z = 13.5$ G, Zeeman splittings at $^3P_1$ and $^1S_0$ are 20 MHz and 10kHz respectively. σ^+- and π-polarized Raman beams are red-detuned by 10 MHz to the $|^1S_0, m_F = 1/2, n\rangle - |^3P_1, m_F = 1/2\rangle$ or $|^1S_0, m_F = -1/2, n-1\rangle - |^3P_1, m_F = 1/2\rangle$ transitions with the resonant two-photon condition between the two ground states.

are loaded only into the cross-section of the two-dimensional (2D) optical lattice, the optical lattice along the X-direction is adiabatically ramped down and held off for 50 ms and then slowly ramped back.

Eventually, we are left with a cloud of ~ 500 ^{171}Yb atoms with root-mean-square sizes of 16μm and 4.8μm along the z and xy directions respectively, which correspond to a peak density of 8.6×10^{10} cm^{-3} and a classical phase space density (PSD) of 4×10^{-5}.

Both the Raman coupling and the optical pumping necessary for the Raman sideband cooling [90] are accomplished with a laser near the $^1S_0 \rightarrow {}^3P_1$ transition with a natural linewidth of $\Gamma = 2\pi \times 180$ kHz. The optical pumping is accomplished with a σ^+-polarized beam along the cavity that is resonant with the $|^1S_0, -1/2\rangle \rightarrow |^3P_1, +1/2\rangle$ transition, while the Raman coupling uses two beams detuned from the $|^1S_0, -1/2\rangle \rightarrow |^3P_1, +1/2\rangle$ transition by $\Delta = -2\pi \times 10$ MHz, one σ^+-polarized beam along the cavity, and a π-polarized beam in the xy plane (see Fig. 5-1). With a magnetic field of 13.7G along the z axis, the relative detuning of those two beams is chosen to match the $|m_F = 1/2, n_x\rangle$ to $|m_F = -1/2, n_x - 1\rangle$ transition between the two ground states that reduces the vibrational quantum number by one, and hence the motional energy by $E/h = 62$ kHz. The optical pumping back to the $|m_F = -1/2\rangle$ state heats the atom on average by $2E_{rec}/h = 7.4$ kHz, where E_{rec} is the recoil energy for the $^1S_0 \rightarrow^3 P_1$ transition. After cooling for 100 ms, we extinguish the Raman beams 5 ms before the optical pumping light in order to initialize atoms in the $|m_F = 1/2\rangle$ level. After the cooling process, the optical lattice along the z direction is ramped down to 1/3 of its initial power to reduce the photon scattering by the trap light.

The atomic temperature is determined by spectroscopy on the spectrally narrow clock transition $^1S_0 \rightarrow {}^3P_0$ using a π-polarized laser beam traveling along the x direction. This laser is stabilized to an ultralow-expansion cavity and measures the population of vibrational states via sideband spectroscopy [16], as shown in Fig. 5-2. The broad Gaussian background underlying the sideband spectrum is attributed to the Doppler profile of floating atoms that are not confined in a single site of the lattice

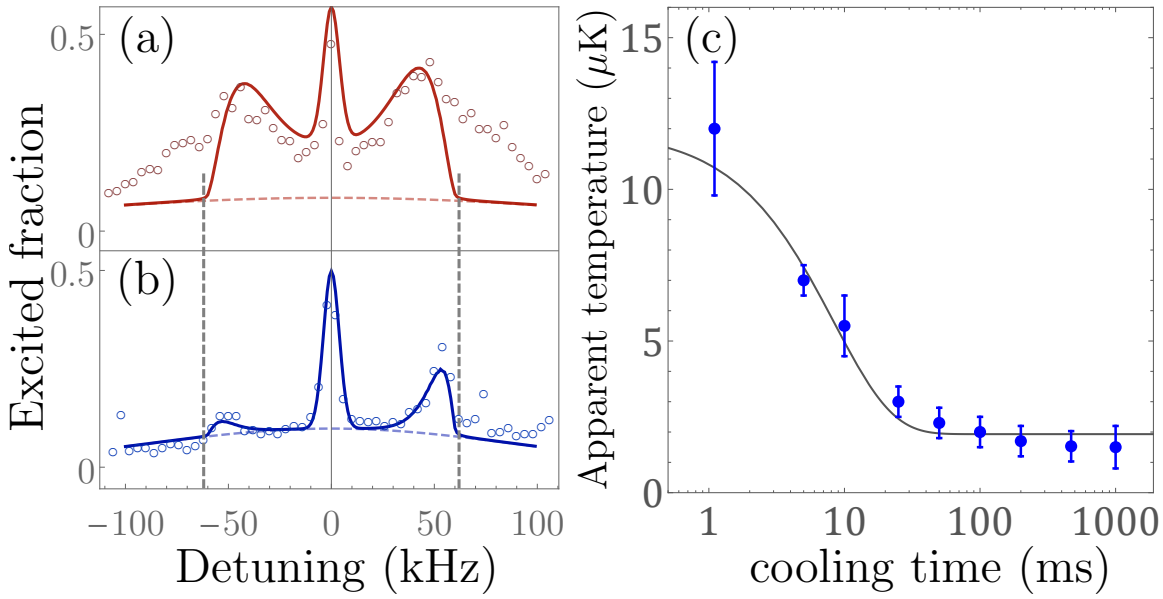


Figure 5-2: Clock state excitation spectroscopy of an atomic cloud loaded into a 2D optical lattice (a) without and (b) with 200ms cooling. Clock pulse lengths of 5 ms and 20 ms in (a) and (b) are applied, respectively. At high temperatures, the large cloud spanned over the harmonic trap, producing a broadening of the clock spectroscopy lineshapes on both the resonance and the trap frequency. At low temperatures, the quantized motion takes over and suppresses the red sideband. Assuming a thermal distribution of the atom, sidebands and carrier are fitted the apparent temperature of the cloud is calculated to be $T = 20 \pm 2\,\mu$K and $T = 1.8 \pm 0.5\,\mu$K with mean occupation number $\overline{n} = 6$ and $\overline{n} = 0.2$ respectively. Broad Doppler Gaussian profile is manually fitted to take into account floating atoms. 141 kHz and 90 kHz standard derivation imply temperatures of 22 μK and 10 μK, respectively.

along x, but are confined by the intracavity trap due to the much larger trap depth. Before the cooling, the blue and red sidebands have similar sizes, which indicates that a mean vibrational quantum number $n_x \gg 1$, while the visible Doppler background in the spectrum suggests a large portion of atoms that are not confined by the x lattice. After 200 ms of Raman sideband cooling, a large imbalance of red to blue sideband is observed, indicating that the atoms are cooled to near the ground state with $\bar{n}_x = 0.2(x)$. The reduced residual Doppler background implies that atoms originally not confined by the x lattice are cooled to the vibrational ground state as well. Fig. 5-2(c) shows a fast initial cooling within the first 10 ms, followed by a slower cooling as the population of the vibrational ground state increases. After 200 ms of cooling, the atomic cloud has root-mean-square (rms) sizes of $z_0 = 12.2\mu$m and $x_0 = 3.2\mu$m, resulting in a peak density of $n_0 = 2 \times 10^{11}$ cm^{-3} and PSD of $2 \times 10^{-}2$. To reach higher PSD, we resort to methods discussed in Sec. 9.2.4 as the future directions.

With the cooling, the optical Rabi oscillation experiences a much smaller dephasing, resulting in strongly improved coherent transfer to the excited clock state $|^3P_0\rangle$ (Fig. 5-3a). After 200 ms of cooling, the transfer fidelity reaches 0.93. The remaining infidelity can be explained by the residual population of vibrational excited states, which experience different Rabi frequencies Ω_m on the $|^1S_0, n_z = m \rightarrow ^3P_0, n_z = m\rangle$ vibrational transition, given by $\Omega_m = \Omega_0 e^{-\eta_x^2/2} L_n(\eta_x^2)$. Here Ω_0 is the Rabi frequency for the vibrational ground state, $\eta_x = 0.25$ is the Lamb-Dicke parameter for our lattice depth, and L_n is the Laguerre polynomial.

From the apparent temperature derived using the sideband spectroscopy above, we also compare it with the performance of the Rabi oscillation as in Fig. 5-3b. We can also calculate the expected $\pi-$ and $2\pi-$pulse fidelity [16] based on the vibrational mode distribution.

From Fig. 5-2, we notice that for cooling times $t > 10$ms the apparent temperature stabilizes. This also applies to the pulse fidelities in Fig. 5-3. However, as we measure the Rabi flopping using cavity, we found that the collective cooperativity NC behaves quite differently from the temperature. We measure the full dynamics of

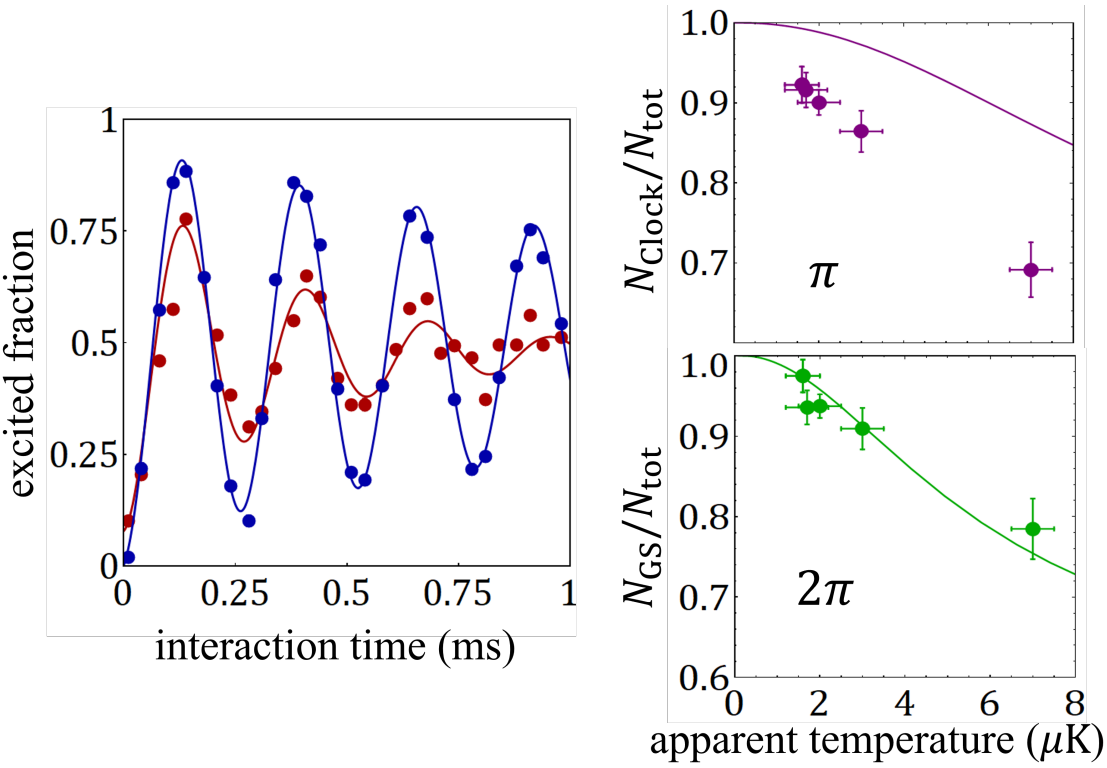


Figure 5-3: Theory from [16], considering a factor of 2 difference between apparent temperature and actual. The difference from the theory for purple points (pi pulse) is due to the fraction of atoms that are not in the 2D trap. It increases when the temperature is higher. *Cooling performances of Raman sideband cooling of ^{171}Yb. X-direction atomic temperatures with different cooling times are measured using the fitting method outlined in Fig. 5-2. The direct measurement quantity is the collective cooperativity NC normalized to the initial condition.*

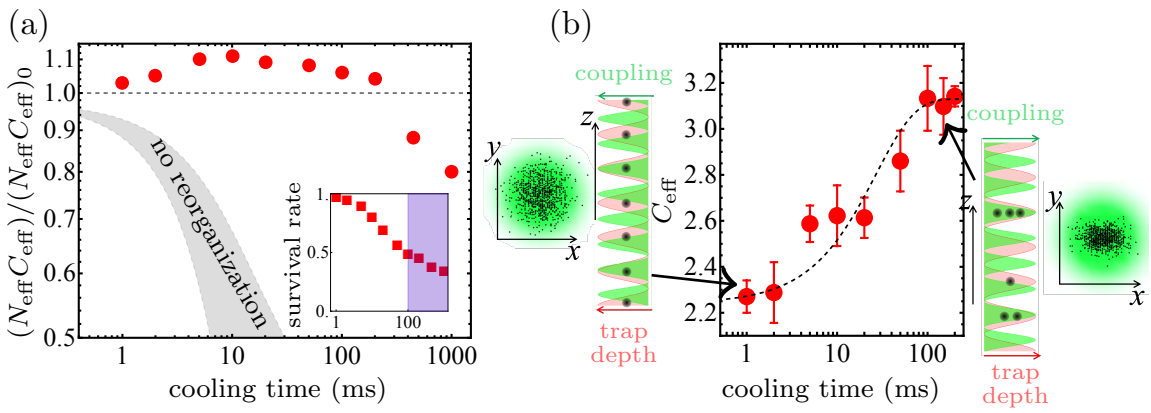


Figure 5-4: Cavity readouts during the cooling process. (a) Signatures of atomic reorganization due to cooling. Collective cooperativity $N_{\rm eff}C_{\rm eff}$ evolution with cooling time, normalized to the initial one. The gray band is calculated from the expected collective cooperativity, assuming that the cooling process drops the atoms weakly coupled to the cooling cavity mode. The lower limit of the band is collective cooperativity when we drop all atoms except those within 1 % of the maximal coupling; similarly, the upper limit is the expectation for the case where we drop all atoms except those within 10% of the maximal coupling. The inset shows the inferred survival rate $N_{\rm tot}(t)/N_{\rm tot}(0)$ as a function of the cooling time t. (b) Effective cooperativity as a function of the cooling time. The dashed line is a double-exponential fit. The illustrations on the side are schematics of atomic distribution among the incommensurate trapping and coupling lattices. Initially, atoms are evenly distributed in the trapping lattice, and after long-time cooling, the atoms are concentrated in lattice sites with high overlap with the coupling lattice.

NC during the cooling in Fig. 5-4(a). As it suggests, we first found that the collective cooperativity NC for a short cooling period increases, and it drops below its original value over long times. Since the atom number N cannot increase, we conclude that $C_{\rm eff}$ must increase during the cooling.

We then measure the quantum projection noise of a coherent spin state after cooling with different atom numbers. Atoms are first optically pumped to the $|^1S_0, +1/2\rangle$ state followed by a radio frequency $\pi/2$ pulse between two magnetic sub-levels of $^1S_0$ ground state. The quantum noise of spin projection S_z measurement scales with the square root of the atom numbers N, while total coupling strength $NC_{\rm eff}$ scales linearly with it. Therefore, comparing the variance of shot-to-shot measurement of S_z with $NC_{\rm eff}$, the average coupling strength can be deduced $C_{\rm eff}$. By changing the cooling time, we obtain the dynamics of $C_{\rm eff}$ as in Fig. 5-4(b). Prior to the cooling

process, atoms are spatially homogeneously distributed at different lattice sites. With a period of cooling, effective cooperativity increases, implying that atom population at weak coupling strength reduces. After 100 ms cooling, almost all atoms are maximally coupled to the cavity field, which is confirmed by the maximal cooperativity observed. In this case, the cooling time can be used as a tuning knob to control the distribution of atom-light interaction in such an optical cavity system.

The mechanism of the increase of C_{eff} is complicated and can be from multiple factors, but ultimately, it means that the atomic position averagely experiences a larger cavity light field. That means the atomic position is either re-distributed along the cavity axis or transversal to the cavity axis. The latter comes directly from the cooling of motional degrees of freedom; however, this cannot explain the whole experiment. On the one hand, as indicated in the sideband spectrum in Fig. 5-2, during the first 10 ms of the cooling, atoms are cooled such that along the Z-direction trap, the transversal radius reduces and thus the effective cooperativity C_{eff} increases as in Fig. 5-4(b). However, the cooperativity further increases with longer cooling times while the temperature remains roughly unchanged. Thus the increasing of cooperativity must be from the reorganization of the incommensurate trap and coupling lattice supported by the cavity. On the other hand, from the imaging result in the beginning, the transversal distribution has a radius of 30μm while the cavity mode waist at the position is 10μm, meaning that the transversal cooling can, at most, improve the single-atom cooperativity by 15%.

The reorganization is thus a must; however, the mechanism is unclear. We lack a quantitative understanding yet, but qualitatively, the atoms have certain reasons to leave the weakly coupled sites. Besides heating from the off-resonance scattering of Raman and optical pumping beams, the primary source of the atom loss in this particular setup is due to the inhomogeneous coupling of the Raman beam to the atomic ensemble, similar to the probe beam. When atoms are weakly coupled to the cavity field, scattering from the free space π-polarized Raman beam dominates atom loss. Since the coupling depends on the cooling process, atoms in the low coupling regime escape the trap while those with a high coupling strength remain. The effect

can be verified by the measurement of effective cooperativity, which is sensitive to the underline distribution of the atoms at different sites in the lattice.

5.2.2 Conclusion and Outlook

In conclusion, we have demonstrated Raman sideband cooling of non-colliding atoms near optical resonance. The method is fast and robust to directionally cool atoms to near motional ground state. Moreover, we realize that the nature of the cavity assistance during the cooling makes the atoms move towards the antinodes of the probing light field lattice to enhance and homogenize the cavity-atom cooperativity. We also found two distinct time scales for the dynamics: the faster one ($\sim$10ms) corresponds to the cooling, and the slower one ($\sim$100ms) corresponds to the reorganization. This enables a continuous tuning from the disordered coupling to the uniform coupling after the atoms are cooled to the motional ground state, which serves as a tunable platform to test the thermalization mechanism and its failure with tunable disorder effects in non-equilibrium states [112, 56] and all-to-all interacting quantum computation applications [237]. The tunability of coupling distribution opens the path to research complex Hamiltonians with different interaction disorders. In the future, a similar approach with a better geometrical setup can be used to cool atoms to the three-dimensional zero motion point with reduced atom loss. The latter, together with compression, can be used to direct laser cool non-colliding Fermions to quantum degeneracy with vanishing losses and in considerably short times. We will revisit this idea in Sec 9.2.4.

5.3 Wineland parameter

The combined effects of light-induced measurement with corresponding backaction, atom-atom interaction, and contrast loss on atomic states can produce a variety of final atomic states. We quantify the utility of these SSSs for metrological applications

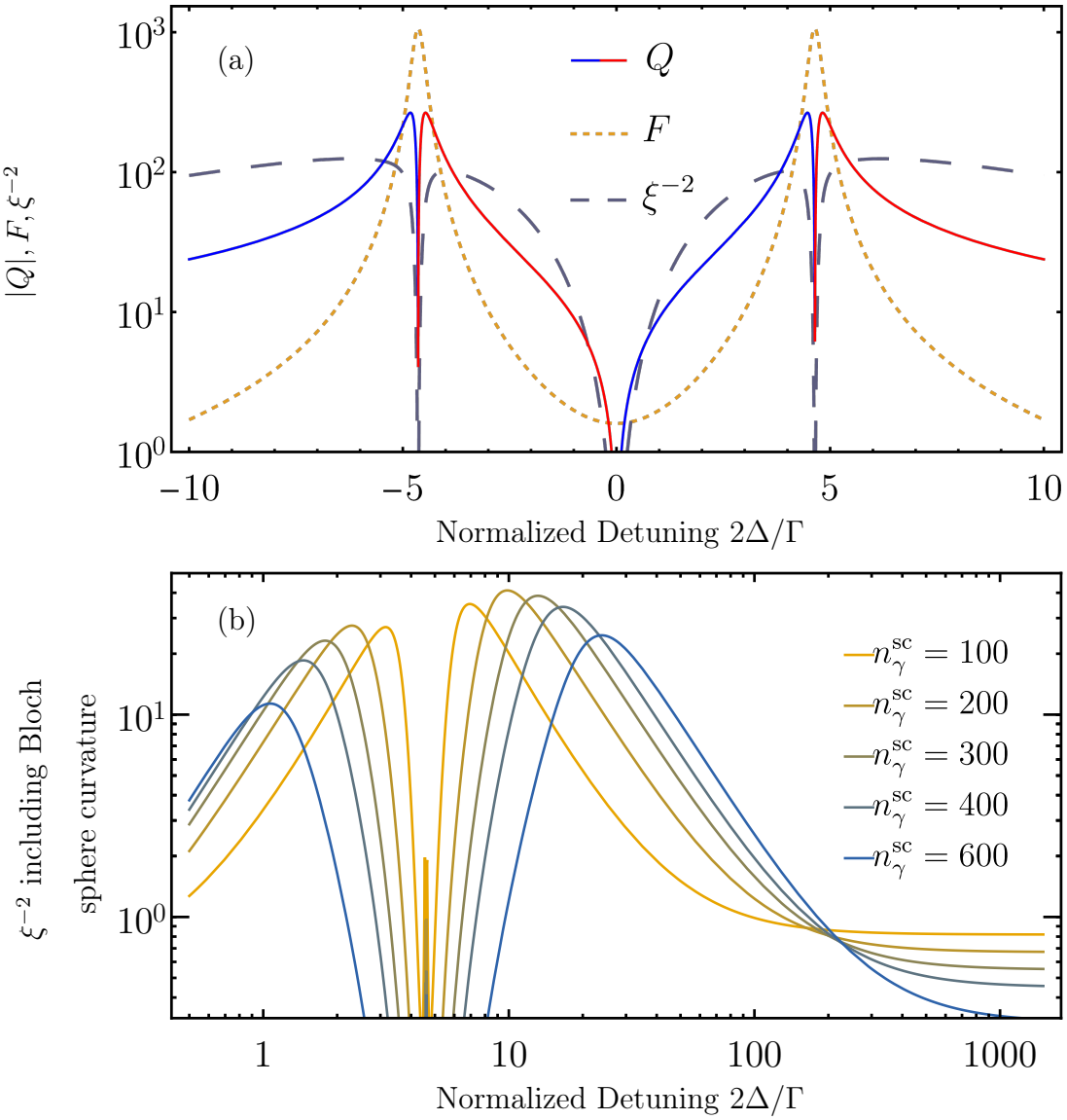


Figure 5-5: Results of cavity feedback squeezing for a cavity that is resonant with the atomic transition, $\omega_c = \omega_a$. (a) Squeezing strength Q, quantum Fisher information F and inverse Wineland parameter ξ^{-2} at fixed scattered photon number $n_\gamma^{sc} = 400$ and collective cooperativity $N_\uparrow\eta = 900$. (These parameters correspond to the conditions of the experiment described in Ref. [25]). For the Q plot, red branches stand for positive Q and blue branches for negative Q. In this calculation, the curvature of the Bloch sphere has been ignored, and the results do not depend on the single-atom cooperativity η. (b) Inverse Wineland parameter including the effect of the Bloch sphere curvature for different scattered photon number n_γ^{sc} calculated for the parameters $N = 1000$, $\langle S_z \rangle = 0$, and $\eta = 1.8$. Both (a) and (b) assume $\kappa/\Gamma = 2.8$ as in the experiment of Refs. [25, 168].

using the Wineland parameter (4.13)

$$\xi^2 = \frac{\xi_{\mathrm{KU}}^2}{C^2} = \frac{1}{C^2}\frac{\Delta\theta^2}{\Delta\theta_{\mathrm{SQL}}^2}, \tag{5.4}$$

In the approach discussed above in Section 3.4.5, the reduction of collective spin projection noise [95] of the final state depends both on Q and the normalized QFI, F. The Kitagawa-Ueda parameter is given by the smaller eigenvalue of the covariance matrix (3.42). Writing all quantities in units of the SQL, the combination of Q, F, and another rotation by an angle α transforms the point $(S_y, S_z)^T$ on Bloch sphere to $(S_y', S_z')^T$ as given by

$$\begin{aligned}\begin{pmatrix} S_y' \\ S_z' \end{pmatrix} &= \begin{pmatrix} \cos\alpha & \sin\alpha \\ -\sin\alpha & \cos\alpha \end{pmatrix} \begin{pmatrix} \sqrt{1+F} & Q \\ 0 & 1 \end{pmatrix} \begin{pmatrix} S_y \\ S_z \end{pmatrix} \\ &\equiv U \begin{pmatrix} S_y \\ S_z \end{pmatrix}\end{aligned} \tag{5.5}$$

The initial distribution of the CSS pointing along the x-axis in units of the SQL is

$$P(S_y, S_z) \sim \exp\bigl(-(S_y, S_z)(S_y, S_z)^T\bigr)$$

and after the transformation, it is given by

$$P(S_y', S_z') \sim \exp\bigl(-(S_y', S_z')\Sigma^{-1}(S_y', S_z')^T\bigr).$$

Making use of that $(S_y, S_z)^T = U^{-1}(S_y', S_z')^T$, the new covariance matrix is

$$\Sigma' \;=\; ((U^{-1})^T U^{-1})^{-1} = UU^T \tag{5.6}$$

and therefore the variance on S_z' is the second diagonal element of Σ',

$$\mathrm{var}(S_z') = 1 - Q\sin 2\alpha + (F + Q^2)\sin^2\alpha. \tag{5.7}$$

By changing α, the minimum and maximum variance is obtained when α satisfies

$$\frac{\mathrm{dvar}(S_z')}{\mathrm{d}\alpha} = -2Q\cos 2\alpha + 2(F+Q^2)\sin\alpha\cos\alpha = 0, \tag{5.8}$$

which implies

$$\tan\alpha = (\sqrt{4Q^2+(F+Q^2)^2} - (F+Q^2))/(2Q). \tag{5.9}$$

The Kitagawa-Ueda parameter is given by

$$\xi^2_{\mathrm{KU},\pm} = \frac{1}{2}\left(2+F+Q^2 \pm \sqrt{4Q^2+(F+Q^2)^2}\right) \tag{5.10}$$

and in the limit of $Q \gg F \sim 1$,

$$\xi^2_{\mathrm{KU}} \sim \frac{1+F}{Q^2}.$$

We see from Eqs. (3.22) and (3.32) that for fixed probing parameters δ, Δ, and N, both the squeezing parameter Q and the QFI F scale linearly with the number of photons scattered into free space. This means that as long as the QFI is small, i.e., $F < 1$, the amount of squeezing ξ^2 will grow quadratically with the number of scattered photons, but when $F \gtrsim 1$, the scaling will become linear. However, for sizeable OAT squeezing, $Q \sim \mathcal{O}(\sqrt{S})$, the curvature of the Bloch sphere induces an additional broadening of the distribution [108, 200]:

$$\xi^2_{\mathrm{KU}} \to \xi^2_{\mathrm{KU}} + \frac{Q^4}{24S^2}. \tag{5.11}$$

Thus the variance of the squeezed direction reaches a minimum for an optimal number of scattered photons, as displayed in Fig. 5-5 (b). The increasing widths of the dips around the atom-cavity resonance at $x_a = 50$ with increasing scattered photon number indicate the effect of the Bloch sphere curvature.

By fixing the atom number N and centering the atomic state at the equator, $\langle S_z\rangle = 0$, i.e., $\langle \hat{N}_\uparrow\rangle = N/2$, one can obtain an optimal frequency that yields the

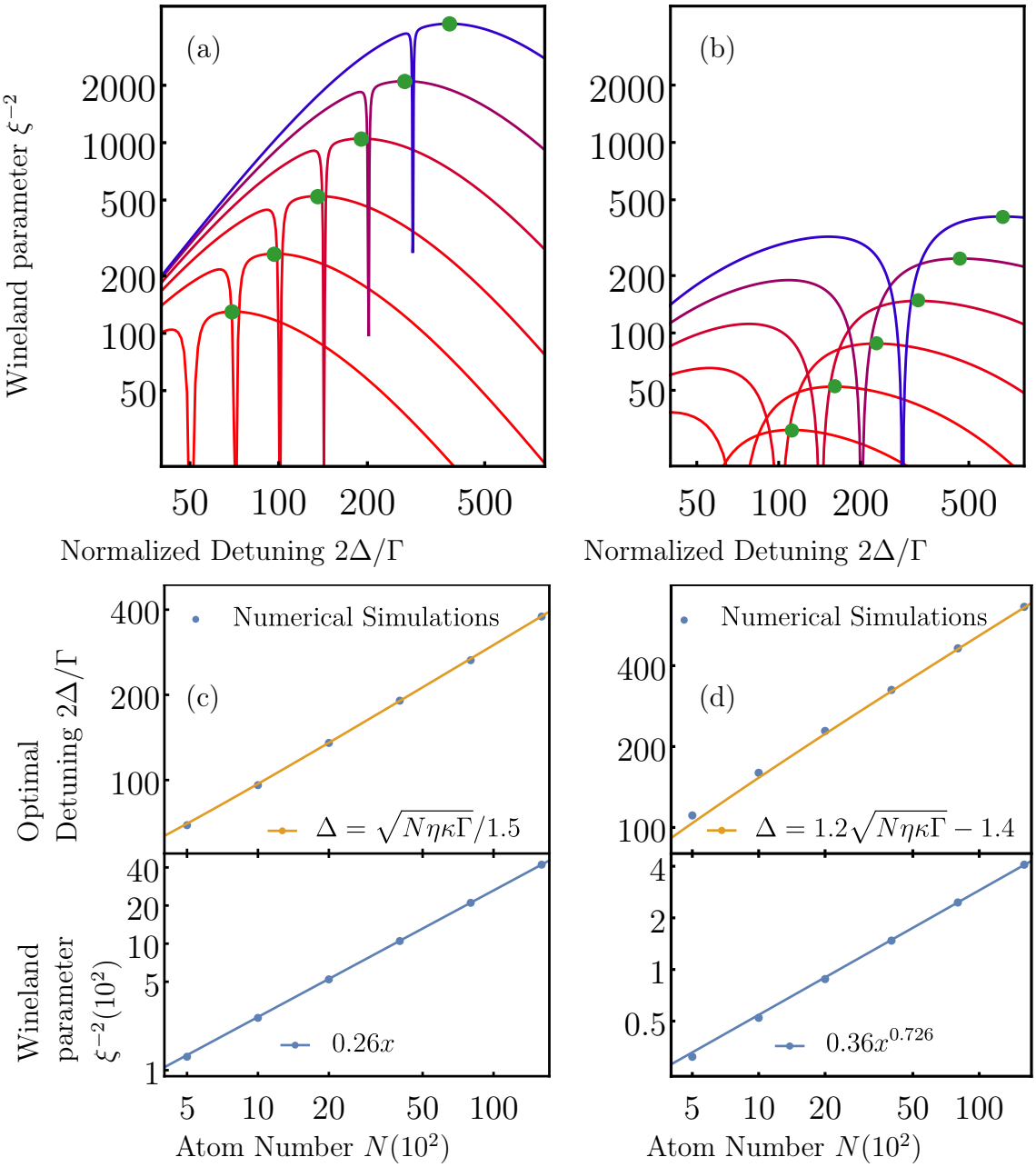


Figure 5-6: (a, b) the optimal Wineland parameter with respect to the optimized photon number at given N and detuning, without (a) and with (b) Bloch sphere curvature effect, where from bottom to top the atom numbers are $N = \{1, 2, 4, 8, 16\} \times 500$. The single-atom cooperativity is $\eta = 1.8$. The green dots indicate the maximum Wineland parameter for a given atom number. (c, d) show the optimum detuning and maximum Wineland parameter as a function of atom number, corresponding to the parameters of the green dots in subfigures (a, b); the data points correspond to numerical simulations and the solid lines represent fits that hold for large atom number $N \gg 1$.

largest inverse Wineland parameter ξ^{-2}, as shown in Fig. 5-6. When varying the atom number, we can see that the optimum detuning is proportional to the vacuum Rabi splitting, as displayed in Fig. 5-6(c). Therefore, no matter how many atoms are loaded, the Q, F parameters per scattered photon (denoted as $\hat{Q} \equiv Q/n_\gamma^{\mathrm{sc}}, \hat{F} \equiv F/n_\gamma^{\mathrm{sc}}$) for the optimal detuning remain the same. The optimal Wineland parameter as a function of the scattered photon number n_γ^{sc} for large N therefore simplifies to

$$\xi^2 = \frac{1+\hat{F}n_\gamma^{\mathrm{sc}}}{(\hat{Q}n_\gamma^{\mathrm{sc}})^2} e^{2n_\gamma^{\mathrm{sc}}/N} \sim \frac{\hat{F}}{\hat{Q}^2 N} p^{-1} e^{2p} \tag{5.12}$$

where $p = n_\gamma^{\mathrm{sc}}/N$ is the average photon number scattered per atom. The minimum Wineland parameter is obtained for $p = 1/2$, and the metrological gain scales as total atom number N, i.e., exhibits Heisenberg scaling [35]. If we consider the curvature effect of the Bloch sphere, Eq. (5.11), then the metrological gain exhibits a scaling with atom number as $N^{0.73}$, as shown in Fig. 5-6 (d) based on numerical results. For the same collective cooperativity $N\eta$, the higher the single-atom cooperativity η, i.e. the smaller the atom number, the more severely the finite size of the Bloch sphere limits the Wineland parameter. We note, however, that there are approaches beyond spin squeezing that are not limited by the curvature of the Bloch sphere [40, 203, 66, 35].

5.4 Experimental Results

We then apply the aforementioned optimization to the experimental setup, where the results are published on [25].

During the experiments, we use two-color pulses as discussed earlier, the two pulses are selected as $\omega_{l1} = 2\pi \times 7.33\,\mathrm{MHz}$, $\omega_{l2} = -2\pi \times 2.0\,\mathrm{MHz}$, and their power ratio is $\gamma = 0.52$. Fixing this pulse, we scan the photon sending in, which equals to scanning Q while keep $Q/F \sim 7$ fixed. After the squeezing, we rotate the state by α clockwise. To compare the data to a theoretical model, we first consider the polar angle of the spin vector, defined as $\tau_\alpha \equiv \sqrt{2S}\arcsin\left(S_z(\alpha)/S\right)$. Its variance $\delta\tau_\alpha$, normalized to the

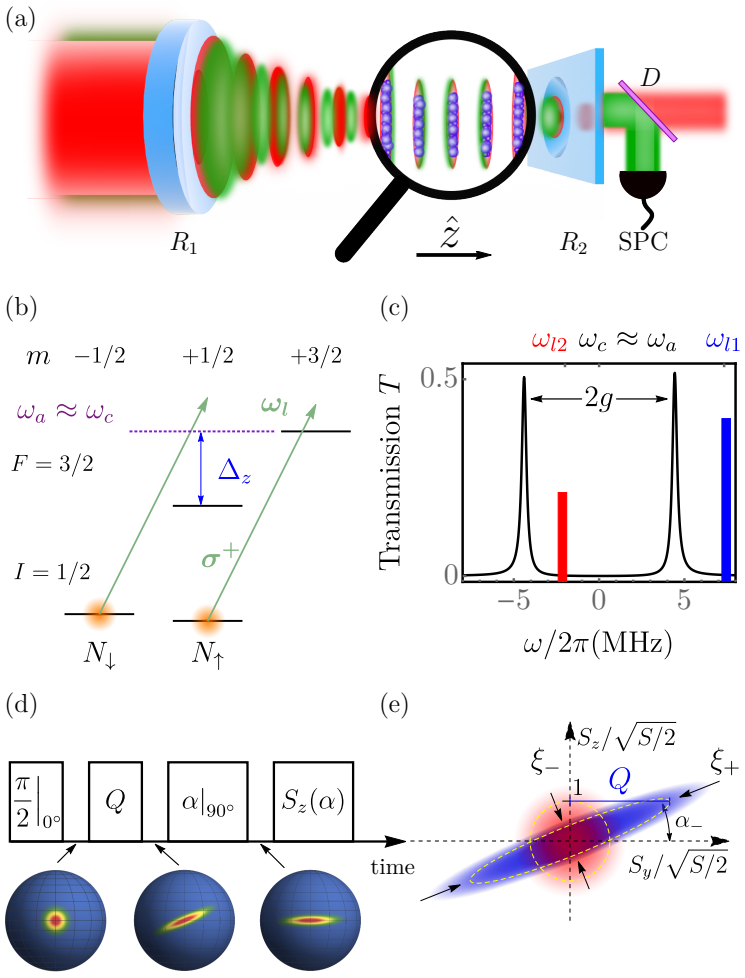


Figure 5-7: (a) Experimental setup. A one-dimensional optical lattice at λ_t=759 nm (red) traps the atoms. Light at λ=556 nm light (green), whose transmission is detected using a dichroic mirror (D) and a single-photon counter (SPC), is used for squeezing and probing. (b) Relevant energy levels of ^{171}Yb with ground state $\left|{}^1S_0, I = \frac{1}{2}\right\rangle$ and excited state $\left|{}^3P_1, F = \frac{3}{2}\right\rangle$. The Zeeman splitting in $\left|{}^3P_1, F = \frac{3}{2}\right\rangle$ is $\Delta_z/(2\pi)$=18.5 MHz for a magnetic field B_z=13.6 G along the cavity axis. (c) Cavity transmission spectrum showing vacuum Rabi splitting for $N\eta$=1800, as well as the two squeezing light pulses ω_{l1} and ω_{l2}. (d) Simplified representation of the squeezing and measurement sequence. (e) Quasiprobability distributions for a CSS (red) and SSS (blue).

variance $\delta\theta_{CSS} = (2S)^{-1}$ of the CSS, is given by

$$\frac{\delta\tau_\alpha}{\delta\theta_{CSS}} = 1 - Q\sin 2\alpha + \left(F + Q^2\right)\sin^2\alpha. \tag{5.13}$$

Here, Q is the dimensionless shearing strength (see Fig. 5-7(e)), defined as the normalized light-induced phase shift $\pm\phi/\Delta\theta_{CSS}$ experienced by a spin displaced by one standard deviation of the CSS from the equator, $S_z = \pm\sqrt{S/2}$ as in Chap. 2. As in (5.10), we find the minimum (ξ_-^2) and maximum (ξ_+^2) variances of the normalized spin angle τ_α,

$$\xi_\pm^2 = \frac{1}{2}\left(2 + F + Q^2 \pm \sqrt{4Q^2 + (F+Q^2)^2}\right), \tag{5.14}$$

obtained at angles $\alpha_-=\arctan[(\sqrt{4Q^2+(F+Q^2)^2}-(F+Q^2))/(2Q)]$ and $\alpha_+=\alpha_-+\pi/2$, respectively. The normalized uncertainty area of the SSS ellipse is therefore given by $A=\xi_+\xi_-=\sqrt{1+F}$. The relation between $\delta\tau_\alpha$ and the normalized spin variance $\sigma^2(\alpha)$ of $S_z(\alpha)$ is given by $\sigma^2(\alpha)=(S/2)[1-\exp(-2\,\delta\tau_\alpha\,/S)]$. For the CSS and the SSS quadrature ξ_-^2, the approximation $\sigma^2(\alpha)\approx\delta\tau_\alpha$ holds, while the antisqueezed quadrature ξ_+^2 is reduced by the curvature of the Bloch sphere.

The solid lines in Fig. 5-8 are obtained by fitting the data to $\sigma^2(\alpha)+\sigma_d^2$ with Q and F as the only fitting parameters, while σ_d^2 is the previously measured detection limit. We find good agreement between the model and the data, allowing us to extract both the shearing strength Q and the QFI F. In Fig. 5-9 we plot Q and F versus the number p_t of transmitted photons during the optical squeezing. For negligible technical noise we expect both Q and F to be proportional to p_t. The solid lines in Fig. 5-9 represent the predicted linear behavior of Q and F obtained from an analytical model of the system without any free parameters; the dotted line includes the effect of finite measurement quality $\sigma_d^2 = -9.4$ dB, that affects the measurement of the squeezed quadrature $\xi_-^2<1$, and hence F, but not Q. The model without any free parameters agrees remarkably well with the measured Q and F, indicating the absence of major technical limitations other than the finite state detection quality σ_d^2.

The attainable metrological gain depends not only on the reduced spin noise ξ_-^2, but also on the signal $\langle|\vec{S}|\rangle$ [240] which determines the contrast C of an interferometric

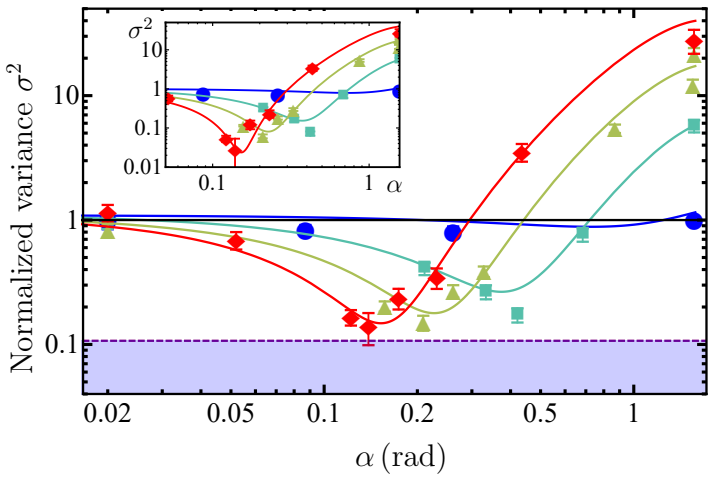


Figure 5-8: Measured normalized spin noise $\sigma^2(\alpha)$, as a function of the state rotation angle α, for shearing strengths $Q = 0.3$ (blue circles), $Q = 2.2$ (green squares), $Q = 4.5$ (yellow triangles), and $Q = 6.3$ (red diamonds). For visualization, the data measured at α=0 are displayed at α=0.02 rad. The solid lines are theoretical fits. States in the violet region below the dashed line at $\sigma^2 = \sigma_d^2 = 0.11$ (detection limit) cannot be directly observed. Inset: σ_{st}^2 of SSS after subtracting measurement noise σ_d^2 for the same parameters.

measurement. The dominant loss of contrast is due to the scattering of photons into free space during squeezing, which projects atoms into $|\uparrow\rangle$ or $|\downarrow\rangle$. The measured Ramsey contrast as a function of Q is shown in Fig. 5-10, together with the a-priori prediction C=$C_0 \exp\left(-(Q/\tilde{Q} + Q^2/2)/N\right)$ with the initial contrast C_0=0.97 in the absence of squeezing as the only fitting parameter. The linear term in exponents is from photon scattering and the quadratic term is from finite size effect (3.44). Here, $\tilde{Q} = 0.050(3)$ is the independently measured shearing strength per scattered photon. The term $Q/\tilde{Q}$ arises from photon scattering into free space, while the second, smaller term accounts for the SSS wrapping around the Bloch sphere.

The metrological gain of a squeezed state is then given by the Wineland parameter ξ_W^2=ξ_-^2/C^2 [240]. Fig. 5-10(a) shows ξ_W^2, the measured spin noise reduction ξ_-^2, and the inferred squeezing ξ_{st}^2=ξ_-^2−σ_d^2 of the state after subtraction of the measurement resolution σ_d^2. For $Q \gtrsim 6$ the measured squeezing ξ_-^2 saturates at σ_d^2; Q=6.3 also optimizes the Wineland parameter at ξ_W^2= − 6.5(4) dB. The inferred squeezing ξ_{st}^2 is consistent with the prediction from the model with no free parameters (solid red

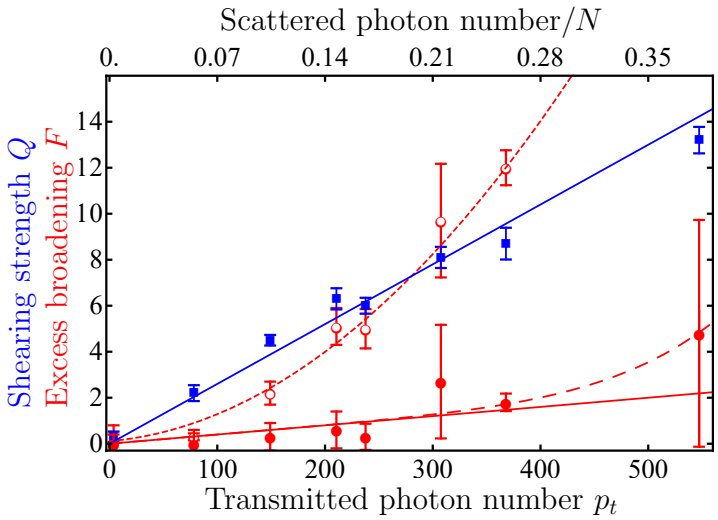


Figure 5-9: Shearing strength Q (filled blue squares) and excess broadening factor F (red circles) plotted vs. the number p_t of transmitted photons. The open red circles correspond to the directly measured data with the theoretical model without free parameters (dotted red line), the solid circles are after subtraction of measurement noise σ_d^2 with a parameter-free model without (solid red line) and with (dashed red line) Bloch-sphere-curvature-induced broadening.

line), which is limited by the Bloch sphere curvature to $\xi_{st}^2 = -15.9(6)$ dB. To our knowledge, this is the first time that the limitation of spin squeezing due to the curvature of the Bloch sphere [108] has been observed. The inferred metrological gain without readout noise is $\xi_W^2 = -12.9(6)$ dB.

Finally, we directly demonstrate an interferometric measurement with a precision beyond the SQL by implementing a Ramsey sequence with a squeezed, nearly uncertainty-limited input state (Q=3.8, area A=$\sqrt{1+F}$=1.3). The state is chosen to provide nearly optimum precision gain in the interferometer and in a future OLC [24], see Fig. 5-10(a). We rotate the squeezed state by α=$\pi/2-\alpha_-$ to align the minimal uncertainty along the phase axis, allowing the state evolve for a Ramsey time τ_R=1.5 ms, and apply a final $\pi/2$ rotation to map the accumulated phase onto S_z. In Fig. 5-10(c) we compare the phase Allan deviation of the SSS (red squares) with that of the CSS (black circles). The Allan deviation for both CSS and SSS Ramsey sequences is derived from 90 sequential measurements. The precision of the CSS interferometer is accurately described by the SQL (black dashed line). The SSS reaches

a given precision 4 times faster than a system at the SQL. The main limitation to longer integration times is magnetic field noise.

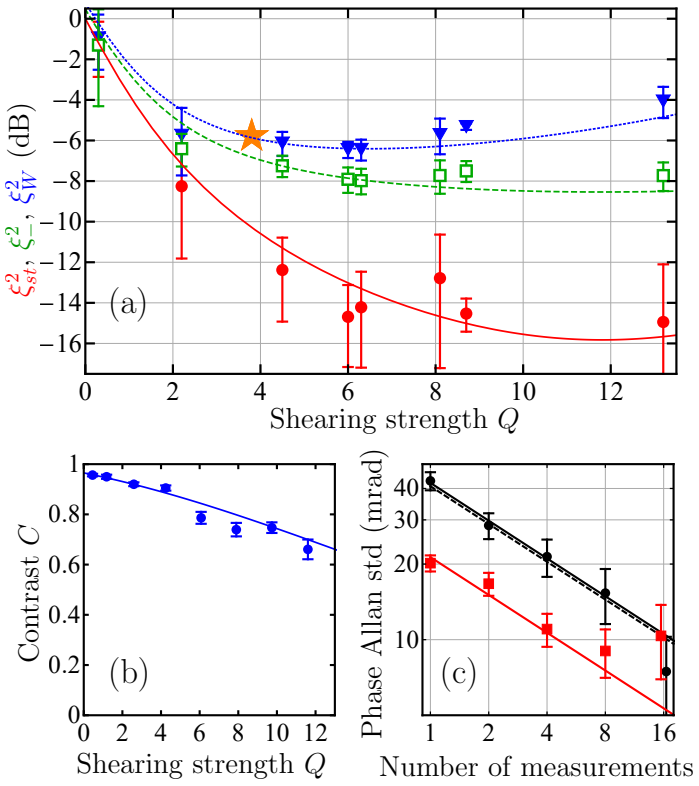


Figure 5-10: (a) Wineland metrological gain ξ^2_W (blue), measured spin noise reduction ξ^2_- (green), and inferred SSS noise ξ^2_{st} (red) as a function of shearing strength Q. ξ^2_- is limited by the measurement resolution and ξ^2_{st} by the curvature of the Bloch sphere. (b) Ramsey contrast as a function of Q with initial contrast as only fitting parameter (solid line). (c) Allan deviation of a phase measurement for a CSS (black squares) with SQL (dashed line) and for a SSS with $Q = 3.8$ (p_t=130), $F = 0.8$ (red data). The red solid line is fit to the first three data points. The reduction in measurement time over the SQL is a factor of 3.7(2), represented by the orange star in (a).

In conclusion, we have demonstrated near-unitary cavity feedback squeezing. Our measurements agree with a model without free parameters that predicts both the area and shape of the squeezed state. The results presented here can be further improved upon in several ways: state detection with a larger applied magnetic field will reduce the Raman scattering and improve the measured spin noise and metrological gain. Alternatively, one can use a squeezing-unsqueezing method [40, 87] that is not limited by the detection quality, and that is also insensitive to the curvature

of the Bloch sphere. The intrinsic squeezing of ξ^2_{st}=−16 dB is already more than halfway (on a logarithmic scale) between the SQL and the ultimate Heisenberg limit at ξ^2_H=−30 dB for N=10^3 atoms. The squeezing performance depends only on the collective cooperativity $N\eta$, and by placing the ensemble at a location in the cavity with higher single-atom cooperativity at constant $N\eta$, i.e., for smaller atom number, the demonstrated performance could already be quite close to the Heisenberg limit. Furthermore, the absolute squeezing will improve with increased collective cooperativity in proportion to $N\eta$. We expect that the spin squeezing can be transferred from the nuclear spin directly to the $|^1S_0\rangle \rightarrow |^3P_0\rangle$ clock transition through an optical π pulse, thus enabling optical-clock operation beyond the SQL. Finally, unitary squeezing can also be used to enable quantum information processing with Gaussian states [235, 163].

Chapter 6

Coherent Operation on the Optical Clock Transition

One of the major reasons we use ytterbium is it has a narrow transition ${}^1S_0 \rightarrow {}^3P_0$. Atomic physics tells us that dipole interaction should not change the spin degrees of freedom; however, due to the spin-orbit coupling, this is lifted by the perturbation. Furthermore, the $J = 0 \rightarrow J = 0$ transition is also forbidden, and this time one needs the nuclear spin or external field to open it up, which makes this transition very weak, and even vanishes for bosonic isotopes where there is no nuclear spin. This so-called clock transition makes ytterbium and strontium the best candidates as the new reference of time standards.

The stability of state-of-the-art optical-lattice clocks (OLCs) is limited both by the interrupted interrogation of the atomic system by the local-oscillator laser (Dick noise [47]) and by the SQL that arises from the quantum noise associated with discrete measurement outcomes. As described in Chap. 4, the CQED setup provides quantum-enhanced metrology and can be applied directly to OLCs as we demonstrated in [168, Pedrozo, et al., Nature (2020)].

6.1 Introduction

For the purpose of improving the OLCs, we created a many-atom entangled state on an OLC transition, and use it to demonstrate a Ramsey sequence with an Allan deviation below the SQL after subtraction of the local oscillator (LO) noise. We got a metrological gain of $4.4^{+0.6}_{-0.4}$ dB over the SQL using an ensemble consisting of a few hundred ^{171}Yb atoms, corresponding to a reduction of the averaging time by a factor of 2.8 ± 0.3. Our results are currently limited by the phase noise of the LO and Dick noise, but demonstrate the available performance improvement in state-of-the-art OLCs [134, 225, 160, 198, 21, 254] through the use of entanglement. This will enable further advances in timekeeping precision and accuracy, with many scientific and technological applications, including precision tests of the fundamental laws of physics [234, 190], geodesy [129, 70, 220], gravitational redshift [21], or gravitational wave detection [109].

As shown in Fig. 1-2, the improvements in the fractional uncertainty in clock performance are slowed down to about 1dB per year in the past few years. A 4.4dB improvement in our experiment is significant for going beyond state-of-the-art OLC.

6.2 Characterizing the OLC performance

A clock operated with N uncorrelated atoms for an averaging time T at the SQL can reach a quantum-noise-limited fractional stability given by

$$\sigma(\tau_R, T) = \frac{1}{\omega_0 \tau_R} \sqrt{\frac{T_C}{T}} \sqrt{\frac{\xi_W^2}{N}}, \tag{6.1}$$

where τ_R is the interrogation time of the atoms by the clock LO laser, T_C the clock cycle time, ω_0 the angular frequency of the clock transition, and the Wineland parameter is ξ_W^2=1 [240] for ideal conditions with perfect quantum-coherent state preparation and detection. The way to understand this formula is as follows. For single measurement with τ_R, the Fourier theorem gives directly the stability $1/\tau_R$, whose relative stability is then $1/(\omega_0\tau_R)$. The rest factors are just uncorrelated atoms/measurements

with a square root reduction of the stability.

If the clock is operated at a duty cycle less than 1 ($T_C > \tau_R$), so that the LO is not locked to the atomic evolution during part of the cycle, then the Dick noise σ^2_{Dick}, arising from aliased high-frequency noise of the LO, should be added to Eq. 6.1 [47, 159]. The Dick noise can be suppressed by using more than one ensemble to eliminate the dead time [198, 159, 21], or by performing simultaneous interrogation of more than one ensembles [219, 156, 254].

The SQL, as described by Eq. 6.1 with ξ^2_W=1, is not a fundamental limit, but can be overcome by means of quantum correlations (entanglement) between the participating atoms. The simplest entangled state offering metrological gain is the SSS [108], where the quantum noise is redistributed between two orthogonal spin quadratures, one with reduced quantum noise (squeezed axis), and the other with increased noise (anti-squeezed axis), see Fig. 6-1d. In this picture, each atom is associated with a spin $\frac{1}{2}$, and the N-atom ensemble with a collective spin $S_0 = N/2$. By orienting the squeezed quadrature of the collective spin along the phase axis during clock operation one can reduce the quantum noise and increase the clock stability. The potential metrological gain over the SQL, expressed in variance, is then given by ξ_W^{-2}, where the Wineland parameter $\xi^2_W = \xi^2/C^2$ [240] incorporates both the the variance reduction ξ^2 of the spin noise compared to an unentangled coherent spin state (CSS), and the magnitude of the mean spin vector $|\langle \vec{S} \rangle| = CS_0$.

Over the last decade, SSSs have been demonstrated in several systems. In neutral atoms, up to 20 dB of spin squeezing beyond the SQL has been demonstrated using optical techniques [88, 38]. However, given that it is more difficult to maintain phase coherence at high frequencies, all spin squeezing so far has involved transitions whose frequencies ω_0 are five to ten orders of magnitude smaller than optical frequencies, and that exhibit proportionally reduced time-keeping precision (see Eq. 6.1). Building on spin squeezing generation between nuclear sublevels of the electronic ground state of ^{171}Yb that we have recently demonstrated [25], here we report the generation of a SSS on an optical transition, and demonstrate for the first time an OLC where the atomic system can provide sensitivity beyond the SQL.

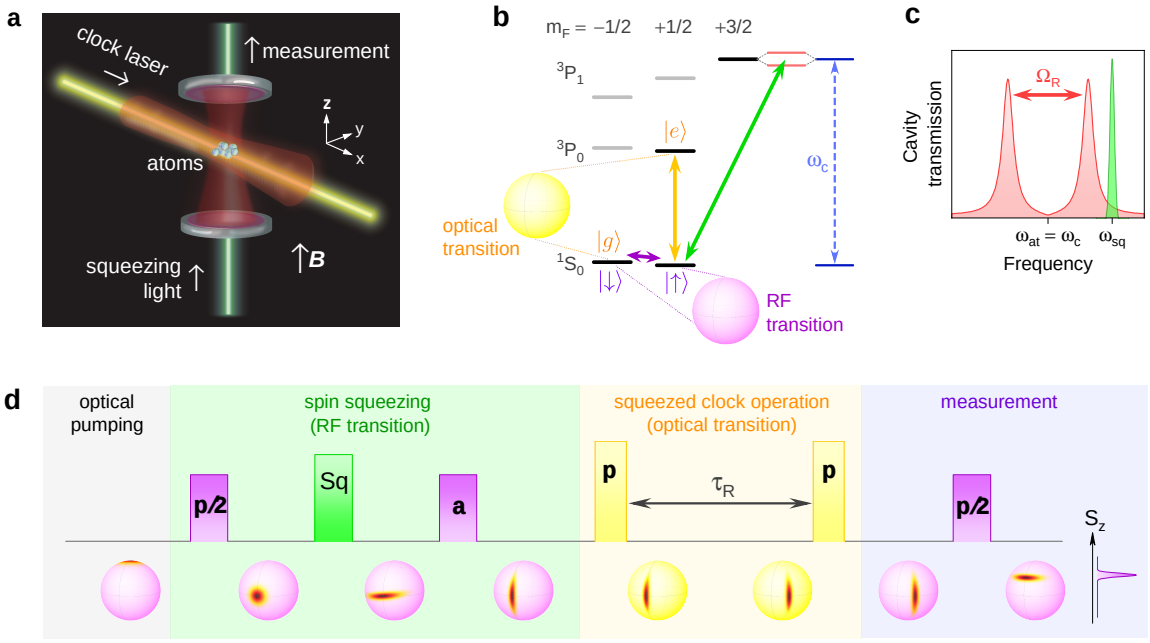


Figure 6-1: **Setup and squeezed-clock sequence. a**, ^{171}Yb atoms are trapped inside an optical cavity in a two-dimensional magic-wavelength optical lattice along the x and z directions (red beams). Light for optical pumping and spin squeezing (green) is applied along the cavity axis z, while the clock laser (yellow) propagates along x. **b**, Energy levels and transitions. Purple, green, and yellow pulses indicate the ground-state radiofrequency (RF) transition $|\downarrow\rangle \rightarrow |\uparrow\rangle$, squeezing transition $\left|^1S_0, m_I = \frac{1}{2}\right\rangle \rightarrow \left|^3P_1, m_F = \frac{3}{2}\right\rangle$ at ω_{at}, and optical-clock transition $|\uparrow\rangle \rightarrow |e\rangle$, respectively. The system evolves either in the ground-state manifold $\{|\downarrow\rangle, |\uparrow\rangle\}$ (purple Bloch sphere), or in the clock-state manifold $\{|g\rangle, |e\rangle\}$ (yellow Bloch sphere). The cavity frequency ω_c is tuned in resonance with the squeezing transition, $\omega_c = \omega_{at}$. **c**, Spin squeezing. Strong coupling of the atoms to the cavity results in vacuum Rabi splitting of the cavity resonance (red peaks). A laser is applied detuned from the Rabi peak at frequency ω_{sq} (green peak) to produce a SSS via cavity feedback [25]. **d**, Squeezed-clock sequence. A SSS is prepared in the ground-state manifold $\{|\downarrow\rangle, |\uparrow\rangle\}$, transferred to the clock manifold $\{|g\rangle, |e\rangle\}$, evolved in a Ramsey sequence for time τ_R, and mapped back onto $\{|\downarrow\rangle, |\uparrow\rangle\}$, where a state measurement is performed. The evolution of the quantum state is depicted on the Bloch spheres for the RF (purple) and optical (yellow) transitions.

Our clock operates with an ensemble of $N = 350 \pm 40$ ^{171}Yb atoms that are confined in a two-dimensional magic-wavelength optical-lattice trap inside a high-finesse ($\mathcal{F}\approx$12000) optical cavity [25] (see Fig. 6-1a), and are Raman sideband cooled to mean vibrational quantum number $\langle n_x \rangle < 0.2$, as explained as in Sec. 5.2. In order to robustly create a SSS on the ultra-narrow optical-clock transition, we first generate spin squeezing between the two nuclear sublevels $|\uparrow\rangle \equiv \left|{}^1S_0, m_I = +\frac{1}{2}\right\rangle$ and $|\downarrow\rangle \equiv \left|{}^1S_0, m_I = -\frac{1}{2}\right\rangle$ of the electronic ground state ${}^1S_0$ using the interaction between the atoms and the optical cavity [121, 25]. Subsequently we transfer the population of $|\uparrow\rangle$ into the $|e\rangle \equiv \left|{}^3P_0, m_I = \frac{1}{2}\right\rangle$ excited clock state with a π pulse of the clock laser, thereby mapping the SSS onto the optical-clock manifold $\{|g\rangle \equiv |\downarrow\rangle, |e\rangle\}$ (see Fig. 6-1b).

The spin squeezing between the ground-state sublevels is achieved by optically pumping the atoms into state $|\uparrow\rangle$, creating a CSS between $|\uparrow\rangle$ and $|\downarrow\rangle$ with a radiofrequency (RF) $\pi/2$ pulse, and then applying a laser pulse near the $|\uparrow\rangle \rightarrow \left|{}^3P_1, m_F = \frac{3}{2}\right\rangle$ transition through the cavity (Fig. 6-1c). The atom-light interaction, amplified by the cavity, approximates the one-axis twisting Hamiltonian [108, 125] with the longitudinal magnetic field, as explained in Sec. 3.3.1, (3.17): $\hat{H} = \beta\hat{S}_z + \chi\hat{S}_z^2$. A spin-echo protocol is then used to cancel the linear term ($\hat{S}_z$), such that the system evolves under an effective one-axis twisting Hamiltonian $\hat{H} = \chi\hat{S}_z^2$ [108] for a time τ_s (see Fig. 6-1d). Finally, the reduced spin projection noise can be oriented along any desired axis in the $\{|\uparrow\rangle, |\downarrow\rangle\}$ ground-state manifold by rotating the SSS around its average spin direction $\langle\vec{S}\rangle$ with another RF pulse. At this stage, we observe a spin noise suppression $\xi^{-2} = 6$ dB (limited by the state detection, with an intrinsic spin noise reduction of 9 dB), and a contrast of $C = 0.97$. The SSS is nearly uncertainty limited, with a detected area 1.9 times larger than the limit set by the Heisenberg's uncertainty principle.

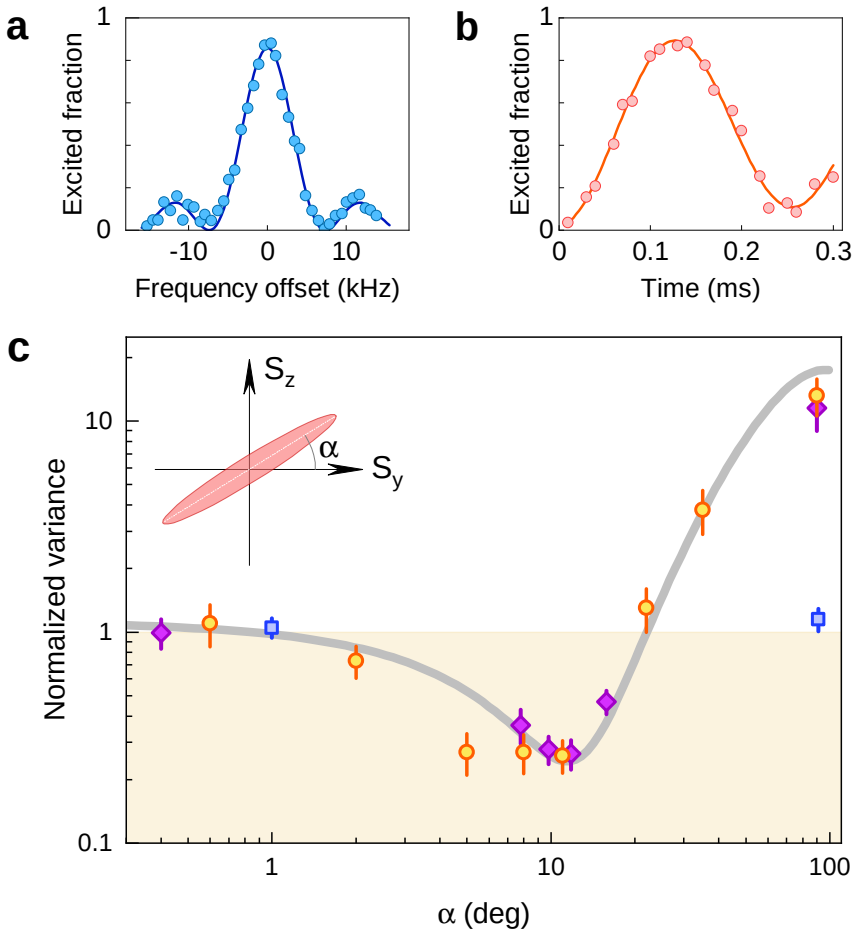


Figure 6-2: **Squeezed state tomography.** **a**, Rabi spectroscopy of the $|\uparrow\rangle \rightarrow |e\rangle$ transition to the clock state. The pulse duration is 0.22 ms. **b**, Rabi oscillations on the clock transition. **c**, Tomographic measurements of the SSS before (purple diamond) and after (orange circle) mapping onto the clock transition and back show very similar degrees of squeezing. The theoretical expectation for a state with $\xi_-^2 = -5.9$ dB is shown as a gray solid line. Two measured data points for a CSS are also shown (blue squares). The shaded area indicates the region below the SQL. Error bars represent 1σ statistical confidence interval.

6.3 Squeezing on the Clock Transition

Having prepared a SSS in the $\{|\uparrow\rangle, |\downarrow\rangle\}$ ground-state manifold, we then map it onto the optical-clock transition ${}^1S_0 \rightarrow {}^3P_0$ by phase-coherently transferring the population of $|\uparrow\rangle$ to the state $|e\rangle$ with an optical π pulse of the LO. We observe a clean Rabi spectrum on the $|g\rangle \rightarrow |e\rangle$ transition (Fig. 6-2a), and coherent Rabi oscillations in time (Fig. 6-2b). The π-pulse has a transfer efficiency of 0.95, mostly limited by finite atomic temperature. This efficiency sets a limit on the observable noise reduction of 13 dB below the projection noise limit, and thus we do not expect any substantial degradation of the spin squeezing to arise from mapping the SSS onto the $|g\rangle \rightarrow |e\rangle$ clock transition.

We first demonstrate that the entanglement survives the transfer $|g\rangle \rightarrow |e\rangle \rightarrow |g\rangle$ by characterizing the spin squeezing remaining after this process in the $\{|\uparrow\rangle, |\downarrow\rangle\}$ manifold via state tomography (Fig. 6-2c). We observe that the squeezed noise dips significantly below the standard quantum limit to a level $\xi^2 = -5.9^{+0.6}_{-0.8}$ dB, where the given uncertainties are 1σ statistical errors, and is essentially the same before and after the mapping onto the clock levels.

Figure 6-3 shows the measured normalized spin noise ξ^2 and Wineland parameter ξ^2_W as a function of Ramsey time on the optical-clock transition for both a CSS, and for a SSS with its squeezed direction oriented along S_z in the $\{|g\rangle, |e\rangle\}$ spin space. In this configuration, that does not improve clock performance, but can be used to characterize the entanglement [121], the LO phase noise does not affect the squeezed quadrature S_z, and we observe that the S_z spin noise remains reduced for times as long as 1 s. While the observed Ramsey contrast decays due to LO phase noise with a time constant of $\tau_{\mathrm{LO}} = 6$ ms, the intrinsic coherence of the atomic state (mean atomic spin vector length $|\langle\vec{S}\rangle|$) can be determined even when the LO phase noise is dominant (see Methods), and the corresponding result is displayed for both the CSS and the SSS in the inset to Fig. 6-3. The ensemble spin coherence on the optical clock transition decays exponentially with a time constant $\tau_{\mathrm{ens}} = (0.8 \pm 0.2)$ s both for the CSS and the SSS. As Fig. 6-3 shows, after an interrogation time of ≈ 0.2 s

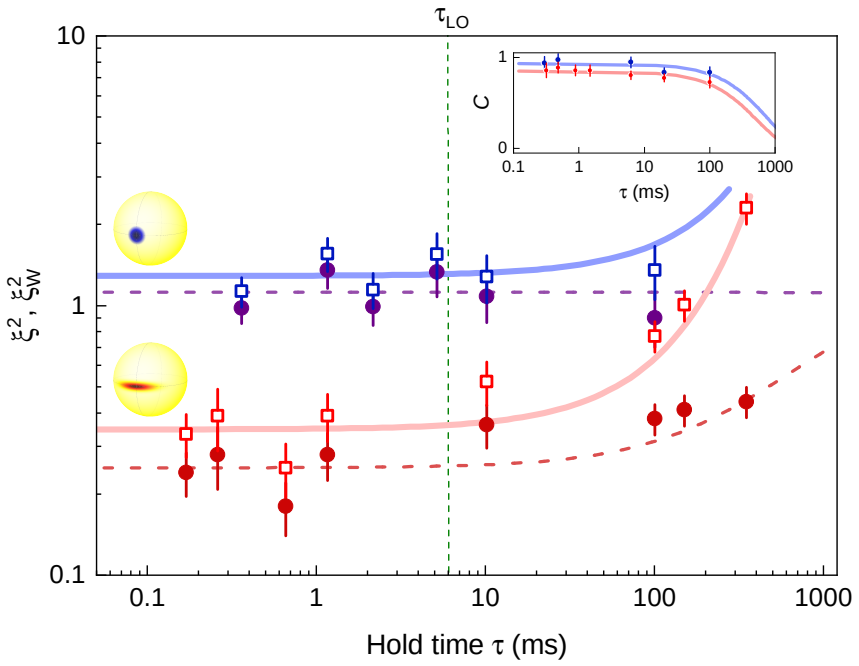


Figure 6-3: **Spin noise and Wineland parameter on the clock transition as a function of time.** The measured normalized S_z spin noise ξ^2 (solid circles) and model (dashed lines) for the CSS (purple) and the SSS with squeezed axis aligned along S_z (dark-red) increases slowly with time. The increase is caused by the finite 800-ms lifetime of the state $|e\rangle$ due to scattering of the trapping light. The Wineland parameter ξ_W^2 (open squares) depends in addition on the contrast loss due to shortening of the atomic collective spin $|\langle\vec{S}\rangle|$ (inset, blue data points for CSS, red for SSS, with exponential fits). The solid lines represent the predicted Wineland parameter using the fit to the measured contrast. τ_{LO} indicates the coherence time of the LO. Error bars represent 1σ statistical confidence interval.

the SSS is no longer sufficiently entangled to overcome the SQL, but it can still offer metrological gain over the CSS for up to 0.5 s.

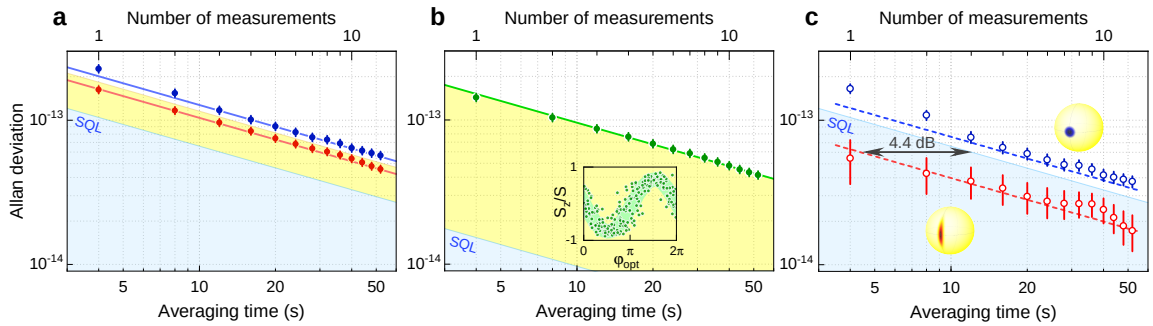


Figure 6-4: **Stability improvement with the squeezed clock.** In all three subfigures, the blue shaded area represents the region below the SQL, while the gray shaded area in a, b, represents the additional contribution from LO phase noise. **a**, Inferred single-clock cycle stability (self-comparison Allan deviation divided by $\sqrt{2}$ [2]) for a CSS (sequence *C1*, blue) and a SSS (*S1*, red) with Ramsey time $\tau_{S1} = 0.17$ ms. The squeezed clock operates within the gray region set by SQL and LO phase noise because the quantum projection noise is reduced below the SQL. **b**, Allan deviation for a SSS (sequence *S2*, green) with longer Ramsey time $\tau_{S2} = 1.16$ ms, where the total noise is dominated by the LO noise. Inset: Ramsey fringes vs. LO phase φ_{opt} of the second Ramsey π-pulse for *S2*. **c**, Data for *C1* and *S1* after subtraction of the LO phase noise, where the latter has been calculated from the data for *S2*. The dashed lines indicate the expected performance estimated from the separately measured Wineland parameter ξ_W^2, see Fig. 6-3. The other parameters for these measurement are: atom number $N = 300 \pm 30$, single-cycle time T_C=4s, Ramsey contrast $C_{C1} = 0.91(1)$ for CSS, $C_{S1} = 0.85(1)$ and $C_{S2} = 0.70(1)$ for SSS. Error bars represent 1σ statistical confidence interval.

6.4 Stability and Allan Deviation

In a fully operating atomic clock, the atomic phase is used to stabilize the LO phase through feedback. Hence clock performance can be improved by the use of SSSs with the squeezed axis oriented along the phase direction, which allow one to measure the phase difference between atoms and LO with higher stability than a CSS, and apply correspondingly better feedback [242]. The optimum Ramsey time that achieves maximum gain over the CSS is determined by the combination of LO coherence time τ_{LO} and Wineland parameter [26].

In Fig. 6-4, we demonstrate the implementation of an OLC Ramsey sequence with an entangled-state input and show that the atomic system provides stability beyond the SQL. We implement the full clock sequence depicted in Fig. 6-1d with Ramsey times of $\tau_{S1} = 0.17$ ms (Ramsey sequence *S1*, Fig. 6-4a) and $\tau_{S2} = 1.16$ ms (Ramsey sequence *S2*, Fig. 6-4b). Fig. 6-4a shows that the squeezed clock, although it does not operate beyond its SQL due to LO phase noise, has an Allan deviation 3 dB lower than the one operated with a CSS. The LO phase noise $\Delta\phi_{LO}$ in our system arises predominantly from sequence-to-sequence frequency variations $\Delta\omega/(2\pi) = (78\pm3)$ Hz of the LO, i.e., $\Delta\phi_{LO} = \tau_R\Delta\omega$ (see Methods), and is measured with the sequence *S2* with longer Ramsey time. We can then remove $\Delta\phi_{LO}$ from the Allan deviation of the *S1* data to obtain the intrinsic stability of the atomic clock system operated with the SSS at Ramsey time τ_{S1} (red circles in Fig. 6-4c). We further show for comparison a clock operated with a CSS under the same conditions, and with LO noise also removed (blue circles). The entangled atomic system exhibits stability that is $4.4^{+0.4}_{-0.6}$ dB below the SQL, and 5.7 dB below the CSS, since the latter is also subject to imperfect state detection and contrast loss. The observed stability improvement due to entanglement is in excellent agreement with that expected from the measured Wineland parameter.

6.5 Outlook

In conclusion, we have generated for the first time spin squeezing for many atoms between atomic levels whose energies differ on the scale of optical photons, and used it to demonstrate an optical-clock sequence where entanglement provides stability in the atomic system beyond the SQL. Our system is currently limited by LO phase noise and Dick noise, and a reduction of both will be required to fully operate an OLC beyond the SQL. With improvements in LO oscillator stability [134, 225, 160, 198] and duty cycles approaching 100%, the Dick noise will be at the same level or smaller than the SQL [159]. Then, a state-of-the-art OLC with 2000 atoms, Ramsey time of $\tau_R = 2$ s, cycle time $T_C = 2.3$ s, and contrast of $C = 0.91$ that is limited by the excited-state lifetime, at a metrological gain of 12 dB that can be obtained by improv-

ing the state detection would reach a fractional stability of $\sigma_{sq} = 1.4 \times 10^{-18}\ \mathrm{s}^{1/2}/\sqrt{T}$. With further improvements in LO performance using novel stabilization schemes [142], we expect no major roadblocks to Ramsey times of tens of seconds using SSSs, and correspondingly improved clock stability in atoms with sufficiently long excited-state lifetime. Moreover, several future fundamental tests based on optical clock transitions, such as the detection of low-frequency gravitational waves [91] or the search for certain types of dark matter [176], require finite bandwidth of the sensor [91, 176]. These applications require short Ramsey time and can fully profit from the sensitivity improvement offered by SSS's. With respect to the Dick noise, some tests of fundamental physics that require the comparison of the transition frequencies between two (or more) atomic ensembles, such as red-shift measurements, gravitational wave detection, and physics beyond the standard model [185, 191, 220], can be performed by interrogating the atomic ensembles simultaneously, thus removing the Dick noise [219, 156]. Finally, while possible systematic limitations to the absolute accuracy of the clock due to the presence of the cavity need to be carefully investigated, we anticipate that those adverse effects can be controlled at the level of 10^{-19} or better.

Chapter 7

Time-Reversal of the Hamiltonian and Its Applications on Quantum Metrology

As both seen in Chap. 5 and Chap. 6, we probably had generated a better spin squeezing but the measurement precision is limited by the final state readout. Not only for squeezed states. It is possible to create more complex many-body entangled states than SSS, and such states can also potentially offer even more improvement over the SQL, but is even more vulnerable to detection and readout protocol.

In order to harness from such complicated states, a particularly interesting possibility is the generation of an evolution effectively backwards in time by switching the sign of a many-body Hamiltonian $\hat{H}$. Since the evolution of a quantum state is governed by the operator $\hat{U} = \exp\left(-i\hat{H}t/\hbar\right)$, such a sign change from $\hat{H}$ to $-\hat{H}$ is equivalent to an evolution backward in time under the original Hamiltonian $\hat{H}$.

It turns out that this type of time-reversal process can be used for quantum metrology well beyond the SQL. Furthermore, this process may potentially allow one to operate a clock close to the truly fundamental Heisenberg Limit. The latter is determined by the Heisenberg uncertainty rules for angular momentum, and sets a limit N^{-1} to the improvement of the clock precision with atom number N, as opposed to the $N^{-1/2}$ SQL. For 10^4 atoms, a clock at the Heisenberg limit could outperform

the SQL by a factor of 100.

In this chapter, I will present our demonstration of such a scheme where a strongly entangled state is generated by a many-body Hamiltonian. This state is highly sensitive to small displacements, and if such a displacement occurs, it can be made directly visible after an evolution "backward in time" with the negative Hamiltonian. This effectively leads to an entanglement-induced signal amplification that enables the operation of a quantum sensor or clock well beyond the SQL, and at a fixed distance from the Heisenberg Limit as we vary the atom number. We achieve a precision improvement that is linear in the atom number, rather than improving only as the square root of the atom number. This system also yields the highest gain, by a factor of 15 (11.8 ± 0.5 dB) beyond the SQL that is the highest among any interferometric device demonstrated so far. Such a reversal-based protocol is called signal amplification through time-reversed interaction (SATIN) protocol, following the proposal in [40]. The demonstrated SATIN protocol can be readily applied to a state-of-the-art optical lattice clock by mapping the generated entangled state on the optical clock transition via a coherent optical π-pulse [168]. It is worth noting that, in order to avoid large systematic errors due to collisions, optical lattice clocks [157, 225] operate with limited total atom number $N = 10^2 - 10^4$, a region that we reach and investigate here with the SATIN protocol.

7.1 Introduction

Our system consists of up to $N = 400$ laser cooled ^{171}Yb atoms that are trapped in an optical lattice inside a high-finesse optical resonator (Fig. 7-1a) [25]. We work in the nuclear-spin manifold $s = \frac{1}{2}$ of the electronic ground state $^1S_0$, and first create a state of the collective atomic spin $\hat{\mathbf{S}} = \sum \hat{\mathbf{s}}_\mathbf{i}$ pointing along the x axis (coherent spin state, CSS). The collective spin operators are defined through the Pauli matrices ($\hat{\sigma}_{x,y,z}$) as $\hat{S}_k = (1/2) \sum_{j=1}^{N} \hat{\sigma}_{k,j}$ with $k = x, y, z$. In this product state of the individual spins $\mathbf{s}_i$, each atom is in a superposition of the states $|\uparrow\rangle \equiv \left|m_s = +\frac{1}{2}\right\rangle$ and $|\downarrow\rangle \equiv \left|m_s = -\frac{1}{2}\right\rangle$.

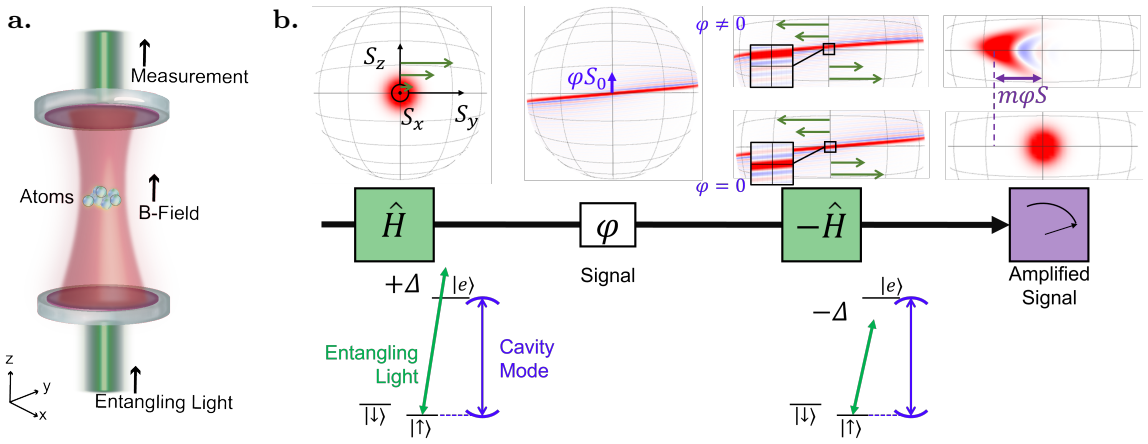


Figure 7-1: **Setup and sequence. a.** ^{171}Yb atoms are trapped inside an optical cavity in an optical lattice. Light for state preparation, entanglement generation, and state measurement (green) is sent through the cavity along the z axis. The static magnetic field defines the quantization axis parallel to z. **b.** SATIN protocol sequence with the quantum-state evolution (top) and relevant energy-levels and cavity mode (bottom). Wigner quasiprobability distribution functions describing the collective quantum state are calculated for an ensemble of $N = 220$ atoms, and are represented on the generalized Bloch sphere for the ground-state manifold $\{|\downarrow\rangle, |\uparrow\rangle\}$. An entangling light pulse is passed through the cavity detuned by $+\Delta$ from the $|\uparrow\rangle \rightarrow |e\rangle$ transition and the cavity mode. This light generates the nonlinear OAT Hamiltonian $\hat{H} \propto \hat{S}_z^2$ which shears the initial CSS state (green arrows on the generalized Bloch sphere), the state depicted here corresponds to a shearing angle of $Q = 0.7\sqrt{N} = 10.4$. A rotation φ about the S_y axis displaces the state such that $\langle \hat{S}_z \rangle = \varphi S_0$; this rotation can be induced both by a direct resonant rf-pulse or effectively via a compound sequence $\mathcal{R}_y(\pi/2)\mathcal{R}_z(\varphi)\mathcal{R}_y(-\pi/2)$ as in Ramsey spectroscopy with squeezed states ($\mathcal{R}_j(\alpha)$ denotes a rotation of angle α about the j axis). We first characterize the protocol by applying a direct rotation along the y axis while later we implement it in a phase sensitive Ramsey sequence, where the $\mathcal{R}_z(\varphi)$ results from the accumulated phase in a spin echo sequence. Subsequently, a (dis)entangling light pulse is sent through the cavity detuned by $-\Delta$ from the $|\uparrow\rangle \rightarrow |e\rangle$ transition and the cavity mode. This pulse generate the negative OAT Hamiltonian $-\hat{H}$ which causes the quantum state to evolve effectively "backwards in time". With $\varphi = 0$ the quantum state evolves back to the original CSS, while for a small angle ($\varphi \neq 0$) the final state is displaced by an angle $m\varphi$ from the original CSS, where m is the SATIN signal amplification.

We then apply the one-axis twisting (OAT) Hamiltonian [108]

$$\hat{H} = \chi \hat{S}_z^2 \tag{7.1}$$

to the CSS to create an entangled state (see Fig. 7-1). The OAT Hamiltonian is generated by the nonlinear interaction between the atoms and light that is being applied to the cavity [25, 168, 125]. The light-atom interaction as a generator of entanglement offers the advantage that it can not only be turned on or off arbitrarily, but also that the sign of $\hat{H}$ can be changed by adjusting the frequency of the incident light, as discussed in Chap. 3. When we apply $\hat{H}$ for a time t, the state evolves under the OAT operator $\hat{U} = \exp\left(-i\frac{Q}{N}\hat{S}_z^2\right)$, where we use the twisting parameter $Q \equiv N\chi t$ as defined in (3.21). Here we also define a normalized parameter $\tilde{Q} \equiv Q/\sqrt{N}$, and $\tilde{Q} = 2\pi$ corresponds to a state wrapped all around the Bloch sphere, as an indication of non-Gaussianity.

7.2 Characterizing the Reversibility

We first characterize the action of the OAT Hamiltonian $\hat{H}$ and the effective evolution "backwards in time" that can be obtained by applying $-\hat{H}$ subsequently to $\hat{H}$. To this end we measure for various twisting strengths $\tilde{Q}_+$ the spin distribution along the S_y axis and its normalized variance $\sigma_y^2 \equiv 2(\Delta S_y)^2/S_0$. (Here $S_0 = N/2$ and the SQL, obtained for the CSS, corresponds to $\sigma_y^2 = 1$). For small $\tilde{Q}_+ \ll 1$, the OAT operator $\hat{U}(\tilde{Q}_+)$ creates an SSS with a Gaussian envelope, while for $\tilde{Q}_+ \geq 0.5$ the state stretches around a substantial portion of the Bloch sphere. As Fig. 7-2a shows, we observe strongly non-Gaussian probability distributions along the S_y axis that agree well with the expected evolution from the OAT Hamiltonian calculated without any free parameters. We also verify that the $\hat{S}_z$ distribution remains unaffected by the OAT.

If we subsequently apply the negative Hamiltonian and the corresponding untwisting operator $\hat{U}(\tilde{Q}_-)$, then for a matched untwisting magnitude, $\tilde{Q}_- = -\tilde{Q}_+$, the state distribution for the S_y axis reverts back to a Gaussian distribution with a variance that is only slightly increased compared to the original CSS (Fig. 7-2a bottom and 7-2b). The residual broadening can be explained by the fact that the OAT Hamiltonian $\hat{H}$ of Eq. 7.1 is only an approximation to the actual physical process, where the

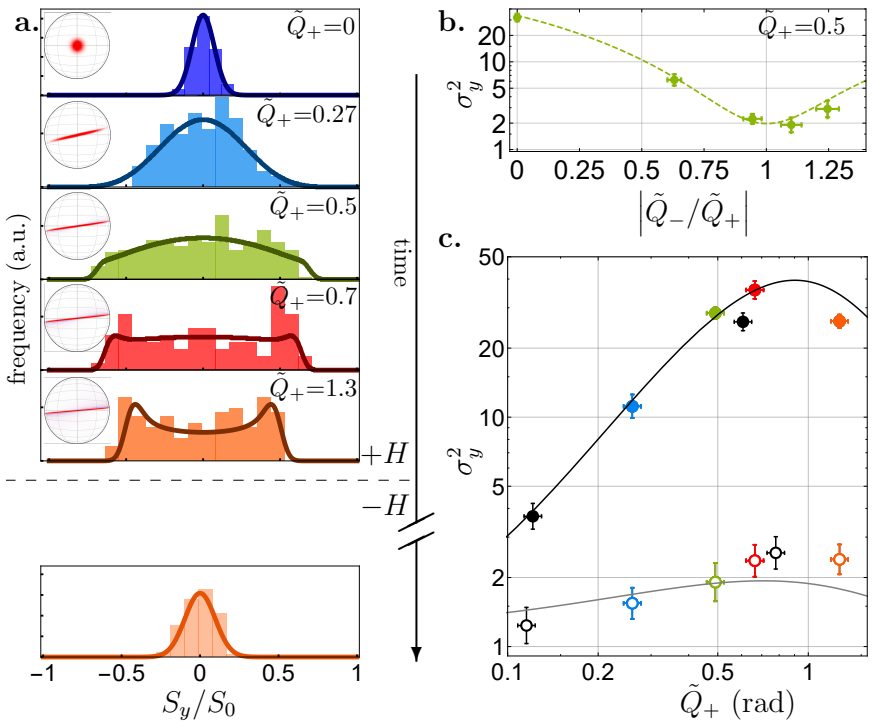


Figure 7-2: **State evolution during SATIN sequence. a.** Histograms showing the distributions of along the S_y axis measured at different times during the SATIN sequence. The system transitions from Gaussian states (blue histogram) to strongly non-Gaussian states (red, orange). After reversing the sign of the Hamiltonian, the original CSS is almost recovered (orange, lower plot). The solid lines are the predicted distributions from a theoretical model including finite contrast $\mathcal{C}$, measurement resolution $\sigma^2_{meas} = 0.15$ (i.e., a resolution of 6 atoms for $N = 220$), and excess broadening from light-atom entanglement $\mathcal{I}$. The Bloch spheres show the expected Wigner quasi-probability distributions at the corresponding times. **b.** The normalized S_y variance ($\sigma_y^2 \equiv 2(\Delta S_y)^2/S_0$) as a function of the unshearing strength $\tilde{Q}_-$ for $\tilde{Q}_+ = 0.5$. The dashed line shows the model prediction. **c.** Measured variances of S_y resulting from shearing with $\tilde{Q}_+$ (solid circles), and after the corresponding unshearing $\tilde{Q}_-$ (open circles), with $\tilde{Q}_- = -\tilde{Q}_+$. Solid lines are theoretical predictions, including $\mathcal{C}$, σ^2_{meas} and $\mathcal{I}$. All error bars represent 1σ statistical uncertainty resulting from 100 to 150 experimental realizations. Error bars of σ_y^2 are inferred by bootstrapping the data.

transmitted and scattered light carries some residual information about the atomic spin $\hat{S}_z$. Then tracing over the unobserved light degrees of freedom causes an excess broadening of σ_y^2 by a factor $1 + \mathcal{I}$ [25]. To quantify the excess broadening $\mathcal{I}$, we fix $\tilde{Q}_+$ and measure σ_y^2 vs. $\tilde{Q}_-$. Data for $\tilde{Q}_+ = 0.5$ and N=220 $\pm$ 12 atoms are shown in Fig. 7-2b. It is clear that σ_y^2 is indeed minimized near $\tilde{Q}_- = -\tilde{Q}_+$, with a small excess broadening of $\mathcal{I} = 0.9 \pm 0.4 \lesssim 1$, comparable to the initial noise area of the

CSS (1 in the chosen units), after accounting for measurement resolution (increasing σ_y^2 by 0.15 ± 0.02) and contrast loss (decreasing σ_y^2 by 0.7 ± 0.1). Our algebraic model, without any fitting parameters, agrees remarkably well with the data. Fig. 7-2c shows the variance of $\hat{S}_y$ resulting from the shearing $\tilde{Q}_+$ (solid circles), and after the unshearing $\tilde{Q}_-$ (open circles). The data points are fitted to the theoretical curve taking into account the different sources of decoherence: excess broadening $\mathcal{I}$, finite contrast $\mathcal{C}$, and measurement resolution σ_{meas}^2.

We next measure the small-signal amplification m provided by the SATIN protocol. To this end, we prepare a strongly entangled state by evolving a CSS under the OAT operator $\hat{U}(\tilde{Q}_+)$, rotate this state by a small angle φ around the y axis such that $\langle \hat{S}_z \rangle = \sin(\varphi) S_0 \sim \varphi S_0$, and apply the untwisting operator $\hat{U}(\tilde{Q}_- = -\tilde{Q}_+)$ which amplifies φ by a factor m and maps it onto the y axis, resulting in $\langle \hat{S}_y \rangle = m \langle \hat{S}_z \rangle \sim m\varphi S_0$. We measure how $\langle \hat{S}_y \rangle / S_0$ scales with φ for different $\tilde{Q}_+$ and present the results in Fig. 7-3a, which compares the signal amplification of the SATIN scheme to a measurement with a CSS (for which $m_{\mathrm{SQL}} = 1$). Note that for large displacements φ the finite size of the Bloch sphere makes the mapping of the rotation angle φ onto $\langle \hat{S}_y \rangle$ nonlinear. The measured data are well described by the model.

Fig. 7-3b shows the amplification m vs. $\tilde{Q}_+$ together with the theoretical model. The amplification scales linearly with $\tilde{Q}_+$ for $\tilde{Q}_+ \ll 1$ and reaches its maximum at $\tilde{Q}_+ \approx 0.7$, larger than the optimum value $\tilde{Q}_+ = 0.4$ for minimizing the variance of the spin squeezed state for the same atom number. Even the state with $\tilde{Q}_+ = 1.3$ outperforms the squeezed state by several dB. This non-Gaussian state has as root-mean-square (rms) phase spread of 1.3 rad, where a state with a uniform distribution between 0 and 2π would have an rms phase spread of $\pi/\sqrt{3} \approx 1.8$ rad. This demonstrates the usefulness of non-Gaussian states for quantum metrology.

The sensitivity $\delta\varphi$ of the SATIN protocol, i.e., the minimal resolvable displacement of a state, can be estimated as the displacement $mS_0\delta\varphi$ at the end of the sequence that equals the measured uncertainty $\Delta S_y = \sigma_y \sqrt{S_0/2}$ after the twisting-untwisting sequence for $\varphi = 0$. Thus, the gain of the SATIN protocol over the SQL with

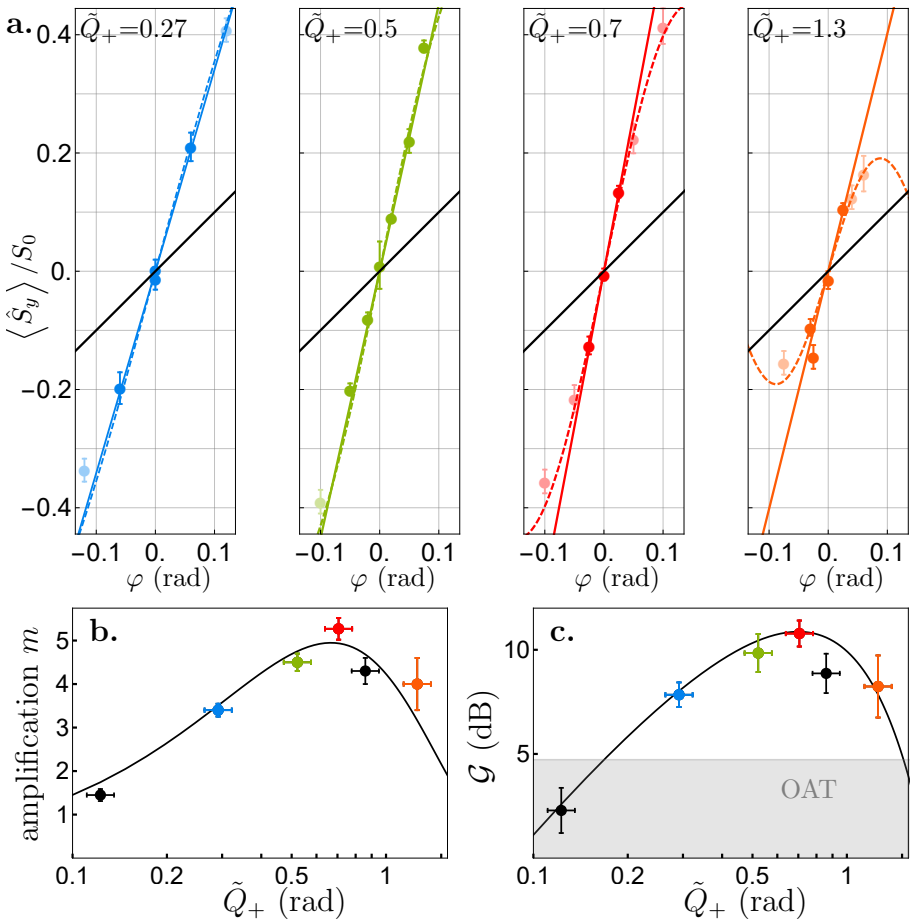


Figure 7-3: **Signal amplification and metrological gain.** All data are taken with $N = 220 \pm 12$ atoms. **a.** The mean value $\langle \hat{S}_y \rangle / S_0$ as a function of the angle φ. The solid black line is the maximal signal that can be reached with a CSS. Dashed lines represent calculations, solid lines are the linear fit to the data for small φ. **b.** The signal amplification as a function of the shearing parameter $\tilde{Q}_+$. The solid line is the model prediction. **c.** The resulting metrological gain $\mathcal{G}$ as a function of the squeezing strength $\tilde{Q}_+$, solid line shows the model prediction. The gray area represents the metrological gain accessible with a simple OAT squeezing in the same system with a measurement resolution $\sigma^2_{meas} = 0.15$ in variance (-8.2 dB). Error bars represent 1σ confidence intervals.

sensitivity $(\Delta\varphi)_{\mathrm{SQL}} = 1/\sqrt{2S_0}$ is given by

$$\mathcal{G} = \frac{(\Delta\varphi)^2_{\mathrm{SQL}}}{(\delta\varphi)^2} = \frac{m^2}{\sigma_y^2} = \frac{S_0}{2}\frac{m^2}{(\Delta S_y)^2}. \tag{7.2}$$

In Fig. 7-3c we present the resulting metrological gain $\mathcal{G}(\tilde{Q}_+)$ for an ensemble of $N = 220$ atoms. Since σ_y^2 does not change significantly when increasing $\tilde{Q}_+$, the

metrological gain approximately follows the behavior of m and peaks around $\tilde{Q}_+ \approx 0.7$. At larger values of $\tilde{Q}_+$ the signal amplitude is reduced due to contrast loss from photon scattering into free space. For $N = 220$ atoms the metrological gain peaks at $\mathcal{G} = 10.8 \pm 0.6$ dB. This is more than 6 dB larger than the maximal gain achievable with spin squeezing in the same system, which is limited by measurement resolution and decoherence to 4.7 dB.

Furthermore, we investigate the scaling of the sensitivity with atom number N. Unlike spin squeezing [108] and the quantum magnification protocol of Ref. [87], the SATIN protocol is not limited by the curvature of the Bloch sphere, and therefore we expect that under optimum conditions the precision improves in proportion to the atom number, corresponding to HS. Fig. 7-4 shows that when we vary N between 50 and 370, we indeed measure a gain over the SQL that varies as $\mathcal{G} \propto N$, achieving HS. This implies that the averaging time necessary to achieve a certain resolution improves as N^2 for the SATIN protocol, as predicted in Ref. [40]. In particular, for $N = 370 \pm 20$ atoms we reach $\mathcal{G} = 12.8 \pm 0.9$ dB.

Finally, we implement a full (phase) interferometer for ac magnetic fields in the form of a spin echo SATIN Ramsey sequence. We first apply the OAT operator, then rotate the oversqueezed state about the S_x axis with a $\pi/2$-pulse, thus making it sensitive to phase perturbations (i.e. rotations about the S_z axis). Subsequently, we rotate the state back by another $\pi/2$ pulse about the S_x axis before subjecting it to the negative Hamiltonian. To cancel fluctuations of the static magnetic field, we apply a spin echo π-pulse, separated from the $\pi/2$ pulses by 1.73 ms, thus realizing an interferometer sensitive to ac magnetic fields with peak sensitivity at 290 Hz. We observe a metrological gain of $\mathcal{G} = 11.8 \pm 0.5$ dB with $N = 340 \pm 20$ atoms in the interferometer (solid red star in Fig. 7-4c), slightly exceeding the previous record of 10.5 ± 0.3 dB [88] in a Ramsey interferometer (atomic clock) with large atom number. The gain $\mathcal{G}$ achieved with the SATIN Ramsey sequence represents a factor of 15 of reduction in averaging time for a desired precision (see Fig.7-4b). Our Ramsey interferometer also performs near the HS limit for the SATIN protocol, as shown by the data point (solid red star) in Fig. 7-4c.

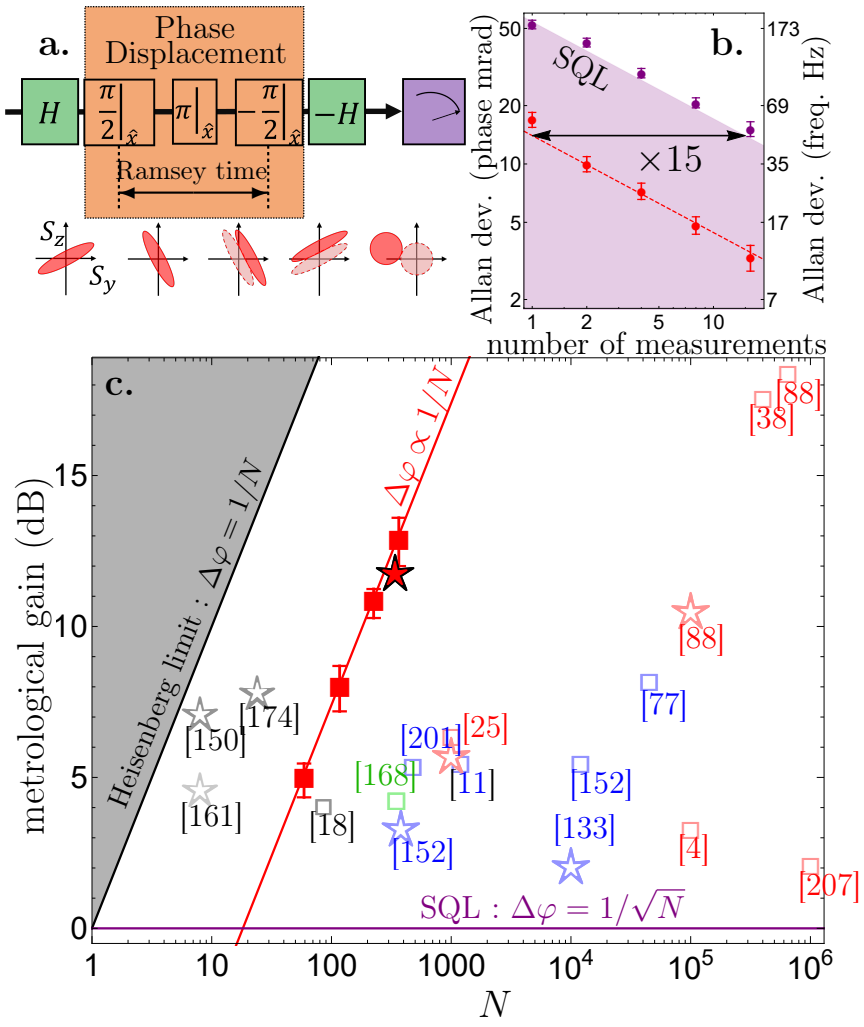


Figure 7-4: **Scaling of sensitivity with atom number and comparison with previous results. a.** Block diagram showing a SATIN scheme applied to a Ramsey interferometry experiment. Here the compound sequence of pulses that maps the phase accumulated during the Ramsey time into a phase displacement about the S_y axis. **b.** Phase Allan deviation plot of Ramsey spin echo interferometry performed with a CSS (purple circles) and an optimally over-squeezed state in a SATIN protocol (red circles). In both cases we used 340±20 atoms in the interferometer. The shaded purple area indicates the region below the SQL. The data for the SATIN sequence is fitted to a white noise model (red dashed line) showing 11.8±0.5 dB of metrological gain over the SQL. **c.** Comparison with previous results. Blue data: BEC experiments [77, 11, 152, 111, 201, 133]. Red data: Thermal atoms [4, 207, 38, 88, 25, 92]. Dark gray data: Ions [150, 18, 174]. Light gray data: Rydberg atoms in a tweezer array [161]. Green data: squeezing generated in an optical-lattice clock [168]. Squares are expected metrological gains, obtained by quantum state characterization. Stars refer to directly measured phase-sensitivity gain. Solid symbols are obtained in this work. Error bars represent 1σ confidence interval. Horizontal error bars are smaller than the markers.

Under ideal conditions, the SATIN protocol provides a metrological gain only 4.3 dB away from the HL [40] for an optimized shearing strength $\tilde{Q}_+^{opt} = 1$. Dissipation in the atomic system, in our system due to photon scattering and light-atom entanglement, reduces the maximum available gain and the optimum shearing parameter $\tilde{Q}_+^{opt}$. For our parameters, $\tilde{Q}_+^{opt} = 0.7$, which reduces the metrological gain by 0.9 dB, while the interferometer contrast loss and non-unitary state evolution under the full Hamiltonian contribute 4.4 dB and 3.2 dB, respectively. The joint effect of these imperfections imposes a distance 12.6 dB from the HL. To move closer to the HL, the dissipation in the system must be reduced by increasing the atom-cavity coupling, as characterized by the single-atom cooperativity η (see Methods). For example, by increasing η by a factor 10 to $\eta = 80$, we expect performance only 8 dB away from the HL. At present, we have seen no deviation from HS, i.e. the measurement precision improves linearly with atom number N. The latter can likely be increased in the future by means of optimized loading protocols, like a recooling and retrapping sequence [90], in the two-dimensional optical lattice.

It is known that in the presence of noise, HS reverts back to a fixed improvement over the SQL (i.e. $N^{-1/2}$ scaling) at sufficiently large atom number [57, 44]. In our system, in the full interferometer demonstrated in Fig. 7-4c, the expected dominant limitation is the finite vacuum that induces an atom loss rate $\gamma_{Loss} = 0.1$ s^{-1}; the latter results in a transition from HS to SQL scaling at $N \approx 4 \times 10^4$ for a Ramsey time of 3.46 ms used here. This is larger than the maximum atom number $(10^2 - 10^4)$ used in optical-transition clocks to keep systematic errors through collisional shifts under control [157, 225]. However, to retain HS to this level, technical parameters, such as the squeezing light and the RF rotation pulses, need to be stringently controlled. Furthermore, the relative photon number of the $\tilde{Q}_+/\tilde{Q}_-$ shearing/unshearing pulses needs to be stable near the shot noise level, which corresponds to a moderate 5% for our ensemble size.

Our protocol can be used for a variety of fundamental and applied purposes, such as tests of fundamental laws of physics [190, 191], the search for physics beyond the Standard Model [176, 45, 6, 234], the detection of gravitational waves [109], or geodesy

[129, 70, 220]. As with all entanglement-based protocols beyond the SQL, they are useful to boost the sensitivity in applications that require performance in a given bandwidth or limited time. For instance, by coherently transferring the entanglement onto the ultra-narrow optical clock transition by means of a high-fidelity optical π-pulse [168, 248], the protocol can be directly used to search for transient changes in the fundamental constants induced by dark matter [45].

Chapter 8

Exponential Dynamics on An Unstable Trajectory; Out-of-Time-Ordered Correlators

In Chap. 7, we described how to implement the SATIN protocol for signal amplification. A question, though it sounds naïve, is actually very important: why is the displacement along S_z-direction while the amplified signal is along S_y direction? The complete answer is highly non-trivial, but to a certain level, this is because the S_z-displacement is generated by the $\hat{S}_y$ operator, which doesn't commute with the system's OAT Hamiltonian.

This idea resonates with the community studying operator dynamics in complicated interacting systems. One of the studies is focusing on initially commuting operators' non-commuting behavior as time evolves, which is now known as the out-of-time-order correlator (OTOC) and quantum scrambling. Quantum scrambling describes the spreading of local information into many degrees of freedom in quantum systems. This provides the conceptual connection among diverse phenomena ranging from thermalizing quantum dynamics to models of black holes. The OAT system, though it is of certain interest in the beginning [63], soon turned out to be trivial since it contains too many integrals of motion and the dynamics is not exponential. In fact, the whole study of time-invariant Hamiltonian within the Bloch sphere can-

not be chaotic due to the number of effective degrees of freedom being two, less than the requirement of chaos.

As one can easily see, this restriction has two workarounds: either to break the time-invariant condition to make it floquet, or search for exponential dynamics and information scrambling without chaos. The first approach is interesting and has been demonstrated in the spinor BEC system with a similar Hamiltonian [224] but intrinsically makes the system hard to control. The second way is exactly what I will take in this chapter, i.e., looking for chaotic-ish dynamics in a non-chaotic quantum system. In this chapter we experimentally probe the exponential scrambling of a multi-particle system near a bistable point in phase space and utilize it for entanglement-enhanced metrology. We use a time-reversal protocol to observe a simultaneous exponential growth of both the metrological gain and the out-of-time-order correlator, thereby experimentally verifying the relation between quantum metrology and quantum information scrambling. Our experiments demonstrate that fast-scrambling dynamics capable of exponentially fast entanglement generation are useful for practical metrology, resulting in 6.8(4) dB gain beyond the Standard Quantum Limit.

But, before I start this chapter, I want to briefly describe Fig. 8-1, which was removed from the manuscript [126] based on the opinions of other coauthors. I, however, find it really important and meaningful. Thus though I agree that Fig. 8-2 better summarizes this chapter as well as [126] and provides a concrete and general statement, I would still bring Fig. 8-1 here.

Basically, quantum information science and quantum metrology, two fields of studies harnessing the nature of quantum entanglement, are closely related. Specific to this chapter, we can find that basically the same process can be understood in different languages and makes perfect sense to experts in the respective fields. In terms of the SATIN quantum metrology, we start with a coherent (classical) state and generate a metrological useful state with a high QFI from the initial state. Then we use this state to detect a small signal and use the time-reversal to readout this signal to obtain the metrological gain. But on the other hand, this can be understood as the quantum system getting scrambled, and then we inject some quantum information.

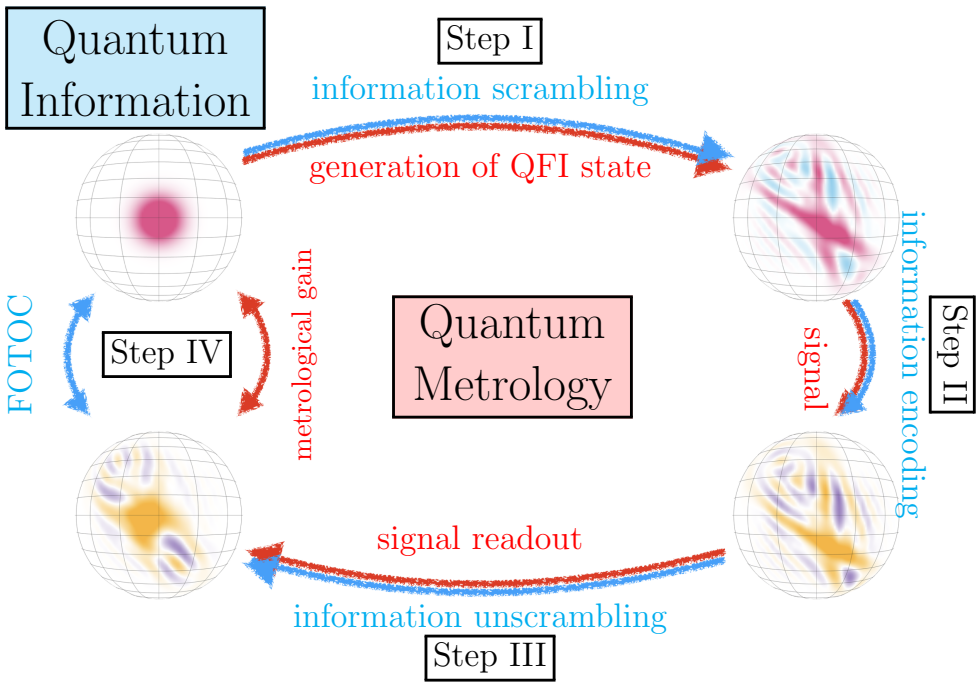


Figure 8-1: **Equivalence of time-reversal based quantum metrology beyond the standard quantum limit (SATIN) and the fidelity out-of-time-order correlator (FOTOC).** The Bloch spheres and the shaded regions represent the Hilbert spaces and the states' Wigner distribution, respectively. The blue lines describe the procedures from the quantum information science point of view, while the red lines are in the quantum metrology language.

The information undergoes unscrambling; then, we can measure the FOTOC from it. So now, let's jump into how this is eventually achieved.

8.1 Introduction to The Big Idea: Quantum Scrambling

Even though all unitary dynamics of quantum systems are in principle reversible, it is extremely challenging in practice to reverse the arrow of time in generic interacting many-body systems. This is because any small perturbations or imperfections in time-reversed dynamics can lead to highly complicated, non-local changes in quantum wavefunctions, similar to the butterfly effect in chaos theory. Dubbed information scrambling [206, 217, 123], this quantum mechanical effect gives rise to a

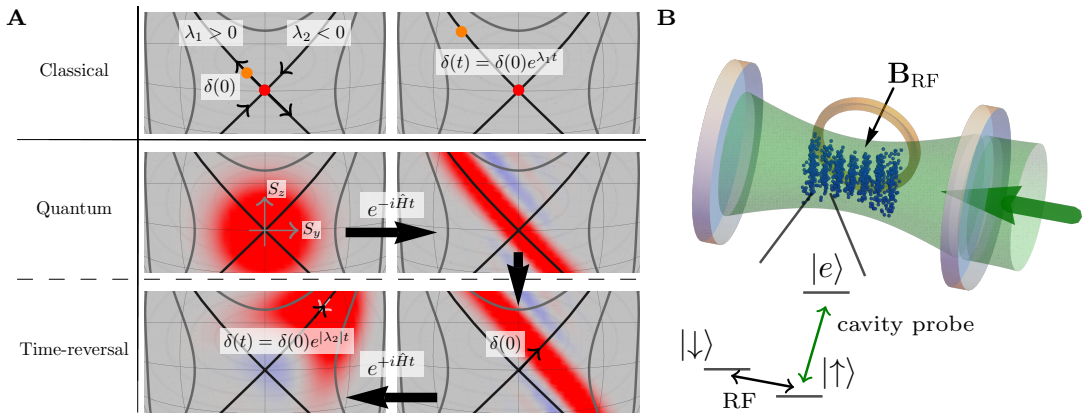


Figure 8-2: **Time-reversal based exponential growth of sensitivity in a system with an unstable fixed point. A**, Classically, for a trajectory with a positive Lyapunov exponent $\lambda_1 > 0$ an initial signal (displacement) $\delta(0)$ increases exponentially over time. For quantum dynamics, however, an initial overlap between two states is preserved under unitary evolution. To amplify the signal similarly to the classical case, one needs to evolve the state under the nonlinear $\hat{H}$, resulting in decreased quantum fluctuations along a direction with negative Lyapunov coefficient $\lambda_2 < 0$. A displacement along this direction followed by application of the negative Hamiltonian $-\hat{H}$ (such that $\lambda_{1,2} \to -\lambda_{1,2}$) is then used to amplify the signal. These plots also correspond to the Bloch sphere, where the S_y and S_z axes are labeled as in the left subplot of the middle row. **B**, Experimental setup. The LMG Hamiltonian is generated by the interaction of the collective atomic spin with light inside a cavity on the transition $|\uparrow\rangle \to |e\rangle$, while a radiofrequency magnetic field is applied to rotate the atomic spin.

variety of novel phenomena and applications ranging from models of quantum gravity [205, 155] to quantum metrology [4]. The speed of information scrambling is quantified by out-of-time-ordered correlators (OTOCs) [117, 107]. In certain systems, the OTOC grows exponentially fast over time $e^{\lambda_Q t}$, where $\lambda_Q > 0$ defines the generalized quantum Lyapunov exponent [107]. OTOCs have been measured [124] and used as probes for various many-body phenomena, such as thermalization [67], quantum phase transitions [236], many-body entanglement growth [63], and quantum scrambling [116, 22, 145]. However, the observation of exponential scrambling has remained elusive.

One approach to effective time-reversal involves changing the sign of the Hamiltonian $\hat{H} \rightarrow -\hat{H}$ during the evolution of highly engineered quantum systems. In the field of quantum metrology, it enables a family of powerful quantum amplification protocols [40, 60, 87, 158, 137, 66, 35, 139] such as signal-amplification-through-time-reversed-interaction (SATIN) [35]. Such protocols can be robust against many limitations that usually affect entanglement-enhanced atomic sensors, including imperfect measurements. In the presence of exponentially scrambling dynamics (see Fig. 8-2a), the SATIN signal is also amplified exponentially over time.

Here we experimentally implement a SATIN protocol for a Lipkin-Meshkov-Glick (LMG) Hamiltonian [128, 51, 255, 77, 216, 153, 169, 173, 154, 125, 139] that exhibits exponential phase space evolution. The LMG Hamiltonian is generated in a cavity QED (cQED) system by adding a global rotation term $\hat{S}_x$ to the One-Axis-Twisting (OAT) [108] Hamiltonian $\hat{S}_z^2$,

$$\hat{H} = \chi \hat{S}_z^2 + \Omega \hat{S}_x, \tag{8.1}$$

here $\hat{\mathbf{S}} = (\hat{\mathbf{S}}_\mathbf{x}, \hat{\mathbf{S}}_\mathbf{y}, \hat{\mathbf{S}}_\mathbf{z})$ represents the total spin of the system comprised of $N = 2S$ spin-$\frac{1}{2}$ particles. While the time evolution is not chaotic due to the conservation of $\hat{S}^2$, the LMG Hamiltonian nevertheless features a quantum Lyapunov exponent for $0 < \Omega/(S\chi) < 2$ due to an unstable (bifurcating) trajectory in the system phase space (see Fig. 8-2A) [166, 188, 173].

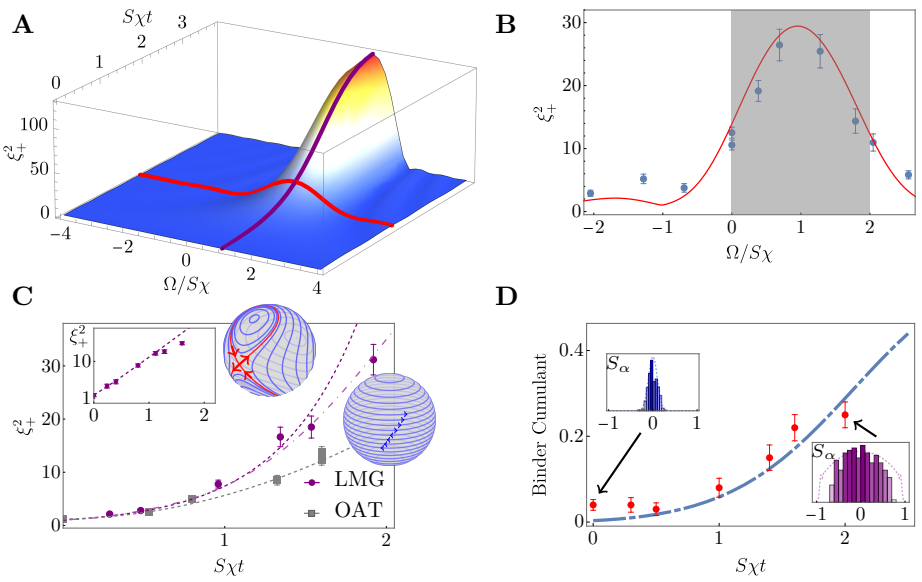


Figure 8-3: **Collective-spin evolution in the CQED system. A,** Numerical calculation of the normalized variance ξ_+^2 of the antisqueezed direction as a function of $S\chi t$ and $\Omega/S\chi$ with linecuts representing the measurements in **B**, **C**. **B,** The antisqueezing for a given $S\chi t = 1.8$ as a function of the rotation strength Ω. The shaded region indicates exponential growth, while in the other regions the time evolution is either quasi-periodic or growing polynomially. **C,** Comparison of antisqueezing ξ_+^2 between the fastest exponential growth for a critical rotation strength $\Omega = S\chi$, and the polynomial growth of pure OAT ($\Omega = 0$). The two Bloch spheres represent the lines of classical evolution in both situations. The dashed and dash-dotted red lines represent exponential growth based on the theoretically predicted Lyapunov exponent and the full numerical result, respectively. The gray dashed line is calculated for $\Omega = 0$. Inset: logarithmic plot for $\Omega = S\chi$ showing the exponential growth of ξ_+^2. **D,** The Binder cumulant, characterizing the shape of the distribution, for the antisqueezed direction for the critical LMG condition $\Omega = S\chi$ vs. time t. Insets: spin distribution with $S\chi t = 0$ (blue) and $S\chi t = 2$ (purple), with the latter being strongly non-Gaussian.

Our experiments operate with $N = 200$ ^{171}Yb atoms whose magnetic sublevels $|\uparrow,\downarrow\rangle$ in the electronic ground state represent a spin-$\frac{1}{2}$ system. One of the two spin states ($|\uparrow\rangle$) couples to an electronically excited state $|e\rangle$ via σ^+-polarized light that circulates inside the optical cavity (Fig. 8-2b). The coupling between a single atom and the cavity is characterized by the single-atom cooperativity $\eta = 8.8(2)$ [222]. We implement the LMG Hamiltonian in the rotating frame by adding an oscillating transverse magnetic field to the OAT Hamiltonian [125] (see Fig. 8-2b).

The experiments start by initializing the system in a coherent spin state (CSS)

pointing along the x-axis by means of optical pumping followed by a $\pi/2$ spin rotation. Analytical solutions using the Holstein-Primakoff approximation [86] show that for $\Omega/(S\chi) < 0$ or $\Omega/(S\chi) > 2$ the system evolution is periodic with a frequency $\omega = \sqrt{\Omega^2 + 2S\chi\Omega}$ [118]. On the other hand, for $0 < \Omega/(S\chi) < 2$ the frequency ω becomes imaginary, corresponding to an unstable-fixed-point exponential evolution with a Lyapunov exponent $\lambda_Q = |\omega|$. For a fixed $S\chi$, choosing $\Omega = S\chi$ results in a maximum Lyapunov exponent $\lambda_Q = |S\chi|$.

We first measure the anti-squeezing (largest variance $\xi_+^2 \equiv \max_\alpha[\mathrm{var}(S_\alpha)]/(S/2)$) of the collective spin $\hat{\mathbf{S}}$ after an evolution under $\hat{H}$ as a function of the ratio $\Omega/(S\chi)$. The anti-squeezing ξ_+ constitutes an upper bound on the quantum Fisher information (QFI) with respect to spin rotations [171]. As shown in Fig. 8-3b, the experimental data for ξ_+^2 agree with the numerical simulation of the model (solid red line), and show a peak at $\Omega = S\chi$, as expected.

We then measure in Fig. 8-3c how ξ_+^2 grows with time for the two cases $\Omega = 0$ (OAT Hamiltonian) and $\Omega = S\chi$ (critically tuned LMG Hamiltonian). The OAT data (gray) exhibit quadratic growth of ξ_+^2, as expected. The LMG data (red) show exponential growth $\xi_+^2 = e^{2\lambda_Q t}$ with $\lambda_Q = S\chi$ for times $t \lesssim (S\chi)^{-1}$. For larger times, the growths slows due to finite particle number and light-induced decoherence [125]. The finite total spin further causes the states to turn non-Gaussian, which we characterize via the Binder cumulant [13], as shown in Fig. 8-3d.

The time evolution under the critically tuned ($\Omega = S\chi$) LMG Hamiltonian $\hat{H}$ quickly prepares an entangled collective quantum state. To implement quantum metrology with the SATIN protocol, we then apply a small rotation $\hat{U}_{\delta\phi} = e^{-i\hat{S}_\alpha \delta\phi}$, where $\hat{S}_\alpha \equiv \hat{S}_y \cos\alpha + \hat{S}_z \sin\alpha$ represents a collective spin operator in the yz-plane. This encodes a signal phase $\delta\phi$ along the α direction, with $\alpha = \pi/4$ chosen to maximize the speed of the increase (see Fig. 8-2a and Supplementary Information). To implement $-\hat{H}$, we switch to another set of laser frequencies incident on the cavity and flip the sign of the transverse field Ω (see Supplementary Information). This generates an effective backward evolution in time that amplifies the applied signal $\delta\phi$. The shifted state then undergoes a bifurcated trajectory for $\delta\phi \lessgtr 0$ (see Fig.

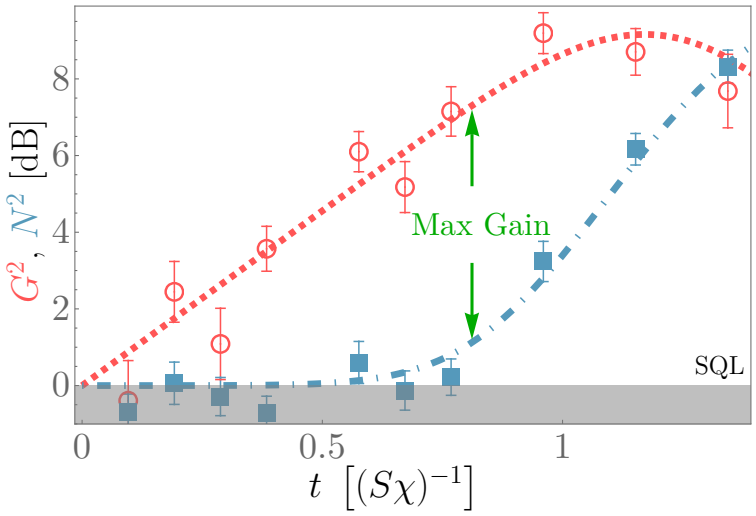


Figure 8-4: **Metrological gain with exponential LMG time-reversal protocol.** The squared signal amplification G^2 (pink open circles) and system noise N^2 (blue solid squares) vs. time t. The orange dashed line represents the exponential growth of the anti-squeezing shown in Fig. 8-3, representing an upper bound to the QFI. The blue dash-dotted line is the calculated noise due to residual light-atom entanglement. The maximum metrological gain is 6.8(4) dB.

8-3c), and results in an exponentially amplified deviation $G\delta\phi$ from the original position, and we measure the mean spin value $\langle \hat{S}_\alpha \rangle = \sin(G\delta\phi) \cdot S$ to infer the signal amplification G. As shown in Fig. 8-4, the squared signal amplification G^2 (orange) increases exponentially with the same exponent $2\lambda_Q$ as the anti-squeezing ξ_+^2 up to times $t \approx (S\chi)^{-1}$. The measured quantum noise N^2, i.e. the variance of spin projection noise along the amplification direction $\hat{S}_\alpha$ normalized to the standard quantum limit (SQL) (blue) remains unity until $t \approx 0.8(S\chi)^{-1}$. The increase of the noise N^2 results from the residual light-atom entanglement [125], and can be improved in the future by optimizing the light detuning. The improvement of the metrological gain over the SQL is 6.8(4) dB. The deviation of G^2 from an exponential for $t \gtrsim (S\chi)^{-1}$ is due to the non-uniform coupling between atoms and the cavity light [89] as well as the residual light-atom entanglement, both of which can be improved in the future [245, 125].

To investigate the QIS aspect of the time-reversal protocol, we measure the Fidelity OTOC (FOTOC) with quantum state tomography using randomized measure-

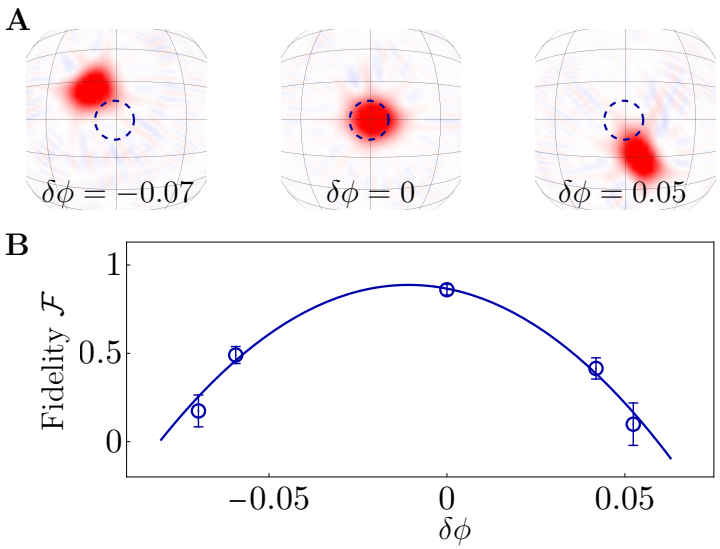


Figure 8-5: **FOTOC and OTOC extracted from quantum state tomography.** **A**, Experimental Wigner functions obtained from quantum state tomography after the LMG SATIN protocol with different signal displacements $\delta\phi$ (for $\Omega = S\chi$ and $t = 0.57(S\chi)^{-1}$). The dashed circle indicates the orginal CSS state. **B**, The solid blue line is a quadratic fit used to extract the OTOC $\mathcal{I}$ (see text and eq. 8.3).

ments [202, 54]. The FOTOC $\mathcal{F}(t)$ can be expressed as the trace between the density matrix $\rho(0)$ of the original state and that of the state displaced by $\delta\phi$ evolved backward in time, $\rho'_t(0) := \hat{U}_t\hat{\rho}(0)\hat{U}_t^\dagger$, where $\hat{U}_t := e^{i\hat{H}t}e^{-i\hat{S}_\alpha\delta\phi}e^{-i\hat{H}t}$,

$$\mathcal{F}(t) \equiv \left\langle \hat{U}_t\hat{\rho}(0)\hat{U}_t^\dagger\hat{\rho}(0)\right\rangle = \mathrm{Tr}\left(\rho'_t(0)\rho(0)\right). \tag{8.2}$$

At fixed forward evolution time t, the FOTOC $\mathcal{F}$ depends on the small displacement $\delta\phi$ and relates to the OTOC $\mathcal{I}(t)$ by its second derivative [236]

$$\mathcal{I}(t) \equiv -\frac{1}{2}\frac{\partial^2\mathcal{F}(t)}{(\partial\delta\phi)^2}\bigg|_{\delta\phi=0} = \left\langle \hat{S}_\alpha(t)\hat{\rho}(0)\hat{S}_\alpha(t)\hat{\rho}(0)\right\rangle, \tag{8.3}$$

with the Hermitian operator $\hat{S}_\alpha(t) := e^{i\hat{H}t}\hat{S}_\alpha e^{-i\hat{H}t}$.

Choosing four different evolution times (such that $S\chi t_1 \in \{0.38, 0.57, 0.77, 0.96\}$), we displace the entangled state for each t_1 by several different small angles $\delta\phi$. We then perform the tomographic reconstruction after a reversed time evolution with $-\hat{H}$ to obtain $\mathcal{F}(t_1)$, as shown in Fig. 8-5(a). The OTOC $\mathcal{I}(t_1)$ is then extracted

from the data by fitting a quadratic function in the displacement $\delta\phi$ to the FOTOC (Fig. 8-5b). We notice that the fitted quadratic curve is slightly shifted from $\delta\phi = 0$, and has slightly reduced peak fidelity. The shift is likely due to a small difference between the assumed and the real Larmor frequencies between the spin states, while the reduction from unit peak fidelity is due to the imperfect time reversal associated with residual light-atom entanglement. The small imperfections do not reduce the metrological gain significantly.

Figure 8-6 summarizes our findings regarding the close relation between quantum scrambling and time-reversal quantum metrology: The antisqueezing ξ_+^2, metrological gain $\mathcal{G} := G^2/N^2$, and OTOC $\mathcal{I}$ all agree with each other and scale exponentially with application time t of the LMG Hamiltonian for $t \lesssim 0.8(S\chi)^{-1}$. The exponential fit yields a Lyapunov exponent $\lambda_Q/(S\chi) = 1.01 \pm 0.03$, in excellent agreement with the theoretical expectation $\lambda_Q/(S\chi) = 1$.

Our experiments demonstrate a CQED realization of the critically tuned ($\Omega = S\chi$) LMG model with an exponential evolution in phase space. Besides, we also point out and experimentally verify that time reversal protocols represent a powerful experimental tool giving access not only to metrological gain beyond the SQL [66, 35, 8], but also enabling the measurement of quantum information scrambling in large many-body systems. This generalizes the possibilities of using quantum information science to enhance quantum metrology [140]. Furthermore, we observe exponential growth of both the OTOC and the metrological gain for the LMG model, thereby experimentally verifying the intrinsic relation between these two concepts from different subfields of quantum science. The demonstrated methods to reverse time may enable the experimental investigation of complex many-body quantum systems where the information spreads exponentially fast within many degrees of freedom, relevant for the simulation of black holes and quantum gravity models in controlled table-top experiments [206]. In addition, we envisage that time-reversal protocols will readily render many fast-scrambling Hamiltonians useful for robust and fast quantum-enhanced metrology.

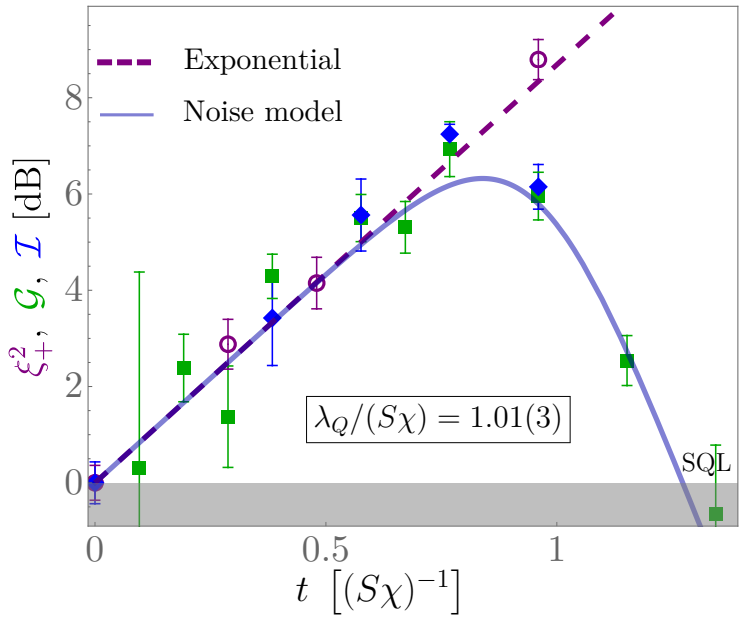


Figure 8-6: **Comparison between quantum information and quantum metrology parameters for the LMG model.** The red open circles, solid green squares, and solid blue diamonds represent the antisqueezing, metrological gain, and OTOC, respectively. All quantities increase initially exponentially with time with a fitted Lyapunov exponent $\lambda_Q = 1.01(3)S\chi$ that agrees well with the theoretical prediction $\lambda_Q = S\chi$. The OTOC errorbars are obtained by using the bootstrapping method [80]. For longer times $t \gtrsim (S\chi)^{-1}$, the metrological gain and OTOC decrease due to decoherence caused by light-atom entanglement, as is well captured by the theoretical model (solid blue line).

Chapter 9

One Small Step For the Machine, One Big Step For the System

9.1 Overview of the Ongoing Upgrading

9.1.1 Fast Rabi Oscillation

The original Rabi drive on the ground state manifold is based on the analog output of a 10kHz voltage signal which drives a MOSFET to generate high AC current and corresponding magnetic field. However, due to the low magnetic dipole moment of the nuclear spin structure, the Rabi frequency we could achieve via this method is very limited. Also, as explained in [24], the power to drive the coil is independent of the windings N. In the original setting, our large-capacitor & MOSFET setup outputs the largest power with a single turn, which produces a mere 220Hz of Rabi frequency.

Audio Amplifier

We have also looked into larger power supplies and found that the audio amplifier would be a reasonable match. And since the audio amplifier has a different maximum output impedance, with more turns of coil that match the audio amplifier's ideal working impedance, we, in principle, can obtain an infinitely long Rabi drive without

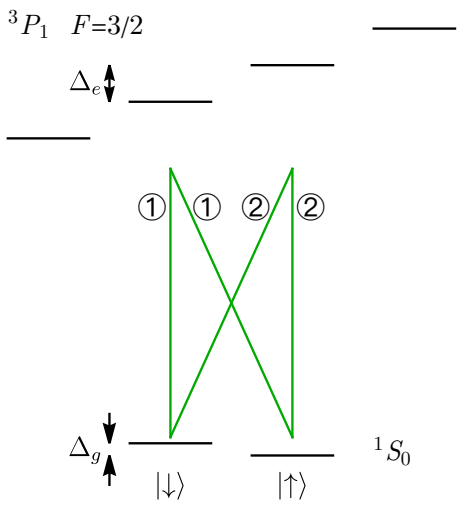


Figure 9-1: Related Yb-171 energy levels and the driving fields. Replicated from [98].

worrying about the capacitor's discharge, and possibly with a larger Rabi frequency.

Optical Rabi Rotation

As motivated by the high fidelity and fast speed of the single-qubit gate in the ytterbium tweezer array system [98], we would also like to achieve spin manipulation using the optical method, which is sending the linear polarized beam transversely such that both ${}^{(\sigma^+ + \sigma^-)}/_{\sqrt{2}}$ and π polarization exists. By making the light far detuned, the two-photon transitions (1), and (2), as in Fig. 9-1, add together to drive the transition between $|\updownarrow\rangle$. Though such a transition is off-resonance due to the detuning generated by the bias field, once the two-photon Rabi frequency is much larger than the two-photon detuning Δ_g, effectively, one can neglect the small detuning and still assume a resonant driving in the ground state.

However, with the same setting as [98], we observe almost zero Rabi frequency, leaving the system only exhibiting pure dephasing due to the incoherent scattering with the transverse drive, no matter how we choose the ratio between π-polarization and ${}^{(\sigma^+ + \sigma^-)}/_{\sqrt{2}}$ polarization, as in Fig. 9-2.

This observation actually makes sense. For simplicity, we can neglect all the Zeeman splittings, and redefine the quantization axis to be along the direction of the transverse beam, say x-axis. The linear-polarized light provides zero vector light

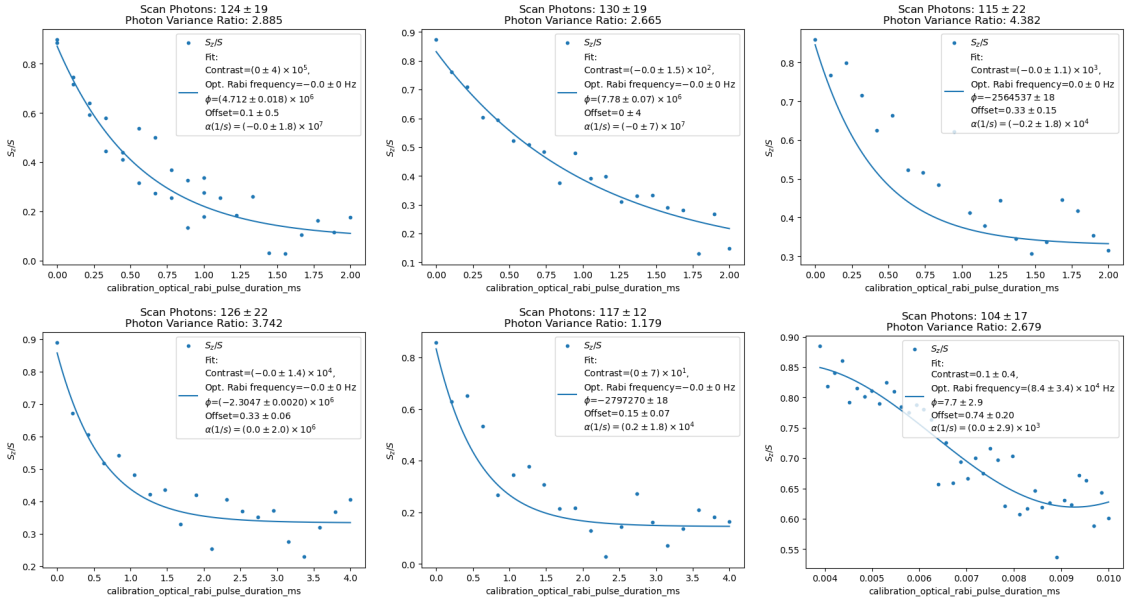


Figure 9-2: Top row: $\theta = 10°, 30°, 40°$, and bottom row: $\theta = 50°, 60°, 60°$, where the last one zoomed in time axis. $\theta = 60°$ is the closest to the paper setup [98].

shift, and thus no $\propto \hat{S}_x$ term would be generated. Such a term only comes from the vector polarizability, which intrinsically comes from the different Clebsch-Gordan coefficients.

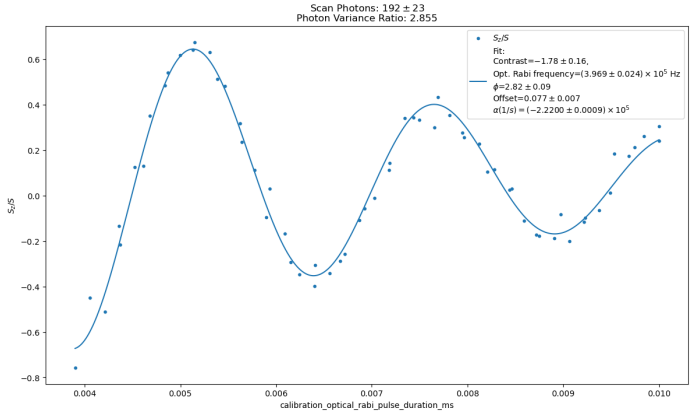


Figure 9-3: Optical Rabi oscillations with 1.2 mW power (supposedly) and 400kHz Optical Rabi Frequency using circularly polarized light.

With the correct circular polarization, we observed fast Rabi oscillation of more than $2\pi \times 400$kHz with only about 1mW of 556nm light as in Fig. 9-3. We can further increase the frequency by going to a higher power, but the room is very limited at this moment. Though in the meantime, we have ordered a completely new 556nm

laser from Precilasers, which outputs more than 1.5W (at least 50 times larger). We will come back to this idea once we have a much larger budget in terms of power.

Also, as we can observe, there are currently problems with the decreasing of the contrast. This is largely due to (1) the inhomogeneity of the laser beam on the atoms, and (2) incoherent scattering. For (1), with the higher power, we can afford to shape the beam wider to obtain a more homogeneous Rabi coupling to the atoms. For (2), the incoherent scattering ratio decreases with the detuning, and with the higher power, we are also allowed to detune the laser frequency further and increase the power since the two-photon process's Rabi-dephasing ratio is irrelevant to the power itself.

9.1.2 Belt Lattice

The belt lattice refers to two counterpropagating light fields with nuance in frequencies. Thus, the positions of the antinodes are actually moving in real-time. When this lattice serves as the optical trapping lattice for cold atoms, as in our 759nm laser, the atoms actually move along with the antinodes.

With the CAD For Precision Optics (C4PO) techniques (see Appendix B), we have built two double-pass AOM boards to control the two beams' frequencies individually. The alignment is first to align one of the beams such that it overlaps with the green MOT's fluorescence, then on the other side, we use a fiber coupler to collect, and then the two light modes should overlap perfectly.

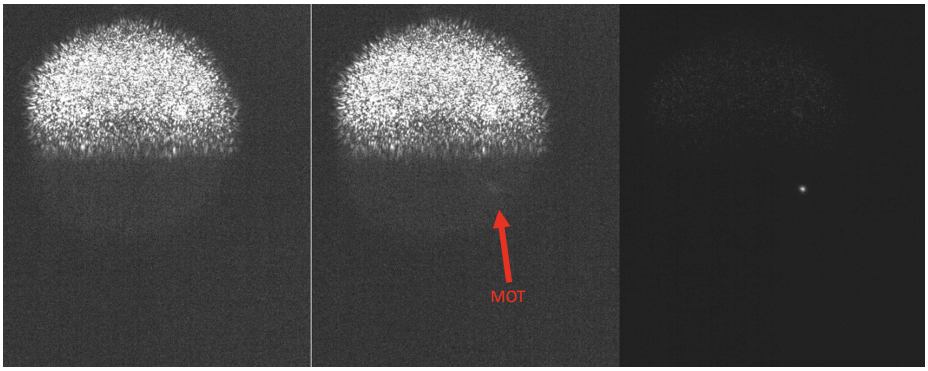


Figure 9-4: Locating the position of the MOT and overlapping it with the transverse lattice. Figure adopted from [209].

We first have to align the transverse lattice along the position of the atoms. This procedure is similar to the case of aligning the imaging beam of the 399nm laser, as described in Sec. 2.2.1. Instead of using the Andor camera, we set up the Thorlabs camera to collect the fluorescence light for the 556nm MOT from the side. We identify the MOT position based on the strong scattering of the substrate scattering, as in Fig. 9-4. Then we add 90dB ND filter to make a 10^{-9}W beam on $\pi(10\mu\text{m})^2$ area, giving 0.3mW/cm^2 such that camera is not burned. Drag the ThorCam such that the new position (shifted by the filter) overlaps with the original region.

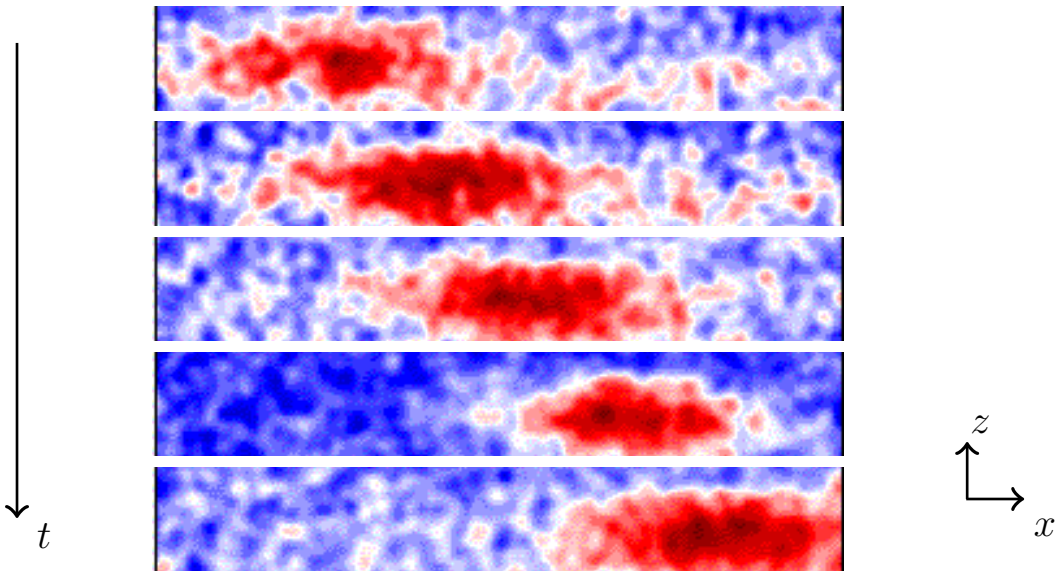


Figure 9-5: Atoms are moving with the belt lattice's transportation.

Then we use the imaging system in Sec. 2.2.1 to further optimize this alignment to make sure that the transverse trap's waist is overlapping with the cavity trap. We first image the position of the cavity trap of atoms, then image the position of atoms directly transferred to the transverse trap while keeping the cavity out of the lock. Since each camera (Andor and Thorlabs) only have information about a 2D plane, we have to iterate the procedure a few times to ensure the overlapping in both directions. Then, we fiber couple the other side to fiber such that we can optimize the mode overlap, and finally, replace the input and the output with a C4PO plate (see Appendix. B).

Recently, we have just demonstrated that the belt lattice technique works, as in Fig. 9-5.

9.1.3 Incoherent Pump to the Clock State

As one can see, it is really hard to get a perfect clock laser, which makes access to the great clock state limited unless one wants to invest a lot in the clock laser system, like what we are doing. This might not be a worthy investment if the interest is not specific to clock-related physics, such as quantum computing .

There is, on the other hand, another approach to get atoms into the clock state: via the incoherent pumping through the $^1S_0 \to {}^3P_1 \to {}^3D_1 \rightsquigarrow {}^3P_0$ process, where one only needs a 1539.15nm laser and the rest would be from a fast (310kHz) spontaneous decay. Similarly, one can repump the atom back to $^3P_0 \to {}^3D_1 \rightsquigarrow {}^3P_1 \rightsquigarrow {}^1S_0$, see Fig. 9-8.

We successfully see the atom number in the 399nm blue MOT can be significantly suppressed by turning on both the 556nm green laser and the 1539nm infrared laser. While loaded into the magic wavelength optical lattice at 759nm, we can use the same way to hide atoms in the clock state and bring them back via the other infrared laser at 1389nm.

9.2 Potential Fun Physics With the Upgraded System

These upgrading infrastructures can provide much potential fun physics to further explore. Here I will name a few.

9.2.1 Quantum Erasure With a Faster Rabi Drive

In our CQED system, the largest energy scale in the rotating-wave approximation is the cavity and atomic decay at hundreds of kHz. However, once we have a drive

that is stronger than these decays, the system will enter a new regime that is barely discussed.

A naïve idea is the erasure experiment to reduce the atom-light entanglement while keeping the residual atom-atom interaction. The idea is very similar to that for dynamical decoupling [228], namely: within the lifetime of the cavity, we apply a fixed probe light input to the cavity field while pulsing the external Rabi drive to apply many π-pulses. The π pulses make $\hat{S}_z \to -\hat{S}_z$ which preserves the Hamiltonian $\hat{S}_z^2$, while the intracavity photon carries information about an average of $\hat{N}_\uparrow$ and $\hat{N}_\downarrow$, which equals $S = N/2$ and thus does not cause the collective dephasing as in Eq. (3.49). By removing such a term, we can go closer to the vacuum Rabi peak and, thus, less individual dephasing from the incoherent scattering. This would allow a much larger metrological gain in the existing setup.

9.2.2 Exploring the Quantum Few-body Chaotic System

With the belt lattice technique as well as multiple transverse lattices, we can first load one ensemble of atoms into the intersection, then move out by the belt lattice while moving in another ensemble. Also, we can just set up another very close belt lattice which is off by $\sim 50\mu$m along the cavity axis direction, and move two (arrays of) ensembles together such that we can generate interaction within each ensemble or between the two ensembles. This also forms a network of clocks which is discussed in [34].

Assume we have the ability to move two atom ensembles in and out of the cavity mode without adding additional decoherence. Then we can Floquet engineer the system using $\hat{H}_0 = \chi(\hat{S}_{z,(1)} + \hat{S}_{z,(1)})^2, \hat{H}_1 = \chi\hat{S}_{z,(1)}^2, \hat{H}_2 = \chi\hat{S}_{z,(2)}^2, \hat{H}_h = h(\hat{S}_{x,(1)} + \hat{S}_{x,(2)})$, where $\hat{S}_{\alpha,(1,2)}$ are the collective spin operators for each ensemble. Then one can engineer a chaotic quantum Hamiltonian [149]:

$$\hat{H} = \chi\hat{S}_{z,(1)}\hat{S}_{z,(2)} + h(\hat{S}_{x,(1)} + \hat{S}_{x,(2)}). \tag{9.1}$$

We can prepare initial states and evolve under this Hamiltonian and measure

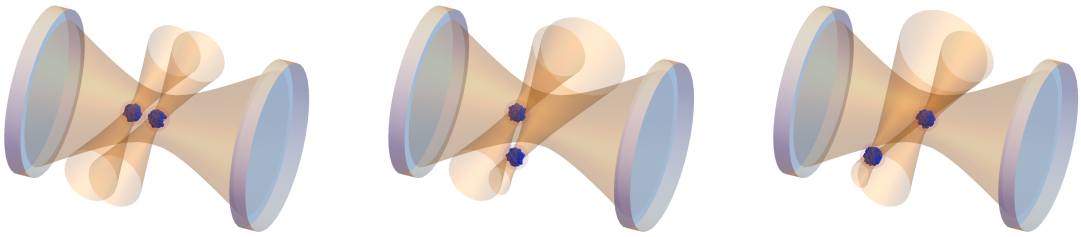


Figure 9-6: Hamiltonian from left to right: $\hat{H}_0 = \chi(\hat{S}_{z,(1)}+\hat{S}_{z,(1)})^2, \hat{H}_1 = \chi\hat{S}^2_{z,(1)}, \hat{H}_2 = \chi\hat{S}^2_{z,(2)}$

whether the correlation hole exists due to the repulsion of the quantum energy levels [227].

One way to measure the correlation hole is through the tomography method used in Chap. 8, which was developed in [202]. However, it will require tons of measurements and makes the detection unreachable. By giving the initial states with additional randomness, the measurement can converge faster, and maybe we would be able to observe some features.

9.2.3 Clock State CQED

By making the cavity resonance with the clock transition, we can directly lock the laser to the magnetic-field insensitive clock transition. Using the four-level generation of (3.8):

$$\mathcal{E}_c^{\mathrm{FL}} = \frac{\mathcal{F}}{\pi}\frac{it_1\mathcal{E}_{\mathrm{in}}}{1+N_\uparrow\eta_\uparrow\mathcal{L}_a(x_a)+N_\downarrow\eta_\downarrow\mathcal{L}_a(x_a+b)-i(x_c+N_\uparrow\eta_\uparrow\mathcal{L}_d(x_a)+N_\downarrow\eta_\downarrow\mathcal{L}_d(x_a+b))} \tag{9.2}$$

Here we assume a practical condition of $N_\uparrow = N_\downarrow = 200$ and $\eta_\uparrow = \eta_\downarrow = 5$, and a Zeeman splitting between the two clock transition is $2\pi \times 5$kHz which is subject to fluctuation. Then we observe two narrow dips under the wide cavity background resonance peak in the spectrum, as in Fig. 9-7. The width is roughly $w = (N_\updownarrow\eta)\Gamma_{\mathrm{clock}}/2$,

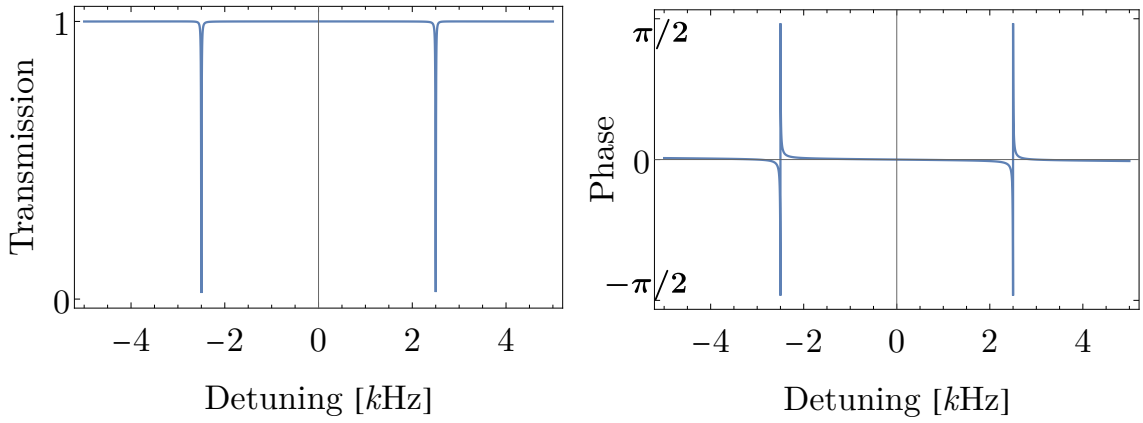


Figure 9-7: The cavity field's amplitude and phase for the symmetric clock situation.

where Γ_{clock} is the clock transition is natural linewidth which is $2\pi \times 7\text{mHz}$. In the condition, the width is $w = 2\pi \times 3.5\text{Hz}$.

The locking to this feature is simply by sending a four-point probe, at the four slopes of the two dips. Then one can estimate the two dips' positions and then the center of them, which is magnetic-field insensitive. The difference between the center and the laser's reference frequency can then be feedback to the laser.

9.2.4 Degenerate Fermi Gas with CQED

For clock operation, cooling is essential as atoms in different vibrational modes have different frequency responses to the clock light. That is especially correct for the low PSD case.

When the PSD increases to near unity for Fermions like ytterbium-171, the quantum degeneracy kicks in, and cooling all atoms to the vibrational ground state becomes increasingly hard. PSD reaching half seems to be an optical condition for clocks.

However, the quantum degenerate Fermi gas also has much physics yet to be investigated.

Improved Raman-sideband Cooling

Though the Raman cooling to BEC is achieved in several elements like Rb [90] and Cs [211], this has not yet been demonstrated in Fermions. For our system, an important factor in improving is to lower the density of states to let the Raman beam easily distinguish between energy levels. The way to achieve such a requirement is to have a 3D optical lattice. Then, by adding one more cooling path, we can perform a Raman sideband cooling in all three directions.

With the degenerate Fermi gas, we can also investigate some ground-state properties under the cavity Hamiltonian. Without the cavity, the band insulator state is the ground state since ytterbium-171 is spin-1/2. The defect of the band insulator introduces the possibility of quantum fluctuation, and the cavity field will cause a long-range interaction of these defects. Will there then be a "remote superposition" state which is topologically highly nontrivial?

Incoherent Pump Clock-state Degenerate Gas

We can also benefit from the incoherent pumping to the clock state process, i.e., ${}^1S_0 \to {}^3P_1 \to {}^3D_1 \rightsquigarrow {}^3P_0$. Now we rely on the long T_1 time of the clock state. A related discussion can be found in [214], but in words, this really uses the fact that the atoms in the ${}^3D_1$ should find a state to decay to as they cannot stay there forever. Since the ${}^3P_0$ state is metastable and also trapped by the 759nm optical lattice, the phase-space density will continuously increase. Meanwhile, the atoms will continuously be loaded into the MOT and then pumped to ${}^3D_1$, and thus the phase-space density will keep increasing, as illustrated in Fig. 9-8.

Competing Between Pauli-blocking and Cavity Enhancement

It could be interesting to see superradiance with degenerate Fermi gas [172, 29]. Some pioneering experiments are already done in Jean-Philippe Brantut's group, and a review paper [147] summarizes the current status of it.

One important question is whether the superradiance would compete with the

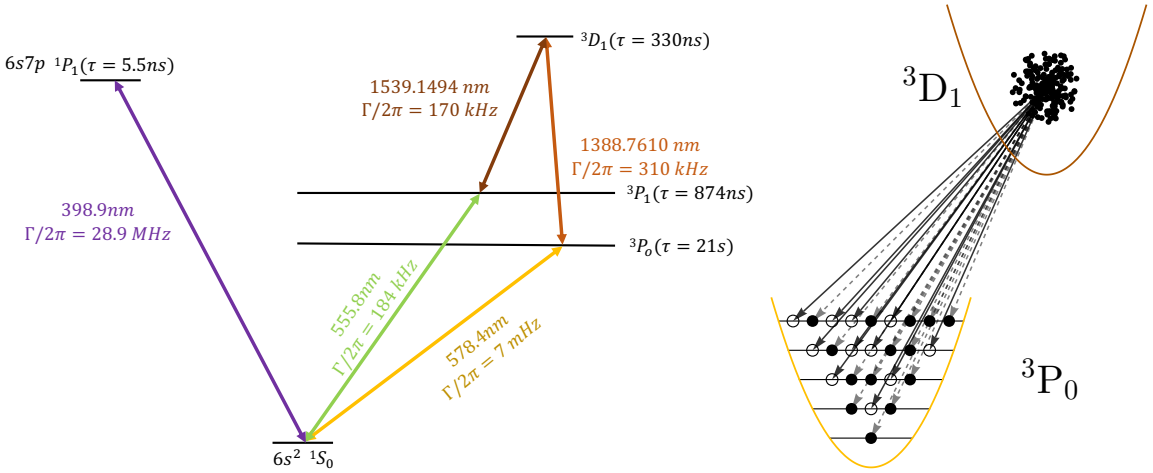


Figure 9-8: Left: Extended energy level of ytterbium-171 atom. Right: Generation of degenerate Fermi gas by pumping to the dark metastable $^3P_0$ clock state.

Pauli-blocking [42, 141, 194] under the presence of the optical cavity. If one probes the atom from the side, the emission into the cavity is enhanced by the Purcell effect but is reduced by the Pauli-blocking. This requires, on the other hand, a very large Fermi momentum to be at the momentum difference between the probing beam and the cavity light. Will there be a phase transition when the PSD increases? Or will there be other effects from an incommensurate lattice? These questions would be really interesting to think about.

9.3 Conclusions and Directions for the Future

In this thesis, I have described our Yb-171 CQED setup and the results for the past 6 years. As the title suggests, I have been exploring novel quantum physics using this setup during this period. The novelty can be understood by two means: to study the novel problem inside the system, as well as to use the system to build novel problems.

For the first part, I believe I can convince the audience that the Ramsey-based squeezing clock is, in principle, able to provide a significant step towards many fabulous quantities. Clock-based fundamental research, such as investigating the Lorentz symmetry violation [193], dark matter detection [93, 104], etc., could all benefit from our progress. With the new Menlo laser, we are not only on track to achieving a state-

of-the-art atomic clock but by integrating our SATIN protocol, we can also achieve a record high level of precision with larger bandwidth than ever before [34].

On the other hand, the path towards novel phenomena out of the CQED system is also clear. Starting with the unstable trajectory in the quantum many-body system, we pave a clear path to link quantum metrology and quantum information science in the context of exponential quantum dynamics and the Lyapunov exponent. The generalization to a real quantum chaotic system is well within reach.

For the future, as discussed above, many ongoing projects are promising with anticipated outcomes. Although the directions may bifurcate at some point, I indeed foresee the prosperity in our Ybclock lab.

Appendix A

Numerical Methods

The CQED system features a large symmetry which in turn makes it possible for an efficient study of the behaviors of the many-particle system using numerical methods. Here we introduce two different methods we used: a full-quantum version heavily relies on the symmetry, and a semi-classical version which also called (second-order) truncated Wigner approximation that simulates up to the second-order moments of the system.

A.1 Full Quantum Numerics

As discussed in Sec. 3.2.1, for the majority of our experiments, the Hilbert space is limited to the $(N+1)$-dimension symmetric subspace, i.e., $\langle \hat{\boldsymbol{S}}^2 \rangle = S(S+1)$. We choose to span the subspace using the Dicke states of $\hat{S}_z$ direction: $|S, S_z\rangle$.

In this basis, the operator $\hat{S}_z$ has a natural diagonal form: $\mathrm{diag}(\hat{S}_z) = [S, S-1, \cdots, -S+1, -S]$. Besides, we also have the relations of the spin-raising and lowering operators

$$\hat{S}_\pm |s, m_s\rangle = \sqrt{s(s+1) - m_s(m_s \pm 1)}\, |s, m_s \pm 1\rangle\,, \tag{A.1}$$

where $\hbar = 1$ is used. Then using

$$\hat{S}_x = \frac{\hat{S}_+ + \hat{S}_-}{2}, \quad \hat{S}_y = \frac{\hat{S}_+ - \hat{S}_-}{2i}$$

we can construct $\hat{S}_x, \hat{S}_y$ operators.

A.1.1 Unitary Evolution

The whole unitary evolution could be calculated using the matrix defined above. In MATHEMATICA®, using `MatrixExp[-I H t].psi` can evolve the state easily.

A.1.2 Lindbladian and Master Equation

Besides the unitary evolution, the optical cavity also produces non-unitary effects discussed in Sec. 3.4. The two effects are (1) the collective dephasing due to the remaining entanglement between the collective spin state and the light emitted from the cavity, and (2) the individual dephasing due to the individual atom incoherently scattering cavity photon into free space photon. The latter one is overcome by moving atoms to the higher cooperativity region of our asymmetric cavity, while the former is inevitable due to the existence of the other transition. Nevertheless, if we assume a perfect Markovian process, then both effects can be described by the master equation using the Lindbladian. Even though some recent results suggest that certain Non-Markovian processes may appear [127], for our single-mode cavity, this effect is negligible.

The master equation is written as

$$\frac{\mathrm{d}\hat{\rho}}{\mathrm{d}t} = -i[\hat{H}, \hat{\rho}] + \gamma_C \mathcal{L}_C[\hat{\rho}] + \gamma_I \mathcal{L}_I[\hat{\rho}], \tag{A.2}$$

where $\hat{H} = \chi \hat{S}_z^2 + H_{\mathrm{RF}}, \mathcal{L}_C[\hat{\rho}] = \hat{S}_z \hat{\rho} \hat{S}_z - \frac{1}{2}\hat{S}_z^2 \hat{\rho} - \frac{1}{2}\rho \hat{S}_z^2$, and $\mathcal{L}_I[\hat{\rho}] = \sum_{k=1}^{N} \hat{\sigma}_z^k \hat{\rho} \hat{\sigma}_z^k - \hat{\rho}$. The individual dephasing will result in the evolution leak out of the symmetric subspace, and there is also an efficient numerical method for that case [208]. As we discussed earlier, the individual dephasing is reduced due to the high cooperativity

between the cavity field and the atomic state, and therefore we can only focus on the collective dephasing induced by the cavity field.

For small N, one can "vectorize" the density matrix such that the dynamics can be calculated using the same matrix exponential method in a $(N+1)^2$ dimension space. However, the calculation speed goes down as n^{-3} where $n = (N+1)^2$ which is not in favor of $N \sim \mathcal{O}(10^2)$ atom number which we typically use.

Instead, we use a 4^{th} order Runge-Kutta method as follows. Assume we have $\hat{\rho}(t)$, and we want to calculate $\hat{\rho}(t + \mathrm{d}t)$. We have

$$\hat{\rho}_1 = \hat{\rho}(t) + \frac{\mathrm{d}t}{2} \underbrace{\left(-i[\hat{H}, \hat{\rho}(t)] + \gamma_C \mathcal{L}_C[\hat{\rho}(t)]\right)}_{\Delta\hat{\rho}_1} \tag{A.3}$$

$$\hat{\rho}_2 = \hat{\rho}(t) + \frac{\mathrm{d}t}{2} \underbrace{\left(-i[\hat{H}, \hat{\rho}_1] + \gamma_C \mathcal{L}_C[\hat{\rho}_1]\right)}_{\Delta\hat{\rho}_2} \tag{A.4}$$

$$\hat{\rho}_3 = \hat{\rho}(t) + \mathrm{d}t \underbrace{\left(-i[\hat{H}, \hat{\rho}_2] + \gamma_C \mathcal{L}_C[\hat{\rho}_2]\right)}_{\Delta\hat{\rho}_3} \tag{A.5}$$

$$\hat{\rho}_4 = \hat{\rho}(t) + \mathrm{d}t \underbrace{\left(-i[\hat{H}, \hat{\rho}_3] + \gamma_C \mathcal{L}_C[\hat{\rho}_3]\right)}_{\Delta\hat{\rho}_4}, \tag{A.6}$$

then

$$\hat{\rho}(t + \mathrm{d}t) = \hat{\rho}(t) + \frac{1}{6}(\Delta\hat{\rho}_1 + 2\Delta\hat{\rho}_2 + 2\Delta\hat{\rho}_3 + \Delta\hat{\rho}_4)\mathrm{d}t + \mathcal{O}(\mathrm{d}t^4). \tag{A.7}$$

This is a $\mathcal{O}(N^4\chi t)$ method, significantly lower than the $\mathcal{O}(N^6)$ "vectorization" method for experimentally feasible $N\chi t$.

A.2 Truncated Wigner Approximation

The OAT Hamiltonian, though creating non-trivial entangled states, is very easy to understand using classical Gaussian description introduced in Sec. 3.4.5. Since to the lowest order it preserves the Gaussianity, we then wonder whether there are other numerical approximation based on such a property to accelerate the calculation.

In fact, there is a very well developed semi-classical method for this type of task called Truncated Wigner Approximation [175]. A detailed explanation specific for the spin system is developed as well [177]. The central concept is to sample the states using a classical distribution. In [177], the sample points for spin-1/2 is based on the four points $\boldsymbol{r}_{(0,0)} = (1,1,1), \boldsymbol{r}_{(0,1)} = (-1,-1,1), \boldsymbol{r}_{(1,0)} = (1,-1,-1), \boldsymbol{r}_{(1,1)} = (-1,1,-1)$ which form a tetrahedron. Call $\Gamma = \{(0,0),(0,1),(1,0),(1,1)\}$, then there is a valid density matrix for each of these points $\forall \alpha \in \Gamma$, $A_\alpha = \frac{1}{2}(\mathbb{I} + \boldsymbol{r}_\alpha \cdot \boldsymbol{\sigma})$, and then the single spin density matrix can be cast as a linear combination $\rho = \sum_{\alpha\in\Gamma} w_\alpha A_\alpha$. Then, the initial product state is described as

$$\rho_0 = \sum_{\alpha_1,\ldots,\alpha_N \in \Gamma} w_{\alpha_1} \cdots w_{\alpha_N} A_{\alpha_1} \otimes \cdots \otimes A_{\alpha_N}. \tag{A.8}$$

Under the time evolution, we have

$$\rho(t) = \sum_{\alpha_1,\ldots,\alpha_N \in \Gamma} w_{\alpha_1} \cdots w_{\alpha_N} \mathcal{A}^{\boldsymbol{\alpha}}_{1\cdots N}(t), \tag{A.9}$$

where the curly $\mathcal{A}$ operators are just the Heisenberg picture of evolved operator $\otimes A$ with the $\boldsymbol{\alpha} = \alpha_1 \cdots \alpha_N$ indicating the index of our basis. All curly operators are therefore a function of time t which are sometimes omitted, and we can take out the one and two-body terms by

$$\mathcal{A}^{\boldsymbol{\alpha}}_i = \mathrm{Tr}_{j\neq i} \mathcal{A}^{\boldsymbol{\alpha}}_{1\cdots N}, \quad \mathcal{A}^{\boldsymbol{\alpha}}_{ij} = \mathrm{Tr}_{k\neq i,j} \mathcal{A}^{\boldsymbol{\alpha}}_{1\cdots N} = \mathcal{A}^{\boldsymbol{\alpha}}_i \mathcal{A}^{\boldsymbol{\alpha}}_j + \mathcal{C}^{\boldsymbol{\alpha}}_{ij}.$$

These operators can be expanded in the Pauli basis

$$\mathcal{A}^{\boldsymbol{\alpha}}_i = \frac{1}{2}(\mathbb{I} + \boldsymbol{a}^{\boldsymbol{\alpha}}_i \cdot \boldsymbol{\sigma}_i), \quad \mathcal{C}^{\boldsymbol{\alpha}}_{ij} = \frac{1}{4} \boldsymbol{\sigma}_i \mathbf{c}^{\boldsymbol{\alpha}}_{ij} \boldsymbol{\sigma}_j.$$

Then, the evolution is pretty much self-contained if assuming that

$$\mathcal{A}^{\boldsymbol{\alpha}}_{ijk} = \mathrm{Tr}_{k\neq i,j,k} \mathcal{A}^{\boldsymbol{\alpha}}_{1\cdots N} \sim \mathcal{A}^{\boldsymbol{\alpha}}_i \mathcal{A}^{\boldsymbol{\alpha}}_j \mathcal{A}^{\boldsymbol{\alpha}}_k + \mathcal{A}^{\boldsymbol{\alpha}}_i \mathcal{C}^{\boldsymbol{\alpha}}_{jk} + \mathcal{A}^{\boldsymbol{\alpha}}_j \mathcal{C}^{\boldsymbol{\alpha}}_{ik} + \mathcal{A}^{\boldsymbol{\alpha}}_k \mathcal{C}^{\boldsymbol{\alpha}}_{ij} + \underbrace{\mathcal{C}^{\boldsymbol{\alpha}}_{ijk}}_{\to 0}. \tag{A.10}$$

Here I directly quote the steps to simulate the dynamics summarized in [177]:

1. Sample phase space points $\boldsymbol{\alpha}$ from the probability distribution $w_{\alpha_1}\cdots w_{\alpha_N} = 2^{-N}\,\mathrm{Tr}\left[\rho_0 \mathcal{A}^{\boldsymbol{\alpha}}_{1\cdots N}(0)\right]$ of the initial state ρ_0, and get the sampling set $S_n = \{\boldsymbol{\alpha}\}$.

2. Compute the corresponding initial values of the Pauli expansion coefficients $\boldsymbol{a}_i^{\boldsymbol{\alpha}} = \mathrm{Tr}\left(\boldsymbol{\sigma}_i^{\boldsymbol{\alpha}} \mathcal{A}^{\boldsymbol{\alpha}}_{1\cdots N}\right)$. Mostly there are no correlations in the begining, $\mathbf{c}_{ij}(t=0) = 0$.

3. Solve the PDEs to get $\boldsymbol{a}_i^{\boldsymbol{\alpha}}(t)$ and $\mathbf{c}_{ij}(t)$.

4. Obtain mean and correlation functions via

$$\langle \sigma_i^\mu \rangle = \sum_{\alpha\in\Gamma^N} w_{\alpha_1}\cdots w_{\alpha_N} a_i^\mu \approx \frac{1}{n}\sum_{\alpha\in S_n} a_i^\mu, \tag{A.11}$$

$$\left\langle \sigma_i^\mu \sigma_j^\nu \right\rangle = \sum_{\alpha\in\Gamma^N} w_{\alpha_1}\cdots w_{\alpha_N}\left(c_{ij}^{\mu\nu} + a_i^\mu a_j^\nu\right) \approx \frac{1}{n}\sum_{\boldsymbol{\alpha}\in S_n}\left(c_{ij}^{\mu\nu} + a_i^\mu a_j^\nu\right). \tag{A.12}$$

An example is for the pure OAT Hamiltonian

$$\hat{H} = \chi \hat{S}_z^2 = \chi \sum_{ij} \sigma_i^z \sigma_j^z, \tag{A.13}$$

and initial state is a CSS along x-direction, by calculating $\boldsymbol{a}_i^{\boldsymbol{\alpha}}(t)$ and $\mathbf{c}_{ij}(t)$, we calculate variance along x-direction (initially zero) for $N = 200$ and sampling size $n = 10000$. The result is shown in Fig. A-1, where the result agrees well with the analytical solution given in [203]:

$$\mathrm{var}(S_x) = \frac{1}{2}[q_1 + q_2] - q_0^2, \tag{A.14}$$

where

$$q_0 = \frac{n}{2}\cos^{N-1}(\chi t), q_1 = \frac{N(N+1)}{4}, q_2 = \frac{N(N-1)}{4}\cos^{N-2}(2\chi t)$$

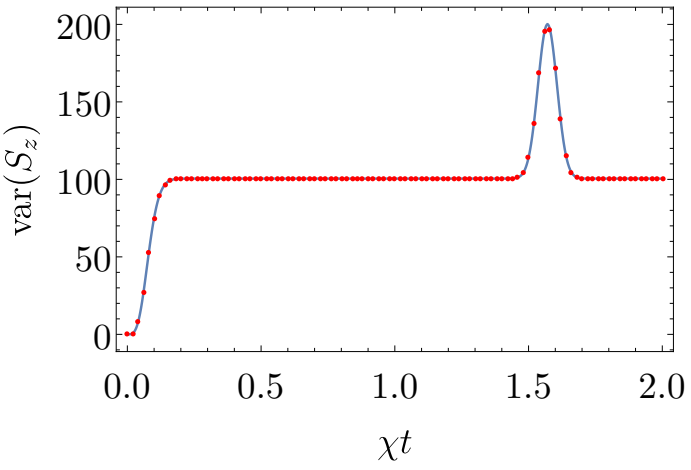


Figure A-1: Variance along x-direction for a CSS under the OAT Hamiltonian. The blue line is from the analytical formula (A.14), and the red dashed line is interpolated numerical results from the truncated Wigner approximation method.

Appendix B

C4PO-board

The original C4PO, or "CAD For Precision Optics", is developed by Issac Chuang's group based on `OpenSCAD`. The idea was to "program" where the optics should be, and output a 3D model for a board with necessary holes and other adapting structures to mount optical elements on.

Unfortunately, due to the slow rendering of the 3D model in `OpenSCAD`, we have to forfeit our goal to use it to replace our old optical setup completely. However, we can adapt the idea and take a step back to make a very well-designed board directly in `Solidworks`. The following are two examples of a conventional double-pass AOM and the green (556nm laser) splitting station described in Fig. 2-7(a). These plates are designed by our new generation graduate student Gustavo Velez and junior UROP student Nicolas Tanaka, respectively.

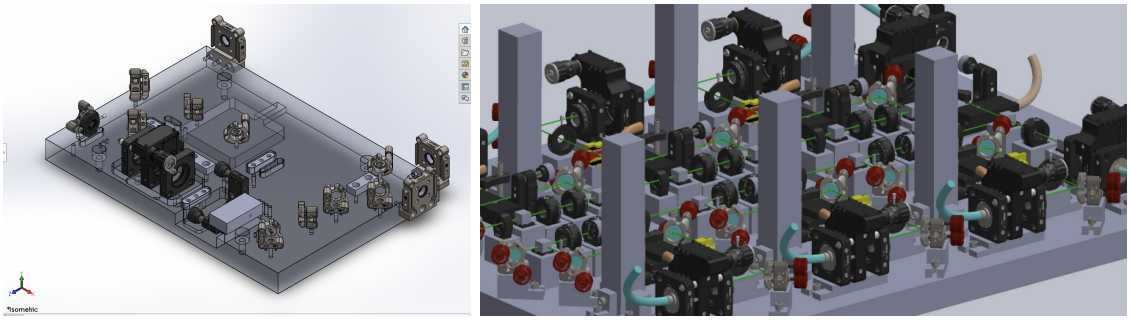


Figure B-1: Solidworks rendering of the C4PO. Left: double-pass AOM. Right: Green power splitting station.

Glossary

AOM Acoustic-Optic Modulator. 43, 48, 51, 52, 168

API Application Programming Interface. 44

BEC Bose-Einstein Condensation. 28, 38, 149, 174

C4PO CAD for Precision Optics. 11, 32, 168, 169, 183

CO Nonlinear Crossover Signal. 14, 49

CQED Cavity Quantum Electrodynamics. 11, 35, 61, 62, 64–66, 69, 75, 78, 83, 129, 170, 172, 173, 175–177

CSS Coherent Spin State. 15, 17, 21–28, 32, 63, 68, 73, 79, 80, 86, 87, 93, 101–103, 106, 122, 123, 125, 126, 133–138, 142–146, 149, 181, 182

DAVLL Dichroic Atomic Vapor Laser Lock. 46, 47

DDS Direct Digital Synthesis. 43, 52

ECDL External Cavity Diode Laser. 46, 54

EOM Electro-Optic Modulator. 14, 43, 48, 52–55

FPGA Field-Programmable Gate Array. 45, 52

FSR Free Spectral Range. 55

FWHM Full Width at Half Maximum. 98

HCL Hollow-Cathode Lamp. 14, 46–49

HWP Half Wave Plate. 53, 54

LO Local Oscillator. 24, 25, 130, 131, 135–139

MOSFET Metal-Oxide-Semiconductor Field-Effect Transistor. 43, 165

MOT Magneto-Optical Trap. 41–43, 51, 52

OAT One-Axis Twisting. 26, 27, 32, 75, 105, 119, 143, 144, 146, 147, 153, 179, 181, 182

OLC Optical Lattice Clock. 125, 129, 130, 138

OTOC Out-of-time Ordered Correlator. 153

PBS Polarizing Beamsplitters. 53, 54

PDH Pound-Drever-Hall Technique. 14, 53, 55, 57, 59

PSD Phase Space Density. 110, 112, 173, 175

QFI Quantum Fisher Information. 10, 16, 17, 36, 66, 76, 78–83, 86–88, 100–103, 118, 119, 123, 154

RAM Residual Amplitude Modulation. 55

SATIN Signal Amplification through Time-reversed InteractioN. 26–28, 142, 143, 145, 146, 148–150, 153–155, 176

SQL Standard Quantum Limit. 22, 25, 28, 118, 125–127, 129–131, 137, 138, 141, 142, 144, 146, 148–151

SSS Squeezed Spin State. 17, 21–25, 65, 74, 102, 103, 116, 122–126, 131–139, 141, 144

TA Tapered Amplifier. 57

UHV Ultra-High Vacuum. 42

ULE Ultra low expansion glass. 43, 52

VCO Voltage-Controlled Oscillator. 43, 52

Bibliography

[1] B. P. Abbott, R. Abbott, T. D. Abbott, M. R. Abernathy, F. Acernese, K. Ackley, C. Adams, T. Adams, P. Addesso, R. X. Adhikari, V. B. Adya, C. Affeldt, M. Agathos, K. Agatsuma, N. Aggarwal, O. D. Aguiar, L. Aiello, A. Ain, P. Ajith, B. Allen, A. Allocca, P. A. Altin, S. B. Anderson, W. G. Anderson, K. Arai, M. A. Arain, M. C. Araya, C. C. Arceneaux, J. S. Areeda, N. Arnaud, K. G. Arun, S. Ascenzi, G. Ashton, M. Ast, S. M. Aston, P. Astone, P. Aufmuth, C. Aulbert, S. Babak, P. Bacon, M. K. M. Bader, P. T. Baker, F. Baldaccini, G. Ballardin, S. W. Ballmer, J. C. Barayoga, S. E. Barclay, B. C. Barish, D. Barker, F. Barone, B. Barr, L. Barsotti, M. Barsuglia, D. Barta, J. Bartlett, M. A. Barton, I. Bartos, R. Bassiri, A. Basti, J. C. Batch, C. Baune, V. Bavigadda, M. Bazzan, B. Behnke, M. Bejger, C. Belczynski, A. S. Bell, C. J. Bell, B. K. Berger, J. Bergman, G. Bergmann, C. P. L. Berry, D. Bersanetti, A. Bertolini, J. Betzwieser, S. Bhagwat, R. Bhandare, I. A. Bilenko, G. Billingsley, J. Birch, R. Birney, O. Birnholtz, S. Biscans, A. Bisht, M. Bitossi, C. Biwer, M. A. Bizouard, J. K. Blackburn, C. D. Blair, D. G. Blair, R. M. Blair, S. Bloemen, O. Bock, T. P. Bodiya, M. Boer, G. Bogaert, C. Bogan, A. Bohe, P. Bojtos, C. Bond, F. Bondu, R. Bonnand, B. A. Boom, R. Bork, V. Boschi, S. Bose, Y. Bouffanais, A. Bozzi, C. Bradaschia, P. R. Brady, V. B. Braginsky, M. Branchesi, J. E. Brau, T. Briant, A. Brillet, M. Brinkmann, V. Brisson, P. Brockill, A. F. Brooks, D. A. Brown, D. D. Brown, N. M. Brown, C. C. Buchanan, A. Buikema, T. Bulik, H. J. Bulten, A. Buonanno, D. Buskulic, C. Buy, R. L. Byer, M. Cabero, L. Cadonati, G. Cagnoli, C. Cahillane, J. Calderón Bustillo, T. Callister, E. Calloni, J. B. Camp, K. C. Cannon, J. Cao, C. D. Capano, E. Capocasa, F. Carbognani, S. Caride, J. Casanueva Diaz, C. Casentini, S. Caudill, M. Cavaglià, F. Cavalier, R. Cavalieri, G. Cella, C. B. Cepeda, L. Cerboni Baiardi, G. Cerretani, E. Cesarini, R. Chakraborty, T. Chalermsongsak, S. J. Chamberlin, M. Chan, S. Chao, P. Charlton, E. Chassande-Mottin, H. Y. Chen, Y. Chen, C. Cheng, A. Chincarini, A. Chiummo, H. S. Cho, M. Cho, J. H. Chow, N. Christensen, Q. Chu, S. Chua, S. Chung, G. Ciani, F. Clara, J. A. Clark, F. Cleva, E. Coccia, P.-F. Cohadon, A. Colla, C. G. Collette, L. Cominsky, M. Constancio, A. Conte, L. Conti, D. Cook, T. R. Corbitt, N. Cornish, A. Corsi, S. Cortese, C. A. Costa, M. W. Coughlin, S. B. Coughlin, J.-P. Coulon, S. T. Countryman, P. Couvares, E. E. Cowan, D. M. Coward, M. J. Cowart, D. C. Coyne, R. Coyne, K. Craig, J. D. E. Creighton, T. D. Creighton, J. Cripe, S. G. Crowder, A. M. Cruise,

A. Cumming, L. Cunningham, E. Cuoco, T. Dal Canton, S. L. Danilishin, S. D'Antonio, K. Danzmann, N. S. Darman, C. F. Da Silva Costa, V. Dattilo, I. Dave, H. P. Daveloza, M. Davier, G. S. Davies, E. J. Daw, R. Day, S. De, D. DeBra, G. Debreczeni, J. Degallaix, M. De Laurentis, S. Deléglise, W. Del Pozzo, T. Denker, T. Dent, H. Dereli, V. Dergachev, R. T. DeRosa, R. De Rosa, R. DeSalvo, S. Dhurandhar, M. C. Díaz, L. Di Fiore, M. Di Giovanni, A. Di Lieto, S. Di Pace, I. Di Palma, A. Di Virgilio, G. Dojcinoski, V. Dolique, F. Donovan, K. L. Dooley, S. Doravari, R. Douglas, T. P. Downes, M. Drago, R. W. P. Drever, J. C. Driggers, Z. Du, M. Ducrot, S. E. Dwyer, T. B. Edo, M. C. Edwards, A. Effler, H.-B. Eggenstein, P. Ehrens, J. Eichholz, S. S. Eikenberry, W. Engels, R. C. Essick, T. Etzel, M. Evans, T. M. Evans, R. Everett, M. Factourovich, V. Fafone, H. Fair, S. Fairhurst, X. Fan, Q. Fang, S. Farinon, B. Farr, W. M. Farr, M. Favata, M. Fays, H. Fehrmann, M. M. Fejer, D. Feldbaum, I. Ferrante, E. C. Ferreira, F. Ferrini, F. Fidecaro, L. S. Finn, I. Fiori, D. Fiorucci, R. P. Fisher, R. Flaminio, M. Fletcher, H. Fong, J.-D. Fournier, S. Franco, S. Frasca, F. Frasconi, M. Frede, Z. Frei, A. Freise, R. Frey, V. Frey, T. T. Fricke, P. Fritschel, V. V. Frolov, P. Fulda, M. Fyffe, H. A. G. Gabbard, J. R. Gair, L. Gammaitoni, S. G. Gaonkar, F. Garufi, A. Gatto, G. Gaur, N. Gehrels, G. Gemme, B. Gendre, E. Genin, A. Gennai, J. George, L. Gergely, V. Germain, Abhirup Ghosh, Archisman Ghosh, S. Ghosh, J. A. Giaime, K. D. Giardina, A. Giazotto, K. Gill, A. Glaefke, J. R. Gleason, E. Goetz, R. Goetz, L. Gondan, G. González, J. M. Gonzalez Castro, A. Gopakumar, N. A. Gordon, M. L. Gorodetsky, S. E. Gossan, M. Gosselin, R. Gouaty, C. Graef, P. B. Graff, M. Granata, A. Grant, S. Gras, C. Gray, G. Greco, A. C. Green, R. J. S. Greenhalgh, P. Groot, H. Grote, S. Grunewald, G. M. Guidi, X. Guo, A. Gupta, M. K. Gupta, K. E. Gushwa, E. K. Gustafson, R. Gustafson, J. J. Hacker, B. R. Hall, E. D. Hall, G. Hammond, M. Haney, M. M. Hanke, J. Hanks, C. Hanna, M. D. Hannam, J. Hanson, T. Hardwick, J. Harms, G. M. Harry, I. W. Harry, M. J. Hart, M. T. Hartman, C.-J. Haster, K. Haughian, J. Healy, J. Heefner, A. Heidmann, M. C. Heintze, G. Heinzel, H. Heitmann, P. Hello, G. Hemming, M. Hendry, I. S. Heng, J. Hennig, A. W. Heptonstall, M. Heurs, S. Hild, D. Hoak, K. A. Hodge, D. Hofman, S. E. Hollitt, K. Holt, D. E. Holz, P. Hopkins, D. J. Hosken, J. Hough, E. A. Houston, E. J. Howell, Y. M. Hu, S. Huang, E. A. Huerta, D. Huet, B. Hughey, S. Husa, S. H. Huttner, T. Huynh-Dinh, A. Idrisy, N. Indik, D. R. Ingram, R. Inta, H. N. Isa, J.-M. Isac, M. Isi, G. Islas, T. Isogai, B. R. Iyer, K. Izumi, M. B. Jacobson, T. Jacqmin, H. Jang, K. Jani, P. Jaranowski, S. Jawahar, F. Jiménez-Forteza, W. W. Johnson, N. K. Johnson-McDaniel, D. I. Jones, R. Jones, R. J. G. Jonker, L. Ju, K. Haris, C. V. Kalaghatgi, V. Kalogera, S. Kandhasamy, G. Kang, J. B. Kanner, S. Karki, M. Kasprzack, E. Katsavounidis, W. Katzman, S. Kaufer, T. Kaur, K. Kawabe, F. Kawazoe, F. Kéfélian, M. S. Kehl, D. Keitel, D. B. Kelley, W. Kells, R. Kennedy, D. G. Keppel, J. S. Key, A. Khalaidovski, F. Y. Khalili, I. Khan, S. Khan, Z. Khan, E. A. Khazanov, N. Kijbunchoo, C. Kim, J. Kim, K. Kim, Nam-Gyu Kim, Namjun Kim, Y.-M. Kim, E. J. King, P. J. King, D. L. Kinzel, J. S. Kissel, L. Kleybolte, S. Klimenko, S. M. Koehlenbeck,

K. Kokeyama, S. Koley, V. Kondrashov, A. Kontos, S. Koranda, M. Korobko, W. Z. Korth, I. Kowalska, D. B. Kozak, V. Kringel, B. Krishnan, A. Królak, C. Krueger, G. Kuehn, P. Kumar, R. Kumar, L. Kuo, A. Kutynia, P. Kwee, B. D. Lackey, M. Landry, J. Lange, B. Lantz, P. D. Lasky, A. Lazzarini, C. Lazzaro, P. Leaci, S. Leavey, E. O. Lebigot, C. H. Lee, H. K. Lee, H. M. Lee, K. Lee, A. Lenon, M. Leonardi, J. R. Leong, N. Leroy, N. Letendre, Y. Levin, B. M. Levine, T. G. F. Li, A. Libson, T. B. Littenberg, N. A. Lockerbie, J. Logue, A. L. Lombardi, L. T. London, J. E. Lord, M. Lorenzini, V. Loriette, M. Lormand, G. Losurdo, J. D. Lough, C. O. Lousto, G. Lovelace, H. Lück, A. P. Lundgren, J. Luo, R. Lynch, Y. Ma, T. MacDonald, B. Machenschalk, M. MacInnis, D. M. Macleod, F. Magaña Sandoval, R. M. Magee, M. Mageswaran, E. Majorana, I. Maksimovic, V. Malvezzi, N. Man, I. Mandel, V. Mandic, V. Mangano, G. L. Mansell, M. Manske, M. Mantovani, F. Marchesoni, F. Marion, S. Márka, Z. Márka, A. S. Markosyan, E. Maros, F. Martelli, L. Martellini, I. W. Martin, R. M. Martin, D. V. Martynov, J. N. Marx, K. Mason, A. Masserot, T. J. Massinger, M. Masso-Reid, F. Matichard, L. Matone, N. Mavalvala, N. Mazumder, G. Mazzolo, R. McCarthy, D. E. McClelland, S. McCormick, S. C. McGuire, G. McIntyre, J. McIver, D. J. McManus, S. T. McWilliams, D. Meacher, G. D. Meadors, J. Meidam, A. Melatos, G. Mendell, D. Mendoza-Gandara, R. A. Mercer, E. Merilh, M. Merzougui, S. Meshkov, C. Messenger, C. Messick, P. M. Meyers, F. Mezzani, H. Miao, C. Michel, H. Middleton, E. E. Mikhailov, L. Milano, J. Miller, M. Millhouse, Y. Minenkov, J. Ming, S. Mirshekari, C. Mishra, S. Mitra, V. P. Mitrofanov, G. Mitselmakher, R. Mittleman, A. Moggi, M. Mohan, S. R. P. Mohapatra, M. Montani, B. C. Moore, C. J. Moore, D. Moraru, G. Moreno, S. R. Morriss, K. Mossavi, B. Mours, C. M. Mow-Lowry, C. L. Mueller, G. Mueller, A. W. Muir, Arunava Mukherjee, D. Mukherjee, S. Mukherjee, N. Mukund, A. Mullavey, J. Munch, D. J. Murphy, P. G. Murray, A. Mytidis, I. Nardecchia, L. Naticchioni, R. K. Nayak, V. Necula, K. Nedkova, G. Nelemans, M. Neri, A. Neunzert, G. Newton, T. T. Nguyen, A. B. Nielsen, S. Nissanke, A. Nitz, F. Nocera, D. Nolting, M. E. N. Normandin, L. K. Nuttall, J. Oberling, E. Ochsner, J. O'Dell, E. Oelker, G. H. Ogin, J. J. Oh, S. H. Oh, F. Ohme, M. Oliver, P. Oppermann, Richard J. Oram, B. O'Reilly, R. O'Shaughnessy, C. D. Ott, D. J. Ottaway, R. S. Ottens, H. Overmier, B. J. Owen, A. Pai, S. A. Pai, J. R. Palamos, O. Palashov, C. Palomba, A. Pal-Singh, H. Pan, Y. Pan, C. Pankow, F. Pannarale, B. C. Pant, F. Paoletti, A. Paoli, M. A. Papa, H. R. Paris, W. Parker, D. Pascucci, A. Pasqualetti, R. Passaquieti, D. Passuello, B. Patricelli, Z. Patrick, B. L. Pearlstone, M. Pedraza, R. Pedurand, L. Pekowsky, A. Pele, S. Penn, A. Perreca, H. P. Pfeiffer, M. Phelps, O. Piccinni, M. Pichot, M. Pickenpack, F. Piergiovanni, V. Pierro, G. Pillant, L. Pinard, I. M. Pinto, M. Pitkin, J. H. Poeld, R. Poggiani, P. Popolizio, A. Post, J. Powell, J. Prasad, V. Predoi, S. S. Premachandra, T. Prestegard, L. R. Price, M. Prijatelj, M. Principe, S. Privitera, R. Prix, G. A. Prodi, L. Prokhorov, O. Puncken, M. Punturo, P. Puppo, M. Pürrer, H. Qi, J. Qin, V. Quetschke, E. A. Quintero, R. Quitzow-James, F. J. Raab, D. S. Rabeling, H. Radkins, P. Raffai, S. Raja, M. Rakhmanov, C. R. Ramet, P. Rapagnani,

V. Raymond, M. Razzano, V. Re, J. Read, C. M. Reed, T. Regimbau, L. Rei, S. Reid, D. H. Reitze, H. Rew, S. D. Reyes, F. Ricci, K. Riles, N. A. Robertson, R. Robie, F. Robinet, A. Rocchi, L. Rolland, J. G. Rollins, V. J. Roma, J. D. Romano, R. Romano, G. Romanov, J. H. Romie, D. Rosińska, S. Rowan, A. Rüdiger, P. Ruggi, K. Ryan, S. Sachdev, T. Sadecki, L. Sadeghian, L. Salconi, M. Saleem, F. Salemi, A. Samajdar, L. Sammut, L. M. Sampson, E. J. Sanchez, V. Sandberg, B. Sandeen, G. H. Sanders, J. R. Sanders, B. Sassolas, B. S. Sathyaprakash, P. R. Saulson, O. Sauter, R. L. Savage, A. Sawadsky, P. Schale, R. Schilling, J. Schmidt, P. Schmidt, R. Schnabel, R. M. S. Schofield, A. Schönbeck, E. Schreiber, D. Schuette, B. F. Schutz, J. Scott, S. M. Scott, D. Sellers, A. S. Sengupta, D. Sentenac, V. Sequino, A. Sergeev, G. Serna, Y. Setyawati, A. Sevigny, D. A. Shaddock, T. Shaffer, S. Shah, M. S. Shahriar, M. Shaltev, Z. Shao, B. Shapiro, P. Shawhan, A. Sheperd, D. H. Shoemaker, D. M. Shoemaker, K. Siellez, X. Siemens, D. Sigg, A. D. Silva, D. Simakov, A. Singer, L. P. Singer, A. Singh, R. Singh, A. Singhal, A. M. Sintes, B. J. J. Slagmolen, J. R. Smith, M. R. Smith, N. D. Smith, R. J. E. Smith, E. J. Son, B. Sorazu, F. Sorrentino, T. Souradeep, A. K. Srivastava, A. Staley, M. Steinke, J. Steinlechner, S. Steinlechner, D. Steinmeyer, B. C. Stephens, S. P. Stevenson, R. Stone, K. A. Strain, N. Straniero, G. Stratta, N. A. Strauss, S. Strigin, R. Sturani, A. L. Stuver, T. Z. Summerscales, L. Sun, P. J. Sutton, B. L. Swinkels, M. J. Szczepańczyk, M. Tacca, D. Talukder, D. B. Tanner, M. Tápai, S. P. Tarabrin, A. Taracchini, R. Taylor, T. Theeg, M. P. Thirugnanasambandam, E. G. Thomas, M. Thomas, P. Thomas, K. A. Thorne, K. S. Thorne, E. Thrane, S. Tiwari, V. Tiwari, K. V. Tokmakov, C. Tomlinson, M. Tonelli, C. V. Torres, C. I. Torrie, D. Töyrä, F. Travasso, G. Traylor, D. Trifirò, M. C. Tringali, L. Trozzo, M. Tse, M. Turconi, D. Tuyenbayev, D. Ugolini, C. S. Unnikrishnan, A. L. Urban, S. A. Usman, H. Vahlbruch, G. Vajente, G. Valdes, M. Vallisneri, N. van Bakel, M. van Beuzekom, J. F. J. van den Brand, C. Van Den Broeck, D. C. Vander-Hyde, L. van der Schaaf, J. V. van Heijningen, A. A. van Veggel, M. Vardaro, S. Vass, M. Vasúth, R. Vaulin, A. Vecchio, G. Vedovato, J. Veitch, P. J. Veitch, K. Venkateswara, D. Verkindt, F. Vetrano, A. Viceré, S. Vinciguerra, D. J. Vine, J.-Y. Vinet, S. Vitale, T. Vo, H. Vocca, C. Vorvick, D. Voss, W. D. Vousden, S. P. Vyatchanin, A. R. Wade, L. E. Wade, M. Wade, S. J. Waldman, M. Walker, L. Wallace, S. Walsh, G. Wang, H. Wang, M. Wang, X. Wang, Y. Wang, H. Ward, R. L. Ward, J. Warner, M. Was, B. Weaver, L.-W. Wei, M. Weinert, A. J. Weinstein, R. Weiss, T. Welborn, L. Wen, P. Weßels, T. Westphal, K. Wette, J. T. Whelan, S. E. Whitcomb, D. J. White, B. F. Whiting, K. Wiesner, C. Wilkinson, P. A. Willems, L. Williams, R. D. Williams, A. R. Williamson, J. L. Willis, B. Willke, M. H. Wimmer, L. Winkelmann, W. Winkler, C. C. Wipf, A. G. Wiseman, H. Wittel, G. Woan, J. Worden, J. L. Wright, G. Wu, J. Yablon, I. Yakushin, W. Yam, H. Yamamoto, C. C. Yancey, M. J. Yap, H. Yu, M. Yvert, A. Zadrożny, L. Zangrando, M. Zanolin, J.-P. Zendri, M. Zevin, F. Zhang, L. Zhang, M. Zhang, Y. Zhang, C. Zhao, M. Zhou, Z. Zhou, X. J. Zhu, M. E. Zucker, S. E. Zuraw, and J. Zweizig. Observation of gravitational waves from a binary black hole

merger. *Phys. Rev. Lett.*, 116:061102, Feb 2016.

[2] Ali Al-Masoudi, Sören Dörscher, Sebastian Häfner, Uwe Sterr, and Christian Lisdat. Noise and instability of an optical lattice clock. *Phys. Rev. A*, 92:063814, Dec 2015.

[3] P. M. Alsing, D. A. Cardimona, and H. J. Carmichael. Suppression of fluorescence in a lossless cavity. *Phys. Rev. A*, 45:1793–1803, Feb 1992.

[4] Jürgen Appel, Patrick Joachim Windpassinger, Daniel Oblak, U Busk Hoff, Niels Kjærgaard, and Eugene Simon Polzik. Mesoscopic atomic entanglement for precision measurements beyond the standard quantum limit. *Proc. Natl. Acad. Sci. U.S.A.*, 106(27):10960–10965, 2009.

[5] F. T. Arecchi, Eric Courtens, Robert Gilmore, and Harry Thomas. Atomic coherent states in quantum optics. *Phys. Rev. A*, 6:2211–2237, Dec 1972.

[6] Asimina Arvanitaki, Junwu Huang, and Ken Van Tilburg. Searching for dilaton dark matter with atomic clocks. *Phys. Rev. D*, 91:015015, Jan 2015.

[7] Han Bao, Junlei Duan, Shenchao Jin, Xingda Lu, Pengxiong Li, Weizhi Qu, Mingfeng Wang, Irina Novikova, Eugeniy E Mikhailov, Kai-Feng Zhao, et al. Spin squeezing of 10^{11} atoms by prediction and retrodiction measurements. *Nature*, 581(7807):159–163, 2020.

[8] Diego Barberena, Sean R. Muleady, John J. Bollinger, Robert J. Lewis-Swan, and Ana Maria Rey. Fast generation of spin squeezing via resonant spin-boson coupling, 2022.

[9] Giovanni Barontini, Leander Hohmann, Florian Haas, Jérôme Estève, and Jakob Reichel. Deterministic generation of multiparticle entanglement by quantum zeno dynamics. *Science*, 349(6254):1317–1321, 2015.

[10] Jacob L. Beckey, M. Cerezo, Akira Sone, and Patrick J. Coles. Variational quantum algorithm for estimating the quantum fisher information. *Phys. Rev. Research*, 4:013083, Feb 2022.

[11] Tarik Berrada, Sandrine van Frank, Robert Bücker, Thorsten Schumm, J-F Schaff, and Jörg Schmiedmayer. Integrated mach–zehnder interferometer for bose–einstein condensates. *Nat. Commun.*, 4:2077, 2013.

[12] Christopher James Billington. *State-dependent forces in cold quantum gases*. PhD thesis, Monash University, 2018.

[13] Kurt Binder. Finite size scaling analysis of ising model block distribution functions. *Zeitschrift für Physik B Condensed Matter*, 43(2):119–140, 1981.

[14] M. Bishof, X. Zhang, M. J. Martin, and Jun Ye. Optical spectrum analyzer with quantum-limited noise floor. *Phys. Rev. Lett.*, 111:093604, Aug 2013.

[15] Lev S Bishop, JM Chow, Jens Koch, AA Houck, MH Devoret, E Thuneberg, SM Girvin, and RJ Schoelkopf. Nonlinear response of the vacuum rabi resonance. *Nat. Phys.*, 5(2):105–109, 2009.

[16] S. Blatt, J. W. Thomsen, G. K. Campbell, A. D. Ludlow, M. D. Swallows, M. J. Martin, M. M. Boyd, and J. Ye. Rabi spectroscopy and excitation inhomogeneity in a one-dimensional optical lattice clock. *Phys. Rev. A*, 80:052703, Nov 2009.

[17] J. G. Bohnet, K. C. Cox, M. A. Norcia, J. M. Weiner, Z. Chen, and J. K. Thompson. Reduced spin measurement back-action for a phase sensitivity ten times beyond the standard quantum limit. *Nat. Photonics*, 8:731, July 2014.

[18] Justin G Bohnet, Brian C Sawyer, Joseph W Britton, Michael L Wall, Ana Maria Rey, Michael Foss-Feig, and John J Bollinger. Quantum spin dynamics and entanglement generation with hundreds of trapped ions. *Science*, 352(6291):1297–1301, 2016.

[19] Guillaume Bornet, Gabriel Emperauger, Cheng Chen, Bingtian Ye, Maxwell Block, Marcus Bintz, Jamie A. Boyd, Daniel Barredo, Tommaso Comparin, Fabio Mezzacapo, Tommaso Roscilde, Thierry Lahaye, Norman Y. Yao, and Antoine Browaeys. Scalable spin squeezing in a dipolar rydberg atom array, 2023.

[20] Tobias Bothwell, Dhruv Kedar, Eric Oelker, John M Robinson, Sarah L Bromley, Weston L Tew, Jun Ye, and Colin J Kennedy. Jila sri optical lattice clock with uncertainty of. *Metrologia*, 56(6):065004, 2019.

[21] Tobias Bothwell, Colin J Kennedy, Alexander Aeppli, Dhruv Kedar, John M Robinson, Eric Oelker, Alexander Staron, and Jun Ye. Resolving the gravitational redshift across a millimetre-scale atomic sample. *Nature*, 602(7897):420–424, 2022.

[22] Jochen Braumüller, Amir H Karamlou, Yariv Yanay, Bharath Kannan, David Kim, Morten Kjaergaard, Alexander Melville, Bethany M Niedzielski, Youngkyu Sung, Antti Vepsäläinen, et al. Probing quantum information propagation with out-of-time-ordered correlators. *Nature Physics*, 18(2):172–178, 2022.

[23] Samuel L. Braunstein and Carlton M. Caves. Statistical distance and the geometry of quantum states. *Phys. Rev. Lett.*, 72:3439–3443, May 1994.

[24] Boris Braverman. *Cavity Quantum Electrodynamics with Ensembles of Ytterbium-171*. Ph.D. thesis, Massachusetts Institute of Technology, 2018.

[25] Boris Braverman, Akio Kawasaki, Edwin Pedrozo-Peñafiel, Simone Colombo, Chi Shu, Zeyang Li, Enrique Mendez, Megan Yamoah, Leonardo Salvi, Daisuke Akamatsu, Yanhong Xiao, and Vladan Vuletić. Near-unitary spin squeezing in ^{171}Yb. *Phys. Rev. Lett.*, 122:223203, Jun 2019.

[26] Boris Braverman, Akio Kawasaki, and Vladan Vuletić. Impact of non-unitary spin squeezing on atomic clock performance. *New J. Phys.*, 20(10):103019, 2018.

[27] Sebastian C. Carrasco, Michael H. Goerz, Zeyang Li, Simone Colombo, Vladan Vuletić, and Vladimir S. Malinovsky. Extreme spin squeezing via optimized one-axis twisting and rotations. *Phys. Rev. Applied*, 17:064050, Jun 2022.

[28] Wenlan Chen, Jiazhong Hu, Yiheng Duan, Boris Braverman, Hao Zhang, and Vladan Vuletić. Carving complex many-atom entangled states by single-photon detection. *Phys. Rev. Lett.*, 115:250502, Dec 2015.

[29] Yu Chen, Zhenhua Yu, and Hui Zhai. Superradiance of degenerate fermi gases in a cavity. *Phys. Rev. Lett.*, 112:143004, Apr 2014.

[30] Zilong Chen, Justin G. Bohnet, Shannon R. Sankar, Jiayan Dai, and James K. Thompson. Conditional spin squeezing of a large ensemble via the vacuum rabi splitting. *Phys. Rev. Lett.*, 106:133601, Mar 2011.

[31] Zilong Chen, Justin G. Bohnet, Joshua M. Weiner, Kevin C. Cox, and James K. Thompson. Cavity-aided nondemolition measurements for atom counting and spin squeezing. *Phys. Rev. A*, 89:043837, Apr 2014.

[32] Logan W Clark, Nathan Schine, Claire Baum, Ningyuan Jia, and Jonathan Simon. Observation of laughlin states made of light. *Nature*, 582(7810):41–45, 2020.

[33] A. A. Clerk, M. H. Devoret, S. M. Girvin, Florian Marquardt, and R. J. Schoelkopf. Introduction to quantum noise, measurement, and amplification. *Rev. Mod. Phys.*, 82:1155–1208, Apr 2010.

[34] Simone Colombo, Edwin Pedrozo-Peñafiel, and Vladan Vuletić. Entanglement-enhanced optical atomic clocks. *Appl. Phys. Lett.*, 121(21):210502, 2022.

[35] Simone Colombo, Edwin Pedrozo-Peñafiel, Albert F. Adiyatullin, Zeyang Li, Enrique Mendez, Chi Shu, and Vladan Vuletić. Time-reversal-based quantum metrology with many-body entangled states. *Nat. Phys.*, 18(8):925–930, Aug 2022.

[36] Kristan L Corwin, Zheng-Tian Lu, Carter F Hand, Ryan J Epstein, and Carl E Wieman. Frequency-stabilized diode laser with the zeeman shift in an atomic vapor. *Applied Optics*, 37(15):3295–3298, 1998.

[37] Ian Counts, Joonseok Hur, Diana P. L. Aude Craik, Honggi Jeon, Calvin Leung, Julian C. Berengut, Amy Geddes, Akio Kawasaki, Wonho Jhe, and Vladan Vuletić. Evidence for nonlinear isotope shift in yb^+ search for new boson. *Phys. Rev. Lett.*, 125:123002, Sep 2020.

[38] Kevin C. Cox, Graham P. Greve, Joshua M. Weiner, and James K. Thompson. Deterministic squeezed states with collective measurements and feedback. *Phys. Rev. Lett.*, 116:093602, Mar 2016.

[39] Harald Cramér. A contribution to the theory of statistical estimation. *Scandinavian Actuarial Journal*, 1946(1):85–94, 1946.

[40] Emily Davis, Gregory Bentsen, and Monika Schleier-Smith. Approaching the heisenberg limit without single-particle detection. *Phys. Rev. Lett.*, 116:053601, Feb 2016.

[41] Emily J. Davis, Avikar Periwal, Eric S. Cooper, Gregory Bentsen, Simon J. Evered, Katherine Van Kirk, and Monika H. Schleier-Smith. Protecting spin coherence in a tunable Heisenberg model. *Phys. Rev. Lett.*, 125:060402, Aug 2020.

[42] Amita B Deb and Niels Kjærgaard. Observation of pauli blocking in light scattering from quantum degenerate fermions. *Science*, 374(6570):972–975, 2021.

[43] Rafal Demkowicz-Dobrzański, Marcin Jarzyna, Jan Kołodyński, and E. Wolf. Chapter four - quantum limits in optical interferometry. In *Progress in Optics*, volume 60, pages 345–435. Elsevier, January 2015.

[44] Rafał Demkowicz-Dobrzański, Jan Kołodyński, and Mădălin Guţă. The elusive Heisenberg limit in quantum-enhanced metrology. *Nat. Commun.*, 3(1063):1063, 2012.

[45] A. Derevianko and M. Pospelov. Hunting for topological dark matter with atomic clocks. *Nat. Phys.*, 10:933–936, 2014.

[46] Andrei Derevianko, Kurt Gibble, Leo Hollberg, Nathan R Newbury, Chris Oates, Marianna S Safronova, Laura C Sinclair, and Nan Yu. Fundamental physics with a state-of-the-art optical clock in space. *Quantum Science and Technology*, 7(4):044002, 2022.

[47] G John Dick. Local oscillator induced instabilities in trapped ion frequency standards. Technical report, CALIFORNIA INST OF TECH PASADENA JET PROPULSION LAB, 1987.

[48] R. H. Dicke. Coherence in spontaneous radiation processes. *Phys. Rev.*, 93:99–110, Jan 1954.

[49] Peter Domokos, Thomas Salzburger, and Helmut Ritsch. Dissipative motion of an atom with transverse coherent driving in a cavity with many degenerate modes. *Phys. Rev. A*, 66:043406, Oct 2002.

[50] Jonathan P. Dowling, G. S. Agarwal, and Wolfgang P. Schleich. Wigner distribution of a general angular-momentum state: Applications to a collection of two-level atoms. *Phys. Rev. A*, 49:4101–4109, May 1994.

[51] L.-M. Duan, A. Sørensen, J. I. Cirac, and P. Zoller. Squeezing and entanglement of atomic beams. *Phys. Rev. Lett.*, 85:3991–3994, Nov 2000.

[52] Yiheng Duan, Mahdi Hosseini, Kristin M. Beck, and Vladan Vuletić. Heralded interaction control between quantum systems. *Phys. Rev. Lett.*, 124:223602, Jun 2020.

[53] William J. Eckner, Nelson Darkwah Oppong, Alec Cao, Aaron W. Young, William R. Milner, John M. Robinson, Jun Ye, and Adam M. Kaufman. Realizing spin squeezing with rydberg interactions in a programmable optical clock, 2023.

[54] Andreas Elben, Steven T. Flammia, Hsin-Yuan Huang, Richard Kueng, John Preskill, Benoît Vermersch, and Peter Zoller. The randomized measurement toolbox, 2022.

[55] Thomas J Elliott, Gabriel Mazzucchi, Wojciech Kozlowski, Santiago F Caballero-Benitez, and Igor B Mekhov. Probing and manipulating fermionic and bosonic quantum gases with quantum light. *Atoms*, 3(3):392–406, 2015.

[56] Dominic V Else, Christopher Monroe, Chetan Nayak, and Norman Y Yao. Discrete time crystals. *Annual Review of Condensed Matter Physics*, 11:467–499, 2020.

[57] BM Escher, RL de Matos Filho, and Luiz Davidovich. General framework for estimating the ultimate precision limit in noisy quantum-enhanced metrology. *Nat. Phys.*, 7(5):406–411, 2011.

[58] N. L. Figueroa, J. C. Berengut, V. A. Dzuba, V. V. Flambaum, D. Budker, and D. Antypas. Precision determination of isotope shifts in ytterbium and implications for new physics. *Phys. Rev. Lett.*, 128:073001, Feb 2022.

[59] Ronald A Fisher. On the mathematical foundations of theoretical statistics. *Philosophical transactions of the Royal Society of London. Series A, containing papers of a mathematical or physical character*, 222(594-604):309–368, 1922.

[60] Florian Fröwis, Pavel Sekatski, and Wolfgang Dür. Detecting large quantum fisher information with finite measurement precision. *Physical review letters*, 116(9):090801, 2016.

[61] Florian Fröwis, Peter C Strassmann, Alexey Tiranov, Corentin Gut, Jonathan Lavoie, Nicolas Brunner, Félix Bussières, Mikael Afzelius, and Nicolas Gisin. Experimental certification of millions of genuinely entangled atoms in a solid. *Nat. Commun.*, 8(1):1–6, 2017.

[62] C. W. Gardiner and M. J. Collett. Input and output in damped quantum systems: Quantum stochastic differential equations and the master equation. *Phys. Rev. A*, 31:3761–3774, Jun 1985.

[63] Martin Gärttner, Justin G Bohnet, Arghavan Safavi-Naini, Michael L Wall, John J Bollinger, and Ana Maria Rey. Measuring out-of-time-order correlations and multiple quantum spectra in a trapped-ion quantum magnet. *Nat. Phys.*, 13(8):781, 2017.

[64] Alexandros Georgakopoulos, Ariel Sommer, and Jonathan Simon. Theory of interacting cavity rydberg polaritons. *Quantum Sci. Technol.*, 4(1):014005, 2018.

[65] I. M. Georgescu, S. Ashhab, and Franco Nori. Quantum simulation. *Rev. Mod. Phys.*, 86:153–185, Mar 2014.

[66] Kevin A Gilmore, Matthew Affolter, Robert J Lewis-Swan, Diego Barberena, Elena Jordan, Ana Maria Rey, and John J Bollinger. Quantum-enhanced sensing of displacements and electric fields with two-dimensional trapped-ion crystals. *Science*, 373(6555):673–678, 2021.

[67] Alaina M. Green, A. Elben, C. Huerta Alderete, Lata Kh Joshi, Nhung H. Nguyen, Torsten V. Zache, Yingyue Zhu, Bhuvanesh Sundar, and Norbert M. Linke. Experimental measurement of out-of-time-ordered correlators at finite temperature. *Phys. Rev. Lett.*, 128:140601, Apr 2022.

[68] Rudolf Grimm, Matthias Weidemüller, and Yurii B Ovchinnikov. Optical dipole traps for neutral atoms. In *Advances in atomic, molecular, and optical physics*, volume 42, pages 95–170. Elsevier, 2000.

[69] Christian Gross, Tilman Zibold, Eike Nicklas, Jerome Esteve, and Markus K Oberthaler. Nonlinear atom interferometer surpasses classical precision limit. *Nature*, 464(7292):1165, 2010.

[70] Jacopo Grotti, Silvio Koller, Stefan Vogt, Sebastian Häfner, Uwe Sterr, Christian Lisdat, Heiner Denker, Christian Voigt, Ludger Timmen, Antoine Rolland, et al. Geodesy and metrology with a transportable optical clock. *Nat. Phys.*, 14(5):437–441, 2018.

[71] Yudan Guo, Ronen M. Kroeze, Varun D. Vaidya, Jonathan Keeling, and Benjamin L. Lev. Sign-changing photon-mediated atom interactions in multimode cavity quantum electrodynamics. *Phys. Rev. Lett.*, 122:193601, May 2019.

[72] Yudan Guo, Varun D. Vaidya, Ronen M. Kroeze, Rhiannon A. Lunney, Benjamin L. Lev, and Jonathan Keeling. Emergent and broken symmetries of atomic self-organization arising from gouy phase shifts in multimode cavity qed. *Phys. Rev. A*, 99:053818, May 2019.

[73] Florian Haas, Jürgen Volz, Roger Gehr, Jakob Reichel, and Jérôme Estève. Entangled states of more than 40 atoms in an optical fiber cavity. *Science*, 344(6180):180–183, 2014.

[74] Bastian Hacker, Stephan Welte, Severin Daiss, Armin Shaukat, Stephan Ritter, Lin Li, and Gerhard Rempe. Deterministic creation of entangled atom–light Schrödinger-cat states. *Nat. Photonics*, 13(2):110–115, January 2019.

[75] Bastian Hacker, Stephan Welte, Gerhard Rempe, and Stephan Ritter. A photon-photon quantum gate based on a single atom in an optical resonator. *Nature*, 536:193, July 2016.

[76] E. Hagley, X. Maître, G. Nogues, C. Wunderlich, M. Brune, J. M. Raimond, and S. Haroche. Generation of einstein-podolsky-rosen pairs of atoms. *Phys. Rev. Lett.*, 79:1–5, Jul 1997.

[77] Chris D Hamley, CS Gerving, TM Hoang, EM Bookjans, and Michael S Chapman. Spin-nematic squeezed vacuum in a quantum gas. *Nat. Phys.*, 8(4):305, 2012.

[78] K. Hammerer, K. Mølmer, E. S. Polzik, and J. I. Cirac. Light-matter quantum interface. *Phys. Rev. A*, 70:044304, Oct 2004.

[79] Klemens Hammerer, Anders S. Sørensen, and Eugene S. Polzik. Quantum interface between light and atomic ensembles. *Rev. Mod. Phys.*, 82:1041–1093, Apr 2010.

[80] W. Hardle and J. S. Marron. Bootstrap Simultaneous Error Bars for Nonparametric Regression. *The Annals of Statistics*, 19(2):778 – 796, 1991.

[81] D. J. Heinzen and M. S. Feld. Vacuum radiative level shift and spontaneous-emission linewidth of an atom in an optical resonator. *Phys. Rev. Lett.*, 59:2623–2626, Dec 1987.

[82] Carl W Helstrom. Quantum detection and estimation theory. *Journal of Statistical Physics*, 1(2):231–252, 1969.

[83] B. Hensen, H. Bernien, A. E. Dréau, A. Reiserer, N. Kalb, M. S. Blok, J. Ruitenberg, R. F. L. Vermeulen, R. N. Schouten, C. Abellán, W. Amaya, V. Pruneri, M. W. Mitchell, M. Markham, D. J. Twitchen, D. Elkouss, S. Wehner, T. H. Taminiau, and R. Hanson. Loophole-free bell inequality violation using electron spins separated by 1.3 kilometres. *Nature*, 526:682, October 2015.

[84] Jacob A. Hines, Shankari V. Rajagopal, Gabriel L. Moreau, Michael D. Wahrman, Neomi A. Lewis, Ognjen Marković, and Monika Schleier-Smith. Spin squeezing by rydberg dressing in an array of atomic ensembles, 2023.

[85] Richard Hobson, William Bowden, Alvise Vianello, Ian R. Hill, and Patrick Gill. Cavity-enhanced non-destructive detection of atoms for an optical lattice clock. *Opt. Express*, 27(26):37099–37110, Dec 2019.

[86] T. Holstein and H. Primakoff. Field dependence of the intrinsic domain magnetization of a ferromagnet. *Phys. Rev.*, 58:1098–1113, Dec 1940.

[87] O. Hosten, R. Krishnakumar, N. J. Engelsen, and M. A. Kasevich. Quantum phase magnification. *Science*, 352(6293):1552–1555, 2016.

[88] Onur Hosten, Nils J. Engelsen, Rajiv Krishnakumar, and Mark A. Kasevich. Measurement noise 100 times lower than the quantum-projection limit using entangled atoms. *Nature*, 529(7587):505–508, January 2016.

[89] Jiazhong Hu, Wenlan Chen, Zachary Vendeiro, Hao Zhang, and Vladan Vuletić. Entangled collective-spin states of atomic ensembles under nonuniform atom-light interaction. *Phys. Rev. A*, 92:063816, Dec 2015.

[90] Jiazhong Hu, Alban Urvoy, Zachary Vendeiro, Valentin Crépel, Wenlan Chen, and Vladan Vuletić. Creation of a bose-condensed gas of 87rb by laser cooling. *Science*, 358(6366):1078–1080, 2017.

[91] Liang Hu, Nicola Poli, Leonardo Salvi, and Guglielmo M. Tino. Atom interferometry with the sr optical clock transition. *Phys. Rev. Lett.*, 119:263601, Dec 2017.

[92] Meng-Zi Huang, Jose Alberto de la Paz, Tommaso Mazzoni, Konstantin Ott, Alice Sinatra, Carlos L Garrido Alzar, and Jakob Reichel. Self-amplifying spin measurement in a long-lived spin-squeezed state. *arXiv:2007.01964*, 2020.

[93] Joonseok Hur, Diana P. L. Aude Craik, Ian Counts, Eugene Knyazev, Luke Caldwell, Calvin Leung, Swadha Pandey, Julian C. Berengut, Amy Geddes, Witold Nazarewicz, Paul-Gerhard Reinhard, Akio Kawasaki, Honggi Jeon, Wonho Jhe, and Vladan Vuletić. Evidence of two-source king plot nonlinearity in spectroscopic search for new boson. *Phys. Rev. Lett.*, 128:163201, Apr 2022.

[94] Ryotaro Inoue, Shin-Ichi-Ro Tanaka, Ryo Namiki, Takahiro Sagawa, and Yoshiro Takahashi. Unconditional quantum-noise suppression via measurement-based quantum feedback. *Phys. Rev. Lett.*, 110:163602, Apr 2013.

[95] W. M. Itano, J. C. Bergquist, J. J. Bollinger, J. M. Gilligan, D. J. Heinzen, F. L. Moore, M. G. Raizen, and D. J. Wineland. Quantum projection noise: Population fluctuations in two-level systems. *Phys. Rev. A*, 47:3554–3570, May 1993.

[96] Matt Jaffe, Lukas Palm, Claire Baum, Lavanya Taneja, Aishwarya Kumar, and Jonathan Simon. Understanding and suppressing backscatter in optical resonators. *Optica*, 9(8):878–885, 2022.

[97] E. T. Jaynes and F. W. Cummings. Comparison of quantum and semiclassical radiation theories with application to the beam maser. *Proceedings of the IEEE*, 51(1):89–109, Jan 1963.

[98] Alec Jenkins, Joanna W. Lis, Aruku Senoo, William F. McGrew, and Adam M. Kaufman. Ytterbium nuclear-spin qubits in an optical tweezer array. *Phys. Rev. X*, 12:021027, May 2022.

[99] Brian Julsgaard, Alexander Kozhekin, and Eugene S Polzik. Experimental long-lived entanglement of two macroscopic objects. *Nature*, 413(6854):400–403, 2001.

[100] Akio Kawasaki. *Towards Spin Squeezed ^{171}Yb Atomic Clock beyond the Standard Quantum Limit*. Ph.D. thesis, Massachusetts Institute of Technology, 2017.

[101] Akio Kawasaki, Boris Braverman, Edwin Pedrozo-Peñafiel, Chi Shu, Simone Colombo, Zeyang Li, Özge Özel, Wenlan Chen, Leonardo Salvi, André Heinz, David Levonian, Daisuke Akamatsu, Yanhong Xiao, and Vladan Vuletić. Geometrically asymmetric optical cavity for strong atom-photon coupling. *Phys. Rev. A*, 99:013437, Jan 2019.

[102] Akio Kawasaki, Boris Braverman, Edwin Pedrozo-Peñafiel, Chi Shu, Simone Colombo, Zeyang Li, and Vladan Vuletić. Trapping ^{171}Yb atoms into a one-dimensional optical lattice with a small waist. *Phys. Rev. A*, 102:013114, Jul 2020.

[103] Akio Kawasaki, Boris Braverman, QinQin Yu, and Vladan Vuletić. Two-color magneto-optical trap with small magnetic field for ytterbium. *J. Phys. B*, 48(15):155302, 2015.

[104] Colin J. Kennedy, Eric Oelker, John M. Robinson, Tobias Bothwell, Dhruv Kedar, William R. Milner, G. Edward Marti, Andrei Derevianko, and Jun Ye. Precision metrology meets cosmology: Improved constraints on ultralight dark matter from atom-cavity frequency comparisons. *Phys. Rev. Lett.*, 125:201302, Nov 2020.

[105] H. J. Kimble. The quantum internet. *Nature*, 453:1023, June 2008.

[106] H Jeff Kimble. Strong interactions of single atoms and photons in cavity qed. *Physica Scripta*, 1998(T76):127, 1998.

[107] Alexei Kitaev. A simple model of quantum holography, 2015. KITP Program: Entanglement in Strongly-Correlated Quantum Matter.

[108] Masahiro Kitagawa and Masahito Ueda. Squeezed spin states. *Phys. Rev. A*, 47:5138–5143, Jun 1993.

[109] S. Kolkowitz, I. Pikovski, N. Langellier, M. D. Lukin, R. L. Walsworth, and J. Ye. Gravitational wave detection with optical lattice atomic clocks. *Phys. Rev. D*, 94:124043, Dec 2016.

[110] Alicia J Kollár, Alexander T Papageorge, Varun D Vaidya, Yudan Guo, Jonathan Keeling, and Benjamin L Lev. Supermode-density-wave-polariton condensation with a bose–einstein condensate in a multimode cavity. *Nat. Commun.*, 8:14386, February 2017.

[111] I Kruse, K Lange, J Peise, Bernd Lücke, L Pezzè, J Arlt, Wolfgang Ertmer, C Lisdat, Luis Santos, A Smerzi, et al. Improvement of an atomic clock using squeezed vacuum. *Physical review letters*, 117(14):143004, 2016.

[112] G. Kucsko, S. Choi, J. Choi, P. C. Maurer, H. Zhou, R. Landig, H. Sumiya, S. Onoda, J. Isoya, F. Jelezko, E. Demler, N. Y. Yao, and M. D. Lukin. Critical thermalization of a disordered dipolar spin system in diamond. *Phys. Rev. Lett.*, 121:023601, Jul 2018.

[113] A Kuzmich, NP Bigelow, and L Mandel. Atomic quantum non-demolition measurements and squeezing. *EPL (Europhysics Letters)*, 42(5):481, 1998.

[114] A. Kuzmich, L. Mandel, and N. P. Bigelow. Generation of spin squeezing via continuous quantum nondemolition measurement. *Phys. Rev. Lett.*, 85:1594–1597, Aug 2000.

[115] A. Kuzmich, L. Mandel, J. Janis, Y. E. Young, R. Ejnisman, and N. P. Bigelow. Quantum nondemolition measurements of collective atomic spin. *Phys. Rev. A*, 60:2346–2350, Sep 1999.

[116] Kevin A Landsman, Caroline Figgatt, Thomas Schuster, Norbert M Linke, Beni Yoshida, Norman Y Yao, and Christopher Monroe. Verified quantum information scrambling. *Nature*, 567(7746):61–65, 2019.

[117] AI Larkin and Yu N Ovchinnikov. Quasiclassical method in the theory of superconductivity. *Sov Phys JETP*, 28(6):1200–1205, 1969.

[118] C. K. Law, H. T. Ng, and P. T. Leung. Coherent control of spin squeezing. *Phys. Rev. A*, 63:055601, Apr 2001.

[119] Jongmin Lee, Geert Vrijsen, Igor Teper, Onur Hosten, and Mark A Kasevich. Many-atom-cavity QED system with homogeneous atom-cavity coupling. *Optics letters*, 39(13):4005–4008, 2014.

[120] Tony E. Lee, Florentin Reiter, and Nimrod Moiseyev. Entanglement and spin squeezing in non-Hermitian phase transitions. *Phys. Rev. Lett.*, 113:250401, Dec 2014.

[121] Ian D. Leroux, Monika H. Schleier-Smith, and Vladan Vuletić. Implementation of cavity squeezing of a collective atomic spin. *Phys. Rev. Lett.*, 104(7):073602, Feb 2010.

[122] Ian D. Leroux, Monika H. Schleier-Smith, Hao Zhang, and Vladan Vuletić. Unitary cavity spin squeezing by quantum erasure. *Phys. Rev. A*, 85:013803, Jan 2012.

[123] RJ Lewis-Swan, Arghavan Safavi-Naini, John J Bollinger, and Ana M Rey. Unifying scrambling, thermalization and entanglement through measurement of fidelity out-of-time-order correlators in the dicke model. *Nature communications*, 10(1):1–9, 2019.

[124] Jun Li, Ruihua Fan, Hengyan Wang, Bingtian Ye, Bei Zeng, Hui Zhai, Xinhua Peng, and Jiangfeng Du. Measuring out-of-time-order correlators on a nuclear magnetic resonance quantum simulator. *Phys. Rev. X*, 7:031011, Jul 2017.

[125] Zeyang Li, Boris Braverman, Simone Colombo, Chi Shu, Akio Kawasaki, Albert F. Adiyatullin, Edwin Pedrozo-Peñafiel, Enrique Mendez, and Vladan Vuletić. Collective spin-light and light-mediated spin-spin interactions in an optical cavity. *PRX Quantum*, 3:020308, Apr 2022.

[126] Zeyang Li, Simone Colombo, Chi Shu, Gustavo Velez, Saúl Pilatowsky-Cameo, Roman Schmied, Soonwon Choi, Mikhail Lukin, Edwin Pedrozo-Peñafiel, and Vladan Vuletić. Improving metrology with quantum scrambling. *Science*, 2023.

[127] Valentin Link, Kai Müller, Rosaria G. Lena, Kimmo Luoma, Fran çois Damanet, Walter T. Strunz, and Andrew J. Daley. Non-markovian quantum dynamics in strongly coupled multimode cavities conditioned on continuous measurement. *PRX Quantum*, 3:020348, Jun 2022.

[128] Harry J Lipkin, N Meshkov, and AJ Glick. Validity of many-body approximation methods for a solvable model:(i). Exact solutions and perturbation theory. *Nuclear Physics*, 62(2):188–198, 1965.

[129] Christian Lisdat, G Grosche, N Quintin, C Shi, SMF Raupach, C Grebing, D Nicolodi, F Stefani, A Al-Masoudi, S Dörscher, et al. A clock network for geodesy and fundamental science. *Nat. Commun.*, 7(1):1–7, 2016.

[130] Y. C. Liu, Z. F. Xu, G. R. Jin, and L. You. Spin squeezing: Transforming one-axis twisting into two-axis twisting. *Phys. Rev. Lett.*, 107:013601, Jun 2011.

[131] Seth Lloyd. Coherent quantum feedback. *Phys. Rev. A*, 62:022108, Jul 2000.

[132] Michael A Lombardi, Thomas P Heavner, and Steven R Jefferts. Nist primary frequency standards and the realization of the si second. *NCSLI Measure*, 2(4):74–89, 2007.

[133] B. Lücke, M. Scherer, J. Kruse, L. Pezzé, F. Deuretzbacher, P. Hyllus, O. Topic, J. Peise, W. Ertmer, J. Arlt, L. Santos, A. Smerzi, and C. Klempt. Twin matter waves for interferometry beyond the classical limit. *Science*, 334(6057):773–776, 2016.

[134] Andrew D. Ludlow, Martin M. Boyd, Jun Ye, E. Peik, and P. O. Schmidt. Optical atomic clocks. *Rev. Mod. Phys.*, 87:637–701, Jun 2015.

[135] Jian Ma, Xiaoguang Wang, Chang-Pu Sun, and Franco Nori. Quantum spin squeezing. *Physics Reports*, 509(2-3):89–165, 2011.

[136] Long-Sheng Ma, Peter Jungner, Jun Ye, and John L Hall. Delivering the same optical frequency at two places: accurate cancellation of phase noise introduced by an optical fiber or other time-varying path. *Optics letters*, 19(21):1777–1779, 1994.

[137] Tommaso Macrì, Augusto Smerzi, and Luca Pezzè. Loschmidt echo for quantum metrology. *Physical Review A*, 94(1):010102, 2016.

[138] MT Manzoni, M Moreno-Cardoner, A Asenjo-Garcia, James V Porto, Alexey V Gorshkov, and DE Chang. Optimization of photon storage fidelity in ordered atomic arrays. *New journal of physics*, 20(8):083048, 2018.

[139] Tian-Wei Mao, Qi Liu, Xin-Wei Li, Jia-Hao Cao, Feng Chen, Wen-Xin Xu, Meng Khoon Tey, Yi-Xiao Huang, and Li You. Quantum enhanced sensing by echoing spin-nematic squeezing in atomic bose-einstein condensate, 2022.

[140] Christian D Marciniak, Thomas Feldker, Ivan Pogorelov, Raphael Kaubruegger, Denis V Vasilyev, Rick van Bijnen, Philipp Schindler, Peter Zoller, Rainer Blatt, and Thomas Monz. Optimal metrology with programmable quantum sensors. *Nature*, 603(7902):604–609, 2022.

[141] Yair Margalit, Yu-Kun Lu, Furkan Çağrı Top, and Wolfgang Ketterle. Pauli blocking of light scattering in degenerate fermions. *Science*, 374(6570):976–979, 2021.

[142] D. G. Matei, T. Legero, S. Häfner, C. Grebing, R. Weyrich, W. Zhang, L. Sonderhouse, J. M. Robinson, J. Ye, F. Riehle, and U. Sterr. 1.5 μm lasers with sub-10 mhz linewidth. *Phys. Rev. Lett.*, 118:263202, Jun 2017.

[143] Robert McConnell, Hao Zhang, Jiazhong Hu, Senka Ćuk, and Vladan Vuletić. Entanglement with negative wigner function of almost 3,000 atoms heralded by one photon. *Nature*, 519(7544):439–442, 2015.

[144] Enrique Mendez. *On the Generation of Entanglement in Ytterbium Clock Atoms and a Novel Interpretation of the Madelung Fluid Theory of Quantum Mechani*. Ph.D. thesis, Massachusetts Institute of Technology, 2023.

[145] Xiao Mi, Pedram Roushan, Chris Quintana, Salvatore Mandrà, Jeffrey Marshall, Charles Neill, Frank Arute, Kunal Arya, Juan Atalaya, Ryan Babbush, et al. Information scrambling in quantum circuits. *Science*, 374(6574):1479–1483, 2021.

[146] ZK Minev, SO Mundhada, Shyam Shankar, Philip Reinhold, Ricardo Gutiérrez-Jáuregui, RJ Schoelkopf, Mazyar Mirrahimi, HJ Carmichael, and MH Devoret. To catch and reverse a quantum jump mid-flight. *Nature*, page 1, 2019.

[147] Farokh Mivehvar, Francesco Piazza, Tobias Donner, and Helmut Ritsch. Cavity qed with quantum gases: new paradigms in many-body physics. *Advances in Physics*, 70(1):1–153, 2021.

[148] Christoffer B Møller, Rodrigo A Thomas, Georgios Vasilakis, Emil Zeuthen, Yeghishe Tsaturyan, Mikhail Balabas, Kasper Jensen, Albert Schliesser, Klemens Hammerer, and Eugene S Polzik. Quantum back-action-evading measure-

ment of motion in a negative mass reference frame. *Nature*, 547:191–195, July 2017.

[149] Debabrata Mondal, Sudip Sinha, and S. Sinha. Quantum transitions, ergodicity, and quantum scars in the coupled top model. *Phys. Rev. E*, 105:014130, Jan 2022.

[150] Thomas Monz, Philipp Schindler, Julio T. Barreiro, Michael Chwalla, Daniel Nigg, William A. Coish, Maximilian Harlander, Wolfgang Hänsel, Markus Hennrich, and Rainer Blatt. 14-qubit entanglement: Creation and coherence. *Phys. Rev. Lett.*, 106:130506, Mar 2011.

[151] Michael Motsch, Martin Zeppenfeld, Pepijn WH Pinkse, and Gerhard Rempe. Cavity-enhanced rayleigh scattering. *New Journal of Physics*, 12(6):063022, 2010.

[152] W. Muessel, H. Strobel, D. Linnemann, D. B. Hume, and M. K. Oberthaler. Scalable spin squeezing for quantum-enhanced magnetometry with Bose-Einstein condensates. *Phys. Rev. Lett.*, 113:103004, Sep 2014.

[153] W. Muessel, H. Strobel, D. Linnemann, T. Zibold, B. Juliá-Díaz, and M. K. Oberthaler. Twist-and-turn spin squeezing in bose-einstein condensates. *Phys. Rev. A*, 92:023603, Aug 2015.

[154] Juan A Muniz, Diego Barberena, Robert J Lewis-Swan, Dylan J Young, Julia RK Cline, Ana Maria Rey, and James K Thompson. Exploring dynamical phase transitions with cold atoms in an optical cavity. *Nature*, 580(7805):602–607, 2020.

[155] Sepehr Nezami, Henry W. Lin, Adam R. Brown, Hrant Gharibyan, Stefan Leichenauer, Grant Salton, Leonard Susskind, Brian Swingle, and Michael Walter. Quantum gravity in the lab. ii. teleportation by size and traversable wormholes. *PRX Quantum*, 4:010321, Feb 2023.

[156] T. L. Nicholson, M. J. Martin, J. R. Williams, B. J. Bloom, M. Bishof, M. D. Swallows, S. L. Campbell, and J. Ye. Comparison of two independent sr optical clocks with 1×10^{-17} stability at 10^3 **s**. *Phys. Rev. Lett.*, 109:230801, Dec 2012.

[157] T.L. Nicholson, S.L. Campbell, R.B. Hutson, G.E. Marti, B.J. Bloom, R.L. McNally, W. Zhang, M.D. Barrett, M.S. Safronova, G.F. Strouse, W.L. Tew, and J. Ye. Systematic evaluation of an atomic clock at 2×10^{-18} total uncertainty. *Nat. Commun.*, 6:–, April 2015.

[158] Samuel P Nolan, Stuart S Szigeti, and Simon A Haine. Optimal and robust quantum metrology using interaction-based readouts. *Physical Review Letters*, 119(19):193601, 2017.

[159] Matthew A. Norcia, Aaron W. Young, William J. Eckner, Eric Oelker, Jun Ye, and Adam M. Kaufman. Seconds-scale coherence on an optical clock transition in a tweezer array. *Science*, 366(6461):93–97, 2019.

[160] E Oelker, RB Hutson, CJ Kennedy, L Sonderhouse, T Bothwell, A Goban, D Kedar, C Sanner, JM Robinson, GE Marti, et al. Demonstration of 4.8×10^{-17} stability at 1 s for two independent optical clocks. *Nat. Photonics*, 13(10):714–719, 2019.

[161] Ahmed Omran, Harry Levine, Alexander Keesling, Giulia Semeghini, Tout T Wang, Sepehr Ebadi, Hannes Bernien, Alexander S Zibrov, Hannes Pichler, Soonwon Choi, et al. Generation and manipulation of Schrödinger cat states in Rydberg atom arrays. *Science*, 365(6453):570–574, 2019.

[162] Koki Ono, Yugo Saito, Taiki Ishiyama, Toshiya Higomoto, Tetsushi Takano, Yosuke Takasu, Yasuhiro Yamamoto, Minoru Tanaka, and Yoshiro Takahashi. Observation of nonlinearity of generalized king plot in the search for new boson. *Phys. Rev. X*, 12:021033, May 2022.

[163] Tomáš Opatrný. Quasicontinuous-variable quantum computation with collective spins in multipath interferometers. *Phys. Rev. Lett.*, 119:010502, Jul 2017.

[164] R. Oswald, A. Nevsky, V. Vogt, S. Schiller, N. L. Figueroa, K. Zhang, O. Tretiak, D. Antypas, D. Budker, A. Banerjee, and G. Perez. Search for dark-matter-induced oscillations of fundamental constants using molecular spectroscopy. *Phys. Rev. Lett.*, 129:031302, Jul 2022.

[165] Tomoki Ozawa, Hannah M. Price, Alberto Amo, Nathan Goldman, Mohammad Hafezi, Ling Lu, Mikael C. Rechtsman, David Schuster, Jonathan Simon, Oded Zilberberg, and Iacopo Carusotto. Topological photonics. *Rev. Mod. Phys.*, 91:015006, Mar 2019.

[166] Silvia Pappalardi, Angelo Russomanno, Bojan Žunkovič, Fernando Iemini, Alessandro Silva, and Rosario Fazio. Scrambling and entanglement spreading in long-range spin chains. *Phys. Rev. B*, 98:134303, Oct 2018.

[167] Krzysztof Pawłowski, Jérôme Estève, Jakob Reichel, and Alice Sinatra. Limits of atomic entanglement by cavity feedback: From weak to strong coupling. *EPL (Europhysics Letters)*, 113(3):34005, 2016.

[168] Edwin Pedrozo-Peñafiel, Simone Colombo, Chi Shu, Albert F Adiyatullin, Zeyang Li, Enrique Mendez, Boris Braverman, Akio Kawasaki, Daisuke Akamatsu, Yanhong Xiao, and Vladan Vuletić. Entanglement on an optical atomic-clock transition. *Nature*, 588(7838):414–418, 2020.

[169] Jan Peise, I Kruse, K Lange, Bernd Lücke, Luca Pezzè, Jan Arlt, Wolfgang Ertmer, Klemens Hammerer, Luis Santos, Augusto Smerzi, et al. Satisfying the einstein–podolsky–rosen criterion with massive particles. *Nat. Commun.*, 6(1):8984, 2015.

[170] Pai Peng, Zeyang Li, Haoxiong Yan, Ken Xuan Wei, and Paola Cappellaro. Comparing many-body localization lengths via nonperturbative construction of local integrals of motion. *Phys. Rev. B*, 100:214203, Dec 2019.

[171] Luca Pezzè, Augusto Smerzi, Markus K. Oberthaler, Roman Schmied, and Philipp Treutlein. Quantum metrology with nonclassical states of atomic ensembles. *Rev. Mod. Phys.*, 90:035005, Sep 2018.

[172] Francesco Piazza and Philipp Strack. Umklapp superradiance with a collisionless quantum degenerate fermi gas. *Phys. Rev. Lett.*, 112:143003, Apr 2014.

[173] Saúl Pilatowsky-Cameo, Jorge Chávez-Carlos, Miguel A. Bastarrachea-Magnani, Pavel Stránský, Sergio Lerma-Hernández, Lea F. Santos, and Jorge G. Hirsch. Positive quantum lyapunov exponents in experimental systems with a regular classical limit. *Phys. Rev. E*, 101:010202, Jan 2020.

[174] I. Pogorelov, T. Feldker, Ch. D. Marciniak, L. Postler, G. Jacob, O. Krieglsteiner, V. Podlesnic, M. Meth, V. Negnevitsky, M. Stadler, B. Höfer, C. Wächter, K. Lakhmanskiy, R. Blatt, P. Schindler, and T. Monz. Compact ion-trap quantum computing demonstrator. *PRX Quantum*, 2:020343, Jun 2021.

[175] Anatoli Polkovnikov. Phase space representation of quantum dynamics. *Annals of Physics*, 325(8):1790–1852, 2010.

[176] M. Pospelov, S. Pustelny, M. P. Ledbetter, D. F. Jackson Kimball, W. Gawlik, and D. Budker. Detecting domain walls of axionlike models using terrestrial experiments. *Phys. Rev. Lett.*, 110:021803, Jan 2013.

[177] Lorenzo Pucci, Analabha Roy, and Michael Kastner. Simulation of quantum spin dynamics by phase space sampling of bogoliubov-born-green-kirkwood-yvon trajectories. *Phys. Rev. B*, 93:174302, May 2016.

[178] E. M. Purcell, H. C. Torrey, and R. V. Pound. Resonance absorption by nuclear magnetic moments in a solid. *Phys. Rev.*, 69:37–38, Jan 1946.

[179] I. I. Rabi, J. R. Zacharias, S. Millman, and P. Kusch. A new method of measuring nuclear magnetic moment. *Phys. Rev.*, 53:318–318, Feb 1938.

[180] J. M. Raimond, M. Brune, and S. Haroche. Manipulating quantum entanglement with atoms and photons in a cavity. *Rev. Mod. Phys.*, 73:565–582, Aug 2001.

[181] C Radhakrishna Rao. Information and the accuracy attainable in the estimation of statistical parameters. *Reson. J. Sci. Educ*, 20:78–90, 1945.

[182] Andreas Reiserer and Gerhard Rempe. Cavity-based quantum networks with single atoms and optical photons. *Rev. Mod. Phys.*, 87:1379–1418, Dec 2015.

[183] Florentin Reiter and Anders S. Sørensen. Effective operator formalism for open quantum systems. *Phys. Rev. A*, 85:032111, Mar 2012.

[184] Max F Riedel, Pascal Böhi, Yun Li, Theodor W Hänsch, Alice Sinatra, and Philipp Treutlein. Atom-chip-based generation of entanglement for quantum metrology. *Nature*, 464(7292):1170–1173, 2010.

[185] Fritz Riehle. Optical clock networks. *Nature Photonics*, 11(1):25–31, 2017.

[186] Helmut Ritsch, Peter Domokos, Ferdinand Brennecke, and Tilman Esslinger. Cold atoms in cavity-generated dynamical optical potentials. *Rev. Mod. Phys.*, 85:553–601, Apr 2013.

[187] Tanya S. Roussy, Luke Caldwell, Trevor Wright, William B. Cairncross, Yuval Shagam, Kia Boon Ng, Noah Schlossberger, Sun Yool Park, Anzhou Wang, Jun Ye, and Eric A. Cornell. A new bound on the electron's electric dipole moment, 2022.

[188] Efim B. Rozenbaum, Leonid A. Bunimovich, and Victor Galitski. Early-time exponential instabilities in nonchaotic quantum systems. *Phys. Rev. Lett.*, 125:014101, Jul 2020.

[189] M. Saffman, D. Oblak, J. Appel, and E. S. Polzik. Spin squeezing of atomic ensembles by multicolor quantum nondemolition measurements. *Phys. Rev. A*, 79:023831, Feb 2009.

[190] M. S. Safronova, D. Budker, D. DeMille, Derek F. Jackson Kimball, A. Derevianko, and Charles W. Clark. Search for new physics with atoms and molecules. *Rev. Mod. Phys.*, 90:025008, Jun 2018.

[191] Marianna S. Safronova. The search for variation of fundamental constants with clocks. *Annalen der Physik*, 531(5):1800364, 2019.

[192] C. Sames, H. Chibani, C. Hamsen, P. A. Altin, T. Wilk, and G. Rempe. Antiresonance phase shift in strongly coupled cavity qed. *Phys. Rev. Lett.*, 112:043601, Jan 2014.

[193] Christian Sanner, Nils Huntemann, Richard Lange, Christian Tamm, Ekkehard Peik, Marianna S Safronova, and Sergey G Porsev. Optical clock comparison for Lorentz symmetry testing. *Nature*, 567(7747):204–208, 2019.

[194] Christian Sanner, Lindsay Sonderhouse, Ross B Hutson, Lingfeng Yan, William R Milner, and Jun Ye. Pauli blocking of atom-light scattering. *Science*, 374(6570):979–983, 2021.

[195] Clement Sayrin, Igor Dotsenko, Xingxing Zhou, Bruno Peaudecerf, Theo Rybarczyk, Sebastien Gleyzes, Pierre Rouchon, Mazyar Mirrahimi, Hadis Amini, Michel Brune, Jean-Michel Raimond, and Serge Haroche. Real-time quantum feedback prepares and stabilizes photon number states. *Nature*, 477(7362):73–77, September 2011.

[196] M. Scala, B. Militello, A. Messina, J. Piilo, and S. Maniscalco. Microscopic derivation of the jaynes-cummings model with cavity losses. *Phys. Rev. A*, 75:013811, Jan 2007.

[197] Nathan Schine, Michelle Chalupnik, Tankut Can, Andrey Gromov, and Jonathan Simon. Electromagnetic and gravitational responses of photonic landau levels. *Nature*, 565(7738):173, January 2019.

[198] M. Schioppo, R. C. Brown, W. F. McGrew, N. Hinkley, R. J. Fasano, K. Beloy, T. H. Yoon, G. Milani, D. Nicolodi, J. A. Sherman, N. B. Phillips, C. W. Oates, and A. D. Ludlow. Ultrastable optical clock with two cold-atom ensembles. *Nat. Photonics*, 11(1):48–52, January 2017.

[199] Monika H. Schleier-Smith, Ian D. Leroux, and Vladan Vuletić. States of an ensemble of two-level atoms with reduced quantum uncertainty. *Phys. Rev. Lett.*, 104:073604, Feb 2010.

[200] Monika H. Schleier-Smith, Ian D. Leroux, and Vladan Vuletić. Squeezing the collective spin of a dilute atomic ensemble by cavity feedback. *Phys. Rev. A*, 81:021804, Feb 2010.

[201] Roman Schmied, Jean-Daniel Bancal, Baptiste Allard, Matteo Fadel, Valerio Scarani, Philipp Treutlein, and Nicolas Sangouard. Bell correlations in a Bose–Einstein condensate. *Science*, 352(6284):441–444, 2016.

[202] Roman Schmied and Philipp Treutlein. Tomographic reconstruction of the wigner function on the bloch sphere. *New J. Phys.*, 13(6):065019, 2011.

[203] Marius Schulte, Victor J. Martínez-Lahuerta, Maja S. Scharnagl, and Klemens Hammerer. Ramsey interferometry with generalized one-axis twisting echoes. *Quantum*, 4:268, May 2020.

[204] Ingrid Schuster, Alexander Kubanek, Andreas Fuhrmanek, Thomas Puppe, Pepijn WH Pinkse, Karim Murr, and Gerhard Rempe. Nonlinear spectroscopy of photons bound to one atom. *Nat. Phys.*, 4(5):382–385, 2008.

[205] Thomas Schuster, Bryce Kobrin, Ping Gao, Iris Cong, Emil T. Khabiboulline, Norbert M. Linke, Mikhail D. Lukin, Christopher Monroe, Beni Yoshida, and Norman Y. Yao. Many-body quantum teleportation via operator spreading in the traversable wormhole protocol. *Phys. Rev. X*, 12:031013, Jul 2022.

[206] Yasuhiro Sekino and L Susskind. Fast scramblers. *Journal of High Energy Physics*, 2008(10):065–065, oct 2008.

[207] R. J. Sewell, M. Koschorreck, M. Napolitano, B. Dubost, N. Behbood, and M. W. Mitchell. Magnetic sensitivity beyond the projection noise limit by spin squeezing. *Phys. Rev. Lett.*, 109:253605, Dec 2012.

[208] Nathan Shammah, Shahnawaz Ahmed, Neill Lambert, Simone De Liberato, and Franco Nori. Open quantum systems with local and collective incoherent processes: Efficient numerical simulations using permutational invariance. *Phys. Rev. A*, 98:063815, Dec 2018.

[209] Chi Shu. *Quantum enhanced metrology in optical lattice clock.* PhD thesis, Harvard University, 2022.

[210] Anthony E. Siegman. *Lasers.* University Science Books, 1986.

[211] Pablo Solano, Yiheng Duan, Yu-Ting Chen, Alyssa Rudelis, Cheng Chin, and Vladan Vuletić. Strongly correlated quantum gas prepared by direct laser cooling. *Phys. Rev. Lett.*, 123:173401, Oct 2019.

[212] Anders Søndberg Sørensen and Klaus Mølmer. Entangling atoms in bad cavities. *Phys. Rev. A*, 66:022314, Aug 2002.

[213] Nicolas Spethmann, Jonathan Kohler, Sydney Schreppler, Lukas Buchmann, and Dan M Stamper-Kurn. Cavity-mediated coupling of mechanical oscillators limited by quantum back-action. *Nat. Phys.*, 12:27–31, 2016.

[214] RJC Spreeuw, T Pfau, U Janicke, and M Wilkens. Laser-like scheme for atomic-matter waves. *Europhysics Letters*, 32(6):469, 1995.

[215] Philip Thomas Starkey. *A software framework for control and automation of precisely timed experiments.* PhD thesis, Monash University, 2019.

[216] Helmut Strobel, Wolfgang Muessel, Daniel Linnemann, Tilman Zibold, David B Hume, Luca Pezzè, Augusto Smerzi, and Markus K Oberthaler. Fisher information and entanglement of non-Gaussian spin states. *Science*, 345(6195):424–427, 2014.

[217] Brian Swingle, Gregory Bentsen, Monika Schleier-Smith, and Patrick Hayden. Measuring the scrambling of quantum information. *Phys. Rev. A*, 94:040302, Oct 2016.

[218] Y. Takahashi, K. Honda, N. Tanaka, K. Toyoda, K. Ishikawa, and T. Yabuzaki. Quantum nondemolition measurement of spin via the paramagnetic faraday rotation. *Phys. Rev. A*, 60:4974–4979, Dec 1999.

[219] Masao Takamoto, Tetsushi Takano, and Hidetoshi Katori. Frequency comparison of optical lattice clocks beyond the dick limit. *Nat. Photonics*, 5(5):288, 2011.

[220] Masao Takamoto, Ichiro Ushijima, Noriaki Ohmae, Toshihiro Yahagi, Kensuke Kokado, Hisaaki Shinkai, and Hidetoshi Katori. Test of general relativity by a pair of transportable optical lattice clocks. *Nature Photonics*, 14(7):411–415, 2020.

[221] M. Takeuchi, S. Ichihara, T. Takano, M. Kumakura, T. Yabuzaki, and Y. Takahashi. Spin squeezing via one-axis twisting with coherent light. *Phys. Rev. Lett.*, 94:023003, Jan 2005.

[222] Haruka Tanji-Suzuki, Ian D. Leroux, Monika H. Schleier-Smith, Marko Cetina, Andrew T. Grier, Jonathan Simon, and Vladan Vuletić. Interaction between atomic ensembles and optical resonators: Classical description. In P.R. Berman E. Arimondo and C.C. Lin, editors, *Advances in Atomic, Molecular, and Optical Physics*, volume 60 of *Advances In Atomic, Molecular, and Optical Physics*, pages 201 – 237. Academic Press, 2011.

[223] Michael Tavis and Frederick W. Cummings. Exact solution for an N-molecule–radiation-field Hamiltonian. *Phys. Rev.*, 170:379–384, Jun 1968.

[224] J. Tomkovič, W. Muessel, H. Strobel, S. Löck, P. Schlagheck, R. Ketzmerick, and M. K. Oberthaler. Experimental observation of the poincaré-birkhoff scenario in a driven many-body quantum system. *Phys. Rev. A*, 95:011602, Jan 2017.

[225] Ichiro Ushijima, Masao Takamoto, Manoj Das, Takuya Ohkubo, and Hidetoshi Katori. Cryogenic optical lattice clocks. *Nat. Photonics*, 9(3):185–189, March 2015.

[226] L. Vernac, M. Pinard, and E. Giacobino. Spin squeezing in two-level systems. *Phys. Rev. A*, 62:063812, Nov 2000.

[227] David Villasenor, Saúl Pilatowsky-Cameo, Miguel A Bastarrachea-Magnani, Sergio Lerma-Hernández, Lea F Santos, and Jorge G Hirsch. Quantum vs classical dynamics in a spin-boson system: manifestations of spectral correlations and scarring. *New Journal of Physics*, 22(6):063036, 2020.

[228] Lorenza Viola, Emanuel Knill, and Seth Lloyd. Dynamical decoupling of open quantum systems. *Phys. Rev. Lett.*, 82:2417–2421, Mar 1999.

[229] Brian Vlastakis, Gerhard Kirchmair, Zaki Leghtas, Simon E. Nigg, Luigi Frunzio, S. M. Girvin, Mazyar Mirrahimi, M. H. Devoret, and R. J. Schoelkopf. Deterministically encoding quantum information using 100-photon schrodinger cat states. *Science*, 342(6158):607–610, November 2013.

[230] Vladan Vuletić *et al.* Chirp measurement of atomic states using cavity qed. , in preparation.

[231] Vladan Vuletić, Hilton W. Chan, and Adam T. Black. Three-dimensional cavity doppler cooling and cavity sideband cooling by coherent scattering. *Phys. Rev. A*, 64:033405, Aug 2001.

[232] Jun Wang, Zhao-Yu Han, Song-Bo Wang, Zeyang Li, Liang-Zhu Mu, Heng Fan, and Lei Wang. Scalable quantum tomography with fidelity estimation. *Phys. Rev. A*, 101:032321, Mar 2020.

[233] Wen-Li Wang, Jie Ye, Hai-Ling Jiang, Zhi-Yi Bi, Long-Sheng Ma, and Xin-Ye Xu. Frequency stabilization of a 399-nm laser by modulation transfer spectroscopy in an ytterbium hollow cathode lamp. *Chinese Physics B*, 20(1):013201, 2011.

[234] P. Wcisło, P. Ablewski, K. Beloy, S. Bilicki, M. Bober, R. Brown, R. Fasano, R. Ciuryło, H. Hachisu, T. Ido, J. Lodewyck, A. Ludlow, W. McGrew, P. Morzyński, D. Nicolodi, M. Schioppo, M. Sekido, R. Le Targat, P. Wolf, X. Zhang, B. Zjawin, and M. Zawada. New bounds on dark matter coupling from a global network of optical atomic clocks. *Science Advances*, 4(12), 2018.

[235] Christian Weedbrook, Stefano Pirandola, Raúl García-Patrón, Nicolas J. Cerf, Timothy C. Ralph, Jeffrey H. Shapiro, and Seth Lloyd. Gaussian quantum information. *Rev. Mod. Phys.*, 84:621–669, May 2012.

[236] K. X. Wei, P. Peng, O. Shtanko, I. Marvian, S. Lloyd, C. Ramanathan, and P. Cappellaro. Emergent prethermalization signatures in out-of-time ordered correlations. *Phys. Rev. Lett.*, 123:090605, 2019.

[237] Stephan Welte, Bastian Hacker, Severin Daiss, Stephan Ritter, and Gerhard Rempe. Photon-mediated quantum gate between two neutral atoms in an optical cavity. *Phys. Rev. X*, 8:011018, Feb 2018.

[238] G Wendin. Quantum information processing with superconducting circuits: a review. *Reports on Progress in Physics*, 80(10):106001, sep 2017.

[239] Tatjana Wilk, Simon C. Webster, Axel Kuhn, and Gerhard Rempe. Single-atom single-photon quantum interface. *Science*, 317(5837):488–490, 2007.

[240] D. J. Wineland, J. J. Bollinger, W. M. Itano, and D. J. Heinzen. Squeezed atomic states and projection noise in spectroscopy. *Phys. Rev. A*, 50:67–88, Jul 1994.

[241] D. J. Wineland, J. J. Bollinger, W. M. Itano, F. L. Moore, and D. J. Heinzen. Spin squeezing and reduced quantum noise in spectroscopy. *Phys. Rev. A*, 46:R6797–R6800, Dec 1992.

[242] David J Wineland, C Monroe, Wayne M Itano, Dietrich Leibfried, Brian E King, and Dawn M Meekhof. Experimental issues in coherent quantum-state manipulation of trapped atomic ions. *Journal of Research of the National Institute of Standards and Technology*, 103(3):259, 1998.

[243] H. M. Wiseman and G. J. Milburn. All-optical versus electro-optical quantum-limited feedback. *Phys. Rev. A*, 49:4110–4125, May 1994.

[244] NC Wong and John L Hall. Servo control of amplitude modulation in frequency-modulation spectroscopy: demonstration of shot-noise-limited detection. *JOSA B*, 2(9):1527–1533, 1985.

[245] Baochen Wu, Graham P. Greve, Chengyi Luo, and James K. Thompson. Site-dependent selection of atoms for homogeneous atom-cavity coupling, 2021.

[246] Megan Yamoah, Boris Braverman, Edwin Pedrozo-Peñafiel, Akio Kawasaki, Bojan Zlatković, and Vladan Vuletić. Robust khz-linewidth distributed bragg reflector laser with optoelectronic feedback. *Optics express*, 27(26):37714–37720, 2019.

[247] D. Yang, C. Laflamme, D. V. Vasilyev, M. A. Baranov, and P. Zoller. Theory of a quantum scanning microscope for cold atoms. *Phys. Rev. Lett.*, 120:133601, Mar 2018.

[248] Aaron W Young, William J Eckner, William R Milner, Dhruv Kedar, Matthew A Norcia, Eric Oelker, Nathan Schine, Jun Ye, and Adam M Kaufman. Half-minute-scale atomic coherence and high relative stability in a tweezer clock. *Nature*, 588(7838):408–413, 2020.

[249] Chenghui Yu, Weicheng Zhong, Brian Estey, Joyce Kwan, Richard H Parker, and Holger Müller. Atom-interferometry measurement of the fine structure constant. *Annalen der Physik*, 531(5):1800346, 2019.

[250] GuoFeng Zhang and Matthew R James. Quantum feedback networks and control: a brief survey. *Chinese Science Bulletin*, 57(18):2200–2214, 2012.

[251] Wei Zhang, MJ Martin, C Benko, JL Hall, J Ye, C Hagemann, T Legero, U Sterr, F Riehle, GD Cole, et al. Reduction of residual amplitude modulation to 1× 10-6 for frequency modulation and laser stabilization. *Optics letters*, 39(7):1980–1983, 2014.

[252] Yan-Lei Zhang, Chang-Ling Zou, Xu-Bo Zou, Liang Jiang, and Guang-Can Guo. Detuning-enhanced cavity spin squeezing. *Phys. Rev. A*, 91:033625, Mar 2015.

[253] Yajuan Zhao, Rui Zhang, Wenlan Chen, Xiang-Bin Wang, and Jiazhong Hu. Creation of Greenberger-Horne-Zeilinger states with thousands of atoms by entanglement amplification. *npj Quantum Inf.*, 7:24, 2021.

[254] Xin Zheng, Jonathan Dolde, Varun Lochab, Brett N Merriman, Haoran Li, and Shimon Kolkowitz. Differential clock comparisons with a multiplexed optical lattice clock. *Nature*, 602(7897):425–430, 2022.

[255] Tilman Zibold, Eike Nicklas, Christian Gross, and Markus K. Oberthaler. Classical bifurcation at the transition from rabi to josephson dynamics. *Phys. Rev. Lett.*, 105:204101, Nov 2010.